MATERIALS AND MOLECULES FOR POLLUTION FREE CLEAN ENERGY

Yuanyuan Shi

UNIVERSITAT ROVIRA i VIRGILI

Materials and Molecules for Pollution Free Clean Energy

YUANYUAN SHI

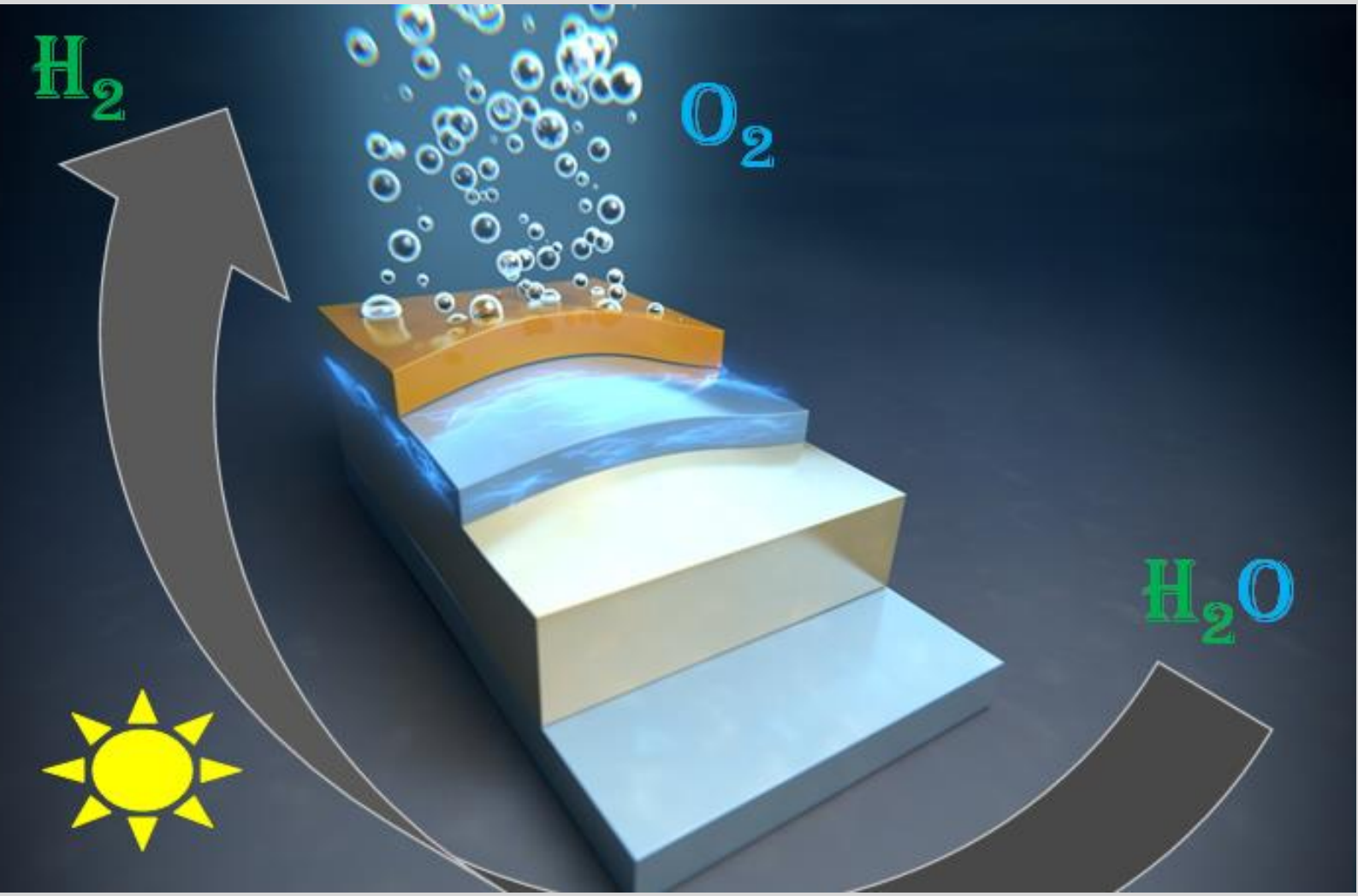

DOCTORAL THESIS
2018

UNIVERSITAT ROVIRA I VIRGILI
MATERIALS AND MOLECULES FOR POLLUTION FREE CLEAN ENERGY
Yuanyuan Shi

UNIVERSITAT ROVIRA I VIRGILI
MATERIALS AND MOLECULES FOR POLLUTION FREE CLEAN ENERGY
Yuanyuan Shi

UNIVERSITAT ROVIRA I VIRGILI
MATERIALS AND MOLECULES FOR POLLUTION FREE CLEAN ENERGY
Yuanyuan Shi

Yuanyuan Shi

Materials and molecules for pollution free clean energy

Doctoral Thesis

Supervised by

Prof. Antoni Llobet Dalmases &

Prof. Mario Lanza Martinez

Institute of Chemical Research of Catalonia (ICIQ)

Tarragona,

2018

UNIVERSITAT ROVIRA I VIRGILI
MATERIALS AND MOLECULES FOR POLLUTION FREE CLEAN ENERGY
Yuanyuan Shi

Accreditation

I STATE that the present study, entitled "Materials and molecules for pollution free clean energy", presented by Yuanyuan Shi for the award of the degree of Doctor, has been carried out under my supervision at the Institute of Chemical Research of Catalonia and that it fulfills all the requirements to be eligible for the International Doctor Distinction.

Tarragona, August 30th, 2018

Doctoral Thesis Director and Tutor

Prof. Antoni Llobet Dalmases

Doctoral Thesis Director

Prof. Mario Lanza Martinez

Acknowledgements

First of all, I would like to thank my directors, Prof. Antoni Llobet and Prof. Mario Lanza for giving me opputinity to start my PhD study and research with them, providing me guidances and suggestions, being my references, and teaching me how to communicate well my scientific discoveries in the community during the whole PhD study. Dr. Carolina Gimbert-Suriñach is specially acknowledged for working with me in the lab, and giving me suggetions whenever I felt confused with the research. Mª Jose Gutiérrez is gratefully acknowledged for providing me addimistraive support. And also, I would like to thank all my labmates: Serena, Laia, Sam, Lorenzo, Roc, Abi, Asmaul, Chuanjun, Laura, Marta, Marcos, Natalii, Nabi, Jan Holub, Jan Oldengott, Pablo, Primavera and Sergi in Prof. Antoni Llobet's group (http://www.iciq.org/research/research_group/prof-antoni-llobet/), and aslo all the members in Prof. Mario Lanza's group (http://lanzalab.com/). All the tecinical and admistative supports at ICIQ and URV are secreally acknowledaged. I specially appreciate the support received from the Institute of Functional Nano and Soft Materials of Soochow University, for allowing me using their clean room and all the characterization techniques as much as I needed and for free.

I also would like to thank all the coauthors of my publications and cooperators, especially to those from Stanford University, Harvard University, University of Coledge Cork, Central European Institute of Technology (CEITEC) and Institute for Microelectronicsand Microsystems of National Research Council of Italy (IMM-CNR). Professor Paul C. McIntyre is sepecially acknowledged here for the techincial discussions and allow me to use the equipments in his lab when I was in Stanford University for the exchange program. I acknowledge the institutions that funded my research for making

possible this amazing project, especially to the Young 1000 Program, the National Science Foundation of China, Institut Català d'Investigació Química, Ministerio de Economía y Competitividad and FEDER (PRI-PIBN-2011-1278, CTQ 2013-49075-R, CTQ 2015-64261-R and CTQ 2016-80058-R), AGAUR (2014 SGR-915).

最后，我想对一直以来鼓励支持我的家人朋友说，谢谢你们，有你们的陪伴，前行的路虽然艰难但并不孤单。

Abstract

Chapter 1: General Introduction

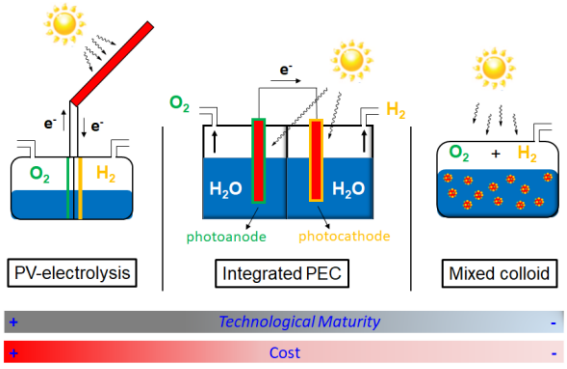

The combustion of fossil fules induced environmental and energy problems are presented firstly in this charpter. The most promising method for solving these problem is to develop pollution free clean energy. Solar-driven water splitting devices are briefly introduced for transferring solar energy to storable and transportable hydrogen. The most promising solar-driven water splitting configurations and efficient water oxidation catayst are discussed and compared. The progress in the design and performance of the latters are also described and their major breakthroughs are highlighted.

Chapter 2: Objectives

Chapter 3: Nanoscale characterization on airborne pollutant particles

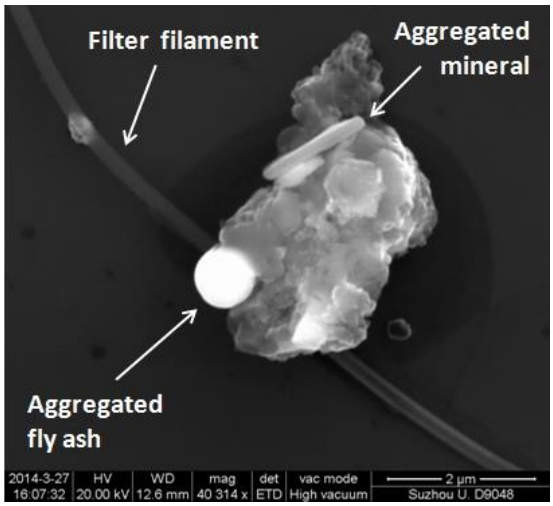

For the first time we combined the morphological, chemical and mechanical characterizations on airbone pollutant particles with the aerodynamics diameters less than 2.5 µm, $PM_{2.5}$ particles. Three kinds of particles are observed most commonly, which are carbon-rich fluffy soot aggregates, elongated minerals with high content of metals, and spherical fly ash made of metal-silicates. Among them, most of the particles are surrounded by a dark trace layer made of carbon alkali metals, hydrogen and CH groups. The soot aggregates show strong adhesiveness and aggregation.

Chapter 4: Cheap metal oxides functionalized silicon photoanodes for photoelectrochemical water splitting devices

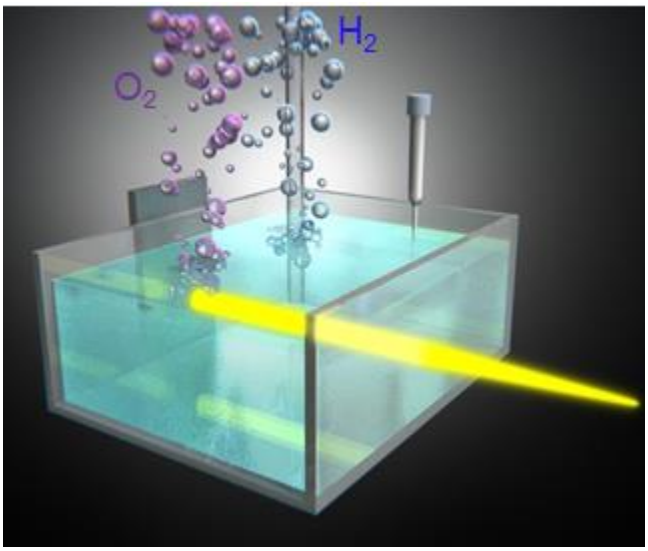

Silicon is a very popular material for photoelectrochemical water splitting devices due to its good photon absorbing ability and suitable bandgap. Here we use cheap metal oxides (CuO and NiO_X) as water oxidation catalysts to functionalize the silicon photoanodes, and exhaustively analyze the reliability and ageing mechanisms of ultrathin Ni coated Si photoanodes. After that, in Ni coated silicon photoanodes, the nickel and silicon interface is enigeered through replacing native silicon oxide by titanium.

Chapter 5: Molecular catalysts for photovoltaic-electrolysis water splitting devices

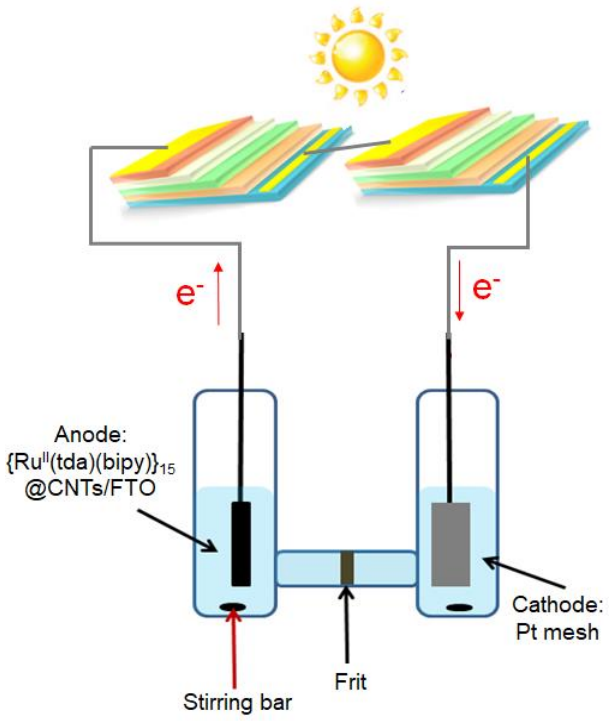

Photovoltaic-elctrolysis (PV-EC) water splitting configuration is with the most mature technology for solar-driven water splitting devices. One of the main challenge that blocks its practical application is the high cost of the involved materials. Therefore, one of the main goals in this field is to achieve a high solar-to-hydrogen (STH) effiency PV-EC water spliiting devices with low cost. Here we implement for the firt time the use of molecular catalysts in the solar-driven PV-EC water splitting configuration by using state of art perovskite amd commercially available triple junction III-V semiconductors based solar cells. The latter shows the highest STH efficiency at neutral pH (room temperature) reported so far. This study may pave the way to realize the large scale production of hydrogen from sunlight.

Chapter 6: General Conclusions

Table of contents

Accreditation I

Acknowledgements II

Abstract V

Table of contents IX

Chapter 1: Introduction 1

1.1 Environmental and energy problems 2

1.2 Solar-driven water splitting devices 5

1.3 Water oxidation catalysis 8

1.4 Photoelectrochemical (PEC) water splitting 11

1.5 Photovoltaic cells based water splitting 16

1.6 References 18

Chapter 2: Objectives 29

Chapter 3: Nanoscale characterization on airborne pollutant particles 33

Paper A = Nanoscale characterization of $PM_{2.5}$ airborne pollutants reveals high adhesiveness and aggregation capability of soot particles 34

Paper B = Interaction between $PM_{2.5}$ airborne pollutants and third bodies 87

Chapter 4: Cheap metal oxides functionalized silicon photoanodes for photoelectrochemical water splitting devices 109

Paper C = CuO-functionalized silicon photoanodes for photoelectrochemical water splitting devices 110

Paper D = Ageing mechanisms of highly active and stable nickel-coated silicon photoanodes for water splitting 139

Paper E = Substitution of native silicon oxide by titanium in Ni-coated silicon photoanodes for water splitting solar cell 163

Chapter 5: Molecular catalysts for PV-EC water splitting devices 187

Paper F = An anode based on a ruthenium molecular water oxidation catalyst for a photovoltaic-electrolysis water splitting with solar to hydrogen efficiency 188

Chapter 6: Conclusions and perspectives 217

Appendix 223

Appendix A: Scientific curriculum vitae 223

Appendix B: Acronyms 231

Chapter 1:

General introduction

In this chapter, the energy and environmental problems derived from fossil fuels combustion will be discussed (section 1.1). In order to solve these problems, solar energy based devices have been widely developed. In this thesis, I will focus on the solar-driven water splitting devices (section 1.2). Particular emphasis on the water oxidation catalysis field, photoelectrochemcial (PEC) water splitting nad photovoltaic-eletrolysis (PV-EC) water splitting will be describled in detail in sections 1.3, 1.4 and 1.5, respectively.

1.1 Environmental and energy problems

The combustion of fossil fuels produces a myriad of toxic air pollutants (Figure 1a) and carbon dioxide (CO_2), which is a significant greenhouse gas and changes our climate (Figure 1b). These emissions have been the most significant threat to global environment, which endanger the health and future of the whole human society. It has been reported that the toxic air pollutant and climate change caused by fossil fuels combustion, result in more and more biological and psychological diseases to young

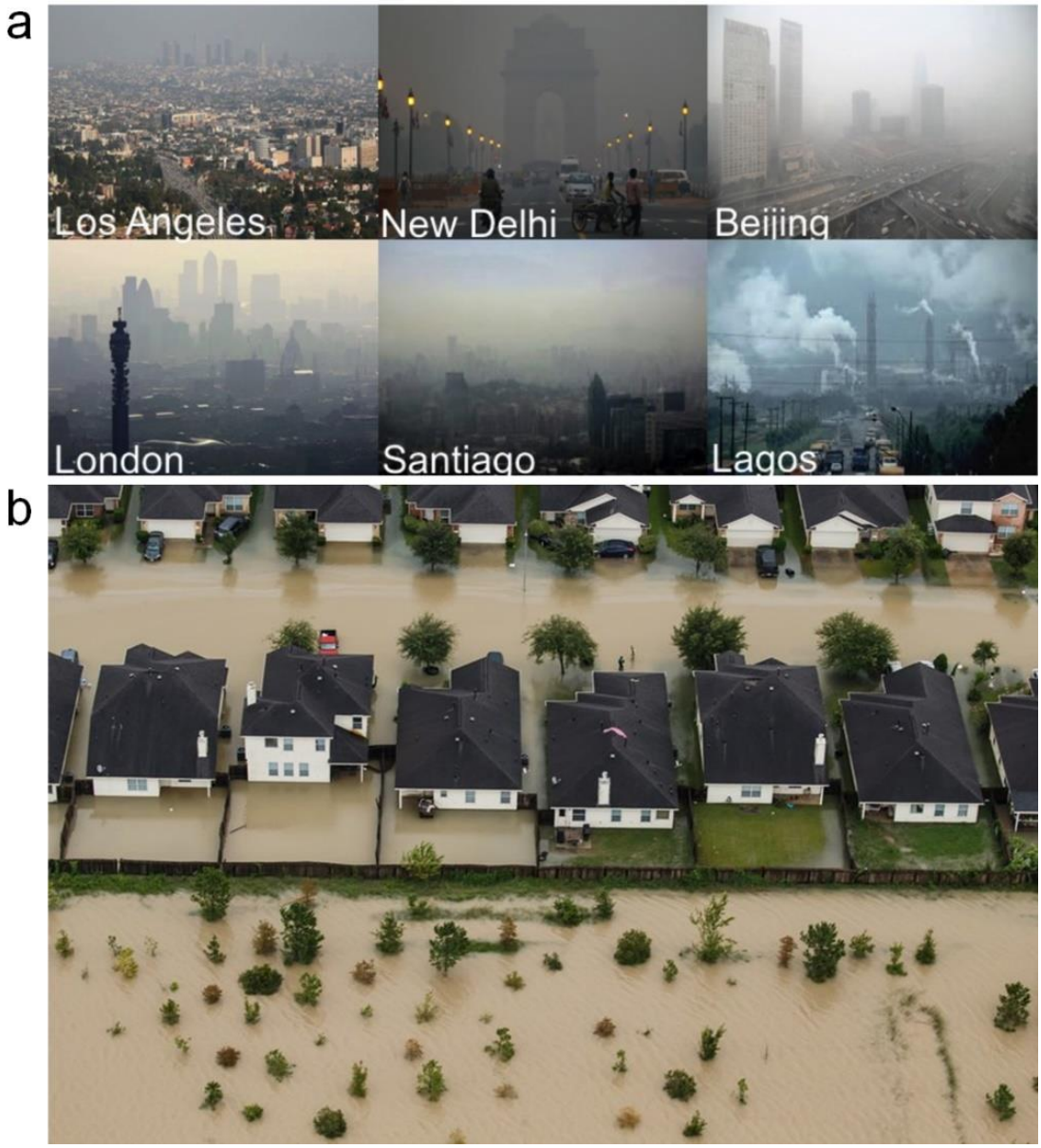

Figure 1. (a) Global air pollution problem. (b) Climate change induced floodwater. Reproduced with permission from Refs. [1] and [2], copyrights 2016 University Corporation for Atmospheric Research and 2017 Time Inc.

childrens.[3] Since the childrens require 3-4 times more food and breathe more air than adults for a body weight basis, in this case they get more exposure to the pollutants from air and food.[4-5] The World Health Organization (WHO) has estimated that the children under 5 years old suffers more than 40 % of environmental related disease and more than 88% of climate change.[6-8] And recently WHO has released that 90% of people worldwide breathe polluted air, in which the fine particles can penetrate into the lungs and cardiovascular system deeply and result in 7 million people dying every year due to polluted air leaded lung cancer, heart disease, stroke, respiratory infections and chronic obstructive pulmonary.[9]

In general, the air pollution is caused by the combustion of fossil fuels including coal, gasoline, diesel fuel, oil and natural gas, which are combusted for electricity production, transportation, heating and industry.[10] This energy related fossil fuel combustion generates almost all nitrogen oxide and sulfur dioxide emissions to the atmosphere,[11] and 85% airbone particulate pollution, which is respirable and causes a long-term inhalation hazard.[12] Moreover, the combustion of these fossil fuels can generate the emission of black carbon, nitrogen and sulfur dioxides, polycyclic aromatic hydrocarbons (PAH), mercury and volatile chemicals, which form the ground level ozone (O_3). It has been pointed out that 300 million children live in areas with air pollution that exceeds international limits at least six times.[13] This is injustice since the adults create the problems by their activities, but the children suffer more to the caused air pollution and climate change. 35 billion metric tons of CO_2 from human activities related to energy consumption are emitted to the atmosphere every year.[14] Most (45%) of the CO_2 emission is from coal combustion (Figure 2a), even though it provides 28% of the total primary energy supply (TPES) for the world in 2015.[15] The CO_2 emission from oil and natural gas consumption accounts for 34 % and 20 %, respectively (Figure 2a).[15] The National

Oceanic and Atmospheric Administration (NOAA) uses the Annual Greenhouse Gas Index to track the influence of climate altering greenhouse gases. From 1990-2016, this index has increased by 40%, most of which are from the increase of CO_2 emission.[16] Moreover, it has been predicted that the CO_2 levels will reach to their highest in the atmosphere in 800,000 years.[17]

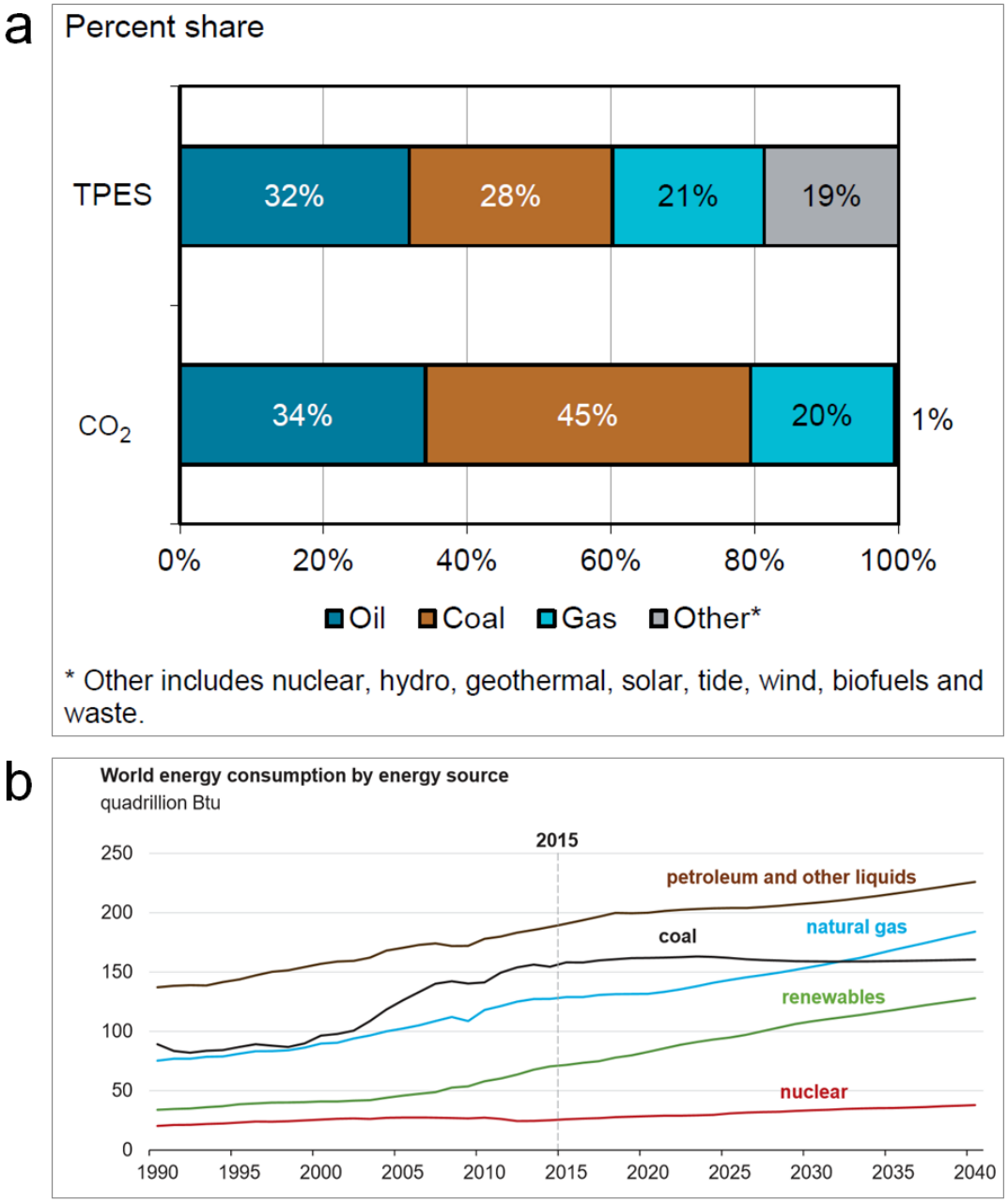

Figure 2. (a) Percentage of CO_2 emissions from the world primary energy supply. (b) The word energy consumption from different types of energy sources in the past and following decades. Reproduced from Refs. [15] and [18], copyrights International Energy Agency (IEA) 2017 and U.S. Energy Information Administration (EIA) 2017.

Except for the air pollution and climate change from consumption of fossil fuels, these fossil fuels are formed from the remains of the living plants and animals that lived millions of years ago, which are not renewable energy sources. The BP statistical Review of World Energy 2016 has calculated[19] how long it lasts until all the fossil fuels reserves run out based on the known reserves and annual production levels in 2015. The reserves-to-product ratio shows that the global coal will run out in 115 years, however the oil and natural gas remaining will run out in ~50 years, respectively.[19] Even though the development of fracking gas may provide enough natural gas for the next century, the CO_2 emissions and air pollution will still endanger the future of the human society. In order to build a sustainable future for next generations, the human activities should become less dependent on the fossil fuels, and the study of renewable and clean energy is necessary to be investigated for letting it become the major energy provider for the next century. The US Energy Information Administration predicts that around half of the world energy consumption will come from renewables by the early 2040s (Figure 2b).[18] As one of the main renewable energy sources (wind, hydropower, solar, etc.),[20] solar energy plays a very important role in the development of renewables, since sunlight is decentralized and inexhaustible in the world. Moreover, the Earth's surface can receive ~ 1.2×10^{14} kJ solar energy per second.[21]

1.2 Solar-driven water splitting devices

Even though the energy harvested from sunlight is a desirable method to fulfill the demand of clean energy for the global world, there are still challenges remaining due to the sunlight's daily and seasonal variability. In order to make the solar energy storable, transportable and available when needed, the sunlight needs to be converted into chemical fuel/chemical bonds efficiently and cost-effectively, with meeting the demand at a global scale.[22-23] In 1972, Fujishima and Honda firstly proposed the solar-driven electrolysis

prototype, which used a n-type TiO_2 electrode as a light absorber for decomposing water to convert solar energy into a simple chemical bond (hydrogen, H_2) (*Equation 1*).[24] After this, solar-driven water splitting has been studied massively as a renewable, storable and green emerging technology (see Figure 3).

Water splitting: $2H_2O \rightarrow O_2 \uparrow + 2H_2 \uparrow$, $\Delta E = 1.23$ V (*Equation 1*)

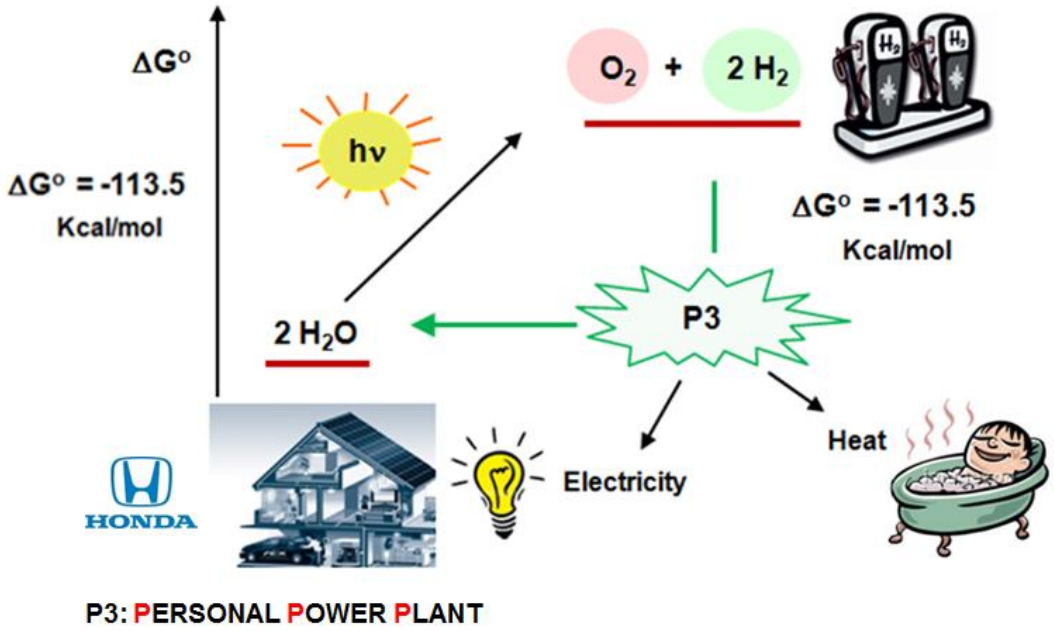

Figure 3. Solar-driven water splitting for home hydrogen fueling station, which is renewable and clean. Reproduced from Ref. [25], copyright 2008 Alternative Energy Info.

There are three main components required for the solar-driven water splitter devices: i) light absorber, ii) catalysts for oxygen and hydrogen evolution half reactions (OER and HER, *Equations 2-3*), iii) a membrane to separate the generated oxygen (O_2) and H_2.

OER: $2H_2O + 4h^+ \rightarrow O_2 \uparrow + 4H^+$ (*Equation 2*)

HER: $4H^+ + 4\,e^- \rightarrow 2H_2 \uparrow$ (*Equation 3*)

Three kinds of solar-driven water splitting devices[26] have been proposed to achieve an efficient, robust and scalable H_2 generation for addressing the terawatt challenge:[27] i) PV-EC water splitting cells,[28-36] ii) integrated PEC water splitting cells,[37-

[41] iii) mixed colloid system (Figure 4).[42-43] The first strategy is a mature technology since it combines a commercial PV module (light absorber) with a water electrolyzer, which are both developed technologies. However, the cost of the PV-EC water splitting devices is too high (estimated US $8 per kg),[44] compared to the traditional methods by using fossil fuels.[45] Considering the economic cost of these three kinds of devices, the mixed colloid system will be the most attractive strategy, but its STH efficiency is very low, which is around 1%-3% up to date.[26, 43] Meanwhile, this system produces a mixture of H_2 and O_2, which need to be separated to avoid the back reactions.[43] The integrated PEC water splitting system is an intermediate strategy between PV-EC cells and mixed colloid system, which may provide a high STH efficiency with an affordable cost (estimated US $3 per kg).[26, 44, 46-49] It has been reported that this technology can be economically feasible and competitive if its efficiency can be improved to > 10 % and with a lifetime of >5 years,[31, 50-51] The details of the PEC water splitting devices are described in section 1.4.

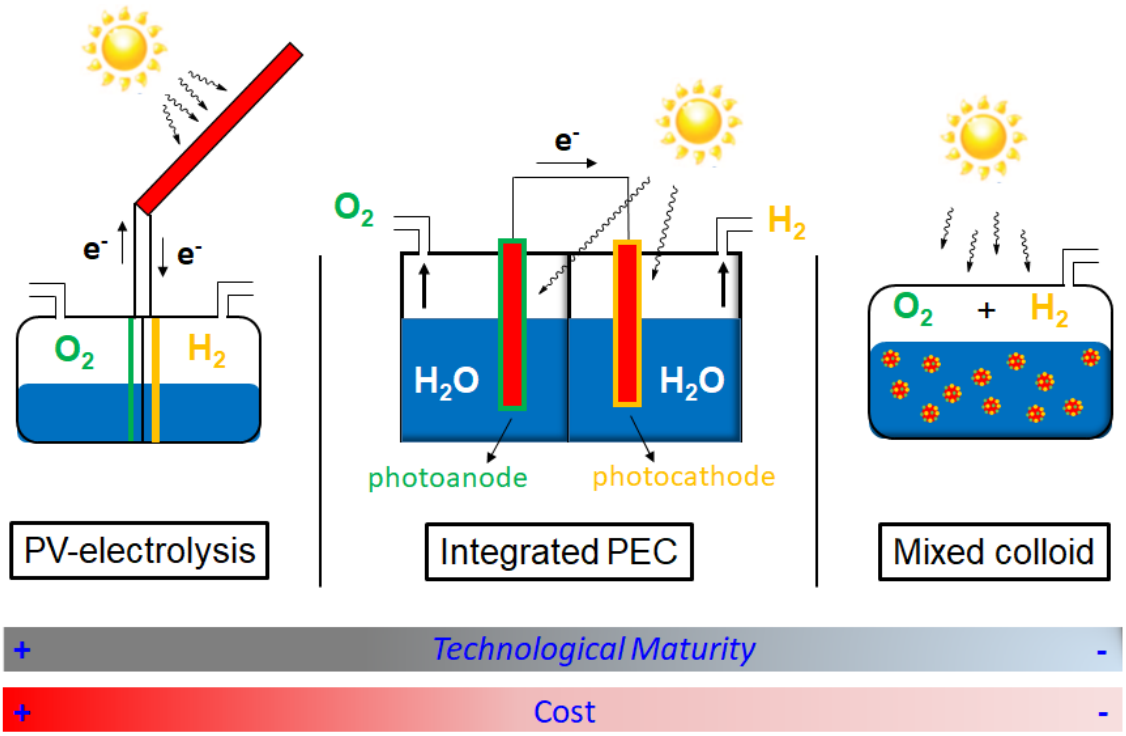

Figure 4. Schematic of the three main solar-driven water splitting systems. (left) PV-EC system, (middle) wired tandem PEC system with a photoanode (red bar with green coating) and a photocathode (red bar with yellow coating), and (right) mixed colloid system. They are ordered by the maturity of the technology and cost of the manufacture.

1.3 Water oxidation catalysis

As it is shown in *Equation 1-3*, the overall water splitting reaction can be devided into two half reactions (OER and HER). The water oxidation half reaction happens at a high thermodynamic potential of E^0 = -1.23 V vs. normal hydrogen electrode (NHE) at pH = 0.[52] It is more difficult than the water reduction half reaction since water oxidation requires the removal of four protons and four electrons from two water molecules and the formation of one O-O bond. Thus, a catalyst with the ability to reduce the overpotential (the additional potential needed to overcome the reaction barriers) is necessary for water oxidation, which should help this half reaction happen at a potential as close as possible to the thermodynamic one.[53] This catalyst should be stable in aqueous solutions and at high oxidation states.[54] In this thesis, two types of water oxidation catalysts have been explored in different solar-driven devices, namely, metal oxides and molecular complexes.

As stated above, the high energy demands of the water oxidation reaction implies that the catalyst should be stable at high potentials and therefore the stability of metal oxides at high oxidative states is very important for the catalytic process. Figure 5

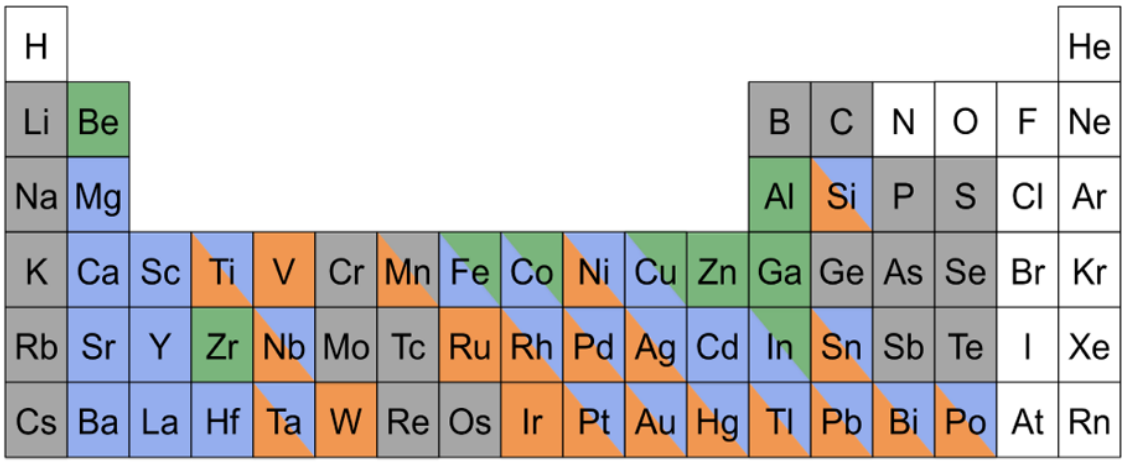

Figure 5. Stability of different metal oxides or hydroxides at different aqueous solutions. The orange, green and blue color represents the stability at low, neutral and high pH electrolytes, respectively. The combination colors (blue/green, and blue/orange) indicates the stability at a wide pH range. The combination of the orange and gray indicates the stability of the moderate oxidative states at low pH electrolytes. Reproduced with permission form Ref. [55], copyright Pergamon Press 1966.

indicates the stability of different metal oxides or hydroxides at low, neutral and high pHs, which shows that earth abundant metals based oxides or hydoxides (at high oxidative states) are more stable in a high pH electrolyte.[55] The use of transition metal oxides or hydroxides have been studied extensively to promote the water oxidation half reaction.[56-58] Among them, IrO_2[59-64] and RuO_2[65-67] are the most active and stable catalysts for OER in both base and acid conditions (depending on the synthesis/deposition methods). However, Ir and Ru are scarce metals on earth, which increases the cost of the H_2 generation. Many first-row transition metals based oxides and (oxy)hydroxides, such as manganese,[68-73] iron,[74-77] cobalt,[78-82] nickel,[83-89] copper oxides,[90-93] have been developed to sever as a low-cost and efficient catalyst for the water oxidation reaction.[58] T. F. Jaramillo et al. have compared the overpotentials of different metal oxides as water oxidation catalysts to achieve a current density of 10 mA/cm^2 after two hours controlled current electrolysis (Figure 6).[94-95] Among the first-row transition metals, cobalt and nickel oxides show very efficient and robust behavior in alkaline electrolytes.[58] Moreover, for nickel oxides based water oxidation catalyst, even accidental iron incorporation (from electrolytes or other sources) into nickel oxides can enhance its catalytic activity.[96]

Even though metal oxides show very active catalytic activity and some of them are earth abundant, their working mechanisms are often unknown or difficult to evaluate and their modification and/or tunability is limited to particle size and morphology. As a

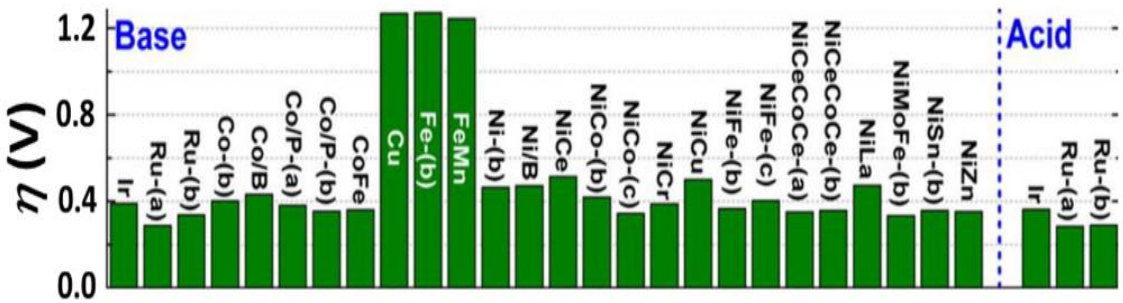

Figure 6. The required overpotential of different metal oxides as water oxidation catalyst to reach a current density of 10 mA/cm^2 after two hours controlled current electrolysis at base (pH 14) and acid (pH 0) conditions. Reproduced from Ref. [94], copyright American Chemistry Society 2015.

consequence, it is difficult to design better metal oxide catalyst in a rational manner. In contrast, it is much easier to tune, design and characterize the active center of molecular catalysts, which helps the understanding of their catalytic mechanisms. The first molecular catalyst capable of oxidizing water to dioxygen was discovered in 1982 by T. J. Meyer,[97] which is around 80 years later than the metal oxides used for water oxidation.[98] By understanding the catalytic mechanisms of molecular catalysts, their designs can be tuned step-by-step to reach a minimum overpotential at maximum Turnover Frequencies (TOFs) and long stability under neutral conditions. Many transition metal complexes can serve as molecular catalysts for OER, including manganese,[99] copper,[100-104] iron,[105] cobalt,[106-108] iridium[109] and ruthenium[110-114] complexes, in which the metals are used as active centers. Most of the mechanistic studies have been done for ruthenium complexes,[115] which can be extended to other transition metals based molecular catalysts.

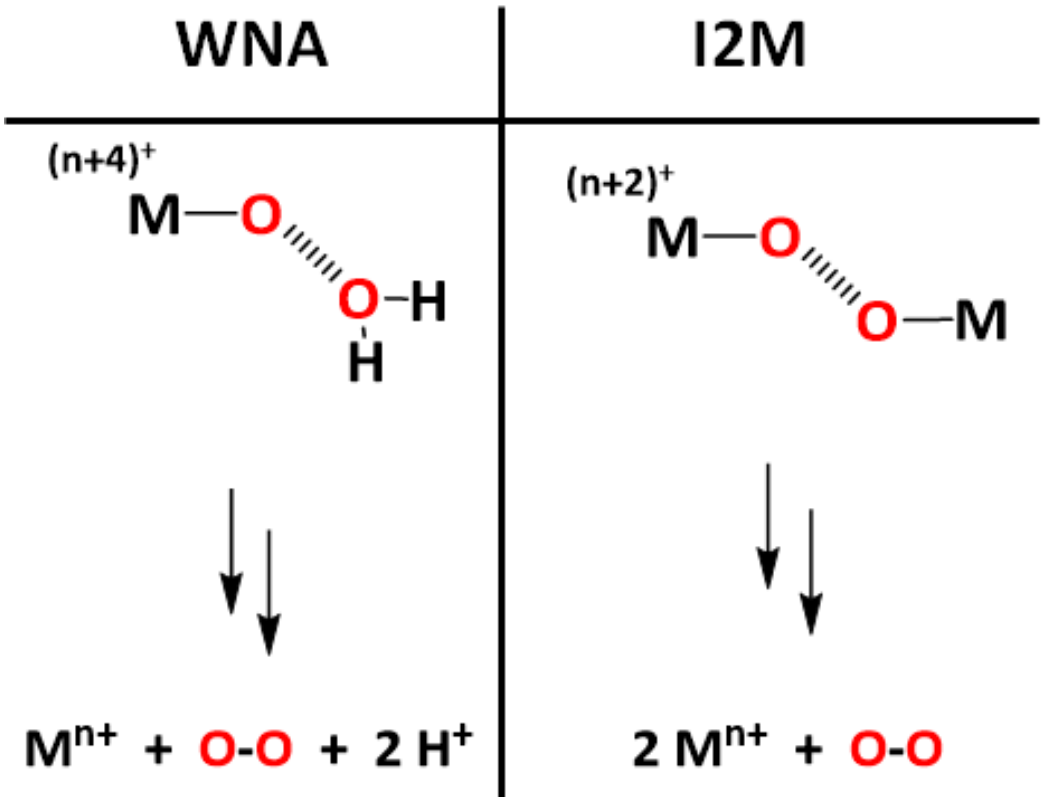

Figure 7. Two kinds of the mostly accepted O-O bond formation mechanisms. Reproduced from Ref. [116], copyright 2014 Royal Society of Chemistry.

One of the important mechanistic steps during the water oxidation reaction is the formation of the O-O bond. There are two kinds of proposed mechanisms, which are i) water nucleophilic attack (WNA) and ii) the interaction of two metal-oxo (M-O) units, which can happen in an inter or intramolecular manner (I2M) (Figure 7).[104, 115] In the WNA mechanism, one water molecule attacks a highly oxidized M-O unit, which helps to break the M-O bond and then forms a hydroperoxide species. Finally, an oxygen molecule can be released after a posterior oxidation process.[103] In contrast, the I2M mechanism is based on the merging of two highly oxidized M-O units.[117-118] In the whole water oxidation process, the formation of O-O bond is very important, which often decides the rate of the whole process.

The mechanistic understanding of the water oxidation reaction by molecular complexes has allowed the field to progress tremendously in the last ten years, reaching catalytic rates higher than that of the Oxygen Evolving Complex in Photosystem II, responsible for the water oxidation reaction in natural photosynthetic systems. In particular, the catalyst [Ru(tda)(py)$_2$] (where tda: [2,2':6',2"-terpyridine]-6,6"-dicarboxylato and py = pyridine) performs at a rate of 7 700 s^{-1} at pH 7 and 50 000 s^{-1} at pH 10.[98]

1.4 PEC water splitting

The main elements of PEC water splitting devices include photoelectrodes as light absorbers and catalytic surface area, electrolyte and a membrane for separating the produced O_2 and H_2. In an integrated PEC system (as it is shown in Figure 4), it needs a n-type semiconductor as the photoanode, and a p-type semiconductor as the photocathode to absorb light. When a semiconductor is illuminated, it can absorb photons with larger energies than its band gap energy (E_g), then a pair of electrons and holes (charge carries) can be created. The electrons will jump to the conduction band (CB) for water reduction,

which will leave the holes in the valence band (VB) for water oxidation. The water oxidation requires the VB potential of the photoanode (under illumination) to be more positive than the thermodynamic water oxidation potential (1.23 V vs. NHE at pH 0). While water reduction requires the CB potential of the photocathode (under illumination) to be more negative than the thermodynamic water reduction potential (0 V vs. NHE at pH 0). Therefore, the selection of suitable materials is very important as photoanodes and photocathodes for PEC water splitting. Figure 8 shows the band positions of various semiconductors, which can be used as photoanode/photocathode in PEC water splitting devices. An idea photoanode or photocathode needs the semiconductor to fit with the following characteristics:[44] i) the semiconductor should be with a bandgap between 1.9 eV and 3.2 eV with suitable CB and VB positions. Since the natural sunlight consists of 43% visible (400-700 nm), 5% UV light (300-400 nm) and 52% infrared light (700-2500 nm), the appreciable absorption of visible light is needed for increasing the STH

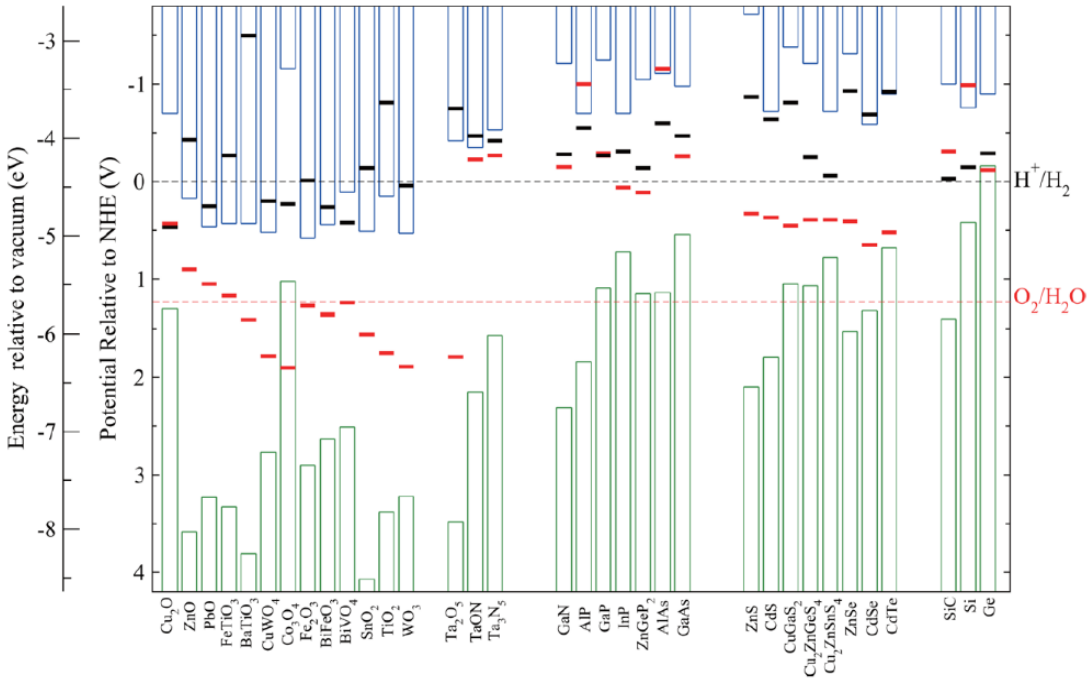

Figure 8. Band gap positions of various semiconductors with respect to the redox potentials (dashed black and red lines) of water splitting at pH 0. The red and black bars represent the calculated reduction and oxidation potentials of different semiconductors at pH 0 and room temperature (298.15 K) with 1 bar pressure. Reproduced with permission form Ref. [119], copyright Royal Society of Chemistry 2012.

Table 1. Earth abundant materials based photoanodes for PEC water splitting. $J_{1.23\ V}$ means the current density of the photoanodes at 1.23 V vs. reversible hydrogen electrode (RHE). Reproduced with permission from Ref. [120], copyright Wiley-VCH 2018.

OER catalyst	Photoactive substrate	Morphology	$J_{1.23\ V}$ [mA/cm^2]	pH	Stability
Co_3O_4	Fe_2O_3	Nanorod	1.2	13.6	–
CoO_x	Fe_2O_3	Multidimential nanoplates	2.29	13.6	–
FeOOH	Fe_2O_3	Plate	0.85	13.6	70 h
FeOOH	Fe_2O_3	Nanorod	1.21	13.6	2.5 h
$NiCeO_x$	Fe_2O_3	Nanorod	-0.8	13.6	–
FeOOH	Ti:Fe_2O_3	Nanorod	2.31	13.6	–
Co_3O_4	Ta_3N_5	Particulate	>1.5 (>420 nm)	13.6	2 h
CoPi	Ba:Ta_3N_5	Nanorod	6.7	13.6	1.7 h
Co_3O_4	Ta_3N_5/Fh	Porous cubic	5.2	13.6	6 h
NiOOH	Ta_3N_5/MoO_3	Porous cubic	≈1.4	13.6	12 h
CoPi	W:BVO_4	Planar	3.6	7.3	–
CoPi	BVO_4/WO_3	Helical nanorod	6.72	7	–
CoO_x/NiO_x	BVO_4	Particulate	3.5	7	16 h
$NiFeO_xBi$	BVO_4	Nanoworm	3.2 (0.6 V)	9.5	10 h
$NiFeO_xBi$	Ni/Mo:BVO_4	Particulate	≈2.6 (0.6 V)	9	1100 h
FeOOH/NiOOH	BVO_4	Nanoporous	4.5	7	48 h
FeOOH/NiOOH	WO_3/(W,Mo):$BiVO_4$	Helical nanorod	5.35	7	
Fe(Ni)OOH	Mo:BVO_4	Nanocone	5.82	7	5 h
FeOOH	BVO_4	Nanoporous	≈1.7	7	6 h
Ni:FeOOH	WO_3/BVO_4	Nanowire	4.5	7	2.7 mA 3 h
CoFe-H	BVO_4	Nanoporous	2.48	7	–
Co/$Co(OH)_2$	n-Si	Planar	>16	13.6	–
CoO_x	n-Si	Planar	23.2	13.6	2500 h
Ni/NiO_x	n-Si	Planar	>10	9.5	80 h
CoO_x/NiO_x	n-Si	Planar	28	13.6	1700 h
NiOOH	n-Si/TiO_2/ITO	Planar	≈18	14	–
CoO_x	p^+n-Si	Nanotexture	17	13.6	24 h
Co_3O_4/$Co(OH)_2$	p^+n-Si	Planar	30.8	13.6	72 h
Ni/NiO_x	p^+n-Si	Planar	29	13.6	1200 h
NiFe alloy	p^+n-Si	Planar	31.2	13.6	10 h
$NiSe_2$	a-Si	Nanowire	5.8	13.6	12 h
NiO_x	a-Si/c-Si	Pyramidal	21.8	13.6	–

efficiency; ii) The charge carriers in the semiconductor needs to be separated and transported efficiently to reduce the charge recombination. The carrier mobility, nanostructure and crystallinity of the semiconductor can decide the efficiency of charge carriers separation and transportation; iii) The semiconductor should show good catalytic

activity and long stability. Surface charge accumulation, which leads to charges recombination, can be avoided by increasing surface reaction kinetics with the presence of specific catalysts. Photocorrosion is one of main problems for reducing the stability of photoanodes/photocathodes in PEC water splitting. When the anodic decomposition potential of the semiconductor is above its valence band potential, the anodic photocorrosion happens. Similarly, when the cathodic decomposition potential of the semiconductor is below its conduction band potential, the cathodic photocorrosion

Table 2. Earth abundant materials based photocathodes for PEC water splitting. $J_{0\ V}$ means the current desity of the photocathodes at 0 V vs. RHE. Reproduced with permission from Ref. [120], copyright Wiley-VCH 2018.

HER catalysts	Photoactive substrate	Morphology	$J_{0\ V}$ [mA/cm^2]	pH	Stability
MoS_{2+x}	$Cu_2O/AZO/TiO_2$	Planar	5.7	1	<7 h
MoS_{2+x}	$Cu_2O/AZO/TiO_2$	Planar	6.3	13.6	<10 h
NiMo alloy	$Cu_2O/AZO/TiO_2$	Planar	6.3	13.6	<10 h
1T-MoS_2	p-Si	Planar	17.6	0	<3 h
MoS_x	n_+p-Si/Mo	Planar	17.5	0	100 h
2H-MoS_2	p-Si	Planar	24.6	0	2.8 h
2H-MoS_2	p-Si	Planar	21.7	0	24 h
$CoMoS_x$	p-Si	Planar	17.5	4.25	-
$CoMoS_x$	p-Si	Microwire	17.2	0	>7 h
MoO_xS_y	p-Si	Microwire	9.83	1	2 h
S:MoP	p-Si	Planar	33.13	0	<2.8 h
$CoSe_2$	p-Si	Nanowire	9	1	-
$NiCoSe_x$	p-Si	Nanopillar	37.5	0	>2 h
$Ni_{12}P_5$	p-Si	Nanowire	21	0	1 h
NiFeLDH	p-Si	Planar	7 mA	13.6	24 h
MoS_x	n^+p^-Si/Ti/TiO_2	Planar	>16	0	-
MoS_2	n^+p^-Si/Al_2O_3	Micropyramid	35.6	0	120 h
MoS_xCl_y	n^+pp^+-Si	Micropyramid	43	0	2 h
$MoSe_xCl_y$	n^+pp^+-Si	Micropyramid	38.8	0	2 h
CoP	n^+p^-Si/Co	Nanowire	15.6	1	<1 h
CoP	n^+p^-Si/Co	Nanowire	17	0	12h
CoP	n^+p^-Si/Co	Planar	20	0	>24h
NiMo alloy	n^+p^-Si/TiO2	Microwire	14.3	0	-
NiP_2	n^+p^-Si/Ni	Micropyramid	12	0	6h
NiMo alloy	n^+p^-Si	Microwire	10.3	4.5	1h
CoPS	n^+pp^+-Si	Micropyramid	35	0	-
NiMo alloy	ZnO/p-i-n a-Si/TiO_2	Planar	11	4.5	12h
Mo_2C	a-Si/AZO/TiO_2	Planar	11.2	0.7/13.6	1h

usually happens. However, for some semiconductors such as TiO_2 and Fe_2O_3, their anodic decomposition potentials are above their valence band, but they show good stability since their decompositions are with very slow kinetics;[44] iv) The semiconductor should be cheap and earth-abundant in order to make commercially available water splitting devices. Tables 1 and 2 summarize the earth abundant materials based photoanodes and photocathodes for PEC water splitting, respectively, which have been reported mostly in the past decades.

There are four kinds of PEC water splitting configurations (Figure 9) mostly reported until now. The first type (Figure 9a) is PEC water splitting with the aid of external bias by using a simple semiconductor as light absorber, which can be used as

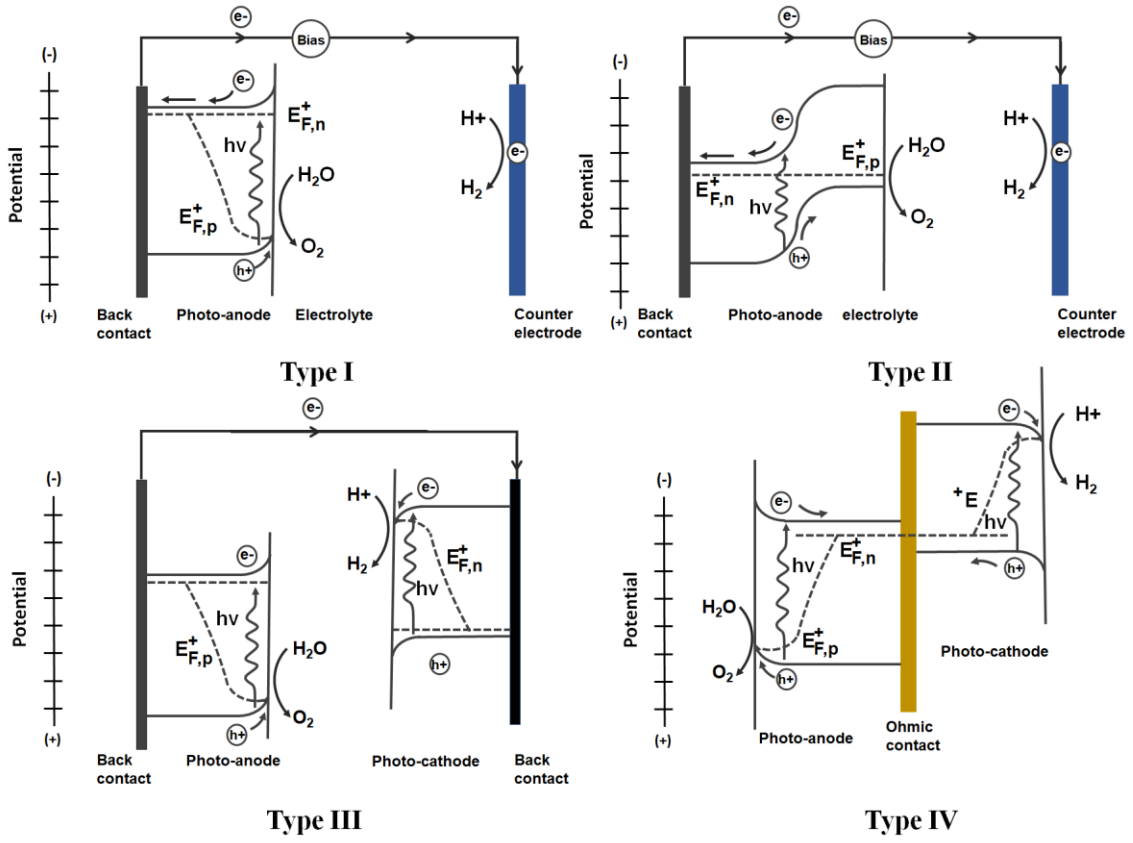

Figure 9. Four kinds of configurations for PEC water splitting devices. (a) External bias assisted PEC water splitting by using a single semiconductor as the photoanode or photocathode. (b) External bias assisted PEC water splitting by using heterojunction semiconductor as the photoanode or photocathode. (c) Wired tandem PEC water splitting by connecting a photoanode and a photocathode. (d) Wireless PEC water splitting based on ohmic contact, which can also rely on p-n junctions.[121] Reproduced with permission from Ref. [44], copyright Royal Society of Chemistry 2017.

either a photoanode or a photocathode. This configuration is simple, but a large external bias is needed to drive the holes and electrons separation for water oxidation and reduction. The second type (Figure 9b) use two or more coupled semiconductors as a light absorber, which can enhance the light absorption and the charge carrier separation.[122] The third and fourth types (Figures 9c and 9d) are spontaneous PEC water splitting devices. In this case, two kinds of semiconductors are needed to severe as the photoanode and photocathode respectively, in which no external bias is needed. For the third type (Figure 9c), a conductive metal wire is used to combine the photoanode and photocathode. The fourth type is wireless (Figure 9d), and uses a transparent conductive substrate as the electron and hole recombination layer. One of the main issue for the PEC spontaneous water splitting is that the maximum valence band of the photocathode must lie more positive than the minimum conduction band of the photoanode to ensure they can work and be stable at a similar current under sunlight illumination and without external bias applied.[44] Among all the configurations shown in Figure 9, the third type (Figure 9c) is the most promising system for PEC water splitting devices, because it needs sunlight as the only energy source, and the generated O_2 and H_2 can be separated.

1.5 Photovoltaic cells based water splitting

There are two kinds of photovoltaic (PV) cells based water splitting configurations, which are PV-PEC and PV-EC water splitting devices, respectively (Figure 10). In the PV-PEC configuration, both the photoanode/photocathode and PV cells can absorb light. In the PV-EC configuration, just the PV cell absorbs light. In both cases, the selection of the materials is much wider than that for spontaneous PEC water splitting devices described in section 1.4, since there is no requirement for the band alignments of the semiconductors in PV based water splitting devices. As mentioned in section 1.2 and

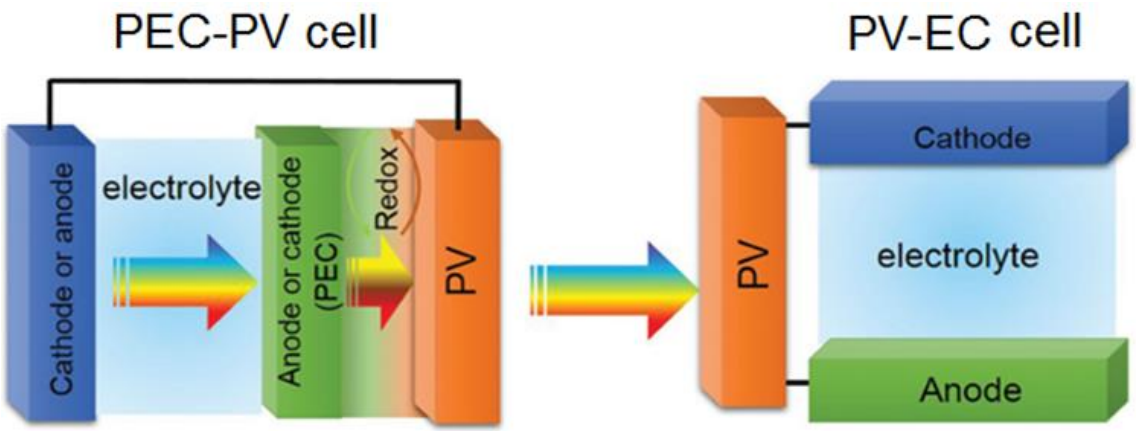

Figure 10. Two configurations of PV cells based unassisted water splitting, including PEC-PV cell and PV-EC cell respectively. Reproduced with permission from Ref. [123], copyright Wiley 2016.

depicted in Figure 4, the PV cell based water splitting is more mature than PEC water splitting approaches, due to the well developed PV technologies. Table 3 compares the requirements and main achievements for PEC, PV-PEC and PV-EC configurations based water splitting devices. It is worth to note that the STH efficiency in the spontaneous water splitting system is calculated through *Equation 4, w*here J_{op} is the operation current density for stability test, in mA/cm^2. η_F is the faradic efficiency, which is the ratio between produced gas and the theoretically generated gas according to the charge passed through the curcuit. P_{in} is the incident light density in mW/cm^2.

$$STH = \frac{(1.23\ V)\times\eta_F\times J_{op}}{P_{solar}} \times 100\ \% \quad (Equation\ 4)$$

In this thesis, we mainly focus the study of PV solar cells based water splitting on the PV-EC configuration. Considering the thermodynamic potential of the water splitting reaction, trade-off current and voltages in light absorbers and state-of-art catalysts, a minimum photovoltage of 1.5-1.9 V must be generated for the spontaneous water oxidation and reduction reactions.[124, 46] However, the single junction based PV cells provide open circuit potentials (V_{OC}) below 1.5 V,[28, 46, 124] so two or multiple single junction PV cells need to be connected for their application in water splitting.[28, 125-126]

Alternatively, a single PV cell with multiple junction can reach a V_{OC} > 1.7 V, which can also be employed to drive the spontaneous water splitting reaction. Some successful reported examples include inter-connected $CuIn_xGa_{1-x}Se_2$ (CIGS),[31] triple junction III-V semiconductors based solar cell,[29, 35, 127] triple junction silicon solar cell,[34] triple junction polymer solar cell.[36] The technology of PV-EC based water splitting is very mature, but until now there is still no commercial PV-EC system available in the market. The major challenge in the field is related to the high materials cost and short device stability.[46]

Table 3. Main requirements and achievements for three kinds of spontaneous water splitting devices. Reproduced with permission from Ref. [123], copyright Wiley 2016.

Parameters	**Integrated PEC cell**	**PV-PEC cell**	**PV-EC cell**
Semiconductor type (n or p-type)	Challenges: anode is n-type, cathode is p-type	Advantage: no requirements	Advantage: no requirements
Band edge	Challenges: band edge of anode satisfies water oxidation, band edge of cathode satisfies water reduction potential	Challenge: band edge satisfies either water oxidation or reduction at least	Advantage: no requirements
Band alignment	Challenge: VB of photocathode must lie more positive than CB of photoanode	Advantage: no requirements	Advantage: no requirements
Catalyst	Challenge: necessary	Challenge: necessary	Challenge: necessary
Bias of PV	Advantage: no requirements	Advantage: low bias	Challenge: > 1.6 V
Numbers of PV	Advantage: no requirements	Challenge: ≥ 1	Challenge: ≥ 2
Charge carrier transport	High loss	High loss	Low loss
Photo-conversion efficiency	Low	Medium	High
Material cost	Low	Medium	High
Stability	High (except gallium and indium phosphide)	Medium/low	High/medium
Theoretical maximum of η_{STH} [123]	29.7%	~ 20%	> 20%
Obtained η_{STH}	2.5% [38]	6.3% [128]	30% [35]

1.6 References

[1] University Corporation for Atmospheric Research, Air Pollution: A Global Problem, https://ral.ucar.edu/pressroom/features/air-pollution-a-global-problem (accessed on 13 August 2018).

[2] TIME, How Architecture Should Adapt to Climate Change**,** http://time.com/4950746/architecture-buildings-climate-change-hurricane-earthquake-destruction/ (accessed on 13 August 2018).

[3] F. Perera, Pollution from fossil-fuel combustion is the leading environmental threat to global pediatric health and equity: solutions exist, *Int. J. Environ. Res. Public. Health* **2017**, *15*, 16.

[4] G. B. Louis, World Health Organization, Principles for evaluating health risks in children associated with exposure to chemicals, World Health Organization: Geneva, Switzerland, **2006**.

[5] Z. Xu, P. E. Sheffield, W. Hu, H. Su, W. Yu, X. Qi, S. Tong, climate change and children's health—a call for research on what works to protect children, *Int. J. Environ. Res. Public. Health* **2012**, *9*, 3298.

[6] K. R. Smith, C. F. Corvalán, T. Kjellström, How much global ill health is attributable to environmental factors? *Epidemiology* **1999**, *10*, 573.

[7] World Health Organization, Healthy Environments for Children: Initiating An Alliance For Action, World Health Organization: Geneva, Switzerland, **2002**.

[8] Y. Zhang, P. Bi, J. E. Hiller, Climate Change and Disability–Adjusted Life Years, *J. Environ. Health* **2007**, *70*, 32.

[9] World Health Organization, 9 out of 10 People Worldwide Breathe Polluted Air, But More Countries Are Taking Action, http://www.who.int/news-room/detail/02-05-2018-9-out-of-10-people-worldwide-breathe-polluted-air-but-more-countries-are-taking-action (accessed on 13 August 2018).

[10] U.S. Environmental Protection Agency. Greenhouse Gas (GHG) Emissions, https://www3.epa.gov/climatechange/ghgemissions/ (accessed on 4 July 2018).

[11] International Energy Agency (IEA), Weo-2016 Special Report

Energy and Air Pollution, International Energy Agency: Paris, France, **2016**, 266.

[12] World Health Organization, Air Quality Guidelines Global Update 2005. Particulate Matter, Ozone, Nitrogen Dioxide and Sulfur Dioxide, WHO: Geneva, Switzerland, **2005**.

[13] UNICEF, Clear the Air for Children. https://www.unicef.org /publications/index92957.html (accessed on 4 July 2018).

[14] International Energy Agency (IEA), CO_2 Emissions from Fuel Combustion—2016 Edition—Key CO2 Emissions Trends. 2016. https://www.iea.org/publications/freepublications/publication/co2-emissions-fromfuel-combustion---2016-edition---excerpt---key-trends.html (accessed on 6 July 2018).

[15] International Energy Agency (IEA), CO_2 Emissions from Fuel Combustion: Overview (2017 edition), website: https://www.iea.

org/publications/freepublications/publication/CO2EmissionsFromFuelCombustion2017Overview.pdf (accesse--d on 4 July 2018).

[16] National Oceanic and Atmospheric Administration (NOAA). Noaa's Greenhouse Gas Index Up 40 Percent Since 1990. 2017, http://www.noaa.gov/news/noaa-s-greenhouse-gas-index-up40-percent-since-1990 (accessed on 6 July 2018).

[17] Climate Central. Highest Levels in 800,000 Years, http://www.climatecentral.org/gallery/graphics/highest-levels-in-800000-years (accessed on 6 July 2018).

[18] U.S. Energy Information Administration (EIA)-International Energy Outlook 2017. https://www.eia.gov/outlooks/ieo/ (accessed on June 12 2018).

[19] BP, BP Statistical Review of World Energy 2016. https://www.bp.com/content/dam/bp/pdf/energy-economics/stat istical-review-2016/bp-statistical-review-of-world-energy-2016 -full-report.pdf (accessed on June 12 2018).

[20] U.S. Energy Information Administration (EIA), Renewable energy explained, https://www.eia.gov/energyexplained/?page =renewable_home (accessed on June 12 2018).

[21] R. E. Blankenship, D. M. Tiede, J. Barber, G. W. Brudvig, G. Fleming, M. Ghirardi, M. R. Gunner, W. Junge, D. M. Kramer, A. Melis, T. A. Moore, C. C. Moser, D. G. Nocera, A. J. Nozik, D. R. Ort, W. W. Parson, R. C. Prince, R. T. Sayre, Comparing photosynthetic and photovoltaic efficiencies and recognizing the potential for improvement, *Science* **2011**, *332*, 805.

[22] N. S. Lewis, Toward Cost-Effective Solar Energy Use, *Science* **2007**, *315*, 798.

[23] M. G. Walter, E. L. Warren, J. R. McKone, S. W. Boettcher, Q. Mi, E. A. Santori, N. S. Lewis, Solar water splitting cells, *Chem. Rev.* **2010**, *110*, 6446.

[24] A. Fujishima, K. Honda, Electrochemical Photolysis of Water at a Semiconductor Electrode, *Nature* **1972**, *238*, 37.

[25] Alternative Energy Info, Honda's Home Hydrogen Fueling Station, http://www.alt-energy.info/hydrogen-power/hondas-ho me-hydrogen-fueling-station/ (accessed on June 12 2018).

[26] J. R. McKone, N. S. Lewis, H. B. Gray, Will solar-driven water-splitting devices see the light of day? *Chem. Mater.* **2014**, *26*, 407.

[27] P. C. K. Vesborg, T. F. Jaramillo, Addressing the terawatt challenge: scalability in the supply of chemical elements for renewable energy, *RSC Adv.* **2012**, *2*, 7933.

[28] J. Luo, J.-H. Im, M. T. Mayer, M. Schreier, M. K. Nazeeruddin, N.-G. Park, S. D. Tilley, H. J. Fan, M. Gratzel, Water photolysis at 12.3% efficiency via perovskite photovoltaics and Earth-abundant catalysts, *Science* **2014**, *345*, 1593.

[29] A. Nakamura, Y. Ota, K. Koike, Y. Hidaka, K. Nishioka, M. Sugiyama, K. Fujii, A 24.4% solar to hydrogen energy conversion efficiency by combining concentrator photovoltaic modules and electrochemical cells, *Appl. Phys. Express* **2015**, *8*, 107101.

[30] C. R. Cox, J. Z. Lee, D. G. Nocera, T. Buonassisi, Ten-percent solar-to-fuel conversion with nonprecious materials, *Proc. Natl. Acad. Sci.* **2014**, *111*, 14057.

[31] T. J. Jacobsson, V. Fjällström, M. Sahlberg, M. Edoff, T. Edvinsson, A monolithic device for solar water splitting based on series interconnected thin film absorbers

reaching over 10% solar-to-hydrogen efficiency, *Energy Environ. Sci.* **2013**, *6*, 3676.

[32] G. Peharz, F. Dimroth, U. Wittstadt, Solar hydrogen production by water splitting with a conversion efficiency of 18%, *Int. J. Hydrog. Energy* **2007**, *32*, 3248.

[33] S. Licht, Over 18% solar energy conversion to generation of hydrogen fuel; theory and experiment for efficient solar water splitting, *Int. J. Hydrog. Energy* **2001**, *26*, 653.

[34] O. Khaselev, High-efficiency integrated multijunction photovoltaic/electrolysis systems for hydrogen production, *Int. J. Hydrog. Energy* **2001**, *26*, 127.

[35] J. Jia, L. C. Seitz, J. D. Benck, Y. Huo, Y. Chen, J. W. D. Ng, T. Bilir, J. S. Harris, T. F. Jaramillo, Solar water splitting by photovoltaic-electrolysis with a solar-to-hydrogen efficiency over 30%, *Nat. Commun.* **2016**, *7*, 13237.

[36] X. Elias, Q. Liu, C. Gimbert-Suriñach, R. Matheu, P. Mantilla-Perez, A. Martinez-Otero, X. Sala, J. Martorell, A. Llobet, Neutral water splitting catalysis with a high FF triple junction polymer cell, *ACS Catal.* **2016**, *6*, 3310.

[37] H. S. Park, H. C. Lee, K. C. Leonard, G. Liu, A. J. Bard, Unbiased photoelectrochemical water splitting in z-scheme device using W/Mo-doped $BiVO_4$ and $Zn_xCd_{1-x}Se$, *ChemPhysChem* **2013**, *14*, 2277.

[38] C. Ding, W. Qin, N. Wang, G. Liu, Z. Wang, P. Yan, J. Shi, C. Li, Solar-to-hydrogen efficiency exceeding 2.5% achieved for overall water splitting with an all earth-abundant dual-photoelectrode, *Phys Chem Chem Phys* **2014**, *16*, 15608.

[39] J.-W. Jang, C. Du, Y. Ye, Y. Lin, X. Yao, J. Thorne, E. Liu, G. McMahon, J. Zhu, A. Javey, J. Guo, D. Wang, Enabling unassisted solar water splitting by iron oxide and silicon, *Nat. Commun.* **2015**, *6*, 7447.

[40] J. H. Kim, H. Kaneko, T. Minegishi, J. Kubota, K. Domen, J. S. Lee, Overall photoelectrochemical water splitting using tandem cell under simulated sunlight, *ChemSusChem* **2016**, *9*, 61.

[41] D. Shao, L. Zheng, D. Feng, J. He, R. Zhang, H. Liu, X. Zhang, Z. Lu, W. Wang, W. Wang, F. Lu, H. Dong, Y. Cheng, H. Liu, R. Zheng, TiO_2 –P3HT: PCBM photoelectrochemical tándem cells for solar-driven overall water splitting, *J. Mater. Chem. A* **2018**, *6*, 4032.

[42] J. Liu, Y. Liu, N. Liu, Y. Han, X. Zhang, H. Huang, Y. Lifshitz, S.-T. Lee, J. Zhong, Z. Kang, Metal-free efficient photocatalyst for stable visible water splitting via a two-electron pathway, *Science* **2015**, *347*, 970.

[43] D. M. Fabian, S. Hu, N. Singh, F. A. Houle, T. Hisatomi, K. Domen, F. E. Osterloh, S. Ardo, Particle suspension reactors and materials for solar-driven water splitting, *Energy Environ. Sci.* **2015**, *8*, 2825.

[44] C. Jiang, S. J. A. Moniz, A. Wang, T. Zhang, J. Tang, Photoelectrochemical devices for solar water splitting – materials and challenges, *Chem. Soc. Rev.* **2017**, *46*, 4645.

[45] J. Nowotny, T. Bak, D. Chu, S. Fiechter, G. E. Murch, T. N. Veziroglu, Sustainable practices: Solar hydrogen fuel and education program on sustainable energy systems, *Int. J. Hydrog. Energy* **2014**, *39*, 4151.

[46] J. W. Ager, M. R. Shaner, K. A. Walczak, I. D. Sharp, S. Ardo, Experimental demonstrations of spontaneous, solar-driven photoelectrochemical water splitting, *Energy Environ. Sci.* **2015**, *8*, 2811.

[47] B. A. Pinaud, J. D. Benck, L. C. Seitz, A. J. Forman, Z. Chen, T. G. Deutsch, B. D. James, K. N. Baum, G. N. Baum, S. Ardo, H. Wang, E. Miller, T. F. Jaramillo, Technical and economic feasibility of centralized facilities for solar hydrogen production via photocatalysis and photoelectrochemistry, *Energy Environ. Sci.* **2013**, *6*, 1983.

[48] S. Chu, W. Li, Y. Yan, T. Hamann, I. Shih, D. Wang, Z. Mi, Roadmap on solar water splitting: current status and future prospects, *Nano Futur.* **2017**, *1*, 022001.

[49] P. Peerakiatkhajohn, J.-H. Yun, S. Wang, L. Wang, Review of recent progress in unassisted photoelectrochemical water splitting: from material modification to configuration design, *J. Photonics Energy* **2016**, *7*, 012006.

[50] M. R. Shaner, H. A. Atwater, N. S. Lewis, E. W. McFarland, A comparative technoeconomic analysis of renewable hydrogen production using solar energy, *Energy Environ. Sci.* **2016**, *9*, 2354.

[51] R. Sathre, C. D. Scown, W. R. Morrow, J. C. Stevens, I. D. Sharp, J. W. Ager, K. Walczak, F. A. Houle, J. B. Greenblatt, Life-cycle net energy assessment of large-scale hydrogen production via photoelectrochemical water splitting, *Energy Env. Sci* **2014**, *7*, 3264.

[52] J. Li, R. Guttinger, R. More, F. Song, W. Wan, G. R. Patzke, Frontiers of water oxidation: the quest for true catalysts, *Chem. Soc. Rev.* **2017**, *46*, 6124.

[53] F. Liu, J. J. Concepcion, J. W. Jurss, T. Cardolaccia, J. L. Templeton, T. J. Meyer, Mechanisms of Water Oxidation from the Blue Dimer to Photosystem II, *Inorg. Chem.* **2008**, *47*, 1727.

[54] H. Inoue, T. Shimada, Y. Kou, Y. Nabetani, D. Masui, S. Takagi, H. Tachibana, The water oxidation bottleneck in artificial photosynthesis: how can we get through it? An alternative route involving a two-electron process, *ChemSusChem* **2011**, *4*, 173.

[55] M. Pourbaix, Atlas of Electrochemical Equilibria in Aqueous Solutions, Pergamon Press: New York, **1966**.

[56] T. R. Cook, D. K. Dogutan, S. Y. Reece, Y. Surendranath, T. S. Teets, D. G. Nocera, Solar Energy Supply and Storage for the Legacy and Nonlegacy Worlds, *Chem. Rev.* **2010**, *110*, 6474.

[57] Y.-F. Li, Z.-P. Liu, Structure and water oxidation activity of 3d metal oxides, *Wiley Interdiscip. Rev. Comput. Mol. Sci.* **2016**, *6*, 47.

[58] B. M. Hunter, H. B. Gray, A. M. Müller, Earth-abundant heterogeneous water oxidation catalysts, *Chem. Rev.* **2016**, *116*, 14120.

[59] S. Hackwood, L. M. Schiavone, W. C. Dautremont-Smith, G. Beni, Anodic evolution of oxygen on sputtered iridium oxide films, *J. Electrochem. Soc.* **1981**, *128*, 2569.

[60] A. Harriman, J. M. Thomas, G. R. Millward, Catalytic and structural properties of iridium-iridium dioxide colloids**,** *New J. Chem*. **1987**, *11*, 757.

[61] A. Mills, T. Russell, Comparative study of new and established heterogeneous oxygen catalysts, *J. Chem. Soc. Faraday Trans.* **1991**, *87*, 1245.

[62] N. D. Morris, T. E. Mallouk, A high-throughput optical screening method for the optimization of colloidal water oxidation catalysts, *J. Am. Chem. Soc.* **2002**, *124*, 11114.

[63] M. Yagi, E. Tomita, T. Kuwabara, Remarkably high activity of electrodeposited IrO2 film for electrocatalytic water oxidation, *J. Electroanal. Chem.* **2005**, *579*, 83.

[64] T. Nakagawa, C. A. Beasley, R. W. Murray, Efficient electro-oxidation of water near its reversible potential by a mesoporous IrO_x nanoparticle film, *J. Phys. Chem. C* **2009**, *113*, 12958.

[65] D. Galizzioli, F. Tantardini, S. Trasatti, Ruthenium dioxide: a new electrode material. I. Behaviour in acid solutions of inert electrolytes, *J. Appl. Electrochem.* **1974**, *4*, 57.

[66] J. Horkans, M. W. Shafer, Effect of orientation, composition, and electronic factors in the reduction of O_2 on single crystal electrodes of the conducting oxides of molybdenum and tungsten, *J. Electrochem. Soc.* **1977**, *124*, 1196.

[67] M. N. Iqbal, A. F. Abdel-Magied, H. N. Abdelhamid, P. Olsén, A. Shatskiy, X. Zou, B. Åkermark, M. D. Kärkäs, E. V. Johnston, Mesoporous ruthenium oxide: a heterogeneous catalyst for water oxidation, *ACS Sustain. Chem. Eng.* **2017**, *5*, 9651.

[68] M. Morita, C. Iwakura, H. Tamura, The anodic characteristics of massive manganese oxide electrode, *Electrochimica Acta* **1979**, *24*, 357.

[69] M. M. Najafpour, T. Ehrenberg, M. Wiechen, P. Kurz, Calcium manganese(III) oxides (CaMn2O4·xH2O) as biomimetic oxygen-evolving catalysts, *Angew. Chem. Int. Ed.* **2010**, *49*, 2233.

[70] A. Indra, P. W. Menezes, I. Zaharieva, E. Baktash, J. Pfrommer, M. Schwarze, H. Dau, M. Driess, Active mixed-valent MnO_x water oxidation catalysts through partial oxidation (corrosion) of nanostructured MnO particles, *Angew. Chem. Int. Ed.* **2013**, *52*, 13206.

[71] Y. Gorlin, T. F. Jaramillo, A bifunctional nonprecious metal catalyst for oxygen reduction and water oxidation, *J. Am. Chem. Soc.* **2010**, *132*, 13612.

[72] J. Suntivich, K. J. May, H. A. Gasteiger, J. B. Goodenough, Y. Shao-Horn, A perovskite oxide optimized for oxygen evolution catalysis from molecular orbital principles, *Science* **2011**, *334*, 1383.

[73] J. Scholz, M. Risch, K. A. Stoerzinger, G. Wartner, Y. Shao-Horn, C. Jooss, Rotating ring–disk electrode study of oxygen evolution at a perovskite surface: correlating activity to manganese concentration, *J. Phys. Chem. C* **2016**, *120*, 27746.

[74] J. E. Turner, The Characterization of doped iron oxide electrodes for the photodissociation of water, *J. Electrochem. Soc.* **1984**, *131*, 1777.

[75] A. G. Joly, J. R. Williams, S. A. Chambers, G. Xiong, W. P. Hess, D. M. Laman, Carrier dynamics in α-Fe_2O_3 (0001) thin films and single crystals probed by femtosecond transient absorption and reflectivity, *J. Appl. Phys.* **2006**, *99*, 053521.

[76] R. D. L. Smith, M. S. Prévot, R. D. Fagan, Z. Zhang, P. A. Sedach, M. K. J. Siu, S. Trudel, C. P. Berlinguette, photochemical route for accessing amorphous metal oxide materials for water oxidation catalysis, *Science* **2013**, 1233638.

[77] I. Cesar, A. Kay, J. A. Gonzalez Martinez, M. Grätzel, Translucent Thin Film Fe2O3 Photoanodes for efficient water splitting by sunlight: nanostructure-directing effect of Si-doping, *J. Am. Chem. Soc.* **2006**, *128*, 4582.

[78] S. Y. Reece, J. A. Hamel, K. Sung, T. D. Jarvi, A. J. Esswein, J. J. H. Pijpers, D. G. Nocera, wireless solar water splitting using silicon-based semiconductors and earth abundant catalysts, *Science* **2011**, *334*, 645.

[79] M. W. Kanan, D. G. Nocera, In situ formation of an oxygen-evolving catalyst in neutral water containing phosphate and $Co2^{+}$, *Science* **2008**, *321*, 1072.

[80] M. W. Kanan, Y. Surendranath, D. G. Nocera, Cobalt–phosphate oxygen-evolving compound, *Chem. Soc. Rev.* **2009**, *38*, 109.

[81] G. Liu, S. K. Karuturi, A. N. Simonov, M. Fekete, H. Chen, N. Nasiri, N. H. Le, P. R. Narangari, M. Lysevych, T. R. Gengenbach, A. Lowe, H. H. Tan, C. Jagadish, L. Spiccia, A. Tricoli, Robust sub-monolayers of Co_3O_4 nano-islands: a highly transparent morphology for efficient water oxidation catalysis, *Adv. Energy Mater.* **2016**, *6*, 1600697.

[82] D. A. Lutterman, Y. Surendranath, D. G. Nocera, A self-healing oxygen-evolving catalyst, *J. Am. Chem. Soc.* **2009**, *131*, 3838.

[83] H. Bode, K. Dehmelt, J. Witte, Zur kenntnis der nickelhydroxidelektrode—I.Über das nickel (II)-hydroxidhydrat, *Electrochimica Acta* **1966**, *11*, 1079.

[84] P. Oliva, J. Leonardi, J. F. Laurent, C. Delmas, J. J. Braconnier, M. Figlarz, F. Fievet, A. de Guibert, Review of the structure and the electrochemistry of nickel hydroxides and oxy-hydroxides, *J. Power Sources* **1982**, *8*, 229.

[85] G. Młynarek, M. Paszkiewicz, A. Radniecka, The effect of ferric ions on the behaviour of a nickelous hydroxide electrode, J. Appl. Electrochem. **1984**, *14*, 145.

[86] D. A. Corrigan, The catalysis of the oxygen evolution reaction by iron impurities in thin film nickel oxide electrodes, *J. Electrochem. Soc.* **1987**, *134*, 377.

[87] M. J. Kenney, M. Gong, Y. Li, J. Z. Wu, J. Feng, M. Lanza, H. Dai, High-performance silicon photoanodes passivated with ultrathin nickel films for water oxidation, *Science* **2013**, *342*, 836.

[88] T. Han, Y. Shi, X. Song, A. Mio, L. Valenti, F. Hui, S. Privitera, S. Lombardo, M. Lanza, Ageing mechanisms of highly active and stable nickel-coated silicon photoanodes for water splitting, *J. Mater. Chem. A* **2016**, *4*, 8053.

[89] Y. Shi, T. Han, C. Gimbert-Suriñach, X. Song, M. Lanza, A. Llobet, Substitution of native silicon oxide by titanium in Ni-coated silicon photoanodes for water splitting solar cells, *J. Mater. Chem. A* **2017**, *5*, 1996.

[90] J. Du, Z. Chen, S. Ye, B. J. Wiley, T. J. Meyer, Copper as a robust and transparent electrocatalyst for water oxidation, *Angew. Chem. Int. Ed Engl.* **2015**, *54*, 2073.

[91] S. Cui, X. Liu, Z. Sun, P. Du, Noble metal-free copper hydroxide as an active and robust electrocatalyst for water oxidation at weakly basic pH, *ACS Sustain. Chem. Eng.* **2016**, *4*, 2593.

[92] X. Liu, S. Cui, M. Qian, Z. Sun, P. Du, In situ generated highly active copper oxide catalysts for the oxygen evolution reaction at low overpotential in alkaline solutions, *Chem. Commun.* **2016**, *52*, 5546.

[93] Y. Shi, C. Gimbert-Suriñach, T. Han, S. Berardi, M. Lanza, A. Llobet, CuO-functionalized silicon photoanodes for photoelectrochemical water splitting devices, *ACS Appl. Mater. Interfaces* **2016**, *8*, 696.

[94] C. C. L. McCrory, S. Jung, I. M. Ferrer, S. M. Chatman, J. C. Peters, T. F. Jaramillo, Benchmarking hydrogen evolving reaction and oxygen evolving reaction electrocatalysts for solar water splitting devices, *J. Am. Chem. Soc.* **2015**, *137*, 4347.

[95] C. C. L. McCrory, S. Jung, J. C. Peters, T. F. Jaramillo, Benchmarking heterogeneous electrocatalysts for the oxygen evolution reaction, *J. Am. Chem. Soc.* **2013**, *135*, 16977.

[96] L. Trotochaud, S. L. Young, J. K. Ranney, S. W. Boettcher, Nickel–iron oxyhydroxide oxygen-evolution electrocatalysts: the role of intentional and incidental iron incorporation, *J. Am. Chem. Soc.* **2014**, *136*, 6744.

[97] S. W. Gersten, G. J. Samuels and T. J. Meyer, Catalytic oxidation of water by an oxo-bridged ruthenium dimer, *J. Am. Chem. Soc*. **1982**, *104*, 4029.

[98] P. Garrido-Barros, C. Gimbert-Surinach, R. Matheu, X. Sala, A. Llobet, How to make an efficient and robust molecular catalyst for water oxidation, *Chem. Soc. Rev.* **2017**, *46*, 6088.

[99] C. W. Cady, R. H. Crabtree, G. W. Brudvig, Functional models for the oxygen-evolving complex of photosystem II, *Coord. Chem. Rev.* **2008**, *252*, 444.

[100] S. M. Barnett, K. I. Goldberg, J. M. Mayer, A soluble copper- bipyridine water-oxidation electrocatalyst, *Nat. Chem.* **2012**, *4*, 498.

[101] M.-T. Zhang, Z. Chen, P. Kang, T. J. Meyer, Electrocatalytic water oxidation with a copper(II) polypeptide complex, *J. Am. Chem. Soc.* **2013**, *135*, 2048.

[102] T. Zhang, C. Wang, S. Liu, J.-L. Wang, W. Lin, A biomimetic copper water oxidation catalyst with low overpotential, *J. Am. Chem. Soc.* **2014**, *136*, 273.

[103] P. Garrido-Barros, I. Funes-Ardoiz, S. Drouet, J. Benet-Buchholz, F. Maseras, A. Llobet, Redox Non-innocent ligand controls water oxidation overpotential in a new family of mononuclear cu-based efficient catalysts, *J. Am. Chem. Soc.* **2015**, *137*, 6758.

[104] P. Garrido-Barros, C. Gimbert-Suriñach, D. Moonshiram, A. Picón, P. Monge, V. S. Batista, A. Llobet, Electronic π-delocalization boosts catalytic water oxidation by Cu(II) molecular catalysts heterogenized on graphene sheets, *J. Am. Chem. Soc.* **2017**, *139*, 12907.

[105] W. C. Ellis, N. D. McDaniel, S. Bernhard, T. J. Collins, Fast water oxidation using iron, *J. Am. Chem. Soc.* **2010**, *132*, 10990.

[106] C.-F. Leung, S.-M. Ng, C.-C. Ko, W.-L. Man, J. Wu, L. Chen, T.-C. Lau, A cobalt(ii) quaterpyridine complex as a visible light-driven catalyst for both water oxidation and reduction, *Energy Environ. Sci.* **2012**, *5*, 7903.

[107] M. L. Rigsby, S. Mandal, W. Nam, L. C. Spencer, A. Llobet, S. S. Stahl, Cobalt analogs of Ru-based water oxidation catalysts: overcoming thermodynamic instability and kinetic lability to achieve electrocatalytic O2 evolution, *Chem. Sci.* **2012**, *3*, 3058.

[108] C. Gimbert-Suriñach, D. Moonshiram, L. Francàs, N. Planas, V. Bernales, F. Bozoglian, A. Guda, L. Mognon, I. López, M. A. Hoque, L. Gagliardi, C. J. Cramer,

A. Llobet, Structural and spectroscopic characterization of reaction intermediates involved in a dinuclear co-hbpp water oxidation catalyst, *J. Am. Chem. Soc.* **2016**, *138*, 15291.

[109] J. F. Hull, D. Balcells, J. D. Blakemore, C. D. Incarvito, O. Eisenstein, G. W. Brudvig, R. H. Crabtree, Highly active and robust Cp* iridium complexes for catalytic water oxidation, *J. Am. Chem. Soc.* **2009**, *131*, 8730.

[110] F. Bozoglian, S. Romain, M. Z. Ertem, T. K. Todorova, C. Sens, J. Mola, M. Rodríguez, I. Romero, J. Benet-Buchholz, X. Fontrodona, C. J. Cramer, L. Gagliardi, A. Llobet, The Ru−Hbpp water oxidation catalyst, *J. Am. Chem. Soc.* **2009**, *131*, 15176.

[111] J. J. Concepcion, J. W. Jurss, J. L. Templeton, T. J. Meyer, One Site is Enough. Catalytic water oxidation by [Ru(tpy)(bpm)(OH_2)]$^{2+}$ and [Ru(tpy)(bpz)(OH_2)]$^{2+}$, *J. Am. Chem. Soc.* **2008**, *130*, 16462.

[112] L. Duan, F. Bozoglian, S. Mandal, B. Stewart, T. Privalov, A. Llobet, L. Sun, A molecular ruthenium catalyst with water-oxidation activity comparable to that of photosystem II, *Nat. Chem.* **2012**, *4*, 418.

[113] R. Matheu Montserrat, Seven-coordinate complexes for water oxidation catalysis: from molecular characterization to solid state photocatalysis, Doctoral dissertation, Universitat Rovira i Virgili, **2017**.

[114] R. Matheu, I. A. Moreno-Hernandez, X. Sala, H. B. Gray, B. S. Brunschwig, A. Llobet, N. S. Lewis, photoelectrochemical behavior of a molecular ru-based water-oxidation catalyst bound to TiO_2-protected Si photoanodes, *J. Am. Chem. Soc.* **2017**, *139*, 11345.

[115] X. Sala, S. Maji, R. Bofill, J. García-Antón, L. Escriche, A. Llobet, Molecular water oxidation mechanisms followed by transition metals: state of the art, *Acc. Chem. Res.* **2014**, *47*, 504.

[116] S. Berardi, S. Drouet, L. Francas, C. Gimbert-Surinach, M. Guttentag, C. Richmond, T. Stolla, A. Llobet, Molecular artificial photosynthesis, *Chem. Soc. Rev.* **2014**, *43*, 7501.

[117] S. Romain, F. Bozoglian, X. Sala, A. Llobet, Oxygen−oxygen bond formation by the Ru-Hbpp water oxidation catalyst occurs solely via an intramolecular reaction pathway, *J. Am. Chem. Soc.* **2009**, *131*, 2768.

[118] I. Funes-Ardoiz, P. Garrido-Barros, A. Llobet, F. Maseras, Single electron transfer steps in water oxidation catalysis. redefining the mechanistic scenario, *ACS Catal.* **2017**, *7*, 1712.

[119] S. Chen, L.-W. Wang, Thermodynamic oxidation and reduction potentials of photocatalytic semiconductors in aqueous solution, *Chem. Mater.* **2012**, *24*, 3659.

[120] D. Li, J. Shi, C. Li, transition-metal-based electrocatalysts as cocatalysts for photoelectrochemical water splitting: a mini review, *Small* **2018**, *14*, 1704179.

[121] P. Peerakiatkhajohn, J.-H. Yun, S. Wang, L. Wang, Review of recent progress in unassisted photoelectrochemical water splitting: from material modification to configuration design, *J. Photon. Energy* **2016**, 7, 012006.

[122] X. An, T. Li, B. Wen, J. Tang, Z. Hu, L.-M. Liu, J. Qu, C. P. Huang, H. Liu, New insights into defect-mediated heterostructures for photoelectrochemical water splitting, *Adv. Energy Mater.* **2016**, *6*, 1502268.

[123] K. Zhang, M. Ma, P. Li, D. H. Wang, J. H. Park, Water Splitting Progress in Tandem Devices: Moving Photolysis beyond Electrolysis, *Adv. Energy Mater.* **2016**, *6*, 1600602.

[124] W. Liu, S. Li, J. Huang, S. Yang, J. Chen, L. Zuo, M. Shi, X. Zhan, C.-Z. Li, H. Chen, nonfullerene tandem organic solar cells with high open-circuit voltage of 1.97 V, *Adv. Mater.* **2016**, *28*, 9729.

[125] M. Gong, W. Zhou, M. J. Kenney, R. Kapusta, S. Cowley, Y. Wu, B. Lu, M.-C. Lin, D.-Y. Wang, J. Yang, B.-J. Hwang, H. Dai, Blending Cr_2O_3 into a NiO–Ni electrocatalyst for sustained water splitting, *Angew. Chem. Int. Ed.* **2015**, *54*, 11989.

[126] J. Li, Y. Wang, T. Zhou, H. Zhang, X. Sun, J. Tang, L. Zhang, A. M. Al-Enizi, Z. Yang, G. Zheng, nanoparticle superlattices as efficient bifunctional electrocatalysts for water splitting, *J. Am. Chem. Soc.* **2015**, *137*, 14305.

[127] S.-H. Hsu, J. Miao, L. Zhang, J. Gao, H. Wang, H. Tao, S.-F. Hung, A. Vasileff, S. Z. Qiao, B. Liu, An earth-abundant catalyst-based seawater photoelectrolysis system with 17.9% solar-to-hydrogen efficiency, *Adv. Mater.* **2018**, *30*, 1707261.

[128] J. Luo, Z. Li, S. Nishiwaki, M. Schreier, M. T. Mayer, P. Cendula, Y. H. Lee, K. Fu, A. Cao, M. K. Nazeeruddin, Y. E. Romanyuk, S. Buecheler, S. D. Tilley, L. H. Wong, A. N. Tiwari, M. Grätzel, Targeting ideal dual-absorber tandem water splitting using perovskite photovoltaics and $CuIn_xGa_{1-x}Se_2$ Photocathodes, *Adv. Energy Mater.* **2015**, *5*, 1501520.

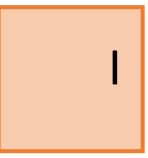

Chapter 2:

Objectives

II

After a brief introduction of the environmental and energy problems in Chapter 1, research studies have been performed with the aim to explore new materials and molecules for next generation of clean and sustainable energy. The objectives of our studies will be displayed in detail in this Chapter.

II

The main goal of this thesis is to study the combustion of fossil fuels induced air pollution problem, then synthesize new materials and design new structures for solar-driven water splitting devices, which can transfer sunlight to storable and transportable hydrogen. This clean and sustainable energy can bring us new breakthroughs to solve current environmental and energy problems. This main goal can be divided into the following three objectives.

The first objective is to study the use of fossil fuels caused environmental problems. As it was mentioned in section 1.1, toxic air pollutants and excessive emissions of CO_2 are the main environmental problems from the combustion of fossil fuels. In this thesis, I will statistically analyze the morphological, chemical and mechanical properties of fine airborne pollutant particles, which are pollutant matters with an aerodynamics diameter less than 2.5 μm ($PM_{2.5}$). I decided to study the $PM_{2.5}$ particles because they are so small that they can be inhaled and penetrate to the lungs and even the circulatory system of the human bodies. These fine particels trigger or worsen chronic disease such as asthma, heart attack, bronchitis and other respiratory problems. Based on the micro/nano-scale characterizations on $PM_{2.5}$ particles, we will understand which parts of these particles are most toxic for our human body, which can provide us some new ideas to filter these airborne pollutant particles.

As mentioned in section 1.2, there are three main systems for solar-driven water splitting devices. In this thesis, I will mainly focus on the exploration of PEC water splitting devices and PV-EC water splitting devices.

The second objective is to functionalize the n-type silicon photoanodes for PEC water splitting device, in which low cost and ultra-thin transition metal (Cu, Ni and Ni/Ti in this thesis) films will be deposited on the silicon photonaodes. These deposited thin metal films can form metal oxides (CuO, NiO_X and NiO_X/TiO_X) to work as efficient water

oxidation catalysts and protect silicon photoanodes from corrosion. In this study, the water splitting reaction will be trigged by both sunlight and external bias, which is expected to be as low as possible.

The third objective is to build a super-efficient anode based on a highly active ruthenium molecular catalyst for spontaneous PV-EC water splitting. In this study, no external bias will be applied, and just sunlight will be used for energy resource. The PV cells (perovskite or III-V semiconductors based solar cells) will absorb sunlight to generate electrons and holes for water reduction and oxidation, respectively. This study is based on a relatively mature technology, which is much closer to be commercially available. And also it will be the fisrt work to explore the use of molecular catalyst in PV-EC water splitting configuration.

II

Chapter 3:

Nanoscale characterization on airborne pollutant particles

III

In this chapter, the airbone pollutant particles ($PM_{2.5}$) are collected and statically characterized. The mechanical property of the $PM_{2.5}$ particles is analyzed for the first time, which is combined with the morphology and chemical composition analysis. Different kinds of $PM_{2.5}$ particles are observed, and the results show the stickiest $PM_{2.5}$ particles are soot aggrates, which are made of carbon. And one kind of the dark trace layers has also been frequencyly observed betwwen the $PM_{2.5}$ particles and the collected substrete, and we find that they are always around 10 nm thick, and mainly composed of alkali metals, hydrogen and CH groups.

The chapter consist of the following independent papers:

Paper A Y. Shi, Y. Ji, H. Sun, F. Hui, J. Hu, Y. Wu, J. Fang, H. Lin, J. Wang, H. Duan, M. Lanza, *Sci. Rep.* **2015**, *5*, 11232.

Paper B Y. Shi, B. Wang, M. Bartrons, M. Kolíbal, P. Bábor, X. Zhang, E. Grustan-Gutierrez, M. Lanza, **2018**, *submitted*

III

Paper A: Nanoscale characterization of $PM_{2.5}$ airborne pollutants reveals high adhesiveness and aggregation capability of soot particles

Y. Shi, Y. Ji, H. Sun, F. Hui, J. Hu, Y. Wu, J. Fang, H. Lin, J. Wang, H. Duan, M. Lanza, *Sci. Rep*. **2015**, *5*, 11232.

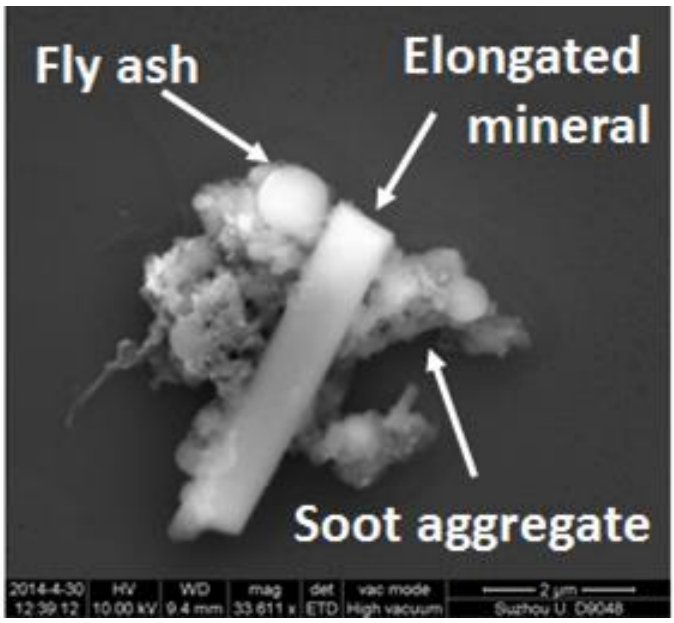

Abstract

In 2012 air pollutants were responsible of seven million human death worldwide, and among them particulate matter with an aerodynamic diameter of 2.5 micrometers or less ($PM_{2.5}$) are the most hazardous because they are small enough to invade even the smallest airways and penetrate to the lungs. During the last decade the size, shape, composition, sources and effect of these particles on human health have been studied. However, the noxiousness of these particles not only relies on their chemical toxicity, but particle morphology and mechanical properties affect their thermodynamic behavior, which has notable impact on their biological activity. Therefore, correlating the physical, mechanical and chemical properties of $PM_{2.5}$ airborne pollutants should be the first step

to characterize their interaction with other bodies but, unfortunately, such analysis has never been reported before. In this work, we present the first nanomechanical characterization of the most abundant and universal groups of $PM_{2.5}$ airborne pollutants and, by means of atomic force microscope (AFM) combined with other characterization tools, we observe that fluffy soot aggregates are the most sticky and unstable. Our experiments demonstrate that such particles show strong adhesiveness and aggregation, leading to a more diverse composition and compiling all possible toxic chemicals.

Contribution

Yuanyuan Shi did the AFM, SEM, EDX and TEM characterizations and prepared the manuscript.

A 1 Introduction

Air pollution has become the major problem of many cities, and it is affecting billions of persons[1-3] around the globe. Among all the noxious pollutants in air, fine particles with an aerodynamic diameter of 2.5 micrometers or less ($PM_{2.5}$) are the most harmful for human health because they are small enough to invade even the smallest airways and penetrate to the lungs.[4] Exposure to this fine particulate matter has been shown to cause respiratory ailments, and can lead to premature death from heart and lung disease.[5] These particles generally come from activities that burn fossil fuels, such as traffic, smelting, and metal processing, which are more abundant in urban areas.[6-8] To give an idea about the magnitude of the problem, while in 2012 the average $PM_{2.5}$ concentration in Los Angeles was 7.4 μg/cm^3, New Delhi established last year a new record registering 575 μg/cm^3 (60 times larger than the values considered safe),[9] and in 2013 Beijing suffered $PM_{2.5}$ concentrations above the limit recommended by the World Health Organization for more than 219 days;[10] according to the Lancet Global Health Burden of Disease Report air pollution is the fourth and sixth cause of death in East and South East Asia[11] (respectively), and in 2012 seven million people worldwide died due to illnesses linked to air pollution.[12] Moreover, $PM_{2.5}$ pollutants can travel long distances on the atmosphere and may affect surrounding areas. A recent study has reported that Chinese pollution contributed, at a maximum, 12–24% of sulfate concentrations over the western United States.[13]

In the past few years, many studies reported the size, shape, density and source of $PM_{2.5}$[6-8], as well as their effect in human health.[14-15] Despite the morphology and chemical composition of $PM_{2.5}$ may vary depending on the location, some groups of particles are omnipresent and have been invariably reported worldwide. Among them, the most common and abundant are Carbon-rich fluffy soot aggregate from incomplete combustion

of hydrocarbons, elongated minerals with high content of metals from coal-fired power plants, and spherical fly ash made of metal-silicates from road dust, construction, coal combustion and secondary atmospheric reactions.[6-8,16,17-19] Cell viability tests indicate that both organic and inorganic $PM_{2.5}$ components generate oxidative stresses responsible of toxic effects in human health.[20-23] While inorganic matter has possibly more impact on the respiratory system, organic particles may induce lethal cardiovascular disease.[24-25] Although chemical toxicity is the number one health concern, chemistry alone does not determine the noxiousness of the particles, and particle morphology (i.e. shape and surface properties) affect their dynamic behavior and thermodynamic properties, which have notable impact on their biological activity.[16] Therefore, nanomechanical properties determine how the particles morph, stick and aggregate, which strongly affect the way in which they interact with other bodies. However, in-depth nanomechanical particle analyses have never been performed. In this report, we present the first morphological and mechanical analysis of $PM_{2.5}$ and, by means of atomic force microscopy (AFM), we reveal essential information about these particles never reported before, such as surface roughness, stickiness, deformation and elasticity. Further scanning electron microscope images (SEM) and energy dispersive X-ray spectroscopy surveys (EDX) allowed to link these properties to the chemical composition and, therefore, to the sources. We analyze the most abundant and universal groups of $PM_{2.5}$ airborne pollutants and, after thoroughly investigating more than 500 fine particles with different tools, our results indicate that $PM_{2.5}$ soot aggregates exhibited the largest surface roughness, stickiness and deformation. Such observation is indeed indicating that these particles, not only can easily compile all other toxic chemicals, but also are difficult to remove when interacting with other bodies, which may cause longer exposure. This general behavior has been statistically corroborated processing experimental data through Weibull analytical models.

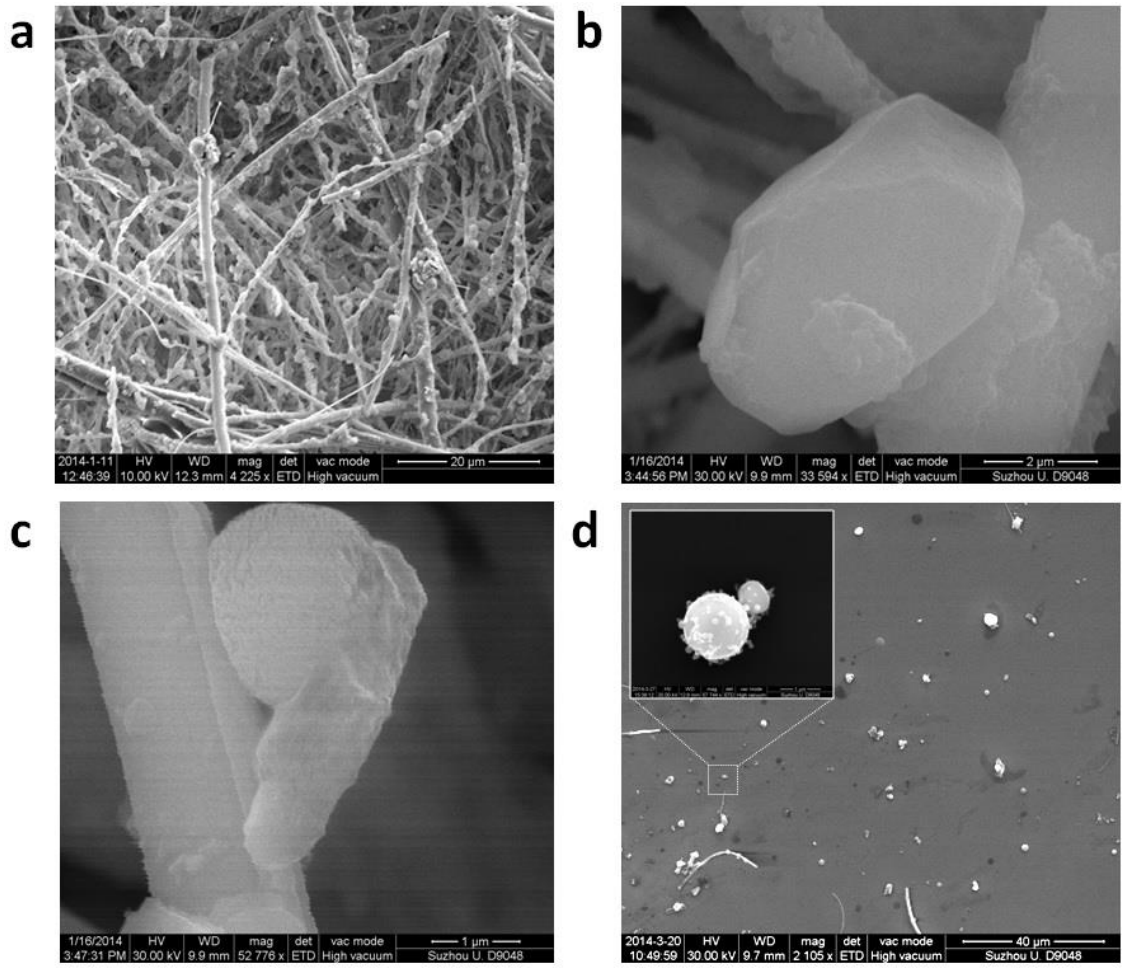

Figure 1. Morphology of $PM_{2.5}$ particles. (a), large area image of as-collected $PM_{2.5}$ on the filamentary filter. (b) and (c), SEM images of a particle with flat and rough top surface, respectively. (d), SEM image of the $PM_{2.5}$ transferred on a Silicon substrate. Inset, zoom-in SEM image of an Iron-rich particle. The scale bars are 20 µm for image (a), 2 µm for image (b), 1µm for image (c), 40 µm for image (d).

A 2 Results and discussion

$PM_{2.5}$ particles have been collected on December 2nd and 7th of 2013 in Beijing, following the regulations established by the US Environmental Protection Agency. For the particle collection, we used the TH-150C Automatic Medium Volume TSP Sampler coupled with TH-$PM_{2.5}$, which is strategically designed to retain in the filters only small particles with diameters below 5 µm (see supplementary information). The initially white filters become darker depending on the degree of pollution of each day, and the particles can be easily detected with the optical microscope (Figures S1 and S2 in the

supplementary information). Figure 1a shows the typical SEM picture of a contaminated filter: a dense network of filaments with incrusted pollutant particles, most of them $PM_{2.5}$. From all detected particles, we focus only on those with an aerodynamic diameter smaller than 2.5 µm and, at a first stage, we analyze their size and composition as collected in the filters - one by one - from SEM pictures and EDX surveys, respectively. The $PM_{2.5}$ exhibited circular, elongated and irregular shapes, as well as high densities of O, Si, C, Fe, Ca, Mg, Al, K, and S (Figures S3, S4 and S5). We start our novel analysis by studying the surface roughness of $PM_{2.5}$. It is widely known that surface roughness can remarkably influence the physical and mechanical properties of a body.[27] Figures 1b and 1c show the typical example of $PM_{2.5}$ particles with flat and rough surfaces (respectively, see also Figure S6). It is worth noting that, while the particle with a flat surface has a well-defined shape, the rough one seems to adapt to the shape of the filament network in the filter, suggesting that it could be easily deformed. When a body can deform its shape to adapt to the contour of another, the contact area between them increases, which enhances their adhesion force (capillary forces, Wan der Waals, electronic attraction).[27]

We analyze the capability of $PM_{2.5}$ to adhere to other bodies and, to do so, the surface properties of the particles are in-depth analyzed by means of AFM and related modes. AFM maps are very powerful to analyze the properties of the particles because they can provide three dimensional information with very high lateral and vertical resolutions. But the main problem is that the filamentary network of the filters used to collect $PM_{2.5}$ doesn't allow reliable AFM analysis, it is too rough.[19,28] Other authors used polycarbonate,[6] quartz[7] and mica substrates[29] but, even if those materials don't present a dense network of filaments, their roughness is still too large, which may lead to confusing images with the AFM. To solve this problem we developed a method to transfer the particles to arbitrary substrates by sonicating the filters together with a target substrate in

the absence of solvent (Figure S8), using a low power (40 W), frequency (40 KHz ± 10%) and short times (1-40 min). The target substrate consists of cleaned Silicon wafers (Figure S7), and allowed direct correlation between AFM and EDX data, and vice versa. Figure 1d shows an SEM picture of $PM_{2.5}$ particles transferred on the Silicon substrate (also in Figure S9); the inset shows the zoom-in image of an Iron- and Oxygen-rich particle similar to those classified as fly ash.[6, 8] We corroborate that the particles under test are representative of the well-established universal groups of $PM_{2.5}$. Figures S10, S11 and S12 in the supplementary information show the shape and chemical composition of the particles in this study and in the literature for the main three groups analyzed: fluffy soot aggregate, elongated minerals with high content of metals and spherical fly ash made of metal-silicates. The striking similarity between the particles in this work and those previously reported worldwide establishes the immediate importance and relevance of our study. We further analyze the reliability of this method comparing the types of particles observed in three different samples: i) in-situ collected on the filter (Figures 1a-c and S3-S5), ii) collected on the filter but transferred to the Silicon (Figures 1d and S10-12), and iii) in-situ collected on a piece of Silicon directly introduced in the collector (Figure S13). We observed a larger density of small particles in in-situ experiments (diameter below 500 nm, see Figure S14a), while after the transfer the particles measured were slightly larger (diameter usually above 500 nm, see Figures S10-S12). Such observation has two implications. The first is that the transfer process didn't fragment the particles. The absence of solvent minimizes particle fragmentation, and only the vibrations necessary to detach the particles from the filter are generated, so that they can precipitate on the target substrate.[30] And the second is that smallest particles couldn't be transferred. We further analyze those particles with SEM and EDX, and observed that their surface and chemical composition is very similar to those larger transferred on the

filter (Figure S14), indicating that they are not a different type of particle, but just smaller pieces of soot, elongated minerals and fly ash. It is worth noting that some atmospheric particles can be semi-to-entirely liquid when they are airborne, which would difficult the filter-to-silicon transfer process. Interestingly, we also observe many particles surrounded by a dark layer on both in-situ (Figure S14d) and after transfer (Figure S29). Due to its regular contour and flat shape, this dark trace may be related to the semi-liquid nature of some particles. Such observations corroborate that we successfully transferred most classes of $PM_{2.5}$ airborne pollutants collected on the filters (without altering them).

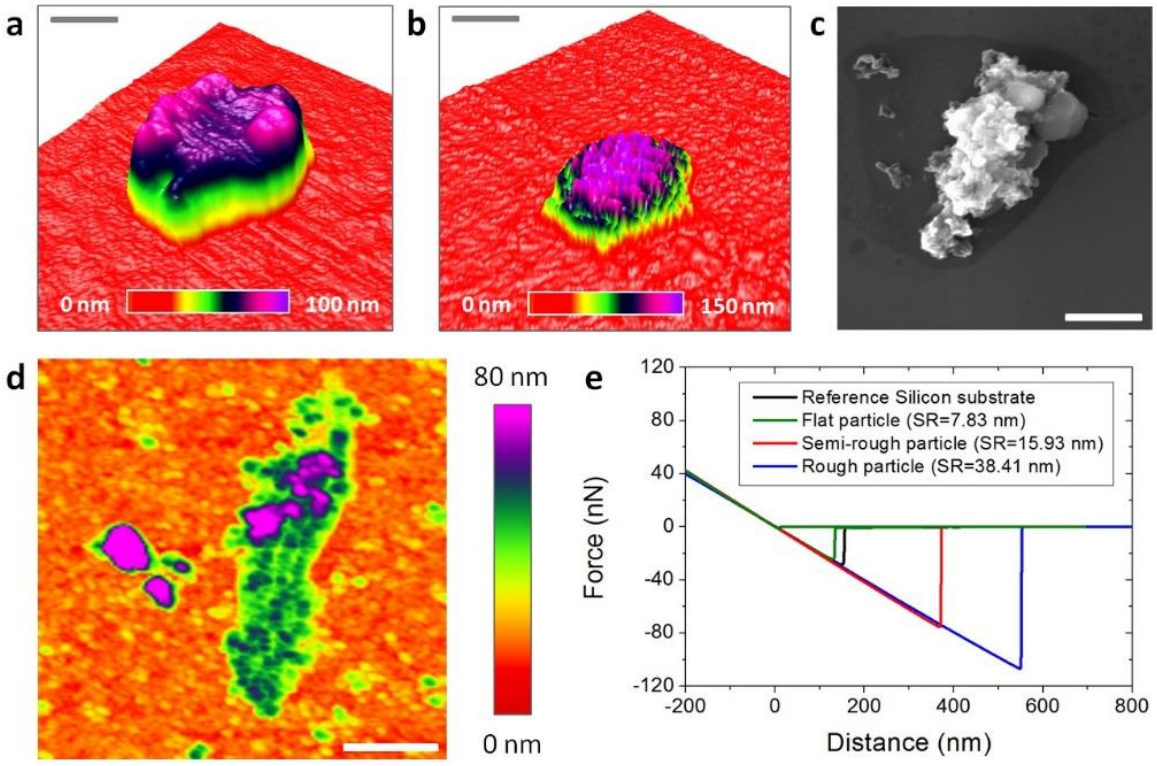

Figure 2. Mechanical properties of $PM_{2.5}$ particles measured with AFM. (a) and (b), three dimensional topographic AFM images of similar $PM_{2.5}$ particles with flat and rough surfaces respectively (on Silicon substrate); the AFM is able to display the surface roughness with a precision of Angstroms. (c) and (d), SEM and topographic AFM images of $PM_{2.5}$ soot aggregate with high surface roughness (respectively). (e), Example of force-distance curves measured on particles with different surface roughness (SR); the negative peak of the backward curve corresponds to the AFM tip-sample adhesion force; particles with higher surface roughness usually exhibited larger adhesion forces. The scale bars are 300 nm for (a) and 2.5 μm for (b), 3 μm for (c), 1.1 μm for (d).

Once the particles rest on flat Silicon, performing accurate AFM research is feasible, and therefore, we scanned the surface of the $PM_{2.5}$-rich Silicon substrate in tapping mode (Figure S15). The AFM characterization has been intentionally performed in air environment to monitor the real properties of the particles in atmosphere. Kollensperger et al.[29] demonstrated that the exposure of $PM_{2.5}$ pollutants to different relative humidities could alter their surface composition. Depending on their wettability, airborne pollutants could retain a water layer at the surface, which could alter the intrinsic adhesiveness of the particles measured by AFM due to the addition of capillary effects.[27,31] Therefore, using vacuum AFM may lead to false imaging of such properties, due to the removal of the natural water layer on the particles.[32,33] During our AFM experiments the temperature and relative humidity of the room ranged between 6-10 ºC and 60-70% (respectively). Figures 2a and 2b show the three dimensional AFM topographic images of $PM_{2.5}$ particles with flat and rough surfaces (respectively). The extraordinary high vertical resolution of the AFM allows displaying the rugosity of the $PM_{2.5}$ surface with an unprecedent precision of Angstroms (correlated SEM images in Figure S16). Using the NanoScope Analysis software of the AFM we have been able to easily and accurately calculate the surface roughness of each particle (Figures S17 and S18), and values of 14.60 nm and 39.51 nm for the particles in Figures 2a and 2b have been obtained (respectively). Moreover, off-line process of the images using the AFM software facilitate the determination of the diameter and area of the $PM_{2.5}$, something that is much more laborious to do from SEM images. The resulting statistical analysis of the particle diameter shows a maximum at 1.34 µm (Figure S19). It is worth noting that, the physical diameter measured in SEM and AFM images may not necessarily correspond to the aerodynamic one and, therefore, some particles with a physical diameter below 2.5 µm may could not strictly be considered $PM_{2.5}$. The relationship between the aerodynamic

diameter, physical diameter and particle density can be expressed as:

$$d_a = d_{ev}\sqrt{\frac{1}{\chi}\frac{\rho_p}{\rho_o}\frac{C_c(d_{ve})}{C_c(d_a)}} \qquad Eq.1$$

where, χ is the dynamic shape factor (in any flow regime), d_a is the aerodynamic diameter, d_{ve} is the volume equivalent diameter, C_c is the Cunningham slip correction factor, ρ_p is the particle density and ρ_o is the standard density (1 g/cm^3)[34]. Different methodologies to measure the particle density have been presented in the past.[35-42] For nonspherical particles, most techniques provide "apparent" or "effective" densities which, as stated in DeCarlo et al.[34], could be not necessarily a true measure of the particle. In any case, the complexity of these techniques makes the calculation of the particles density to be out of the scope of this study. Despite filtering the particles only by diameter may induce some degree of error, we believe it is small and we could evaluate it. Previous $PM_{2.5}$ studies reported particle densities mainly between 1 g/cm^3 and 3 g/cm^3 [40,41]. As the particle density in Eq.1 is inside the square root, a maximum increase of density (ρ_p) up to 3 g/cm^3 would produce an increase of 1.73 in the aerodynamic diameter (d_a). That would imply that, for a maximum particle with a density of 3 g/cm^3, a physical diameter below 1.44 µm would ensure an aerodynamic diameter of 2.5 µm or less. Interestingly, in the statistical analysis of the diameter (shown in Figure S19) most of the particles we analyzed are below 1.44 µm in diameter (the maximum peak of the distribution is at 1.34 µm). Despite a remarkable amount of particles with physical diameters between 1.44 and 2.5 µm are analyzed in our work, it is also reasonable to think that not all particles will reach the maximum densities above mentioned. Furthermore, Kelly and McMurry[42] and Schleicher et al.[38] observed that the calculated densities of aggregates were much lower than the bulk density of the particle material. Therefore, since many of the largest particles analyzed in this study may be aggregates (with diameters between 1.4 and 2.5 µm, see Figures S10-S12), in this work we will rely on the physical diameters measured in the

SEM and AFM images, as many other authors did in the past.[6,8,19]

Subsequently, the mechanical properties of airborne pollutants with a physical diameter below 2.5 µm (most of them $PM_{2.5}$) were analyzed by means of AFM topographic maps and Force-Distance (F-Z) curves in contact mode. The shape of the F-Z curves in contact mode can provide information about tip/particle adhesion, particle deformation, elasticity, rupture and indentation.[43-44] It should be noted that such experiment has never been performed before, and all previous AFM studies mostly analyzed the particles by topographic/phase maps in tapping mode. The main reason is that, in contact mode, conventional AFM tips may move the particles on the surface of the substrate, leading to false imaging. To avoid this problem, we use specific AFM tips with a very long cantilever (450 µm) and low spring constant (0.2 N/m) from Bruker (see methods). Using this methodology, we are able to monitor the intrinsic topography of the samples without introducing external modification. As an example, Figures 2c and 2d show the SEM and AFM images (respectively) of a $PM_{2.5}$ soot aggregate (see EDX composition analysis in Figure S20). As Figure 2d reveals, all the tiny features of its characteristic fluffy surface can be clearly observed with AFM. By sequences of topographic maps measured at the same location using different contact forces, we analyze the deformation and elasticity of the particles. As an example, the particle in Figure 2d exhibited shape changes, increasing its length and decreasing its height, as displayed in successive sections (Figure S20). Further AFM maps didn't reveal any other shape change, indicating that the particle cannot recover its initial shape, leading to plastic deformation (elastic deformation and shape recovery has been rarely observed). We also analyze the stickiness/adhesiveness of the particles by F-Z curves. Figure 2e shows the F-Z curves collected on particles with different surface roughness (the F-Z curves measured on bare Silicon are also shown as reference). The adhesion forces measured on

flat particles are ~20 nN respectively, close to the values of non-sticky flat surfaces such as Silicon, glass and aluminum; on the contrary, rough particles showed adhesion forces above ~100 nN, a stickiness comparable to that of scotch tape or laboratory Carbon tape (Figure S21). A low percentage of ultra-sticky $PM_{2.5}$ rich in Carbon may attach to the AFM tips (Figure S22). The adhesion and deformation of the particles have been also analyzed by scanning the surface of the samples with the Peak Force Quantitative Nanomechanical Mapping (QNM) tool from Bruker Dimension Icon AFM (see methods), which provides information at each pixel of the image (Figure S23). As an example,

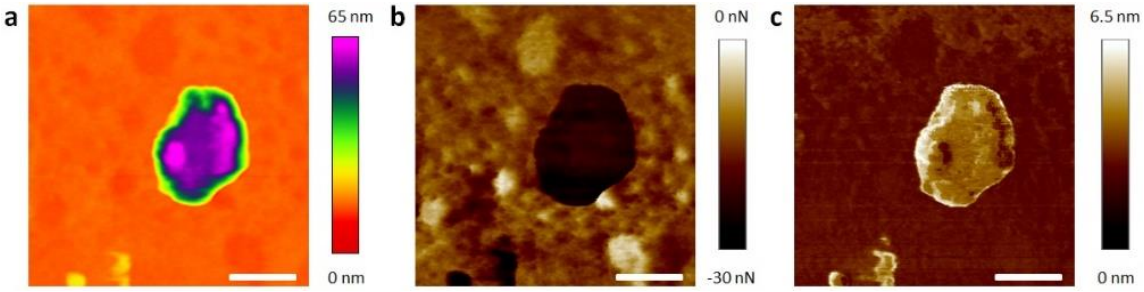

Figure 3. Adhesion and deformation of $PM_{2.5}$ particles. (a), (b), and (c), topographic, contact force and deformation maps of a $PM_{2.5}$ particle with a flat surface (respectively). The images reveal a more complete picture of the mechanical properties of the particle. Since many particles can be analyzed during the same scan, this AFM mode paves the way to statistically analyze the mechanical properties of the particles. The scale bars are 300 nm for (a-c).

Figures 3a, 3b and 3c show the topographic, adhesion and deformation maps (respectively) of a typical $PM_{2.5}$ particle with a flat surface. The negative contact force in Figure 3b indicates adhesive force, i.e. the particle shows an adhesion force of 25 nN (contact force of -25nN). As it can be observed, the values of adhesion force and deformation at each image deviate from the maximum/minimum values detected on the flat Silicon, and local differences can also be detected. More specifically, the particle displayed in Figure 3 holds a very flat surface with more progressive height changes than local fluctuations, which interestingly, produces an almost constant adhesion force. Such behavior has been

observed in particles with regular shapes and fine surfaces, while rough morphologies normally showed larger deviations. The genuine capability of this tool to analyze the adhesiveness and deformation of many particles during the same scan allows for the first time the statistical analysis of these properties.

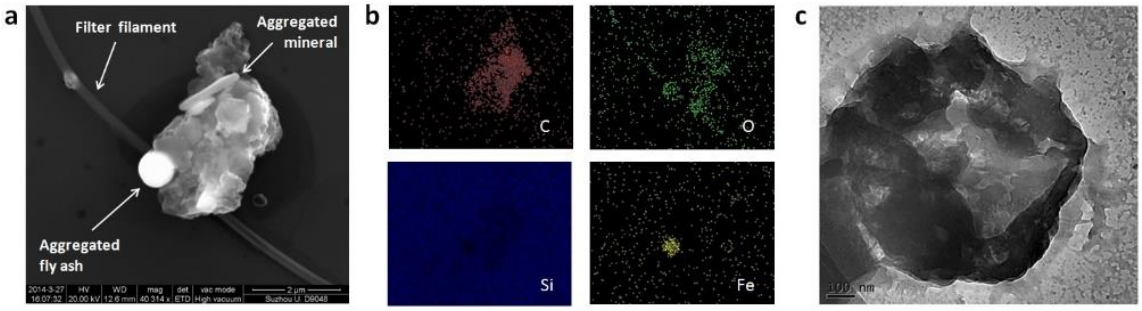

Figure 4. Aggregate of $PM_{2.5}$ particles. (a) and (b), SEM and EDX analyses of a $PM_{2.5}$ particles aggregate on clean Silicon; the rough Carbon-rich soot particle shows to be very sticky and can attach Iron-rich spherical fly ash, elongated minerals and even rip off filter filaments during the transfer. (c), TEM analysis of an organic particle showing hierarchical structure and proving the aggregation of small flakes and nanoparticles. The scale bars are 2 μm for (a) and 100 nm for (c).

The large stickiness of some $PM_{2.5}$ has been also proved from SEM/EDX analysis. Figures 4a and 4b show the SEM and EDX images of a sticky $PM_{2.5}$ soot particle. As it can be observed, the rough particle made of Carbon can aggregate other with typical shapes and chemical compositions, such as Iron- and Oxygen-rich fly ash and elongated minerals. The ability of fluffy soot particles to aggregate the rest has been repeatedly observed (Figure S24), which could increase the toxicity of the particle. Some particles are so sticky that they can even rip out some filter filaments during the transfer. The aggregation capability of soot $PM_{2.5}$ has also been observed from Transmission Electron Microscope (TEM) images (Figure 4c), which indicate that the sticky nature of these pollutants leads to a hierarchical structure made of thin layers and small particles

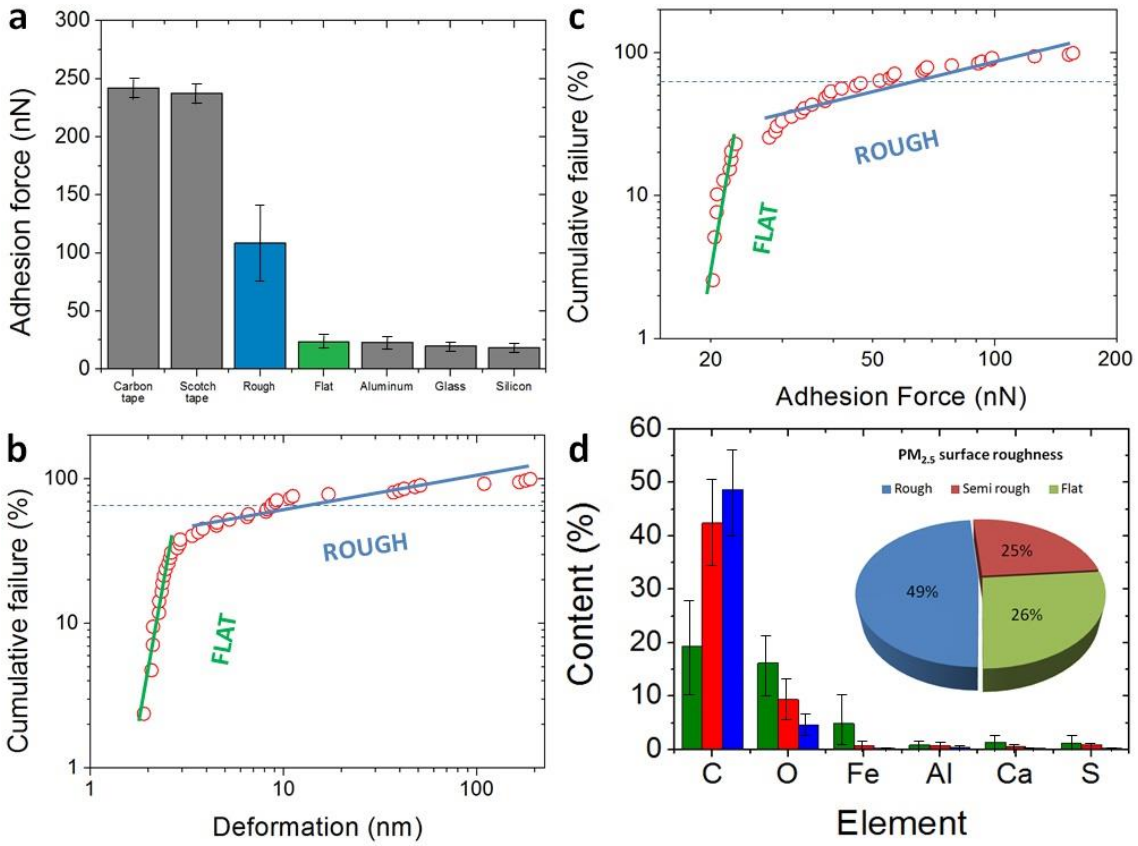

Figure 5. Relationship between mechanical properties and chemical composition of $PM_{2.5}$. (a), Adhesion force of $PM_{2.5}$ with rough and flat surfaces compared to standard sticky and non-sticky substrates. (b), Weibull probability plot of the adhesion force collected on two groups of $PM_{2.5}$ particles (with low and high surface roughness); (c), statistical analysis of the deformation of the same particles; both studies corroborate the different mechanical properties of rough and flat $PM_{2.5}$ particles, and stickier particles usually show a larger deformation. (d), EDX Chemical composition histogram of the particles collected with SEM/EDX classified by surface roughness; a larger surface roughness (and therefore, stickiness and deformation) link to a larger content of Carbon, while particles with a flat surface (low stickiness and viscosity) are richer in Oxygen and metals.

aggregated on them. Compared to the reference substrates, fluffy-rough particles showed larger adhesion forces in F-Z curves (Figure 5a), which is responsible of nanoparticle aggregation. The $PM_{2.5}$ aggregates analyzed in this study systematically showed large densities of Carbon (Figures S23, S24 and S25). Smith et al.[17] studied the $PM_{2.5}$ in London air, and suggested that organic pollutants may tend to aggregate, while pure metals and minerals do not. The larger adhesiveness and deformation of fluffy soot aggregate particles have been statistically corroborated through the Weibull probability plots

(Figure 5b and 5c). The mass mobility and fractal dimension of soot aggregate is especially important because it remarkably affects the way in which it interacts with other bodies, and hence, the exposure experienced by the receptor.[16] The lower slope of the Weibul plots for fluffy-rough particles rich in Carbon (soot aggregates) reveal a larger variability of these characteristics, indicating that they are more unstable from a mechanical point of view. On the contrary, particles with a flat surface and rich on stable metallic oxides and silicates (fly ash and elongated minerals) exhibited lower and uniform stickiness and deformation. The larger content of Carbon of rough, sticky and deformable particles (soot aggregates) has been statistically corroborated with EDX (Figure 5d). We quantified the amount of particles of each type and concluded that, in the more than 500 particles analyzed: 49% are rich on Carbon, sticky, deformable and unstable, 26% showed larger stability and were composed of metallic oxides, and the remaining 25% showed an intermediate behavior. The first group can be clearly linked to fluffy soot aggregate, while the last two groups correspond to elongated minerals and fly ash indistinctly. These values are comparable to those previously reported.[16-19, 45] Finally, we observe that 54% of the $PM_{2.5}$ particles analyzed appeared surrounded by a dark area in the SEM images. We analyze the morphology of such layer by means of AFM and observed that such areas are flat plateaus with thicknesses between 2 and 10 nm (Figure S29). Despite EDX analyses were unable to assess the chemical composition of these plateau-like areas, the observation of regular contours make us think that such layer may be formed by semi-liquid particles. The observation of much more particles surrounded by this layer in in-situ experiments on Silicon further supports this hypothesis: semi-to-entirely liquid particles may be difficult to transfer from the filters to the flat Silicon substrate. We further analyzed the stickiness of this plateau-like layer by means of, AFM F-Z curves and adhesion/deformation maps, but did not reveal any increase of the adhesion force,

suggesting the formation of an inert layer. Probably Oxygen atoms from the $PM_{2.5}$ particle may interact with the underlying Silicon substrate leading to the formation of a thin SiO_2 layer.[46] Such oxidation may be responsible for some of the toxic effects of $PM_{2.5}$ on human cellular tissue.[8] Future cell viability assays should conduct to clarify of the degree of toxicity of these specific particles.

A 3 Conclusion

In conclusion, we statistically analyzed the physical and chemical properties of the most representative and universal groups of $PM_{2.5}$ airborne pollutants by means of AFM, SEM, TEM and EDX. After a thorough characterization of more than 500 particles, our study reveals that fluffy soot particles show the capability to retain other species with different sizes and chemical compositions, increasing the chemical toxicity of the resulting aggregate. Our unprecedented AFM analysis revealed that such capability is related to the intrinsic high adhesiveness of soot aggregates. The experimental methodologies used here, including a method to transfer $PM_{2.5}$ from rough collection filters to flat analysis-friendly substrates, pave the way for future in-deep nanoscale characterization of airborne pollutants.

A 4 Methods

In this investigation, we developed a method to transfer $PM_{2.5}$ particles on flat substrates for friendly physical and mechanical characterization with Atomic Force Microscope. A piece of polluted filter and cleaned Si substrate were placed together in a plastic tube box; the tube was then immersed in a glass with water and sonicated for different times to let the particles precipitate on the Silicon (see supplementary information). The relationship between surface roughness and chemical composition was

studied by using the Quanta 200FEG Scanning Electron Microscope coupled with Energy Dispersive X-ray Spectrometer (SEM-EDX). High-resolution Transmission Electron Microscope (HRTEM) images were obtained with the Tecnai G2 F20 using standard copper grid and a field voltage of 20 KV. The mechanical properties of the particles were analyzed using two kinds of AFM: the Multimode V AFM and Dimension Icon AFM form Bruker. The first one was used to measure F-Z curves in contact mode using standard commercially available AFM tips from Bruker (model SCM-PIC). These tips were made by Silicon micromachining and were coated first with a 20 nm thick layer of Pt–Ir, which is a 95% platinum and 5% iridium alloy (the iridium is used to enhance the stability of the platinum layer). The other main characteristics of these tips are: thickness = 2 µm, width = 50 µm, length = 450 µm, spring constant = 0.2 N/m, resonance frequency = 13 kHz and nominal tip radius = 20 nm. The Dimension Icon AFM was used to measure adhesion and deformation maps. The images are built from the information collected at each point (which represents the value of each pixel of the map (see supplementary information). For these experiments Co-Cr coated Silicon tips from Burker were used. The main characteristics of the tip are: thickness = 1.85 µm, width = 30 µm, length = 125 µm, spring constant = 5 N/m, resonance frequency = 150 kHz and nominal tip radius = 35 nm. The maps were recorded using a scan frequency of 1 Hz, and a drive amplitude of 5V. All AFM data were analyzed with the NanoScope Analysis AFM software from Bruker (version 1.40), and the plots were generated with OriginLab 8.0.

A 5 Associated content

Supporting Information available: $PM_{2.5}$ collection process, Digital camera pictures of the contaminated filters, Optical microscope pictures of the contaminated filters, SEM-EDX study of most representative particles on the filters, Methodology to

select particles with rough and flat surfaces from SEM images, Silicon substrates used in this investigation, Process to transfer $PM_{2.5}$ from rough filters to flat analysis-friendly substrates, Representative SEM images of $PM_{2.5}$ transferred on Silicon, Representative AFM images of $PM_{2.5}$, transferred on Silicon, Correlation between AFM and SEM images, Quantification of the particles roughness with AFM, Statistical analysis of $PM_{2.5}$ size transferred on Silicon, Universal groups of $PM_{2.5}$ airborne pollutants, Analysis of $PM_{2.5}$ deformation from topographic AFM maps, Values of adhesion force in reference substrates, Particle adhesion to the AFM tip, Measurement of the adhesion and deformation with AFM, Ability of Carbon-rich soot to aggregate other particles, Effect of some of $PM_{2.5}$ to surrounding areas.

A 6 Funding sources

This work has been supported by Major State Basic Research Development Program of China (Grant No. 2011CB013101), National Natural Science Foundation of China (NSFC) under Grants No. 11225208 and 10872003.

A 7 Acknowledgment

Professors Luis Liz-Marzan and Lifen Chi are acknowledged for scientific discussion and laboratory access respectively. Zequn Cui is acknowledged for technical support in AFM measurements and Professor Yao He and Fei Peng are acknowledged for biological advice.

A 8 References

[1] C. A. Pope, D. W. Dockery, Air pollution and life expectancy in China and beyond, *Proc. Natl. Acad. Sci USA.* **2013**, *110*, 12861.

[2] Y. Chen, A. Ebenstein, M. Greenstone, H. Li, Evidence on the impact of sustained exposure to air pollution on life expectancy from China's Huai River policy. *Proc. Natl. Acad. Sci USA.* ***2013***, *110*, 12936.

III

[3] J. Qiu, Fight against smog ramps up, *Nature* **2014**, *506*, 273.

[4] J. Marshall, PM 2.5. Proc. *Natl. Acad. Sci. USA* **2013**, *110*, 8756.

[5] K. A. Miller, D. S. Siscovick, L. Sheppard, K. Shepherd, J. H. Sullivan, G. L. Anderson, J. D. Kaufman, Long-term exposure to air pollution and incidence of cardiovascular events in women. *N. Engl. J. Med.* **2007**, *356*, 447**.**

[6] W. Yue, X. Li, J. Liu, Y. Li, X. Yu, B. Deng, T. Wan, G. Zhang, Y. Huang, W. He, W. Hua, L. Shao, W. Li, S. Yang, Characterization of PM2.5 in the ambient air of Shanghai city by analyzing individual particles. *Sci. Total Environ.* **2006**, *368*, 916.

[7] G. Labrada-Delgado, A. Aragon-Pina, A. Campos-Ramos, T. Castro-Romero, O. Amador-Munoz, R. Villalobos-Pietrini, Chemical and morphological characterization of PM2.5 collected during MILAGRO campaign using scanning electron microscopy, *Atmos. Pollut. Res.* **2012**, *3*, 289.

[8] X. Feng, Z. Dang, W. Huang, L. Shao, W. Li, Microscopic morphology and size distribution of particles in PM2.5 of Guangzhou City. *J. Atmos. Chem.* **2009**, *64*, 37.

[9] S. Banerjee, *Delhi loses air pollution control race to Beijing.* (2014) Available at: http://www.cseindia.org/content/delhi-loses-air-pollution-control-race-beijing (Accessed: 28th April 2014)

[10] J. Li, *Only 3 of 74 Chinese cities meet air quality standard.* (2014) Available at: http://www.scmp.com/news/china/article/1443762/only-3-74-chinese-cities-meet-air-quality-standard (Accessed: 28th April 2014)

[11] R. Horton, GBD 2010: understanding disease, injury, and risk. *Lancet* **2012**, *380*, 2053.

[12] T. Jasarevic, G. Thomas, N. Osseiran, *7 million premature deaths annually linked to air pollution*. (2014) Available at: http://www.who.int/mediacentre/news/releases/2014/air-pollution/en/ (Accessed: 28th April 2014)

[13] J. Lin, D. Pan, S. J. Davis, Q. Zhang, K. He, C. Wang, D. G. Streets, D. J. Wuebbles, D. Guan, China's international trade and air pollution in the United States. *Proc. Natl. Acad. Sci. USA* **2014**, *111*, 1736.

[14] E. Longhin, J. A. Holme, K. B. Gutzkow, V. M. Arlt, J. E. Kucab, M. Camatini, M. Gualtieri, Cell cycle alterations induced by urban PM2.5 in bronchial epithelial cells: characterization of the process and possible mechanisms involved. *Part. Fibre Toxicol.* **2013**, *10*, 63.

[15] X. Deng, F. Zhang, W. Rui, F. Long, L. Wang, Z. Feng, D. Chen, W. Ding, PM2.5-induced oxidative stress triggers autophagy in human lung epithelial A549 cells. *Toxicol. Vitro* **2013,** *27*, 1762.

[16] D. Broday, R. Rosenzweig, Deposition of fractal-like soot aggregates in the human respiratory tract. *J. Aerosol. Sci.* **2011**, *42*, 372.

[17] S. Smith, M. Ward, R. Lin, R. Brydson, M. Dall'Osto, R. M. Harrison, Comparative study of single particle characterisation by Transmission Electron Microscopy and time-of-flight aerosol mass spectrometry in the London atmosphere. *Atmos. Environ.* **2012**, *62, 400.*

[18] Y. Chen, N. Shah, F. E. Huggins, G. P. Huffman, W. P. Linak, C.A. Miller, Investigation of primary fine particulate matter from coal combustion by computer-controlled scanning electron microscopy, *Fuel Process. Technol.* **2004**, *85*, 743.

[19] P. G. Satsangi, S. Yadav, Characterization of PM2.5 by X-ray diffraction and scanning electron microscopy–energy dispersive spectrometer: its relation with different pollution Sources. *Int. J. Environ. Sci. Technol.* **2014**, *11*, 217.

[20] S. Billet, G. Garçon, Z. Dagher, A. Verdin, F. Ledoux, F. Cazier, D. Courcot, A. Aboukais, P. Shirali, Ambient particulate matter (PM2.5): physicochemical characterization and metabolic activation of the organic fraction in human lung epithelial cells (A549), *Environ. Res.* **2007**, *105*, 212.

[21] K. S. Kouassi, S. Billet, G. Garçon, A. Verdin, A. Diouf, F. Cazier, J. Djaman, D. Courcot, P. Shirali, Oxidative damage induced in A549 cells by physically and chemically characterized air particulate matter (PM2.5) collected in Abidjan, Côte d'Ivoire. *J. Appl. Toxicol.* **2010**, *30*, 310.

[22] G. Viola, R. Bortolozzi, E. Hamel, S. Moro, P. Brun, I. Castagliuolo, M. G. Ferlin, G. Basso, MG-2477, a new tubulin inhibitor, induces autophagy through inhibition of the Akt/mTOR pathway and delayed apoptosis in A549 cells. *Biochem. Pharmacol.* **2012**, *83*, 16.

[23] S. Yi, F. Zhang, F. Qu, W. Ding, Water-insoluble fraction of airborne particulate matter (PM10) induces oxidative stress in human lung epithelial A549 cells. *Environ. Toxicol.* **2014**, *29*, 226.

[24] F. Goodarzi, Morphology and chemistry of fine particles emitted from a Canadian coal-fired power plant. *Fuel* **2006**, *85*, 273.

[25] R. J. Klemm, R. M. Mason, Aerosol research and Inhalation Epidemiological Study (ARIES): air quality and daily mortality statistical modeling--interim results. *J. Air Waste Manage. Assoc.* **2000**, *50*, 1433.

[26] Y. Ando, Lowering friction coefficient under low loads by minimizing effects of adhesion force and viscous resistance. *Wear* **2003**, *254*, 965.

[27] B. Cappella, G. Dietler, Force-distance curves by atomic force microscopy. *Surf. Sci. Rep.* **1999**, *34*, 1.

[28] P. Gwaze, H. J. Annegarn, J. Huth, G. Helas, Comparison of particle sizes determined with impactor, AFM and SEM. *Atmos. Res.* **2007**, *86*, 93.

[29] G. Köllensperger, G. Friedbacher, R. Kotzick, R. Niessner, M. Grasserbauer, M. In-situ atomic force microscopy investigation of aerosols exposed to different humidities. *Fresenius J. Anal. Chem.* **1999**, *364*, 296.

[30] Chemical Methods Ontology (CMO) of the Real Society of Chemistry. Prospects (2014) Available at: http://www.rsc.org/publishing/journals/prospect/ontology.asp?id=CMO:0001708 (Accessed: 14th July 2014).

[31] J. N. Israelachvili, in *Intermolecular and surface forces*, Vol. 1, Ch. 17.11, 456-461, Academic Press, Burlington, MA **2011**.

[32] M. Lanza, T. Gao, Z. Yin, Y. Zhang, Z. Liu, Y. Tong, Z. Shen, H. Duan, Nanogap based graphene coated AFM tips with high spatial resolution, conductivity and durability, *Nanoscale* **2013**, *5*, 10816.

[33] M. Lanza, A. Bayerl, T. Gao, M. Porti, M. Nafria, G. Y. Jing, Y. F. Zhang, Z. F. Liu, H. L. Duan, Graphene-coated atomic force microscope tips for reliable nanoscale electrical characterization, *Adv. Mater.* **2013**, *25*, 1440.

[34] P. F. DeCarlo, J. G. Slowik, D. R. Worsnop, P. Davidovits, J. L. Jimenez, Particle Morphology and Density Characterization by Combined Mobility and Aerodynamic Diameter Measurements. Part 1: Theory, *Aerosol Sci. Technol.* **2004**, *38*, 1185.

[35] E. P. Emets, V. A. Kascheev, P. P. Poluektov, A new technique for the determination of the density of airborne particulate matter, *J. Aerosol Sci.* **1992**, *23*, 27.

[36] P. McMurry, A review of atmospheric aerosol measurements, *Atmos. Environ*. **2000**, *34*, 1959.

[37] K. Adachi, S. H. Chung, P. R. Buseck, Shapes of soot aerosol particles and implications for their effects on climate, *J. Geophys. Res.* **2010**, *115*, *6469.*

[38] B. Schleicher, S. Künzel, H. Burtscher, In situ measurement of size and density of submicron aerosol particles, *J. Appl. Phys.* **1995**, *78*, 4416.

[39] E. Le Bronec, A. Renoux, D. Boulaud, M. Pourprix, Effect of gravity in differential mobility analysers. A new method to determine the density and mass of aerosol particles, *J. Aerosol Sci.* **1999**, *30*, 89.

[40] L. Morawska, G. Johnson, Z. D. Ristovski, V. Agranovski, Relation between particle mass and number for submicrometer airborne particles, *Atmos. Environ.* **1999**, *33*, 1983.

[41] M. Pitz, J. Cyrys, E. Karg, A. Wiedensohler, H.-E. Wichmann, J. Heinrich, Variability of apparent particle density of an urban aerosol, *Environ. Sci. Technol.* **2003**, *37*, 4336.

[42] W. P. Kelly, P. H. McMurry, Measurement of particle density by inertial classification of differential mobility analyzer–generated monodisperse aerosols, *Aerosol Sci. Technol.* **1992**, *17*, 199.

[43] A practical guide to AFM force spectroscopy and data analysis. JPK Instruments. Technical note (2014) Available at: http://www.jpk.com/afm.230.en.html. (Accessed: 14th July 2014).

[44] J. Zivkovic, AFM force spectroscopy of viral systems. PhD thesis, Radboud University (2013).

[45] J. Han, B. Han, P. Li, S. Kong, Z. Bai, D. Han, X. Dou, X. Zhao, Chemical characterizations of PM10 profiles for major emission Sources in Xining, Northwestern China. *Aerosol Air Qual. Res.* **2014**, *14*, 1017.

[46] G. Mende, J. Finster, D. Flamm, D. Schulze, Oxidation of etched silicon in air at room temperature; Measurements with ultrasoft X-ray photoelectron spectroscopy (ESCA) and neutron activation analysis, *Surf. Sci.* **1983**, *128*, 169.

III

A 9 Supporting Information

Paper A: Nanoscale characterization of $PM_{2.5}$ airborne pollutants reveals high adhesiveness and aggregation capability of soot particles

Index

$PM_{2.5}$ collection process

Digital camera pictures of the contaminated filters

Optical microscope pictures of the contaminated filters

SEM-EDX study of most representative particles on the filters

Methodology to select particles with rough and flat surfaces from SEM images

Silicon substrates used in this investigation

Process to transfer $PM_{2.5}$ from rough filters to flat analysis-friendly substrates

Representative SEM images of $PM_{2.5}$ transferred on Silicon

Universal groups of PM2.5 airborne pollutants

Reliability of the transfer method

Representative AFM images of $PM_{2.5}$ transferred on Silicon

Correlation between AFM and SEM images

Quantification of the particles roughness with AFM

Statistical analysis of $PM_{2.5}$ size transferred on Silicon

Analysis of $PM_{2.5}$ deformation from topographic AFM maps

Values of adhesion force in reference substrates

Particle adhesion to the AFM tip

Measurement of the adhesion and deformation with AFM

Ability of Carbon-rich soot to aggregate other particles

Effect of some of $PM_{2.5}$ to surrounding areas

III

$PM_{2.5}$ collection process

$PM_{2.5}$ airborne pollutants have been collected according to the regulations established by the US Environmental Protection Agency, Code of Federal Regulations 40, Part 53: "Ambient air monitoring reference and equivalent methods". For more information, please check: http://www.ecfr.gov. Mass concentrations of daily $PM_{2.5}$ were acquired from the continuous monitoring using a TH-150C Automatic Medium Volume TSP Sampler (Wuhan Tianhong instruments Co. Ltd) with TH-$PM_{2.5}$. Both equipments were located at the stepped platform in front of the laboratory building at No. 7 PanjiayuanNali road, in the Chaoyang District of Beijing (zip code 100021), in China. The particles were collected on December 2^{nd} and 7^{th}, with concentrations of 106 $\mu g/m^3$ and 298 $\mu g/m^3$, respectively. We analyzed more than 30 samples and systematically detected three groups of universal particles: fluffy soot aggregate, elongated minerals and spherical fly ash (see Figures S10-S12). These three groups have been previously reported by many other authors at different locations of the world, including US, UK, Mexico, India, Italy and China (see Figures S10-S12). Therefore, the particles reported in this study are representative of the global collective of $PM_{2.5}$ worldwide, and the aim of this work is not to further report their size/shape, amount and composition, but to thoroughly analyze the nanoscale properties of these three well-identified groups of $PM_{2.5}$airborne pollutants.

Digital camera pictures of the filters

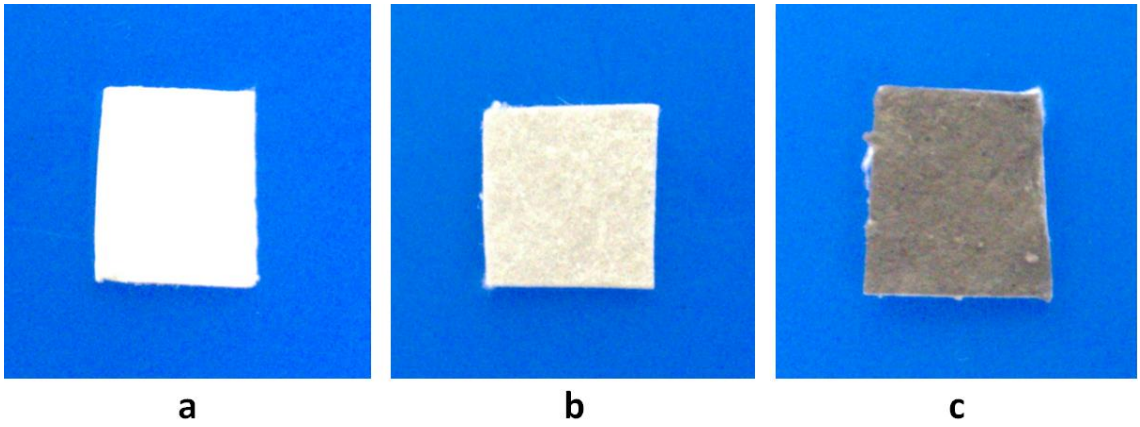

Figure S1. Pictures collected with a digital camera for the clean filter (a), and the particles exposed to atmospheric air on December 2nd (b) and December 7th(c). Sizes: 1 cm x 1 cm.

Optical microscope pictures of the contaminated filters

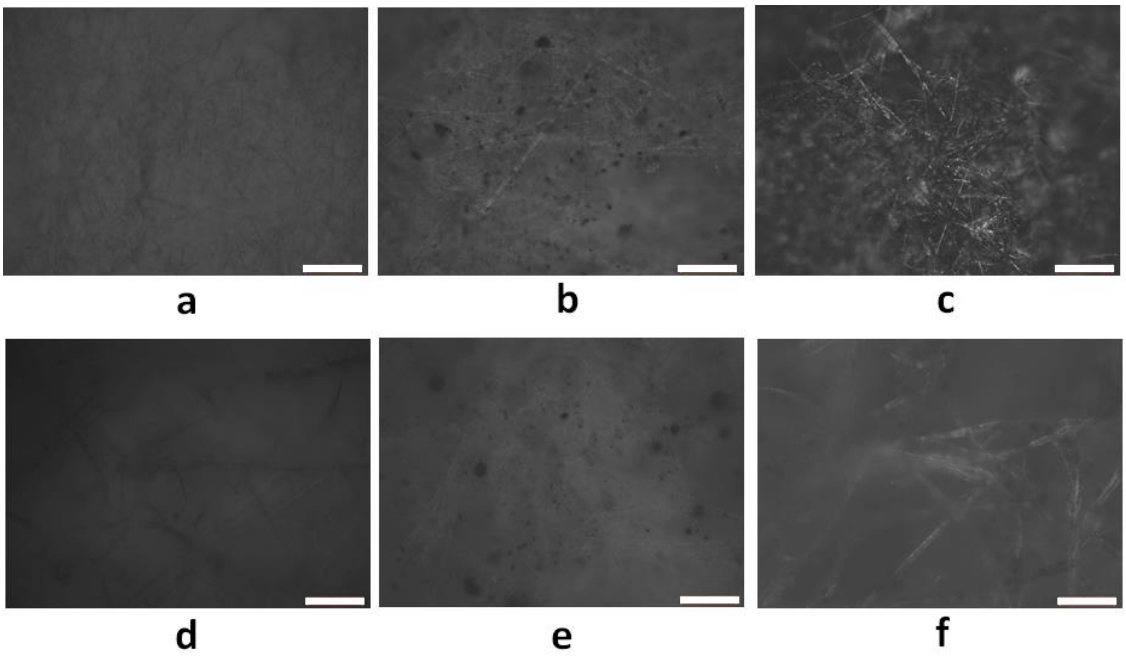

Figure S2. Optical microscope collected on clean filter ((a) and (d)), intermediate polluted filter ((b) and (e)), and very polluted filter ((c) and (f)). Polluted filters show larger amount of particles (black spots). The scale bars are 100 µm for images (a-c) and 20 µm for images (d-f).

SEM-EDX study of most representative particles on the filters

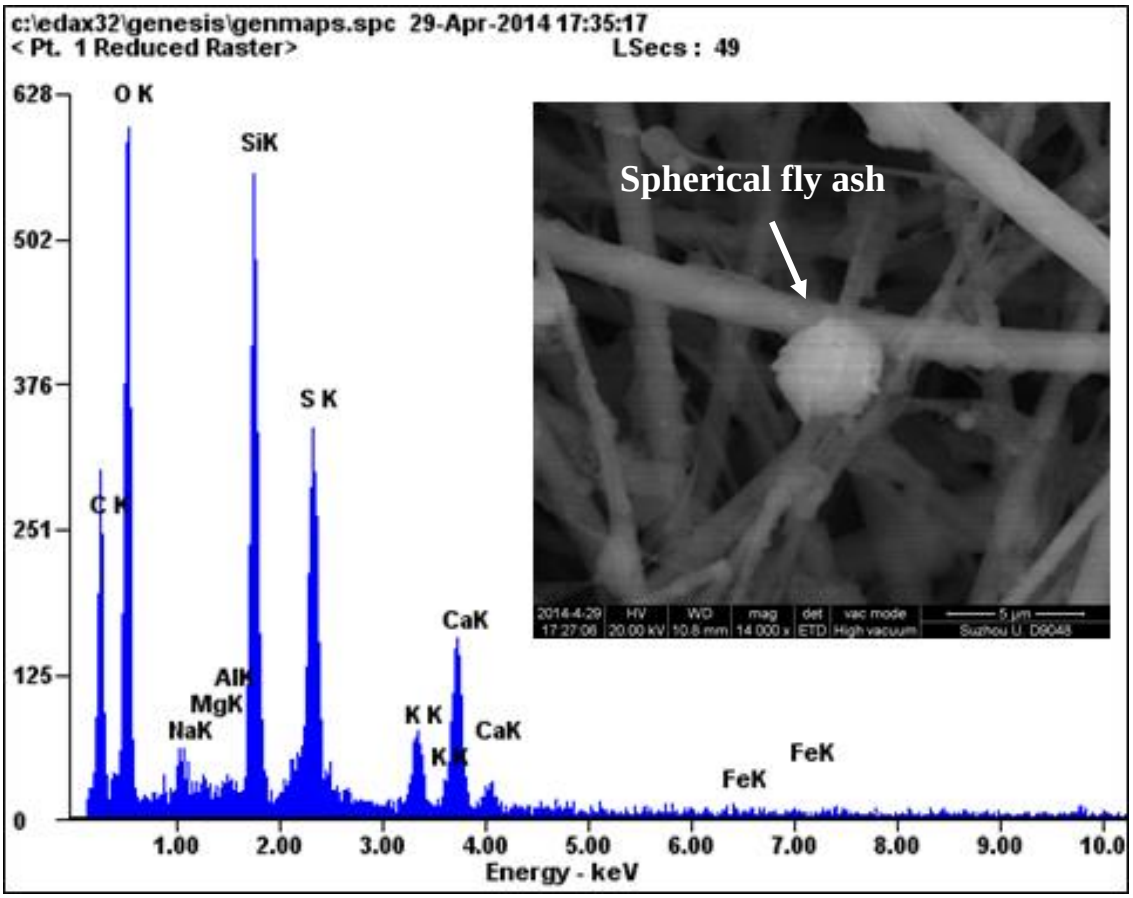

Figure S3. SEM picture and EDX analysis for one representative $PM_{2.5}$ particle on the filter.

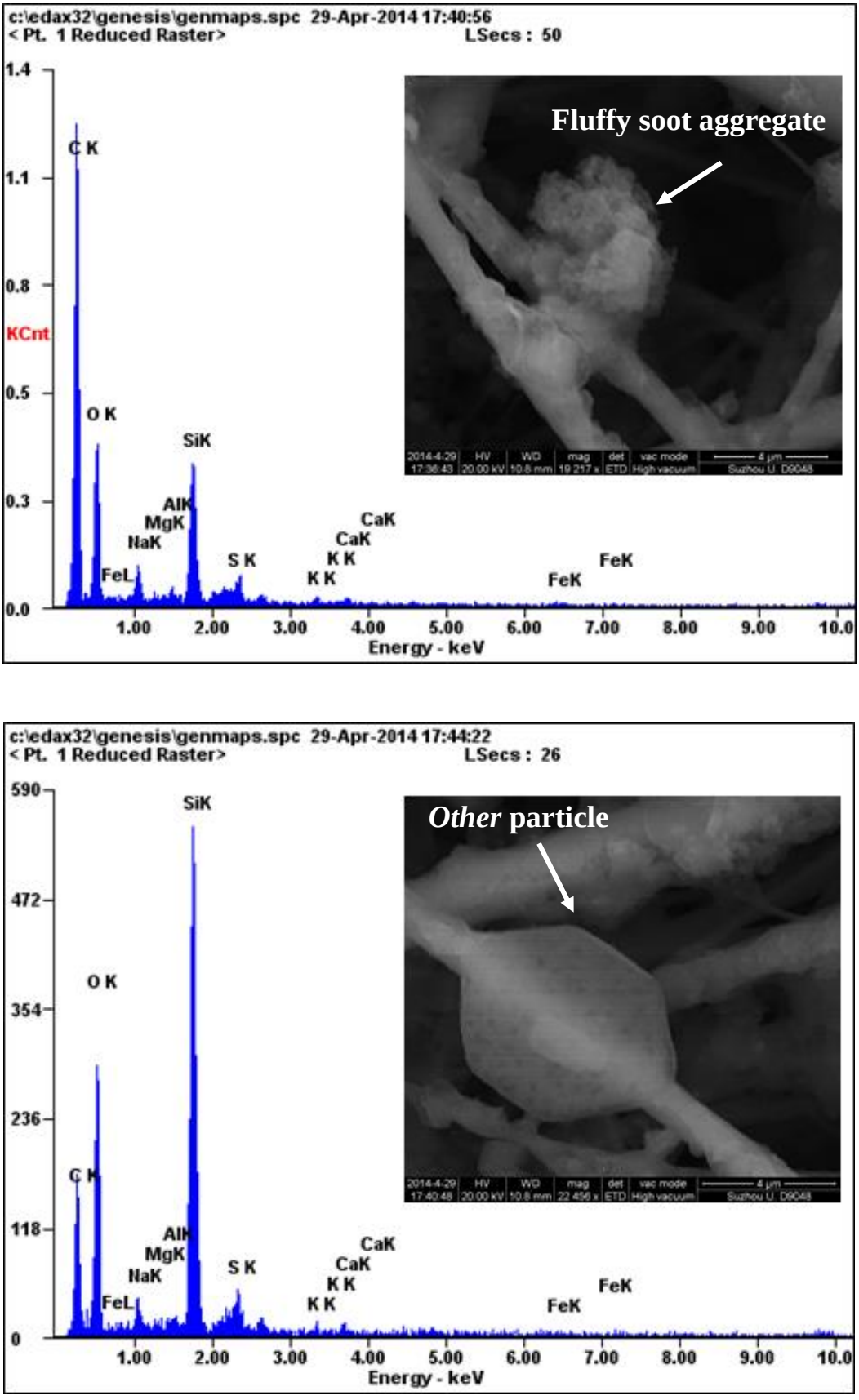

Figure S4. SEM pictures and EDX analyses for two representative $PM_{2.5}$ particles on the filter.

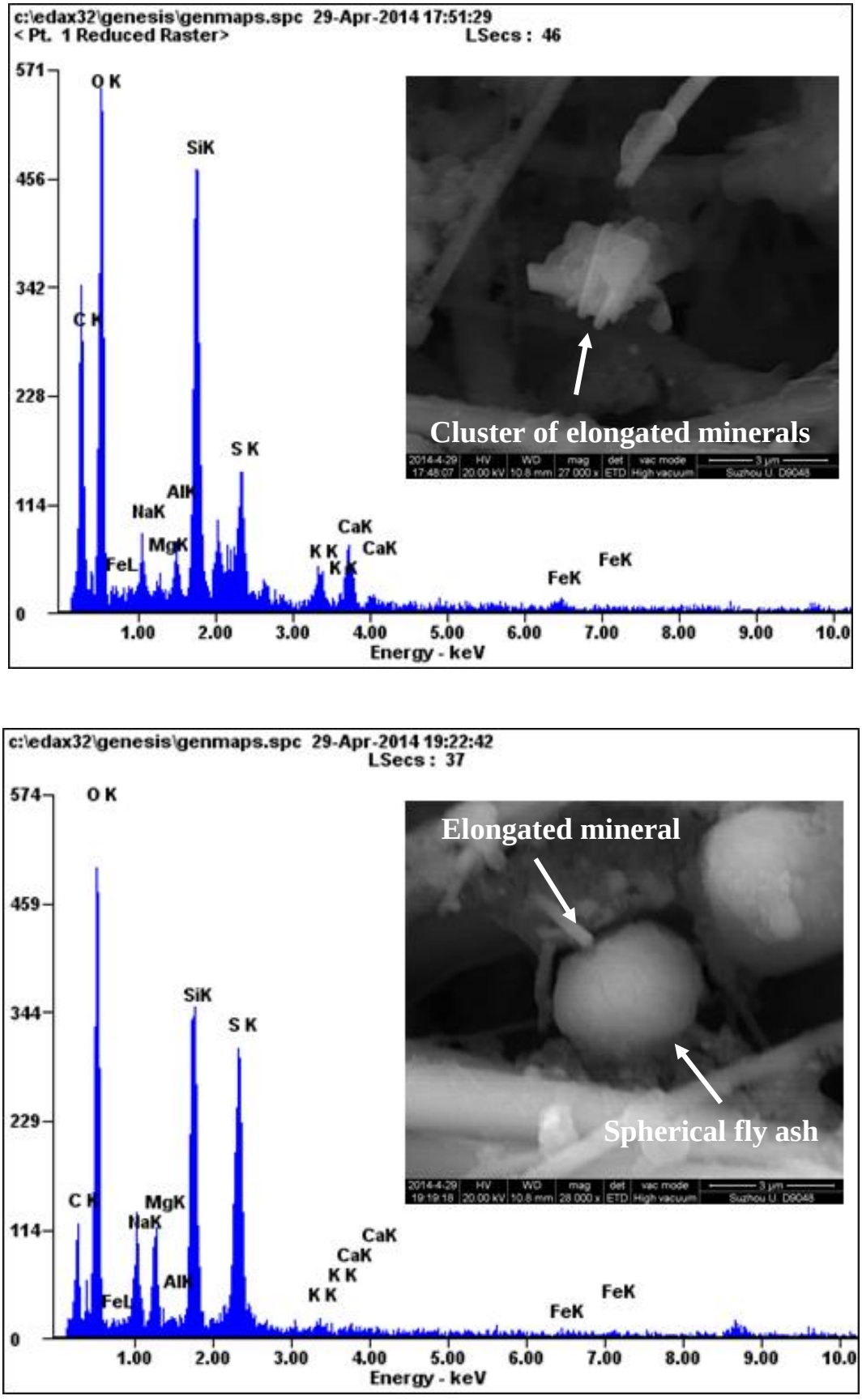

Figure S5. SEM pictures and EDX analyses for two representative $PM_{2.5}$ particles on the filter.

Methodology to select particles with rough and flat surfaces from SEM images

According to the user manual from FEI [RS1], the SEM pictures collected by the Quanta 200FEG tool (used in this investigation) result from interactions between an electron beam with the secondary electrons of the atoms at or near the surface of the sample. Due to the very narrow electron beam, SEM micrographs have a large depth of field, which allows displaying the features of a sample at different heights. Such topographic differences are displayed with different values of the grayscale in JPG files recorded. Therefore, the SEM images can also reveal information about the roughness of the samples.

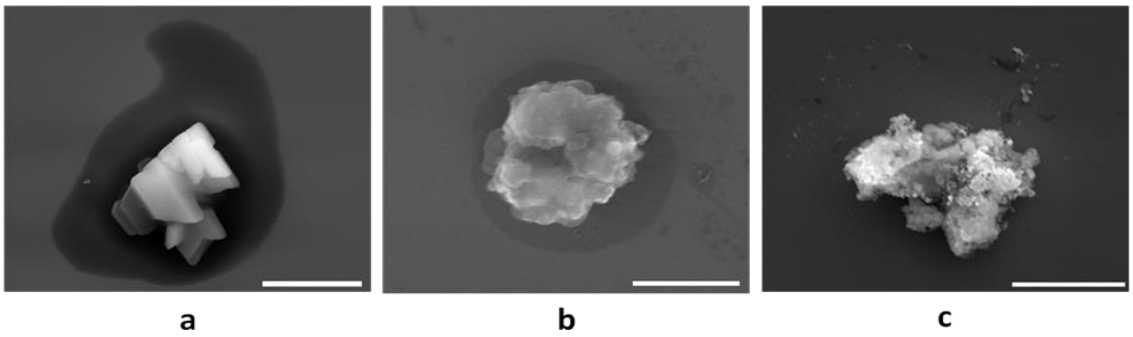

Figure S6. Representative $PM_{2.5}$ particles with flat (a), semi-rough (b), and rough (c) surfaces. The scale bars are 4 μm for (a), 1 μm for (b) and 4μm for (c).

Moreover, most of the particles scanned with SEM can also be found with the AFM tip. After transferring the particles on the grid-like SiO2/Si substrate, we perform SEM images of the samples to find out the $PM_{2.5}$. Then, we zoom out until a global picture of the whole sample at macroscopic scale is obtained. Finally, we go to the AFM and locate the tip at the same place and perform a large area scan. Despite the shape of some $PM_{2.5}$ could be slightly modified during the scan, we found relatively easy most of the particles analyzed with EDX/SEM in tapping mode. In contact mode it was more difficult because the AFM tip may induce particle shape modification, especially in those with less stable shapes. SEM/AFM corrlation is also possible on bare Silicon depending on the particle

size and shape. The AFM then can quantitatively compare the differences on the surface roughness of the particles by using both the roughness analysis and cross section tools. Please see the section "Correlation between AFM and SEM images" of this supplementary information document for more details.

Silicon substrates used in this investigation

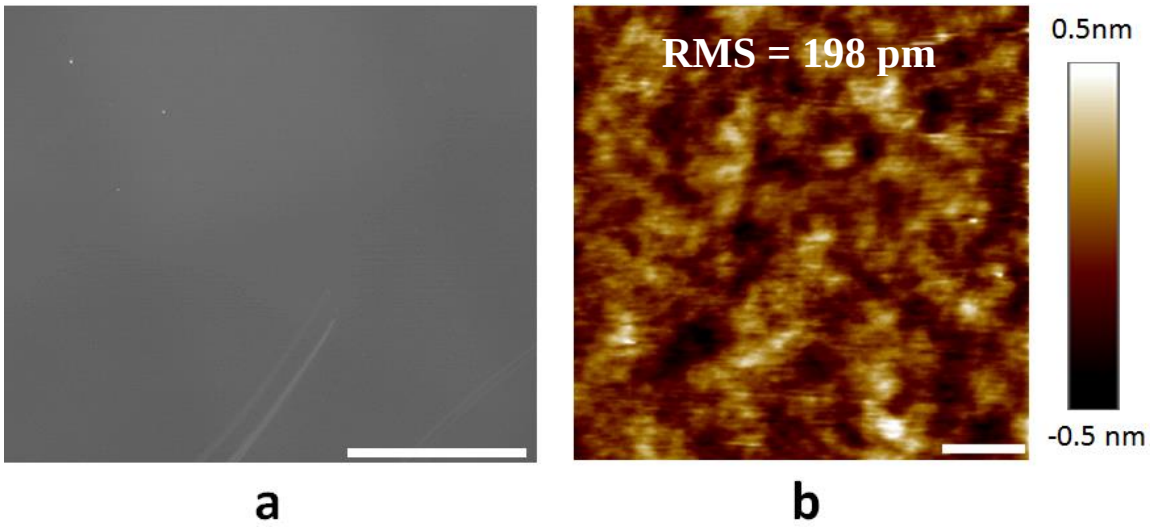

Figure S7. SEM (a) and AFM (b) images of clean Si. For this investigation, a n-type Si with natural oxide layer from Kejing Co. Ltd. was used. Before $PM_{2.5}$ transfer, the wafers were cleaned in isopropyl alcohol in ultrasonic bath for 5 minutes and then rinsed in pure water during 10 seconds (without sonication). The samples were dried with dry nitrogen gas. Nearly no particles exist on the surface of clean Si. The scale bars are 500µm for (a) and 1.6µmfor (b). The roughness of the Si substrate is very low and suitable for particle detection.

Process to transfer PM2.5 from rough filters to flat analysis-friendly substrates

This is a method commonly used in chemistry to homogenize solutions, and it basically introduces mechanical stresses in the sonicated samples. According to the Royal Society of Chemistry (ref. 31 in the manuscript), ultrasonication can be defined as: the irradiation of a liquid sample with ultrasonic (>20 kHz) waves resulting in agitation. Sound waves propagate into the liquid media result in alternating high-pressure (compression) and low-

pressure (rarefaction) cycles. During rarefaction, high-intensity sonic waves create small vacuum bubbles or voids in the liquid, which then collapse violently (cavitation) during compression, creating very high local temperatures. In our case, we sonicate the samples in the absence of any solvent. As shown in Figure S8, we used no water or any other solvent in the tube (between the Silicon substrate and filter). On the other hand, both the glass and sonicator contained water. Such configuration produced the continuous vibration of both the tube and the sample, but no aggressive reaction took place on the $PM_{2.5}$ surface. As a result, the particles can detach from the filer and precipitate on the target substrate, but no remarkable particles size change or fragmentation has been observed in further SEM images. It is worth noting that the density of particles (number per mm^2) is not representative (it cannot be controlled), since the mechanical stress and filter/Silicon distance may not be homogeneous during the transfer process, and we didn't find any characteristic value of particle density.

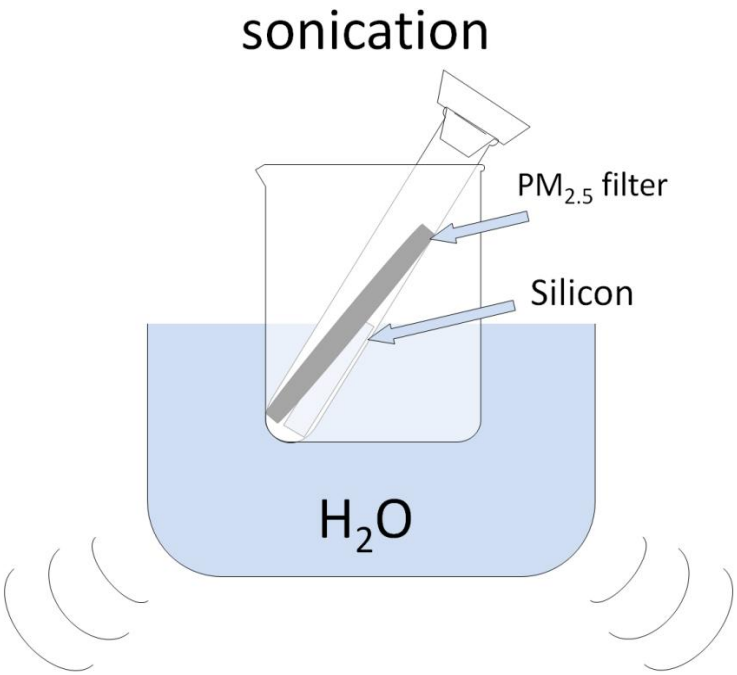

Figure S8. Schematic of process followed to transfer $PM_{2.5}$ from rough filamentary filters to clean Si. A piece of polluted filter and cleaned Si are introduced in a plastic tube box (free of any solvent). Then, the tube is placed in a glass with water and introduced into the ultrasonic bath for different times. By this method, the $PM_{2.5}$ can be effectively transferred to a flat substrate avoiding particle modification.

Representative SEM images of $PM_{2.5}$ transferred on Silicon

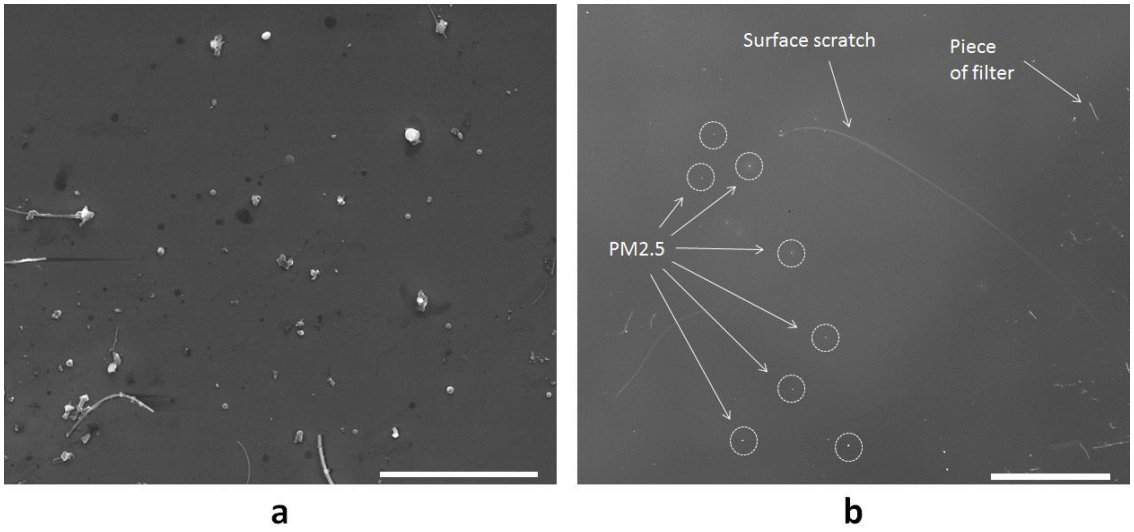

Figure S9. Large area SEM images of the particles on clean Si after the transferring process described above. The $PM_{2.5}$ particles, pieces of filters and surface scratch can be clearly observed on the surface of clean Si. The whitish dots in (a) and (b) are the $PM_{2.5}$ particles. The short filaments are parts of filters, and the long trace in (b) is just the surface scratch. The scale bars are 40 μm for (a) and 500 μm for (b).

III

Universal groups of $PM_{2.5}$ airborne pollutants: carbon-rich fluffy soot aggregate

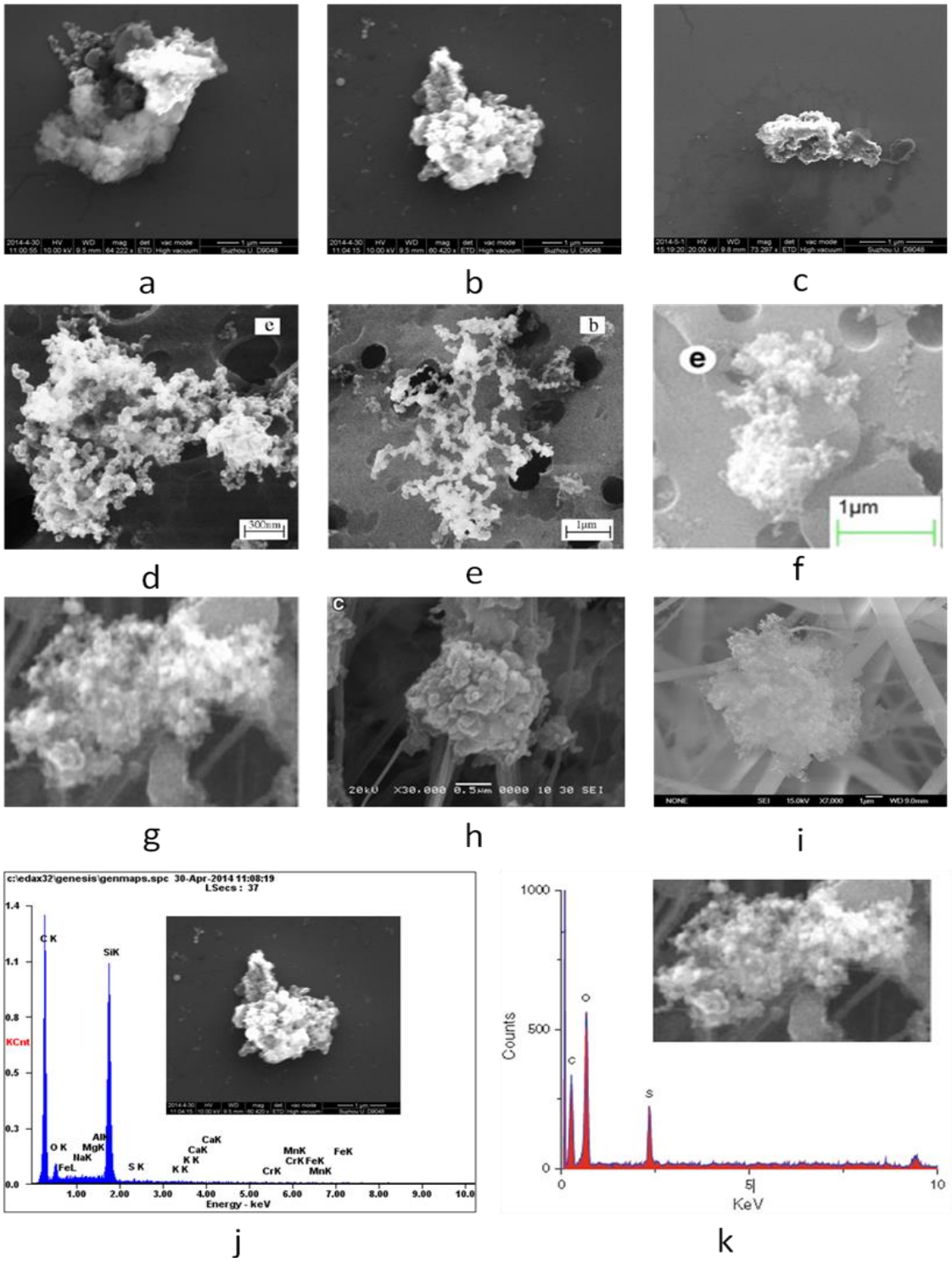

Figure S10. SEM images of soot aggregate. (a-c) and (j) are data from this investigation (Beijing, China). (d) and (e) are from reference [3] (Shanghai, China). [f] is from reference [5] (Guangzhou, China). (g-h) and (k) are from reference [19] (Pune, India). (i) is from reference [RS5] (Wellington, New Zealand). The chemical composition in (j) and (k) by EDX.

III

Universal groups of $PM_{2.5}$ airborne pollutants: elongated minerals rich in metal-silicates

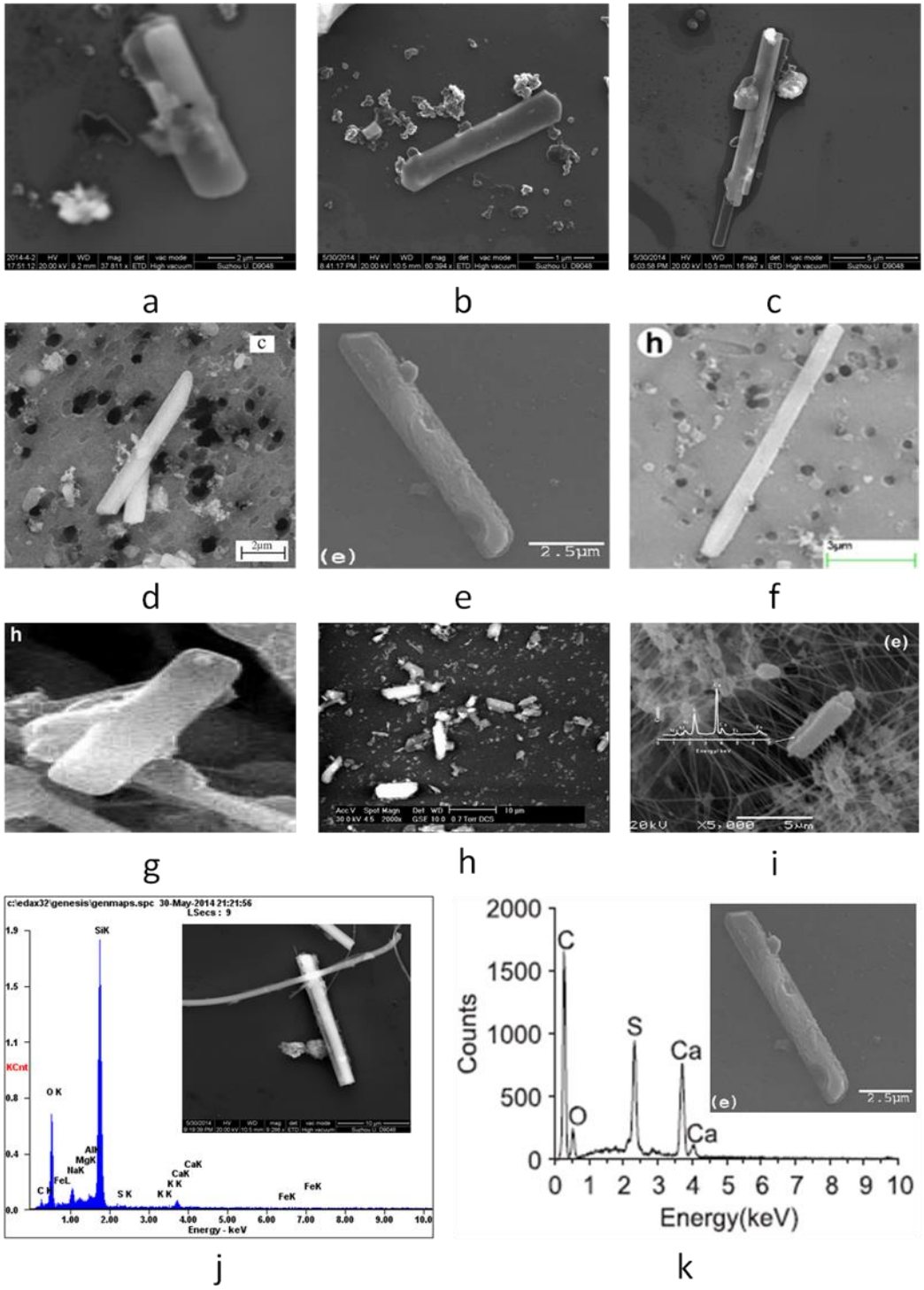

Figure S11. SEM images of elongated minerals. (a-c) and (j) are data from this investigation. (d), (f) and (g) are from references [3] (Shanghai, China), [5] (Guangzhou, China) and [19] (Pune, India), respectively. (e) and (k) are from reference [18] (all aroundUSA). (h) is from reference [RS6] (Gujarat, India). (i) is from [RS7] (Tianshan, China).

III

Universal groups of $PM_{2.5}$ airborne pollutants: spherical fly ash rich in metals

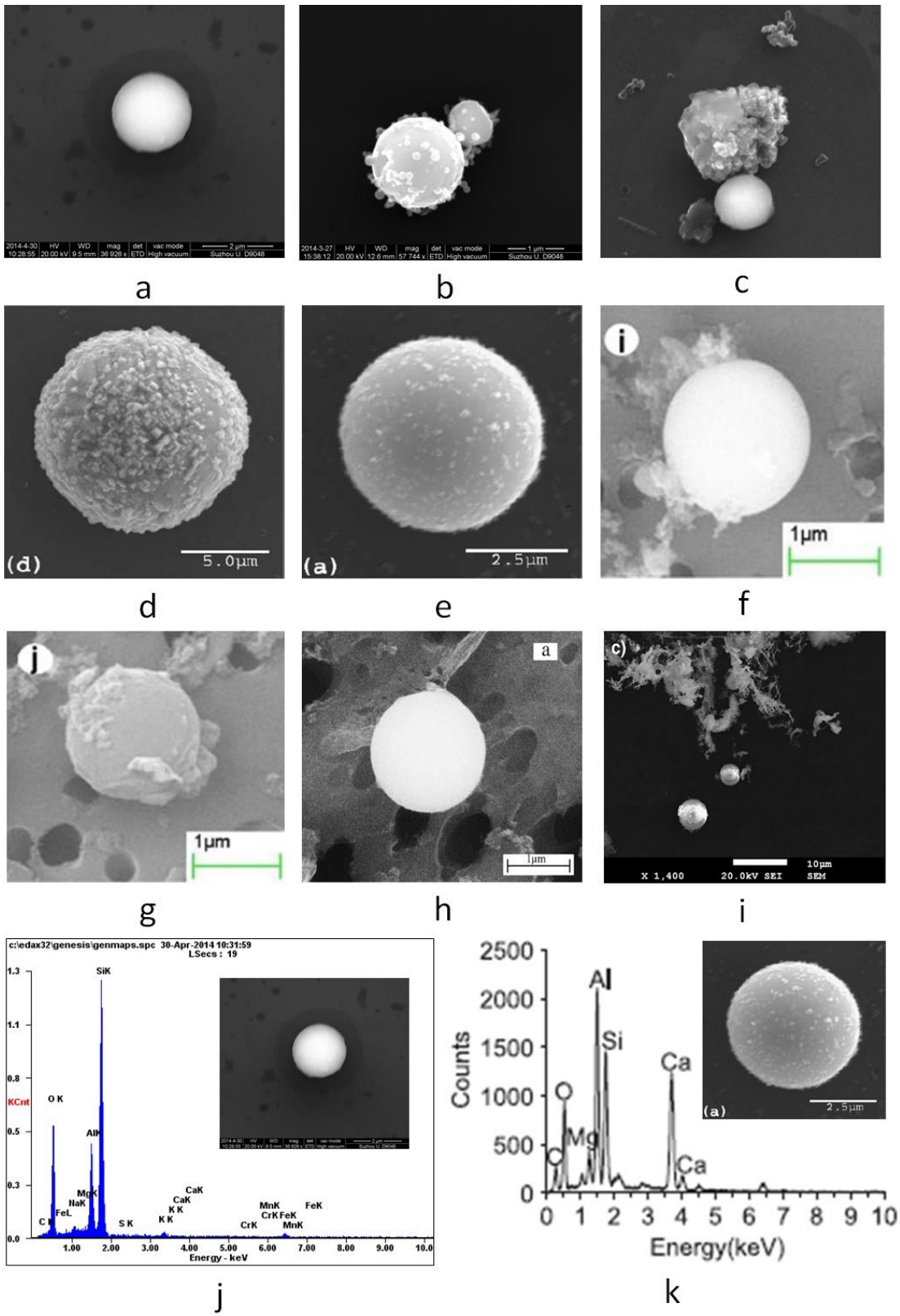

Figure S12. SEM images of fly ash. (a-c) and (j) are data from this investigation. (d), (e) and (k) are form reference [18] (all around USA). (f) and (g) are from reference [5] (Guangzhou, China). (h) is from reference [3] (Shanghai, China). (i) is from reference [RS8] (Lisbon, Portugal).The scale bars for (b) and (c) are 3 µm.

Reliability of the transfer method

In order to analyze the reliability of the transfer method we performed an additional experiment, which consisted on attaching a piece of Silicon on the filters before introducing them in the $PM_{2.5}$ collector (Figure S13a). We in-situ collected the $PM_{2.5}$ particles on the Silicon substrate, and we observed many particles with sizes, shapes and compositions very similar to those reported after the transfer (Figure S13b-f and S10-12). This is indeed demonstrating that the transfer process didn't dramatically alter the properties of the particles we reported in the manuscript.

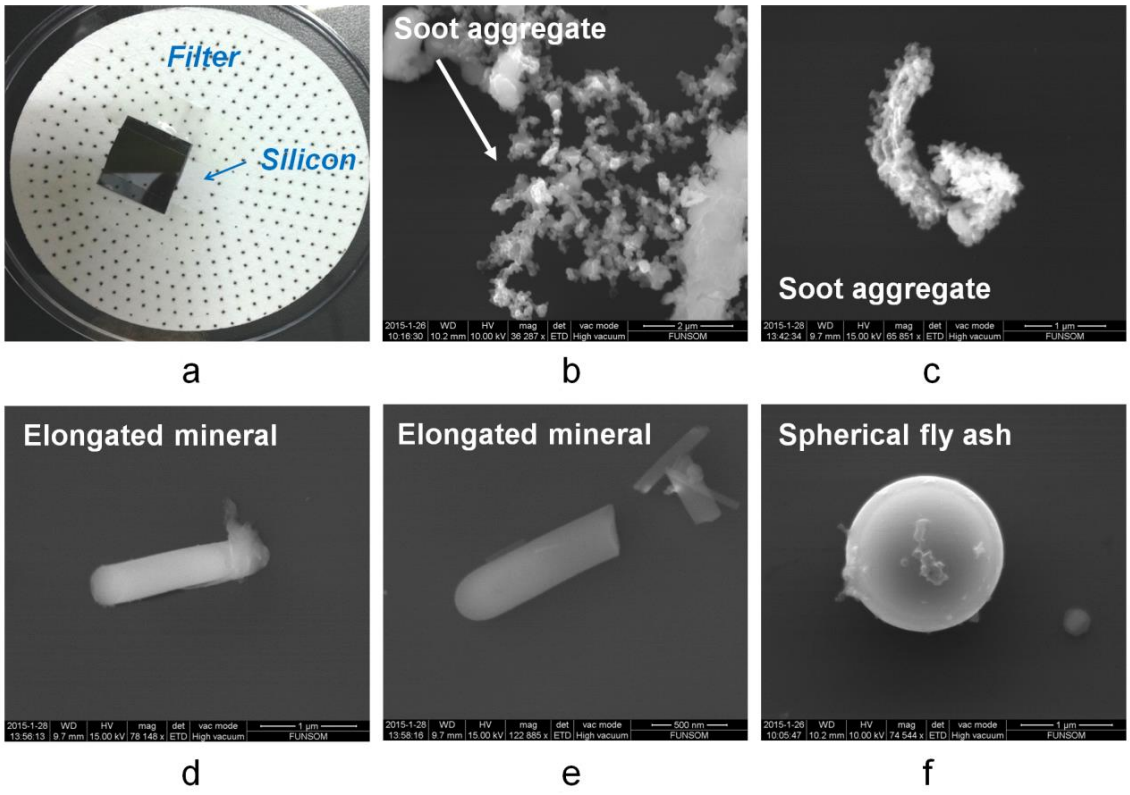

Figure S13. (a) Filter with a piece of Silicon in the center. This filter was directly introduced in the collector for in-situ studies. (b-f) In-situ collected particles on the Silicon substrate. The particles collected are very similar to those observed in the manuscript after transfer.

It is worth noting that after a carefully analysis of the particles, we observed that the density of small particles (diameter below 500 nm) attached to the Silicon remarkably increased when using in-situ collection (Figure S14a). This indicates that some smaller

particles attached in the filter couldn't be transferred on the Silicon during ultrasonication. Probably, due to their smaller mass, the detaching force was smaller than the adhesion force to the filter, and therefore such small particles just remained on the filter. Finally, some atmospheric particles can be semi-to-entirely liquid when they are airborne, which would difficult the filter-to-Silicon transfer process. Interestingly, many particles collected in both in-situ (Figure S14d) and transferred (Figure S29) experiments show a dark trace that, due to its regular contour and flat shape, may be related to the semi-liquid nature of some particles

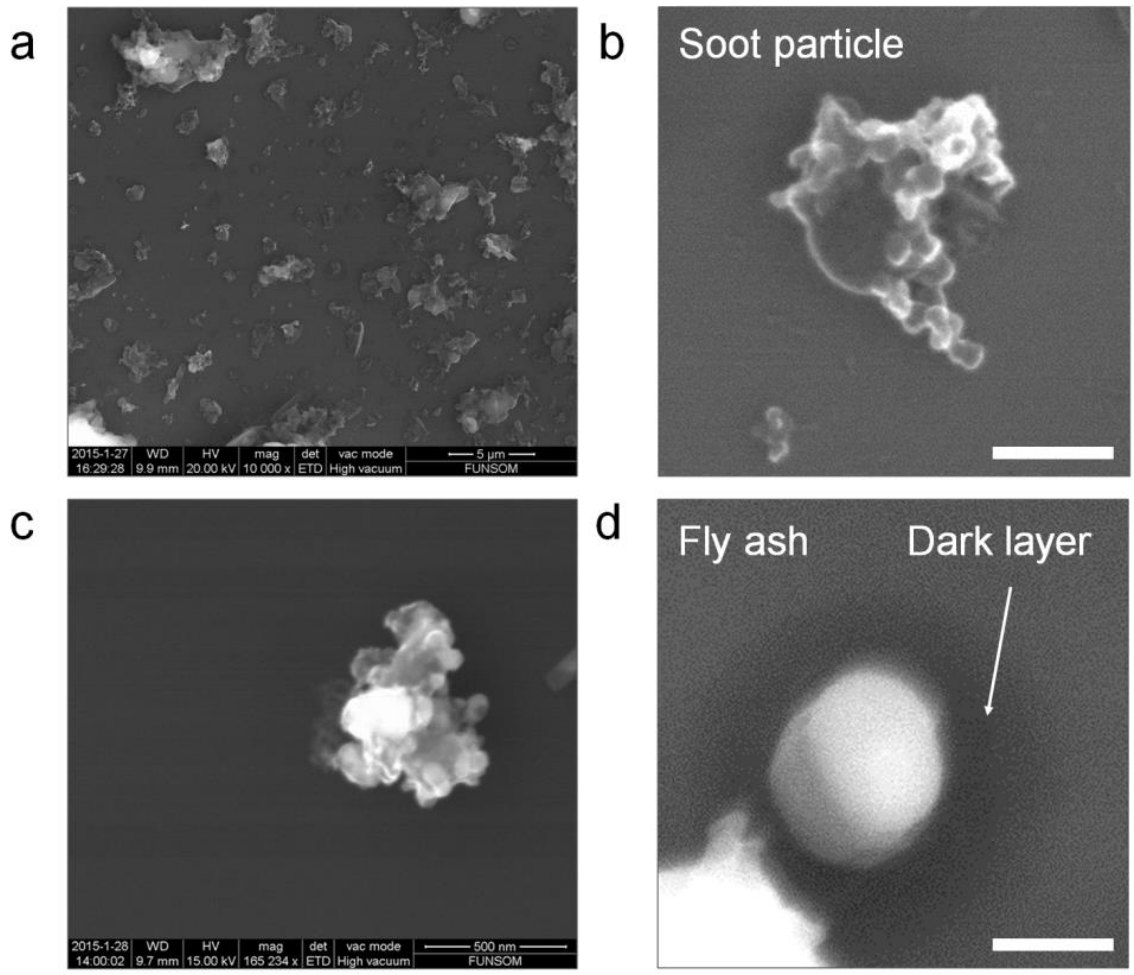

Figure S14. (a-b) SEM image of the in-situ collected particles on the Silicon filters. Unlike after particle transfer, a large density of small particles has been observed on the Silicon. (b-c) Examples of small size particles showing that their nature is very similar to the larger ones, indicating that they may be related to small portion of those reported in the manuscript, rather than a different type of particles. (d) Example of a particle surrounded by a dark layer that may be related to liquid particles. The scale bars in (b) and (c) are 250 nm and 200 nm respectively.

We careful analyzed the morphology of these small particles by SEM and observed that their morphology and composition is very similar to that of larger particles (Figures S14b-c and Figures S10-12), indicating that they may not necessarily correspond to a new type of particles, but they could be just small fragments of soot. We would like to highlight that, using in-situ collection on Silicon, we observe a larger density of particles surrounded by a darker layer (as shown in Figure S14). The long and straight shapes of this surrounding layer make us think that this could be related to the semi-liquid particles.

Representative AFM images of $PM_{2.5}$ transferred on Silicon

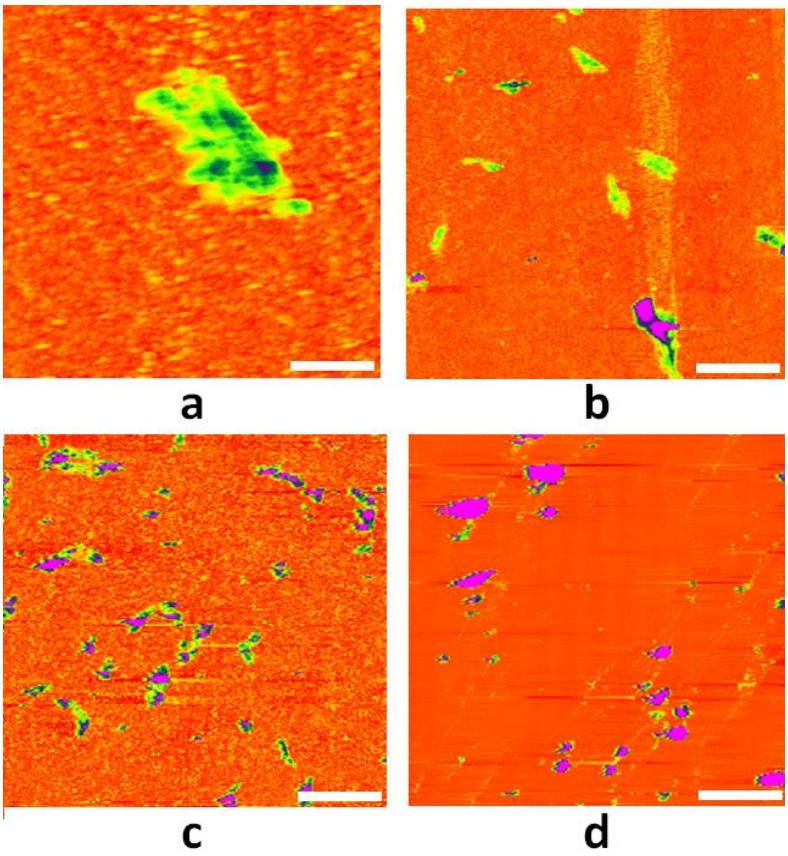

Figure S15. Topographic AFM images displaying different types of $PM_{2.5}$. The particles in Figures (a) and (b) have a 2 nm Au coating (a-b), while (c) and (d) were measured as-transferred. In the paper, all topographic images were displayed without gold coating. The substrate used in Figures (a-c) was glass, while Figure (d) used Si. Many $PM_{2.5}$particles can be observed in all the AFM images and they usually exhibit different shapes. The AFM used in these experiments was the Veeco Multimode V AFM from Bruker in tapping mode. For tapping measurements Si tips from Nanoworld(model NCH-20) were used. We used a scan line frequency of 1 Hz and the amplitude setpoint ranged between 100-300 mV. The scale bars are 1µmfor image (a), 5 µm for image (b), 10 µm for image (c) and 4 µm for image (d).

Correlation between AFM and SEM images

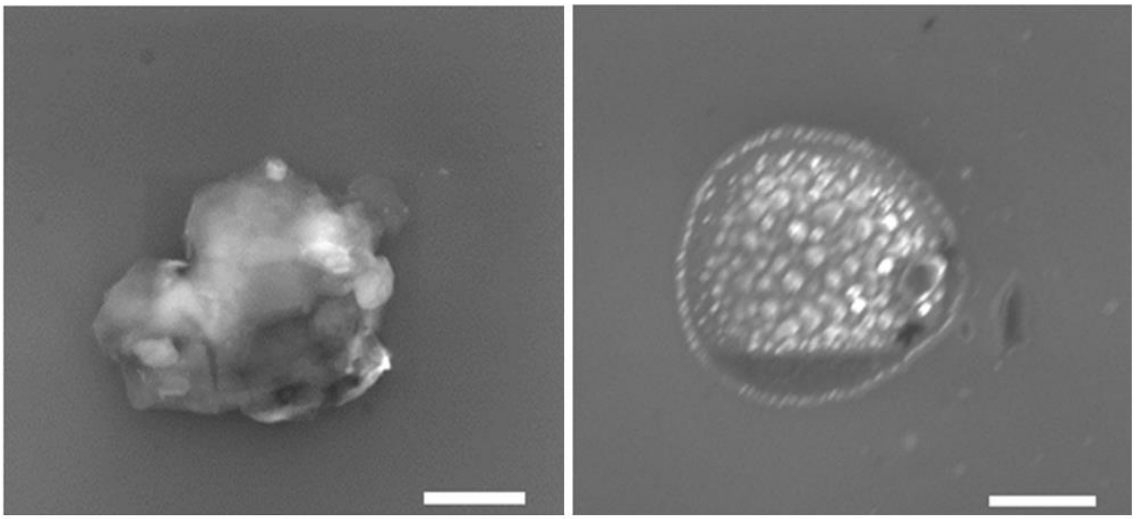

Figure S16. (a) and (b) show the SEM images correlated to the three dimensional AFM topographic maps in Figures 2a and 2b of the article (respectively). Most of the particles can be found with the tip of the AFM after SEM and vice versa. The scale bars are 1 µm for (a) and (b).

Quantification of the particles roughness with AFM

Among other uses, the high lateral and vertical resolution of the AFM can be used to quantify differences on the surface roughness of the particles, so that they can be accurately classified. For this purpose, we use the Roughness tool of the AFM can be used to calculate the RMS value of an area selected. The layout of the AFM tool in the AFM software is shown in Figure S17. The *Rq* value corresponds to the standard deviation of the Z values within the box cursor, calculated as:

$$Rq = \sqrt{\frac{\sum(Z_i)^2}{N}}$$

where *Zi* is the current Z value, and *N* is the number of points within the box cursor.

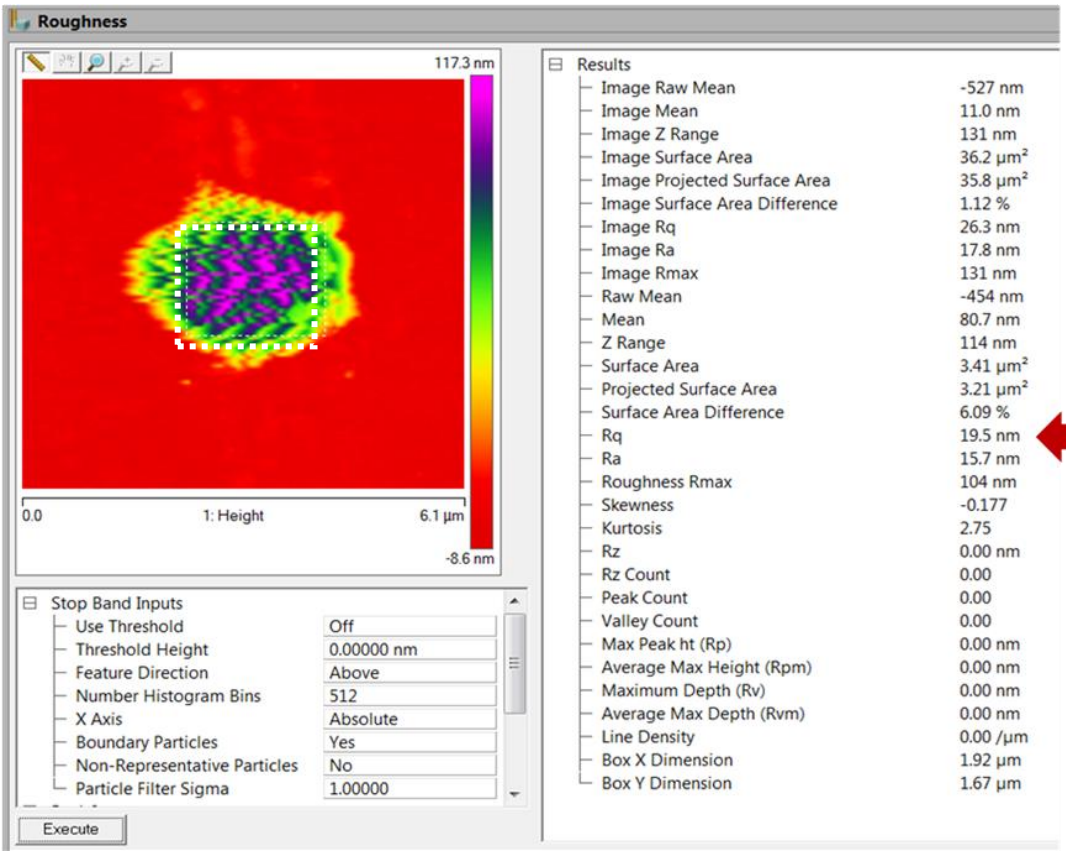

Figure S17. Layout of roughness analysis in Bruker Nanoscope Analysis Bruker version 1.40.

Additionally, we compare the roughness of the particles with the section tool. In this case, the software provides the standard deviation (*RMS*) of the Z values between the reference markers.

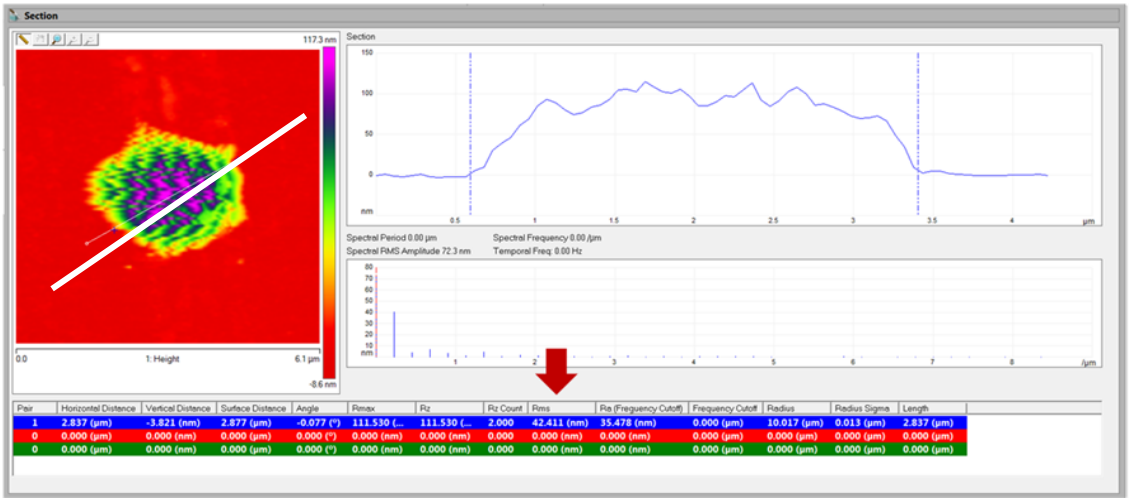

Figure S18. Layout of the cross-section tool in Bruker Nanoscope Analysis Bruker version 1.40.

$$RMS = \sqrt{\frac{\sum(Z_i - Z_{ave})^2}{N}}$$

Where *Zi* is the current Z value, *Zave* is the average of the Z values between the reference markers, and *N* is the number of points between the reference markers.

Despite we observe differences on the values calculated, the AFM software allows reliable comparison of the surface roughness of the particles. It is worth noting that the Rq value calculated with the roughness can change depending on the box size. For this reason, we used a constant box size of 500nm x 500 nm for all analyzed particles. The numerical data obtained with the software of the AFM correlate with the visual observations made from SEM images in 88.46 % of the particles analyzed.

Statistical analysis of $PM_{2.5}$size transferred on Silicon

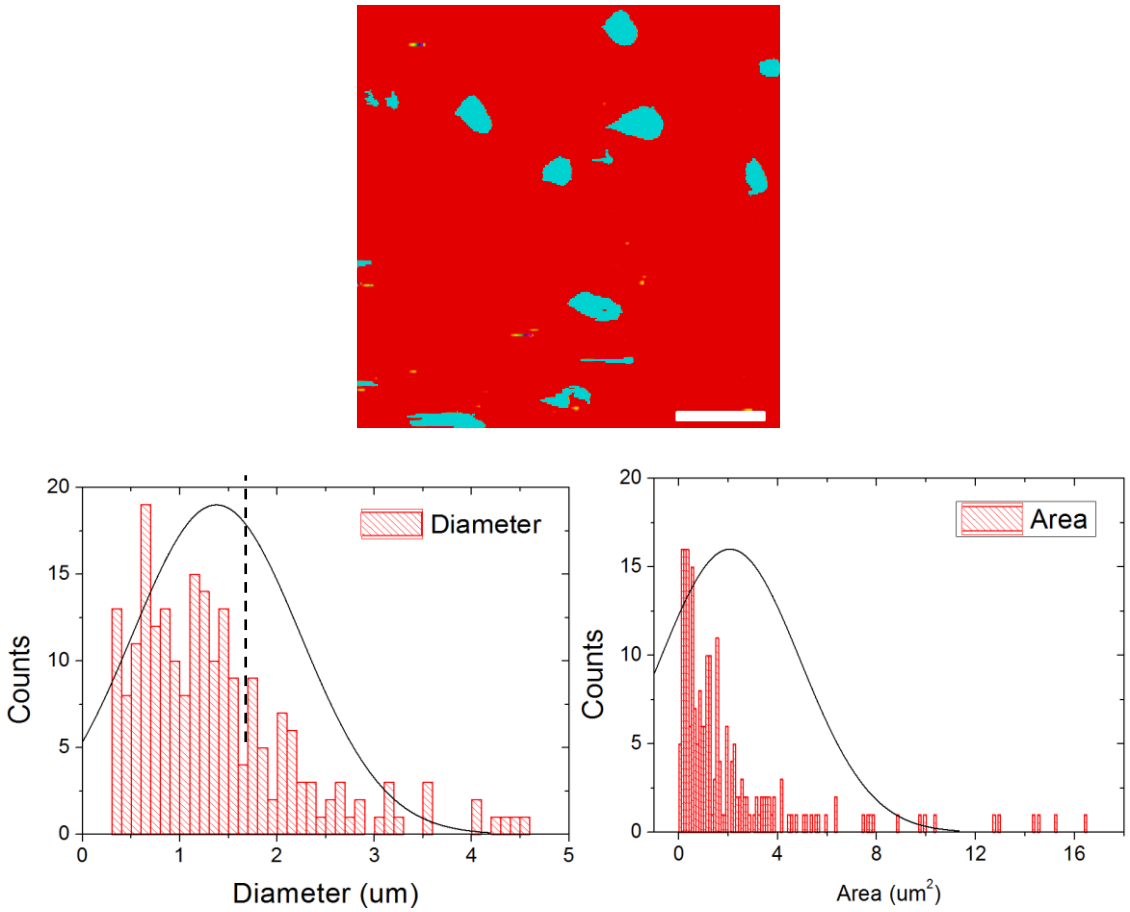

Figure S19. Statistical analysis of the physical diameter (b), and area (c) of $PM_{2.5}$ particles transferred on clean Si. The AFM software, NanoScope Analysis V1.4 was used to do the particle analysis. As an example, panel (a) shows the typical aspect of the processed images, with areas above a threshold height highlighted in blue. The threshold height was selected to be 10 nm above the most repeated value of the image histogram, which is represent the average height of the Silicon substrate. In total 217 particles in different images were analyzed. As it is shown in (b), the main diameters of the $PM_{2.5}$ range from 0.4-2.2 µm, in agreement with the values reported in other works [RS2-4] and expected values (below 2.5 µm). As indicated in the manuscript, despite the values here displayed represent the physical size, the quadratic relationship between particle density and aerodynamic diameter (see Eq.1 of the manuscript), the values of $PM_{2.5}$ densities previously reported and the fact that aggregates of particles show a much lower density than bulk materials allows considering that most of the particles in Figure S19b are in fact $PM_{2.5}$ airborne pollutants. The corresponding area-counts histogram further demonstrates the main size of these particles. The scale bar in (a) is 10 µm.

Analysis of $PM_{2.5}$ deformation from topographic AFM maps

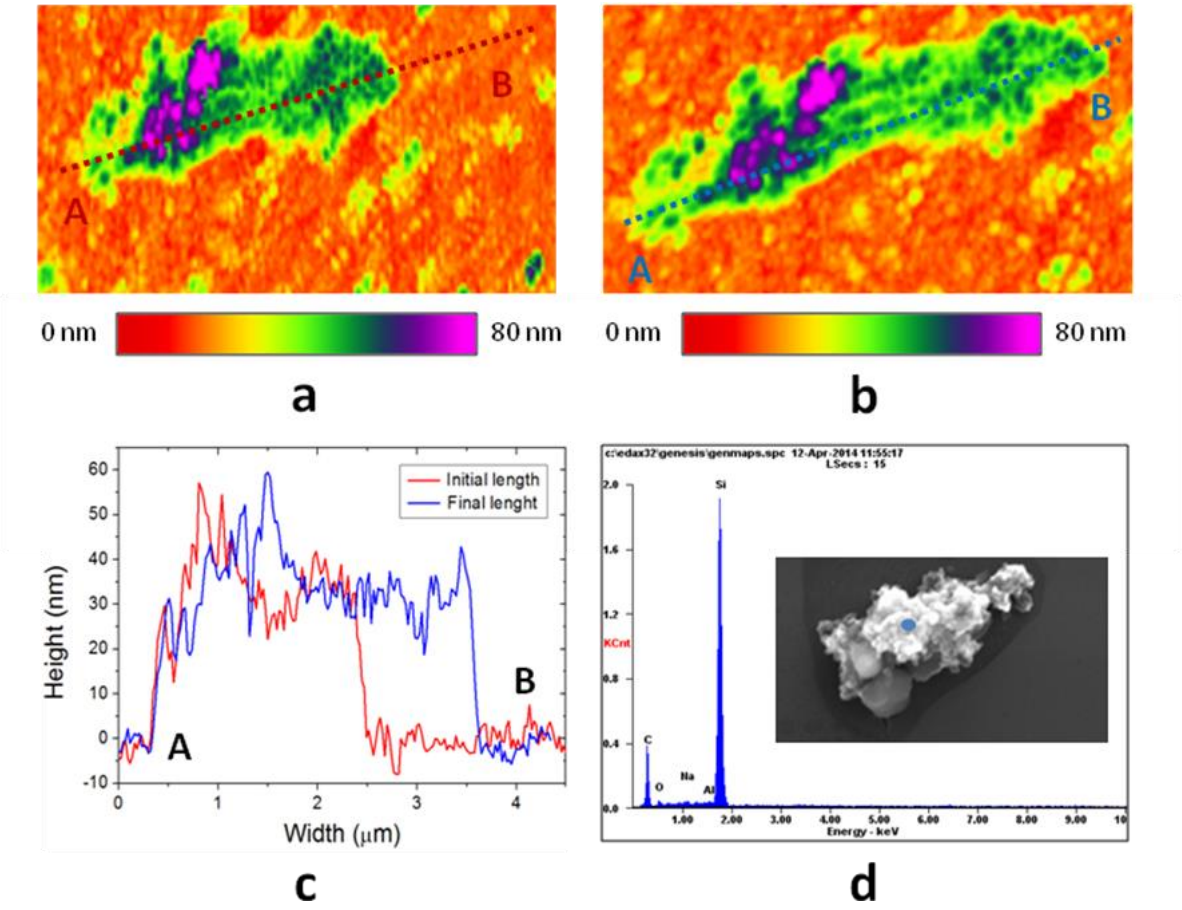

Figure S20. First (a) and fourth (b) topographic AFM images of $PM_{2.5}$ particles transferred on clean Si. Both scale sizes are 5.5μm, and the drive amplitude used during each scan was 100 mV for (a) and 300 mV for (b). The drive amplitude is a parameter used when scanning in tapping mode and it is directly proportional to the tip/particle contact force. As it can be observed, at higher contact forces the particle can be elongated. It is worth noting that (for this particle) deformation has been achieved when applying a drive amplitude of 300 mV, while drive amplitudes of 100 mV and 200 mV didn't produce deformation. Shape modification can be also observed from the cross sections (c). Further topographic maps measured with high and low contact forces didn't show additional shape modificationrespect to (b), indicating that the particle modification was plastic (larger viscosity), and elastic particles that recover the initial shape have been rarely detected. The chemical composition analysis with EDX (d) revealed that $PM_{2.5}$ with such morphology and shows that this elastic particle contains a lot of carbon.

Values of adhesion force in referent substrates

To better understand the meaning of the adhesion force values measured on the $PM_{2.5}$, we perform additional F-Z curves on four reference substrates: Silicon, Glass Aluminum plate for AFM samples and adhesive tapes: usual scotch tape and laboratory carbon tape.

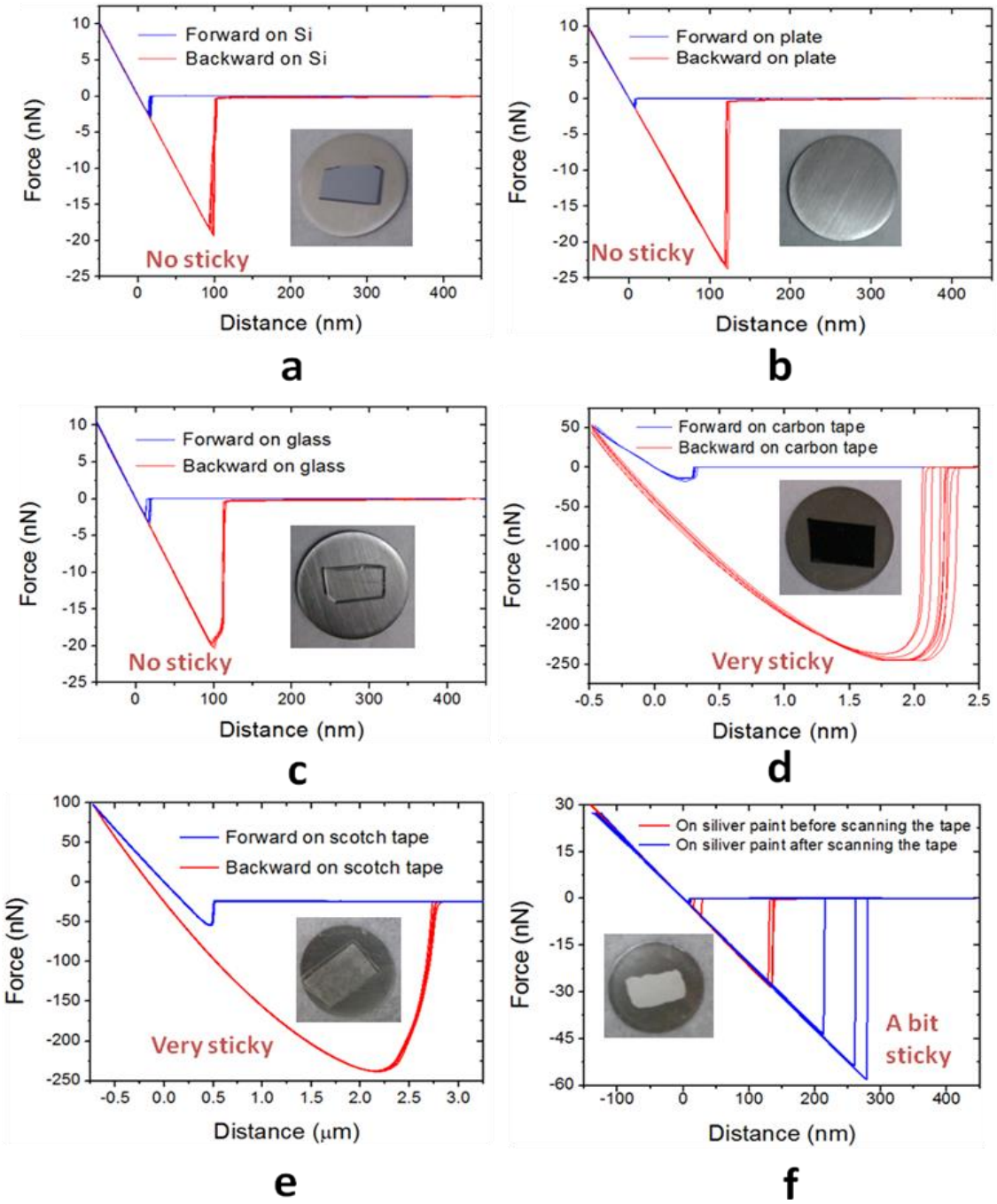

Figure S21. Force-Distance curves on four reference substrates with different stickiness: cleaned Si (a), Aluminum plate (b), cleaned glass (c) carbon tape (d), scotch tape (e). (f) F-Z curves on dried silver paint before and after the scotch tape experiments in (e). The large stickiness alters the properties of the AFM tip, the same behavior observed in some specific ultra-sticky particles.

The Force-Distance curves measured on Silicon revealed adhesion forces around -20 nN (Figure S21a) consistent with values previously reported [RS9]. Similar experiments performed on AFM sample holders made of aluminum (b) and a glass slides (c) revealed values of the same order of magnitude than silicon. On the contrary when measuring Force-Distance curves on sticky carbon tape, adhesion forces more than ten times larger (around -230 nN) have been observed. The conventional scotch tape used also showed similar adhesion force values. Figure S21e shows the F-Z curves on a plate covered with dried silver paint before and after the scotch tape experiments. Therefore, the $PM_{2.5}$ particles with adhesion values close to 20 nN could be considered non sticky, while those near 200 nN should be highlighted as very sticky.

Particle adhesion to the AFM tip

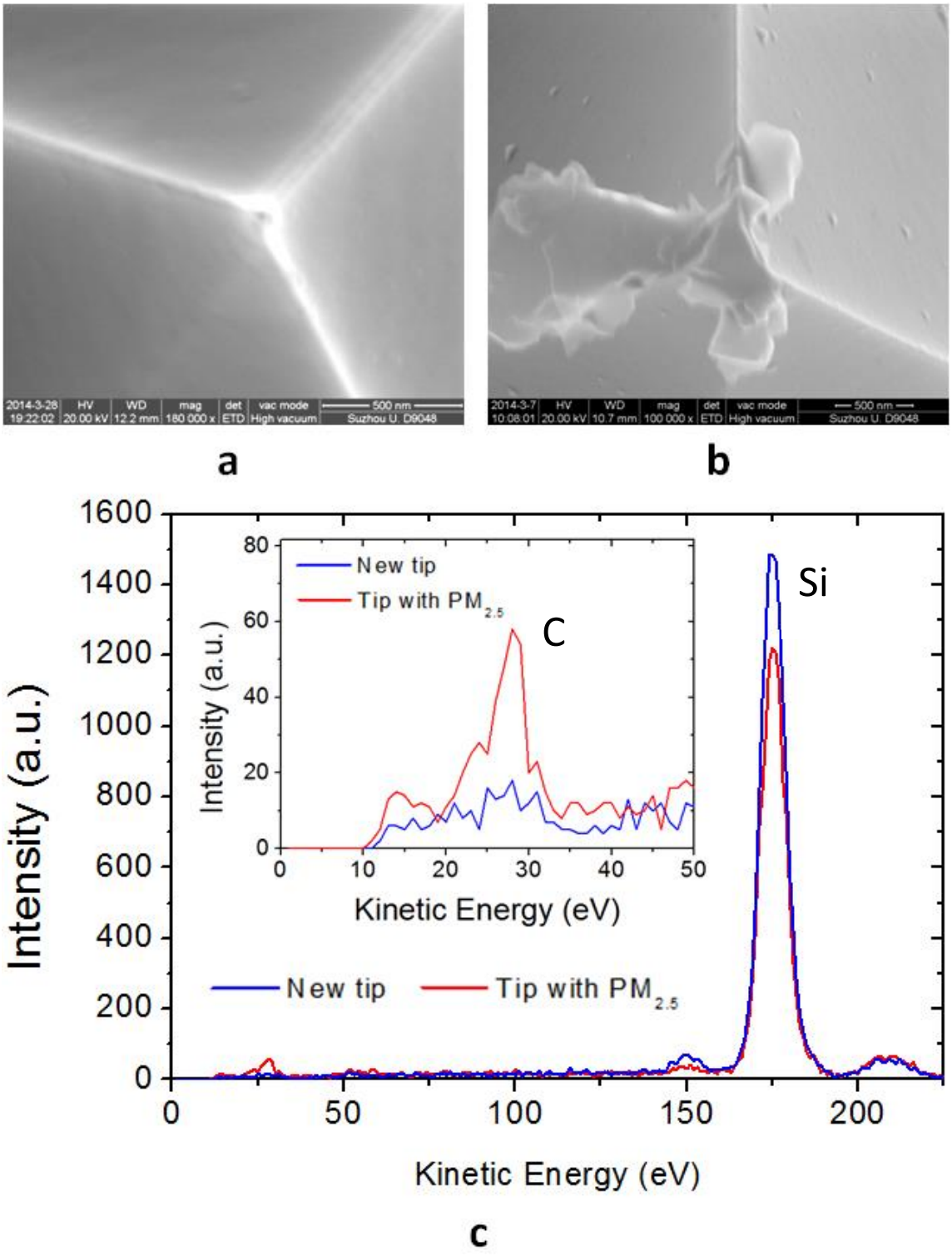

Figure S22. SEM images of a Pt-Ir coated AFM tip before (a) and after (b) scanning very sticky $PM_{2.5}$ particles on clean Si in contact mode. The EDX survey measured on the tip apex of each image (c)is shown below. Something attached to the tip in (b), which shows similar chemical composition to the sticky $PM_{2.5}$ particles in (c). This further demonstrates the adhesion property of $PM_{2.5}$. The scale bars are 500 nm for (a-b).

Measurement of the adhesion and deformation with AFM

When analyzing the properties of small particles with the AFM, the shape of sequences of Force-Distance (F-Z) curves can provide information about electrostatic force, tip/particle adhesion, particle deformation and particle rupture and [29].The Force-Distance curves were recorded with the Multimode AFM working in contact mode using a Pt-Ir coated AFM tip from Bruker. The tips we used were standard commercially available AFM tips from Bruker (model SCM-PIC). These tips were made by silicon micromachining and were coated first with a 20 nm thick layer of Pt–Ir, which is a 95% platinum and 5% iridium alloy (the iridium is used to enhance the stability of the platinum layer). The other main characteristics of the tip are: thickness = 2 µm, width = 50 µm, length =450 µm, spring constant =0.2 N/m, resonance frequency = 13 kHz and nominal tip radius =20 nm. More sophisticated AFM allow analyzing the tip-sample interaction in real time during an scan in tapping mode. Using the Dimension Icon AFM from Bruker we have access to the Peak Force Quantitative Nanomechanical Mapping (QNM) tool. Using this mode particle adhesion and deformation maps can be built from the information collected at each point (pixel) during the scan (see Figure 3). During this mode, we usedCo-Cr coated silicon tips from Burker. The main characteristics of the tip are: thickness = 1.85 µm, width = 30 µm, length = 125 µm, spring constant = 5 N/m, resonance frequency = 150 kHz and nominal tip radius = 35 nm. The maps were recorded using a scan frequency of 1 Hz and a drive amplitude of 5V.

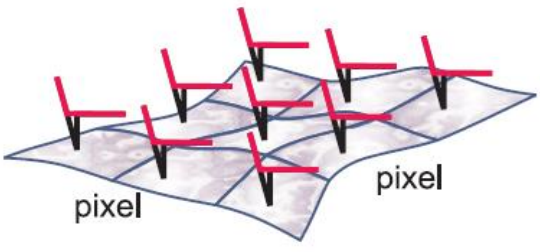

Figure S23. Schematic representation of the Peak Force QNM tool of the Dimension Icon AFM. Reproduced from [29]. Copyright @ 2013, by Jelena Zivkovic.

III

Ability of Carbon-rich soot to aggregate other particles

The fluffy Carbon-rich soot aggregate (which is sticky) can retain other species

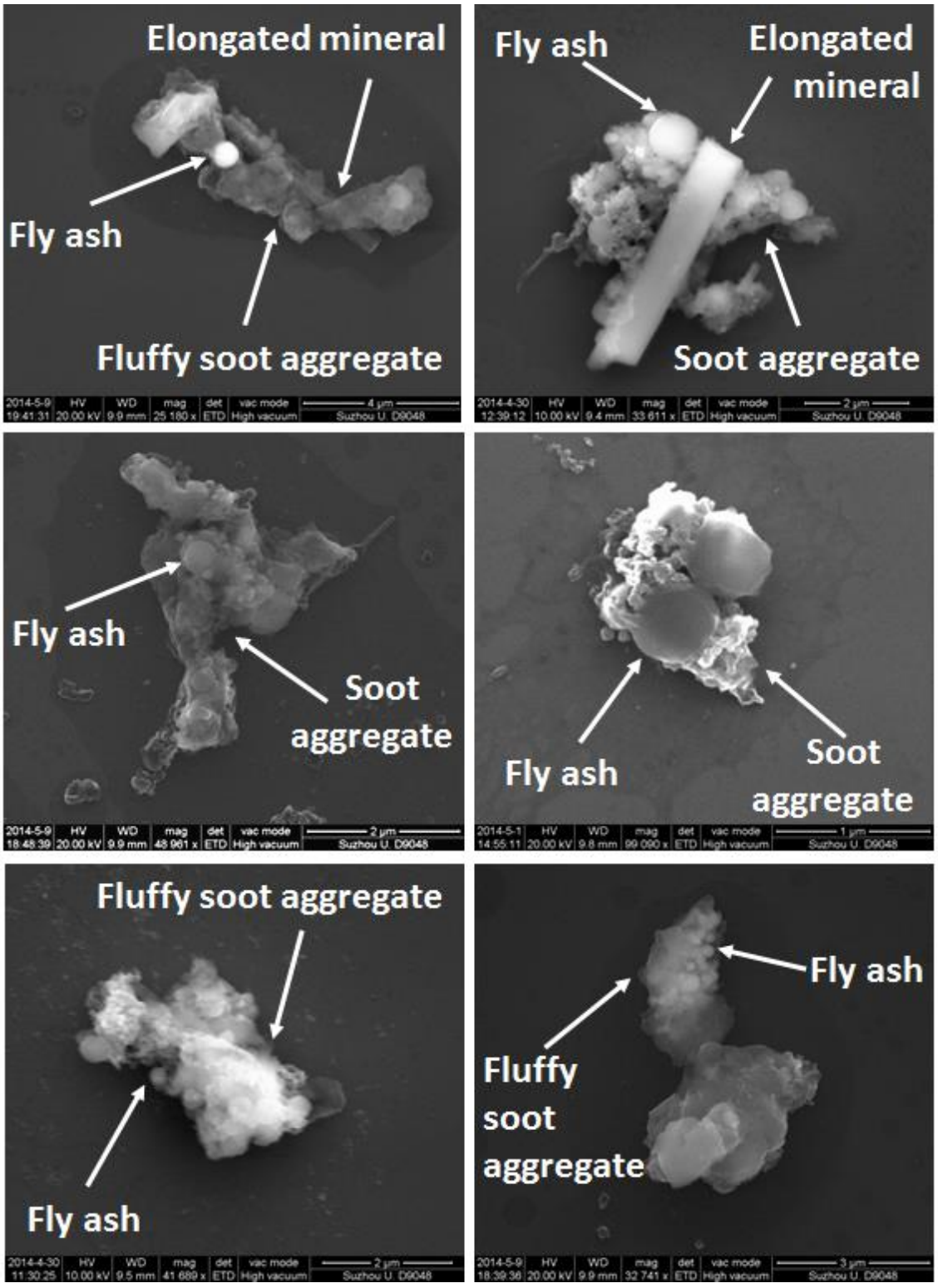

Figure S24. Examples of $PM_{2.5}$ aggregate surrounded by a fluffy soot aggregate network.

We confirm the composition of the sticky network formed by the fluffy soot aggregate particles by means of EDX. As an example, the images below show an aggregate of fly ash circular particles made of aluminum and iron oxides. The network of particles is aggregated by a continuous mass of fluffy Carbon -rich soot particles.

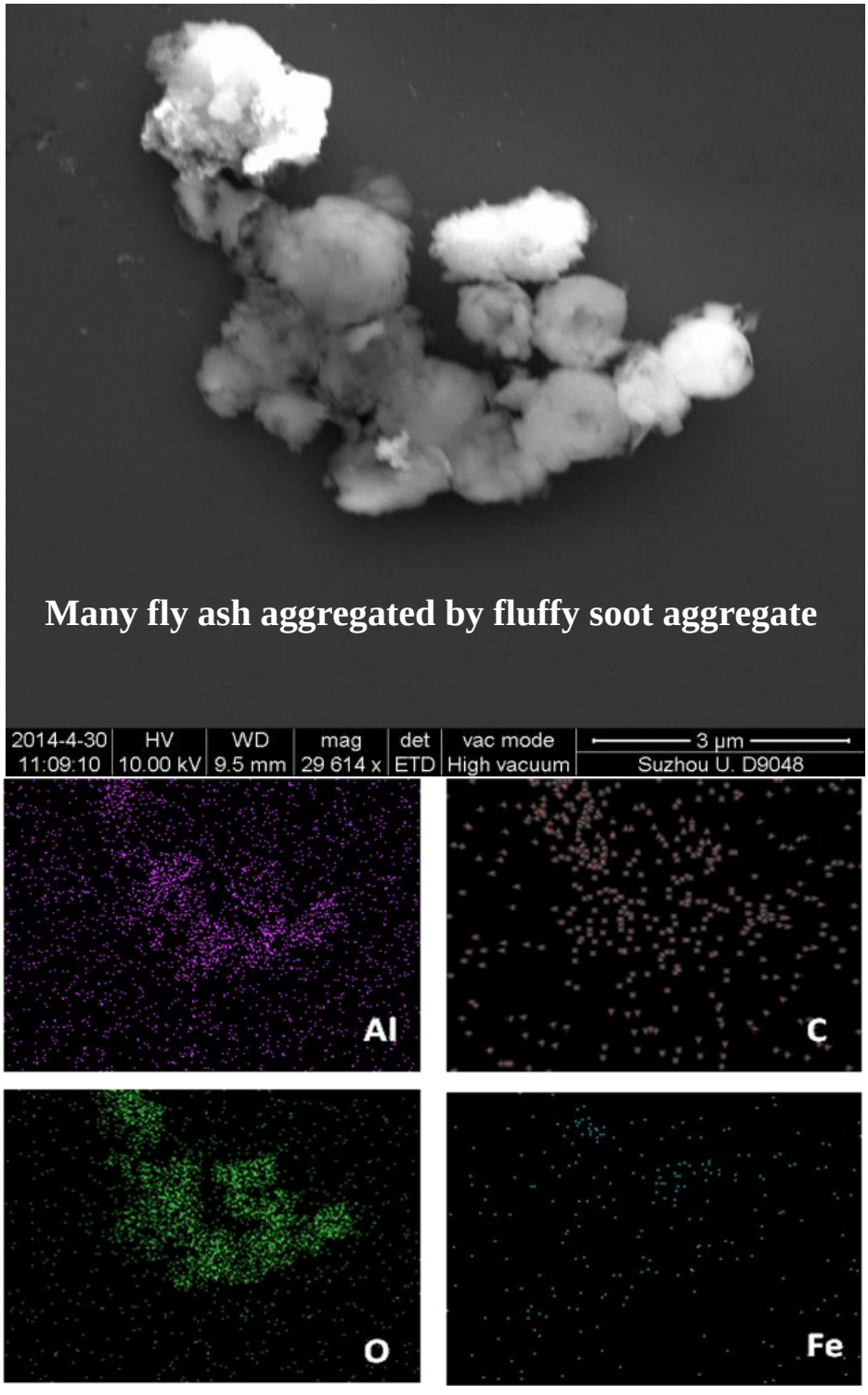

Figure S25. SEM image (up) and EDX maps of a fluuffy soot aggregate particles.

III

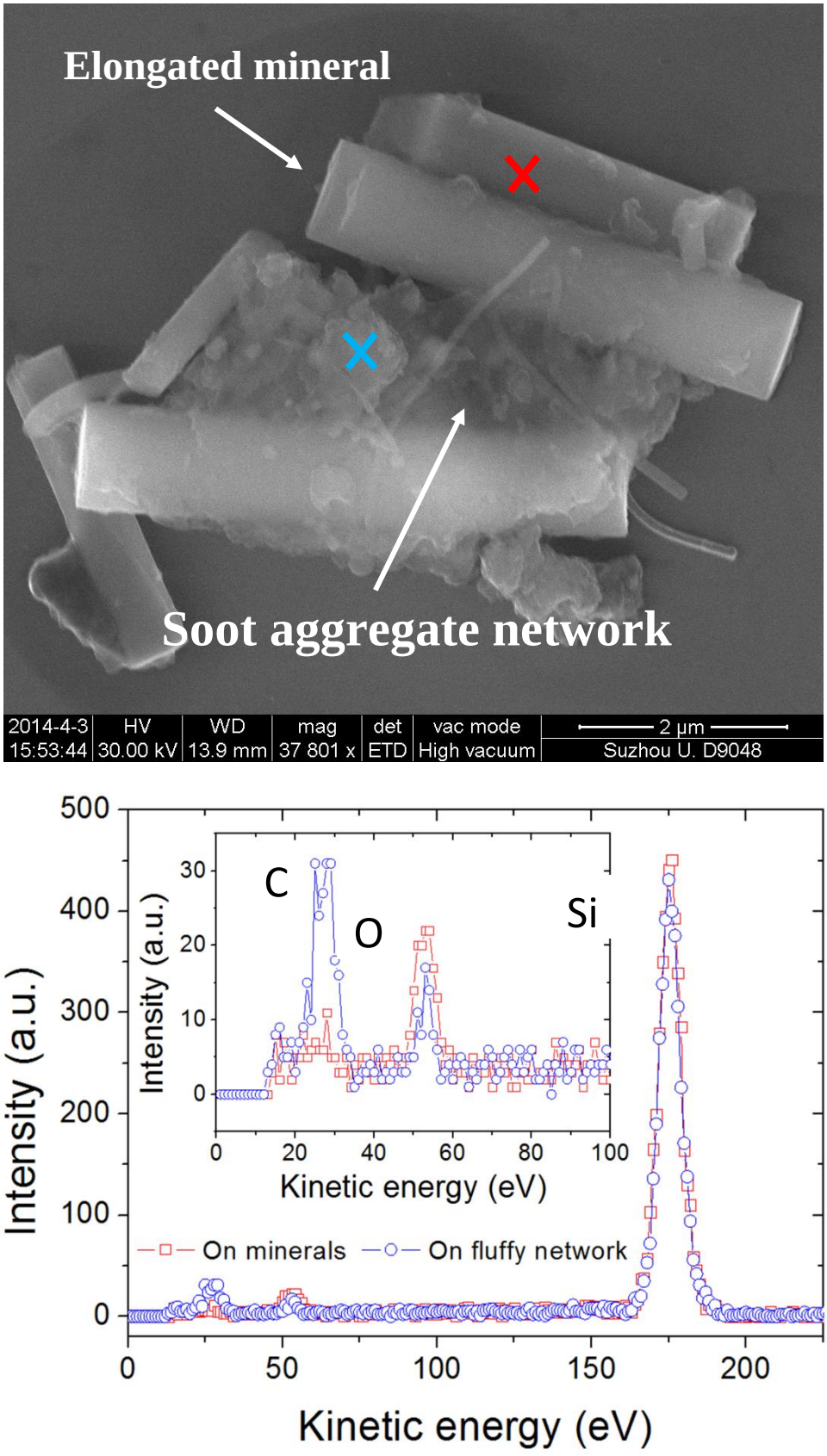

Figure S26. Another example of $PM_{2.5}$ aggregate. The top SEM and bottom EDX images show a particle cluster and its chemical composition. The elongated mineral and fly ash get trapped in the Carbon-Oxigen rich network.

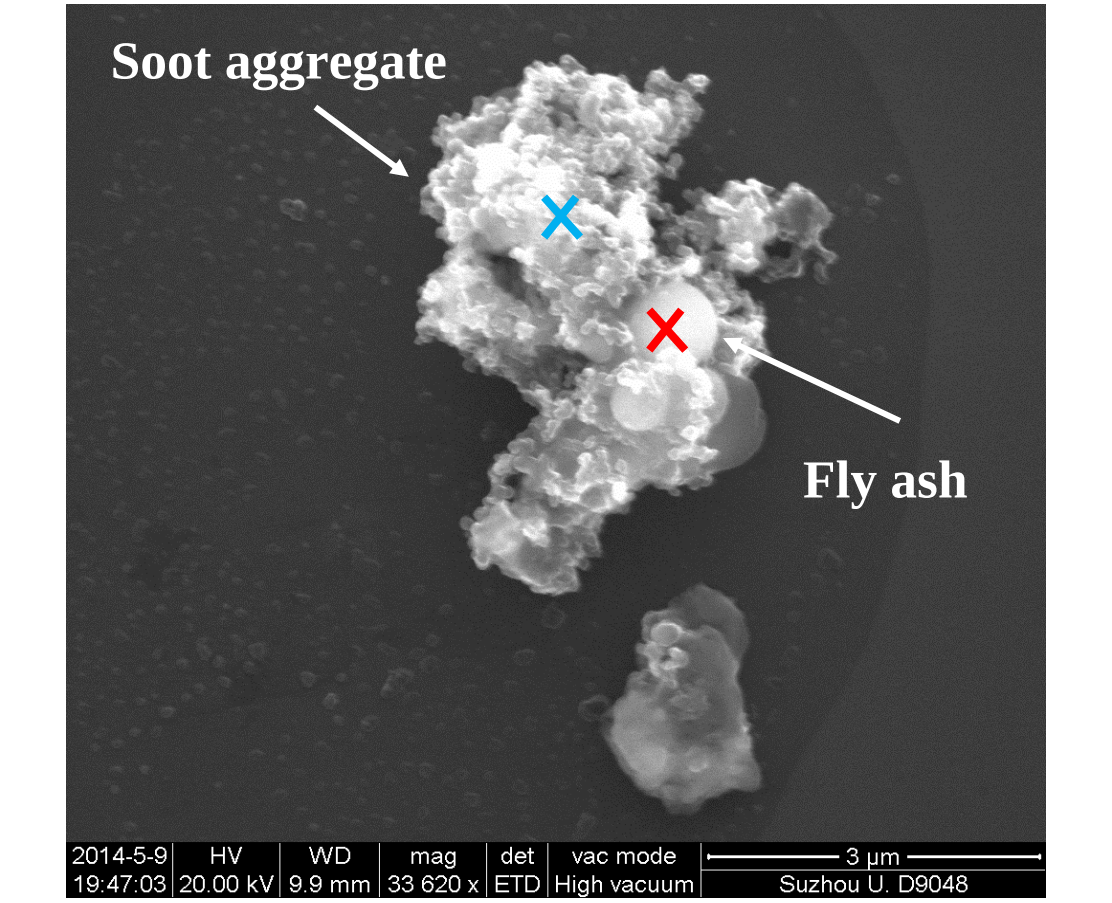

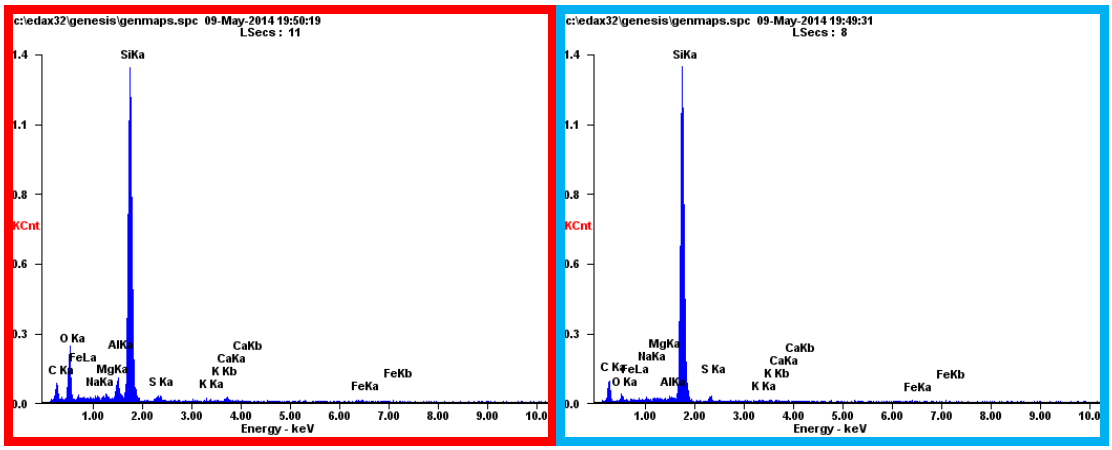

Figure S27. Another example of $PM_{2.5}$ aggregate. The EDX analyses show a larger concentration of Sulfur and Oxygen on the fly ash, while the Carbon peak is larger on the soot aggregate.

III

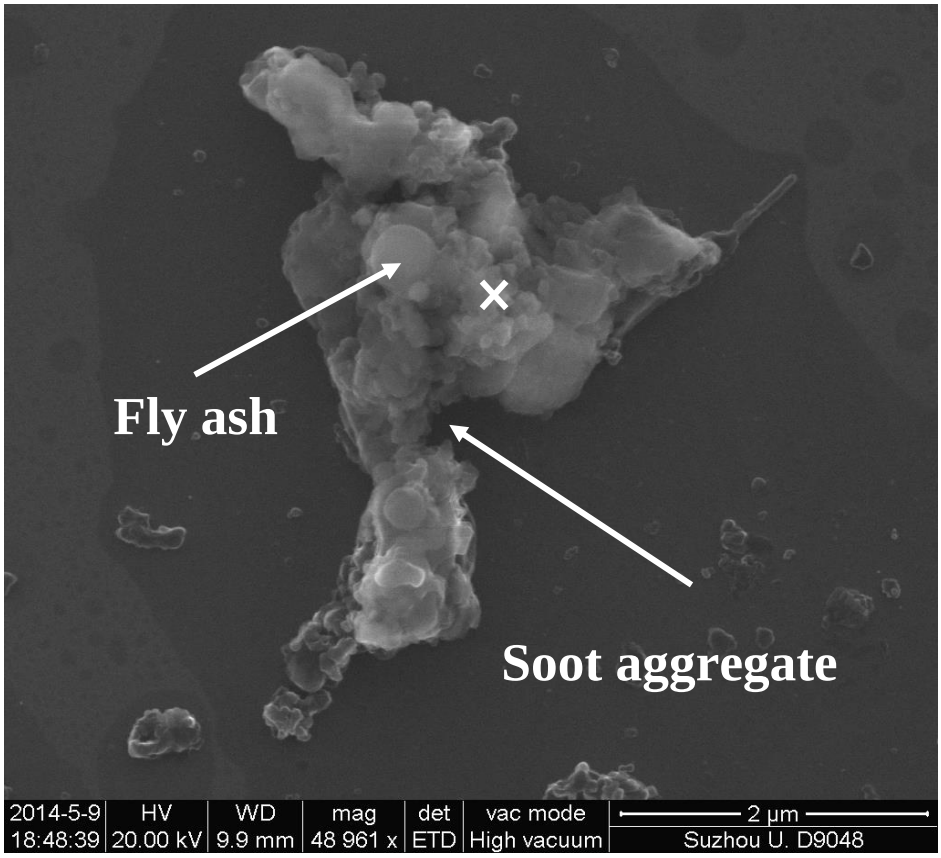

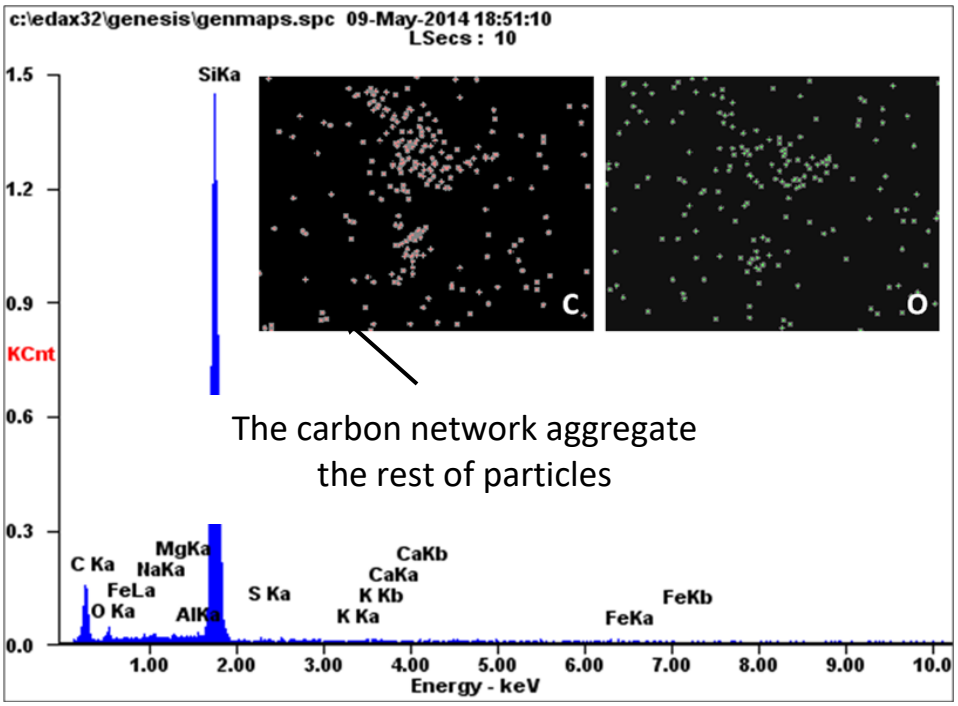

Figure S28. Another example of $PM_{2.5}$ aggregate. The top SEM and bottom EDX images show a particle cluster and the chemical composition (respectively).

Effect of some of $PM_{2.5}$ to surrounding areas

Some particles detected with the SEM/AFM revealed some degree of interaction with the Silicon substrate by forming a thin (2 to 10 nm thick) circular layer around them. As mentioned in the manuscript and Figure S14, this layer may be related to small semi-liquid particles attached the bigger one. Despite EDX analyses were unable to assess the chemical composition of these plateau-like areas, AFM F-Z curves and adhesion/deformation maps, didn't revealed any increase of the adhesion force, suggesting the formation of an inert layer (a liquid would increase the adhesion force (27). Probably oxygen atoms from the $PM_{2.5}$ particle may interact with the underlying Silicon substrate leading to the formation of a thin SiO_2 layer The formation of thin SiO_2 layers from oxygen diffusion has been previously reported [30].

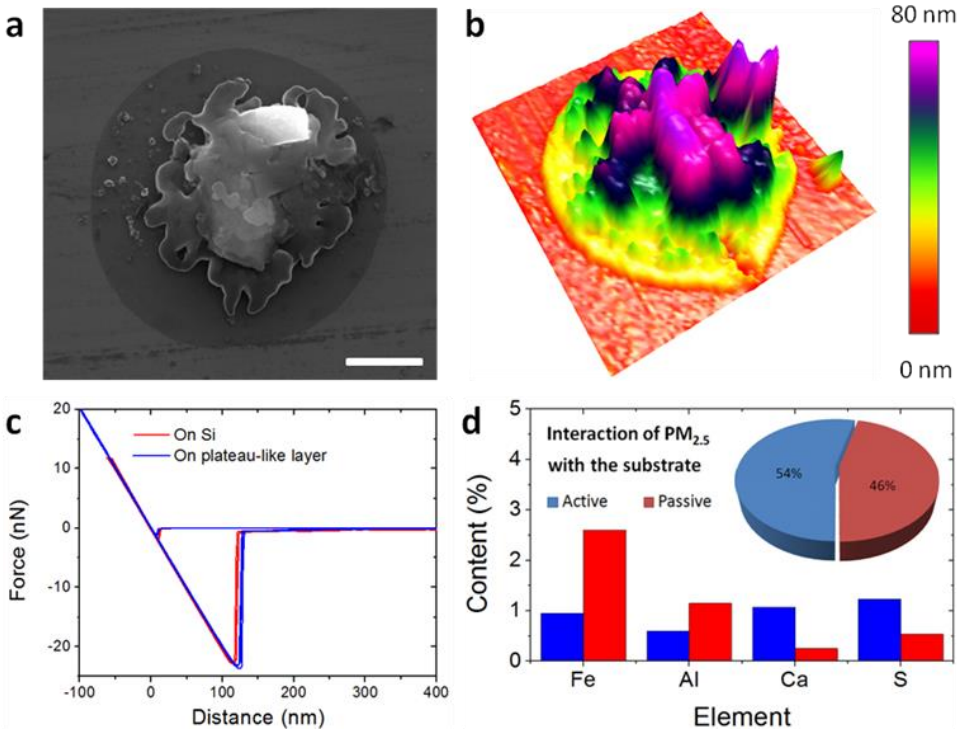

Figure S29. a, SEM image of one $PM_{2.5}$ particle on clean Silicon showing a characteristic dark circular trace around it. **b**, Three dimensional topographic AFM map of a similar particle; the black trace showed heights between 2 and 10 nm. c, Force distance curves on both the Silicon and plateau-like layer. d, EDX Chemical composition histogramof the particles with trace (active) and without trace (passive); no clear chemical composition difference between the two groups has been observed. The scale bars are 4 μm for (a) and 750 nm for (b).

The EDX analysis reveal that passive particles are richer in stable metallic oxides like Iron and Aluminum, while passive contain more Cadmium and Sulfur. Probably the particles with stable oxides don't let the oxygen atoms interact with the Silicon substrate, limiting the oxidative effect. Since cell oxidation has been proved to be an important source of toxic effects for cellular tissue, these particles may be specially hazardous.

Supplementary Information References

[1] User manual of the Quanta 200FEG Scanning Electron Microscope coupled with Energy Dispersive X-ray Spectrometer (SEM-EDX).

[2] W. Yue, X. Li, J. Liu, Y. Li, X. Yu, B. Deng, T. Wan, G. Zhang, Y. Huang, W. He, W. Hua, L. Shao, W. Li, S. Yang, Characterization of PM2.5 in the ambient air of shanghai city by analyzing individual particles, *Sci. Total Environ.* **2006**, *368*, 916.

[3] G. Labrada-Delgado, A. Aragon-Pina, A. Campos-Ramos, T. Castro-Romero, O. Amador-Munoz, R. Villalobos-Pietrini, Chemical and morphological characterization of PM2.5 collected during MILAGRO campaign using scanning electron microscopy, *Atmos. Pollut. Res.* **2012**, *3*, 289.

[4] X. Feng, Z. Dang, W. Huang, L. Shao, W. Li, Microscopic morphology and size distribution of particles in PM2.5 of Guangzhou City, *J. Atmos. Chem.* **2009**, *64*, 37.

[5] T. Ancelet, P. K. Davy, W. J. Trompetter, A. Markwitz, D. C. Weatherburn, Carbonaceous aerosols in an urban tunnel, *Atmos. Environ.* **2011**, *45*, 4463.

[6] D. Majumdar, S. P. M. P. William, Chalk dustfall during classroom teaching: particle size distribution and morphological characteristics, *Environ. Monit. Assess.* **2009**, *148*, 343.

[7] Z. Li, S. Zhao, R. Edwards, W. Wang, P. Zhou, Characteristics of Individual Aerosol Particles over Ürümqi Glacier No. 1 in Eastern Tianshan, Central Asia, China, *Atmos. Res.* **2011**, *99*, 57.

[8] U. Fernandes, M. Costa, Particle Emissions from a Domestic Pellets-Fired Boiler, *Fuel Process. Technol.* **2012**, *103*, 51.

[9] L. Sirghi, O. Kylián, D. Gilliland, G. Ceccone, F. Rossi, Cleaning and Hydrophilization of Atomic Force Microscopy Silicon Probes, *J. Phys. Chem. B* **2006**, *110*, 25975.

III

Paper B: Interaction between $PM_{2.5}$ airborne pollutants and third bodies

Y. Shi, B. Wang, M. Bartrons, M. Kolíbal, P. Bábor, X. Zhang, E. Grustan-Gutierrez, M. Lanza (*Submitted*, 2018)

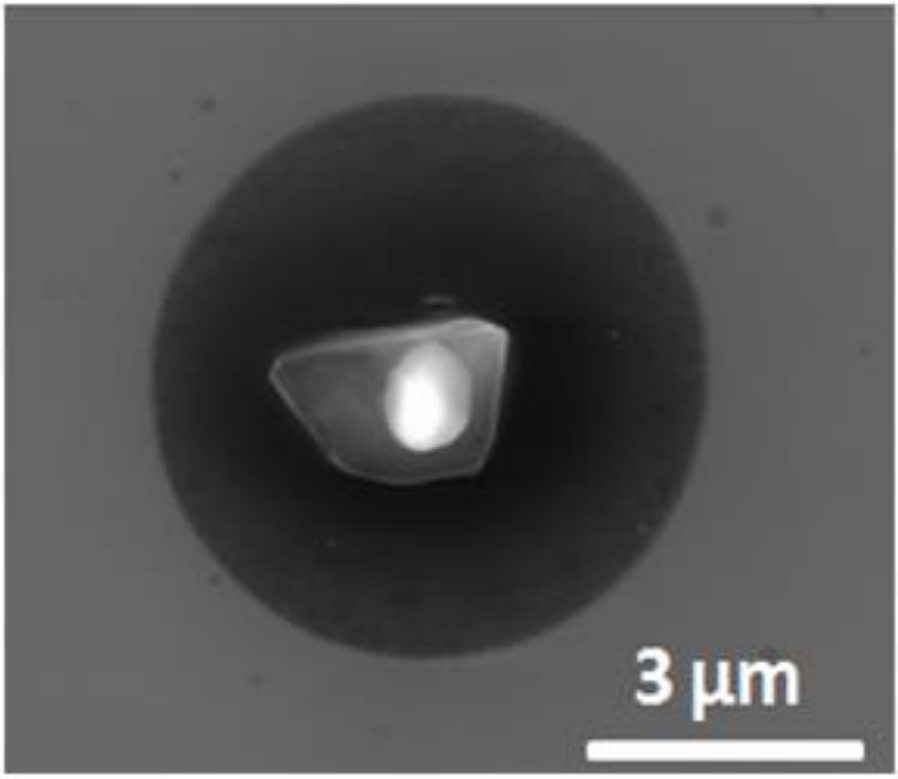

Abstract

In May 2016, The World Health Organization (WHO) reported that more than 80% of urban areas have levels of air pollution higher than its recommended limits. The report was specifically referring to particulate matter (PM): dust, dirt, soot and smoke grouped together according to diameter for legislative reasons. PM_{10} for particles 10 µm or less, $PM_{2.5}$ for particles 2.5 µm or less. Air pollution increases the risk of many diseases including respiratory conditions, heart disease, stroke and cancers. The size, shape, composition and sources of $PM_{2.5}$ particles have been abundantly studied during the past

decade. However, the interaction of these fine particles with third bodies still remains unclear. In this study, we report that more than 50% of $PM_{2.5}$ particles strongly interact with the substrates on which they are collected or transferred. More specifically, we observe the formation of a dark trace on the substrates surrounding all the $PM_{2.5}$ particles, independently of their size, shape and chemical composition. In depth nanoscale mechanical and chemical analyses of this trace reveal that it is around 10 nm thick and very stable even under local mechanical stresses, and that it is formed by alkali metals, hydrogen and CH groups. These results raise new concerns related to the effect of $PM_{2.5}$ airborne pollutants in contact with third bodies, giving insight to previous and future biomedical studies.

Contribution

Yuanyuan Shi designed and performed the experiments and prepared the manuscript.

B 1 Introduction

Particulate matter with an aerodynamic diameter smaller than 2.5 μm ($PM_{2.5}$) is an airborne pollutant with noxious consequences for human health,[1-3] due to both the effect of the particles themselves and their potential capacity to absorb carcinogenic organic pollutants—such as polycyclic aromatic hydrocarbons (PAHs)—on their surface. The fact that these particles can travel long distances in air makes $PM_{2.5}$ pollution a matter of global interest.[4] Most investigations in this field analyzed the amount, size, shape and composition of $PM_{2.5}$ pollutants by collecting the particles on a filter and scanning them using a Scanning Electron Microscope (SEM) and/or an Electron Dispersive X-Ray Spectroscopy (EDX).[5-9] Using these techniques different types of $PM_{2.5}$ particles have been reported, being carbon-rich fluffy soot aggregate, elongated minerals and spherical fly ash the most common an abundant worldwide, i.e. they have been observed in several countries, including China,[10] India,[11] Korea,[7] Japan,[12] United States,[13] Mexico,[9] United Kingdom,[14] Portugal,[15] and New Zealand,[16] among others.

Only a few works went beyond that and reported the nanoscale properties of $PM_{2.5}$. Fu et al.[17] used a Transmission Electron Microscope (TEM) to analyze the structure of $PM_{2.5}$ at the atomic scale, and reported that this high lateral resolution technique is able to differentiate single particle and aggregates. Additional factors such as surface roughness and adhesiveness could also have an important effect on their interaction with third bodies, as well as on their biological activity.[18] De Oliveira et al.[19] observed that surface roughness can alter the frictional coefficient of the particles, and Szoszkiewic et al.[20] reported that the stickiness of many particles is related to their elasticity and plasticity. However, the study of these properties is more complex and requires mechanical characterization tools with higher spatial resolution.

One of the most powerful techniques used in materials science for analyzing mor-

-phological and mechanical properties of different kinds of nanoparticles is atomic force microscopy (AFM), but interestingly in $PM_{2.5}$ research it has been barely used. Kollensperger et al.[21] used AFM to analyze the density and size of $PM_{2.5}$ particles, but no information about their surface roughness or stickiness was reported, as their images were collected in tapping mode. Kundu et al.[22] also analyzed the surface roughness of different nanostructured polymers at the sub-nanometer scale via AFM. The adhesiveness and stickiness of a material/particle can be also accurately monitored by using an AFM recording Force-Distance (F-Z) curves. Despite these capabilities, the use of the AFM in $PM_{2.5}$ research is being hindered by the filamentary surface of the filters used to collect the particles, which are too rough impeding reliable AFM analyses.[13,23] In a previous work, we used an ultrasonic bath to transfer $PM_{2.5}$ particles from rough filters to ultra flat silicon wafers, reporting the first adhesiveness analyses using F-Z curves collected with the tip of an AFM on this type of particles.[24-25]

In this study the interaction between $PM_{2.5}$ airborne pollutants and third bodies is analyzed at the nanoscale using a combination of characterization tools. By using SEM, AFM, EDX and Auger electron spectroscopy (AES) essential data about topography, roughness, adhesiveness, deformation and chemical composition of particles have been collected. Our results indicate that most of the particles (both particles transferred and collected directly on the substrates) interact with the substrates presenting a dark trace layer (halo) around them. We statistically analyze the dark trace layers and find that they are always around 10 nm thick, and mainly composed of alkali metals, hydrogen and CH groups. These results reveal a very strong interaction between $PM_{2.5}$ and third bodies, which in turn may represent a worrying concern for the health of the inhabitants of cities that suffer high concentrations of $PM_{2.5}$ in air.

B 2 Experimental methods

$PM_{2.5}$ collection process: The particles have been collected according to the "Ambient air monitoring reference and equivalent methods" established by the US Environmental Protection Agency (Federal Register, Vol. 64, No. 74).[26] We used a TH-150C Automatic Medium Volume TSP Sampler (Wuhan Tianhong instruments Co. Ltd) with TH-$PM_{2.5}$ impactor to continuously monitor the mass concentration of the daily $PM_{2.5}$. The equipment was located at the building at No. 7 of Panjiayuan Nali road (Chaoyang District, Beijing), and the particles were collected on December 2nd and 7th of 2015, with concentrations of 106 µg/m^3 and 298 µg/m^3, respectively. The filters used for particle collection consisted on standard rough networks of quartz filter filaments from Whatman (model 1820-90). In order to allow nanomechanical characterization with the AFM, the $PM_{2.5}$ particles were transferred from the rough filters to flat silicon substrates using the ultrasonic bath. The reliability of this transfer method was analyzed by performing an additional experiment: a piece of silicon was introduced in the collector together with the filters during the $PM_{2.5}$ collection process. We observe that the sizes, shapes and compositions of the particles deposited directly on the substrate in the collector are very similar to those transferred from the rough filters to the silicon. For comparison, $PM_{2.5}$ particles have been also collected directly on flatter substrates (Si wafer, Al foil), by introducing them in the particle collector.

$PM_{2.5}$ characterization: A Quanta 200FEG Scanning Electron Microscope coupled with Energy Dispersive X-ray Spectrometer (SEM-EDX) was used to analyze the relationship between the morphology and chemical composition of the particles. An AES from Omicron (NanoSAM Omicron) was also used for the high-resolution chemical composition analysis. Before the AES characterization, the samples were annealed under UHV conditions (5×10^{-10} mbar) at 300 °C for 1 hour to desorb impurities, and thus to

increase the signal-to-noise ratio. This procedure did not induce any morphological changes, as confirmed by *in situ* monitoring. After this treatment, AES analysis was performed using 5 keV electron beam, 1 nA beam current. The mechanical properties of the particles were characterized using two kinds of AFM equipments: the Multimode V AFM and Dimension Icon AFM, both from Bruker. The Force-Distance (F-Z) curves were measured in contact mode using the Multimode V AFM with Pt-Ir coated silicon tips from Bruker (SCM-PIC, item no. A009/07-07/14). Adhesion and deformation maps were measured in peak-force tapping mode by the Dimension Icon AFM with Co-Cr coated silicon tips from Bruker (MESP-RC), which have a spring constant of 5 N/m. The maps were obtained with a scan frequency of 1 Hz and a drive amplitude of 5 V. The AFM maps were analyzed with the NanoScope Analysis (version 1.40) software of the AFM and the plots were generated with OriginLab 8.5.

Mapping of chemical composition of a dark trace layer around particles was done by Time-of-Flight Secondary Ion Mass Spectrometry (ToF-SIMS) using ToF-SIMS 5 instrument (IonTOF company). During ToF-SIMS analysis, a solid sample surface is bombarded by pulsed primary ion beam (Bi^+). Atomic and molecular ions (positive or negative) are sputtered from the outer layers of the surface and extracted. Their mass is measured in the time of flight analyzer. For 2D mapping a Bi^+ fine-focused primary ion beam operating at 30-keV impact energy and a current of 0.1-0.3 pA was used. The maximal lateral resolution was ~200 nm. Intensity of the secondary ions was higher in the surrounding of the particle than from the particle itself because complicated morphology of the particle and charging of the particle.

B 3 Results and discussion

After particle collection, the filters were scanned with SEM; the $PM_{2.5}$ particles

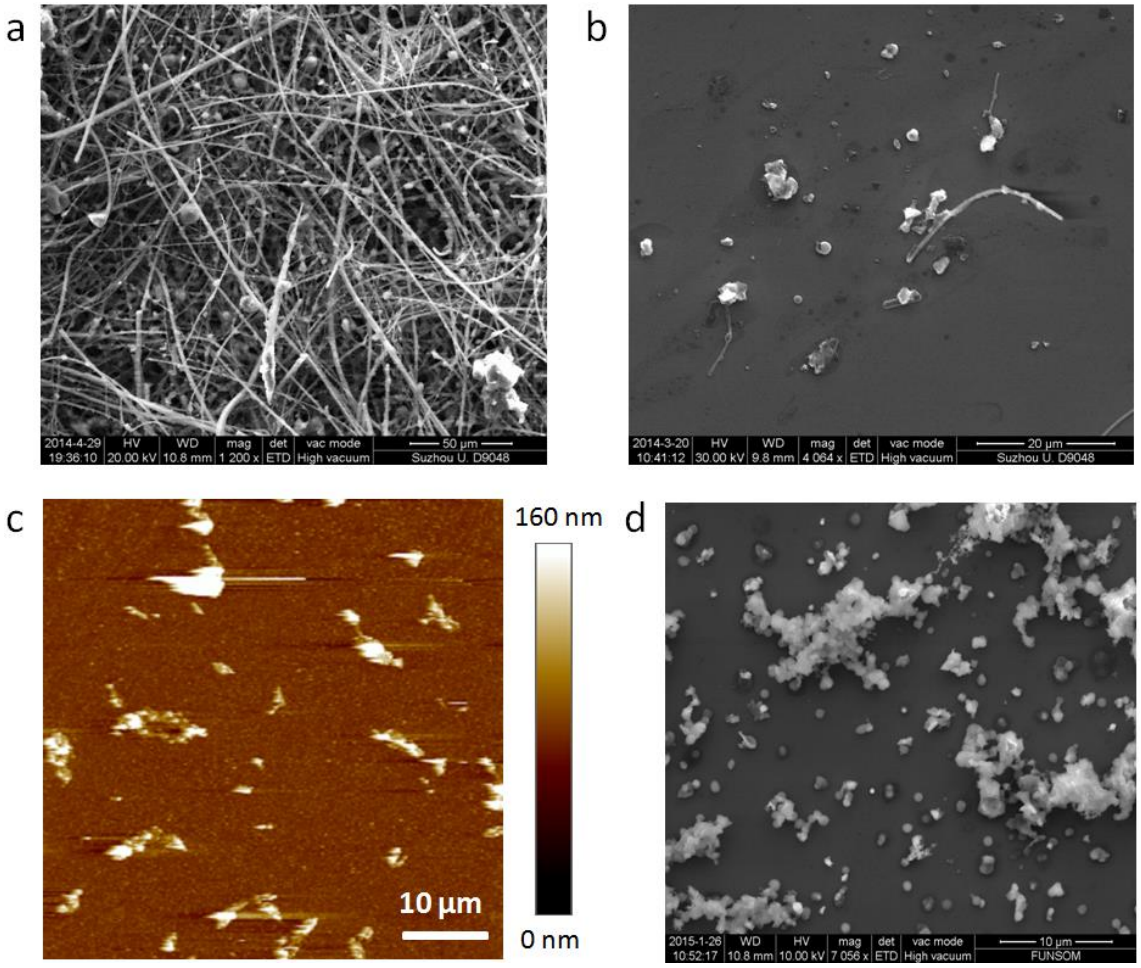

Figure 1. SEM morphology of the as-collected PM2.5 particles on the filter (a), and the particles transferred on the clean silicon substrate (b) at large scale. (c) Topography map of transferred $PM_{2.5}$ particles on clean Si, collected by the Multimode V AFM. (d) SEM morphology of the $PM_{2.5}$ particles collected directly on the clean silicon substrate. The size of the particles in (b) and (d) is similar, only the density is different.

trapped at the cavities between the filaments could be clearly observed (Figure 1a). For the AFM characterization we used two kinds of samples: one containing particles transferred on silicon wafers using an ultrasonicator, and another one containing particles collected *in situ* on flat substrates (silicon wafers and aluminum foils were introduced in the particle collector). Figures 1b and 1c show the SEM images and AFM topographic maps of the $PM_{2.5}$ particles after transfer to silicon substrate (respectively). Figure 1d shows the SEM image of the $PM_{2.5}$ particles collected *in situ* on a silicon substrate. By comparing Figures 1b and 1d it can be concluded that the sizes and shapes of the particles in both samples were similar, just the density of particles changed. This observation

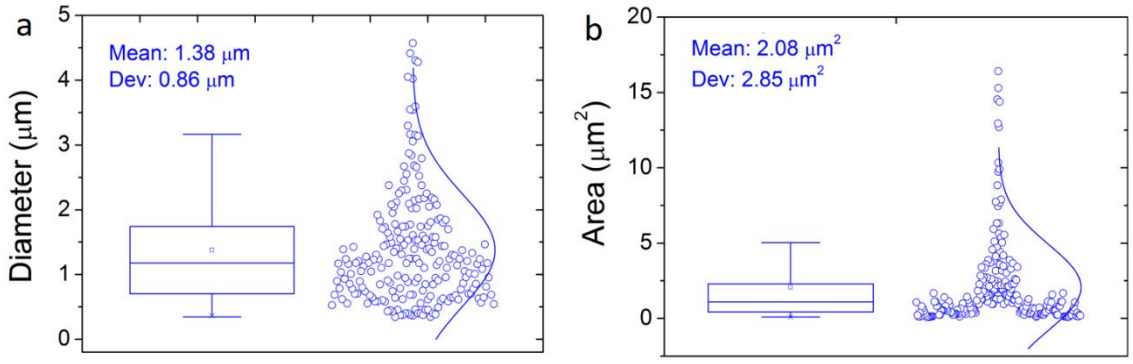

Figure 2. Statistical analysis of the physical diameter (a), and area (b) of $PM_{2.5}$ particles transferred on clean Si. The AFM software, NanoScope Analysis V1.4, was used for the particle analysis.

indicates that the transfer process did not significantly alter the properties of the particles.

The AFM images allow an accurate and fast statistical analysis of the particle size using the NanoScope AFM software. To do so, we select a threshold height of 10 nm above the most repeated value of the image histogram, which represents the average height of the silicon substrate (see Figure S1). The statistical analysis of the diameter and area of the $PM_{2.5}$ particles transferred on clean silicon is shown in Figures 2a and 2b (respectively). According to the AFM manufacturer (Bruker), the values of the diameter given by the NanoScope software correspond to the aerodynamic diameter of the particles.[23] In total, 217 particles from different images (collected at random locations) were analyzed. As shown in Figure 2a, 83% of the $PM_{2.5}$ particles have a diameter ranging between 0.4 and 2.2 µm. These values are expected because we selected that size in the particle collector, and demonstrate that the collection process was successful.

Upon individual scrutiny of the $PM_{2.5}$ particles in the SEM images, an interesting and unreported behavior is exposed: 54% of the particles collected display a dark trace on the substrate surrounding them (Figure 3). Repeated and thorough experiments revealed that the dark trace is not coming from the beam contamination, which could possibly explain such observation. The dark trace is present in all the samples and it is

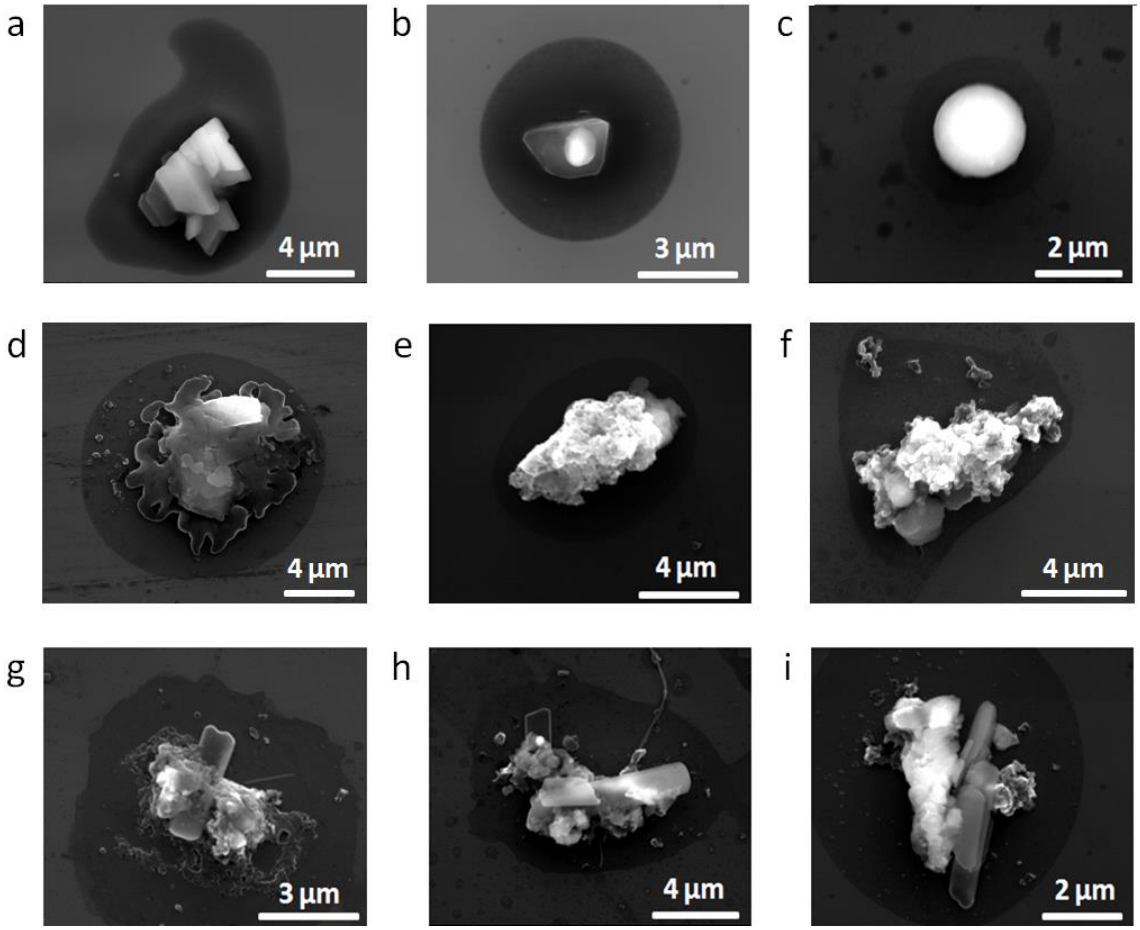

Figure 3. Different kinds of $PM_{2.5}$ particles with the dark trace layer. (a)-(c) are the particles with flat surface. (d)-(f) are the soot aggregates. And (g)-(i) shows the soot aggregates, elongated minerals, and spherical fly ash gather together, also with the dark trace. The dark trace appears almost at all kinds of $PM_{2.5}$ particles, indicating that it is not source-dependent.

independent of i) the collection method: it is present for both directly collected particles (on 300 nm SiO_2/Si wafers, Figure S2) and transferred particles (Figure 3); ii) the morphology of the particles: soot aggregates, elongated minerals and spherical fly ash indistinctly show this feature; and iii) their chemical composition (Figure S3). Furthermore, not only the individual particles appear to be surrounded by these dark traces (Figures 3a-3f), but also their aggregates (see Figures 3g-3i). These observations indicate that the particle formation and trace generation should be independent processes. The regular contour and the good homogeneity observed in the SEM images (i.e. the contrast is the same along all the dark trace) suggest that these dark traces might be related to the

presence of liquid layer, originally surrounding the particles. It is known that some particles could be semi-to-entirely liquid when they are airborne,[27] and that $PM_{2.5}$ can trap water molecules when suspended on the wind (due to the relative humidity of the atmosphere).

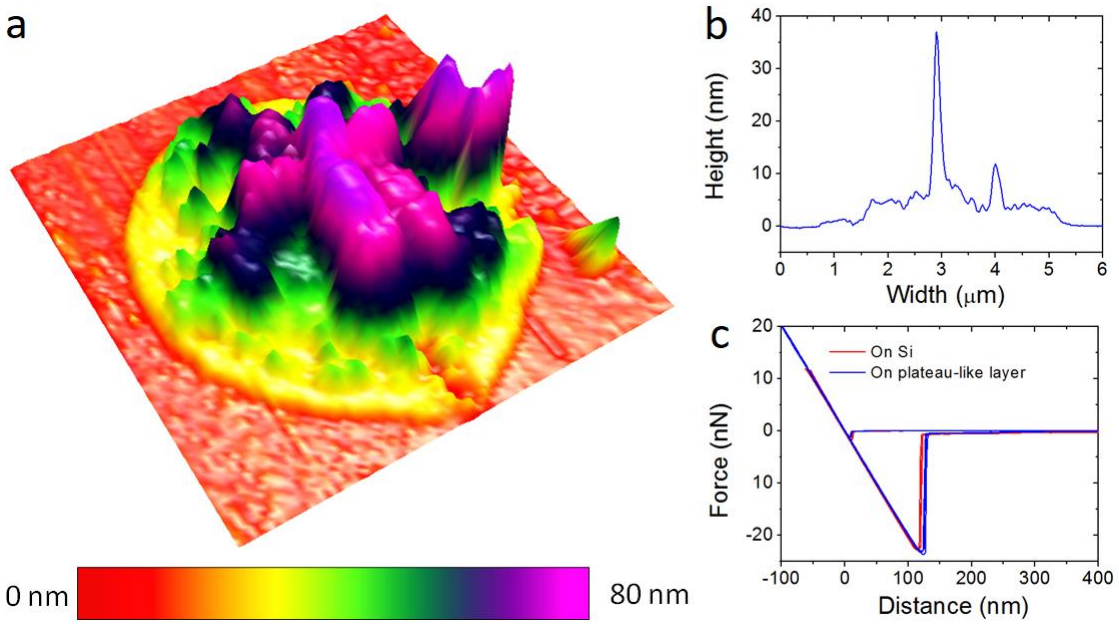

Figure 4. (a) Three dimensional topographic AFM map of a particle with the dark trace layer, similar to those in Figure 3. (b) Typical cross-section analysis on the particle with trace layer. Both the AFM topographic map (a) and the typical cross section (b) show the black trace layers have around 10 nm in height. (c) F-Z curve on the plateau-like layer (the trace) in (a), and the F-Z curve on the silicon substrate has also been obtained as reference. The scan size is 3.75 μm × 3.75 μm for (a).

To get deeper insight into the properties of the dark traces, the samples were scanned using AFM. Topographic AFM images of $PM_{2.5}$ particles that appear with a dark trace in SEM pictures are shown in Figures 4a and 5a. The dark traces surrounding the particles in SEM images appear as a flat plateau in the topographic AFM maps. Using the cross sectional tool of the AFM software, we observe that these traces were around 10 nm thick (Figure 4b). Interestingly, no topographic modification has been observed in consecutive topographic maps collected with the AFM, which suggests that the layer is not in liquid state. The nature of this plateau-like traces was further analyzed from

sequences of F-Z curves collected on the bare silicon substrate and on the plateaus. According to previous reports, liquid films can increase the adhesion force between the tip and the sample during such experiments.[28] Therefore, if the film would be liquid an increase of the (negative) adhesion force peak in the F-Z curve should be observed.[28] The F-Z curves measured on the silicon revealed adhesion forces around -20 nN (Figure. 4c, red line) consistent with values previously reported.[29] Similar experiments performed on the plateau-like layer (the dark trace) reveal that the adhesion value of the dark trace is very similar to the silicon substrate (it is also around 20 nN). Such observation has been statistically corroborated on different particles and using different AFM probe tips (e.g. in Figure 5a both the particles on the top left and bottom right show this plateau-like shape). Peak-force error and adhesion AFM maps (Figures 5b and 5c) further support these observations, and they do not reveal any increase of the adhesion force on the dark trace. The dark trace layer is also stable in UHV condition. This result further supports that the dark trace layer is not a liquid film in its current state.

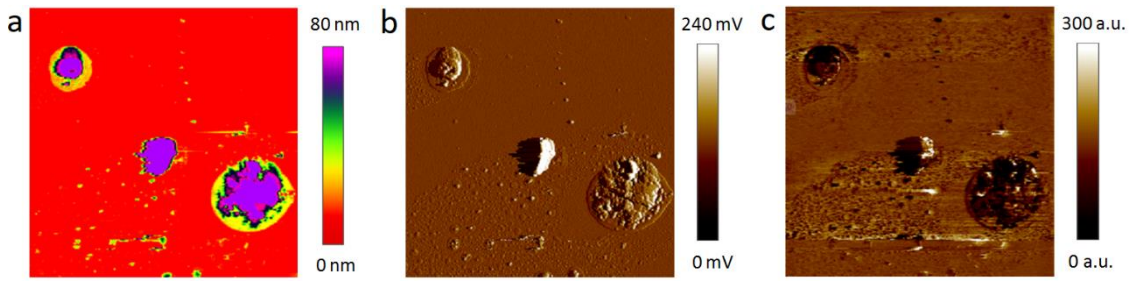

Figure 5. (a) Topography, (b) peak-force error, and (c) adhesion maps of the particles with trace. The trace can be observed clearly in (a), (b) and (c), and it shows the similar properties to the surrounded particles. The scan sizes are 10.7 µm × 10.7 µm for (a)-(c).

While the chemical composition of the $PM_{2.5}$ could be easily detected by EDX,[6-9] the analysis of the ultra thin (<10 nm) dark traces requires tools with a larger surface sensitivity. Therefore, instead of using EDX (which information applies to the underlying 1 µm), AES was selected for its better spatial resolution. Figures 6a and 6c show the SEM

images of the $PM_{2.5}$ particles with the dark trace layer on the native SiO_2/Si and Al foil (respectively). The corresponding AES surveys (shown in Figures 6b and 6d) indicate that the dark trace layer surrounding the particles contains mainly carbon. The oxygen peak that appears on the Al surface (red line in Figure 6d) is related to the native oxide on the Al foil.[30] However, the oxygen was not detected on the dark trace layer (grey line in Figure 6d); probably this is due to its non-negligible thickness (~ 10 nm from the AFM measurements).

The chemical composition of the particles has been further analyzed via ToF- SIMS, for which the average depth of analysis is approximately 1 nm. Figure 7 shows the SEM image of a

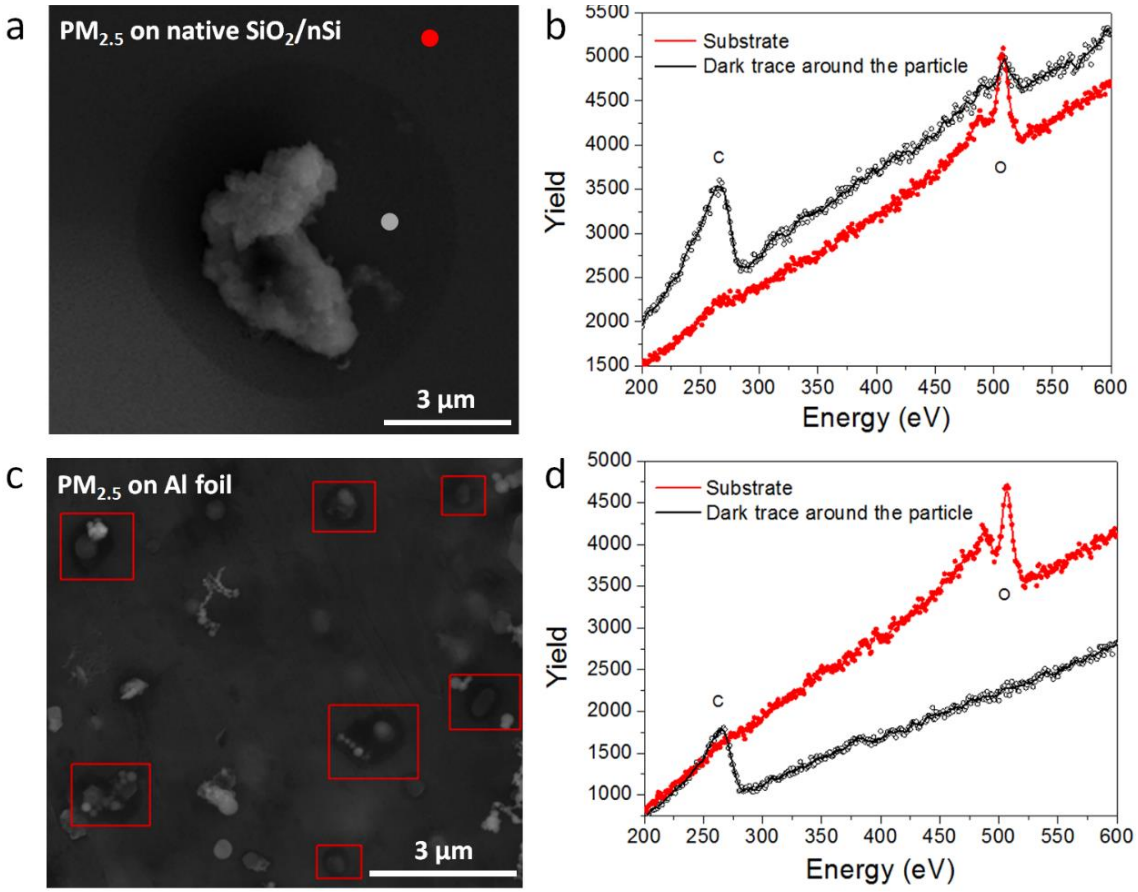

Figure 6. SEM and AES characterization of the $PM_{2.5}$ particles on native SiO_2/Si substrate (a-b) and Al foil (c-d). (a) A $PM_{2.5}$ particle with a dark trace layer that were transferred on the Si substrate with native SiO_2. (b) AES characterization on the bare substrate (red dot in a) and the dark trace around the particle (grey dot in a). (c) $PM_{2.5}$ particles collected directly on the Al foil, some of which are surrounded by the dark trace layer. The corresponding AES characterization is shown in (d).

$PM_{2.5}$ particle with a dark trace surrounding it, and the SIMS maps displaying its composition. It can be observed that the dark trace also contains alkali metals, hydrogen and CH groups, indicating that the carbon present in the trace could be a mix of soot and decomposed complex hydrocarbons.

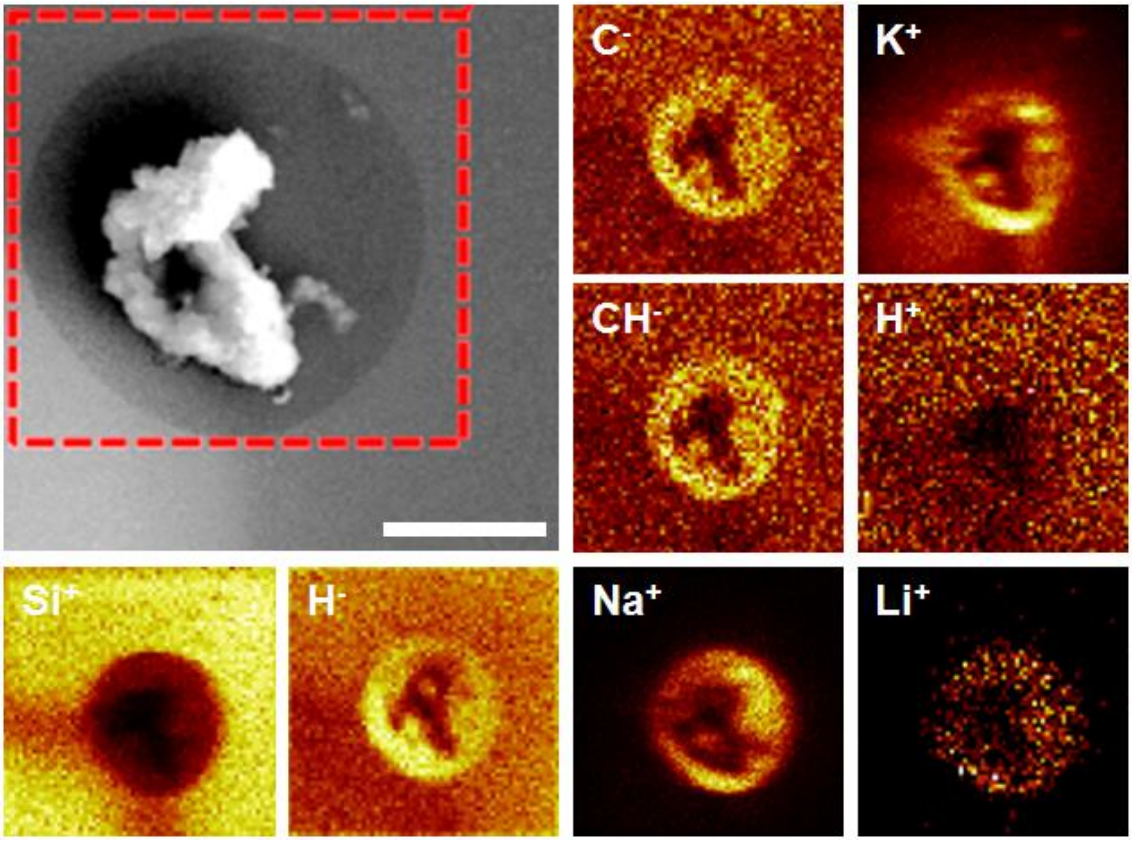

Figure 7. SEM image of a $PM_{2.5}$ image with a dark trace and chemical composition maps at the same location obtained using SIMS. There is a presence of alkali metals, hydrogen and CH groups, and the composition is clearly different from the Si substrate. The scale bar in the SEM image is 4 μm. The color scale for the SIMS maps is in arbitrary units (black/white indicate low/high concentrations).

Taking into account the information gained from SEM, AFM, AES and SIMS, we propose a dynamic mechanism for the dark trace formation. The dark trace may be related to semi-to-entirely liquid phase particles attached to the $PM_{2.5}$ while traveling suspended on the air. This is supported by the fact that the dark trace is observed for different types of particles (i.e. fluffy soot aggregate, elongated minerals and spherical fly ash), as well as by the regular contour and homogenous color observed in the SEM images. When the

particles are collected on the flat SiO_2/Si and Al substrates for SEM/AFM inspection, the liquid phase particles interact with the underlying substrate, forming a solid inert layer (or partially evaporate/freeze if inserted into vacuum chamber). It is widely known that liquids can interact with the substrates (made of Al and Si) to form stable compounds. The chemical composition of the dark trace analyzed by AES and SIMS indicates the presence of alkali metals, hydrogen and CH groups. This observation indicates that, during their travel in the air, $PM_{2.5}$ particles may have absorbed not only water, but also other materials. In the worse scenario, the liquid may be composed by toxic hydrocarbons, such as the carcinogenic PAHs. PAHs are strongly potent carcinogens or mutagens,[32] widespread distributed around the globe.[33] These PAHs are a mixture of hydrocarbons composed of multiple aromatic rings produced by the incomplete combustion of organic matter, e.g. coal burning, gasoline/diesel engine emission, industrial activities like aluminum, iron and steel production, waste incineration, oil refining, or forest fires. Once introduced to the human body, these particles are released and could potentially enter the blood stream.[31] The results herein suggest that the dark trace observed in the SEM images (Figure 3) could certainly be composed of PAHs. The potential link between PAHs and airborne $PM_{2.5}$ has been suggested also recently.[34-38] Traffic emission and coal combustion seem to be the principal sources of PAHs associated with $PM_{2.5}$. More information is needed regarding the characterization of $PM_{2.5}$-bound toxic organics, their transport, spatial distribution and health impacts but PAHs bounded to $PM_{2.5}$ could be responsible for a significant portion (if not most) of the overall carcinogenicity of $PM_{2.5}$.

B 4 Conclusions

In this study, more than 500 *in situ* collected and transferred $PM_{2.5}$ particles have been investigated at the nanoscale via SEM, AFM, AES and SIMS. For more than 50%

of these particles a dark trace layer around the particles (and their aggregates) was observed. Further analyzes reveal that this trace is a stable film of around 10 nm thickness, and that it is composed by alkali metals, hydrogen and CH groups. These results indicate a strong interaction between $PM_{2.5}$ airborne pollutants and third bodies, and may represent a very important concern for human health. Biological studies should clarify what is the impact of such interaction for the health of living beings.

B 5 Acknowledgement

This work has been supported by the Young 1000 Global Talent Recruitment Program of the Ministry of Education of China, the National Natural Science Foundation of China (grants no. 61502326, 41550110223, 11661131002), the Jiangsu Government (grant no. BK20150343), the Ministry of Finance of China (grant no. SX21400213) and the Young 973 National Program of the Chinese Ministry of Science and Technology (grant no. 2015CB932700). Part of the work was carried out with the support of CEITEC Nano Research Infrastructure (ID LM2015041, MEYS CR, 2016–2019), CEITEC Brno University of Technology. The Collaborative Innovation Center of Suzhou Nano Science & Technology, the Jiangsu Key Laboratory for Carbon-Based Functional Materials & Devices, and the Priority Academic Program Development of Jiangsu Higher Education Institutions are also acknowledged. We thank professor Dapeng Yu (Peking University) for granting us access to his CAFM lab, and professor Rainer Waser for RS mechanism discussion.

B 6 References

[1] J. Marshall, PM 2.5, *Proc. Natl. Acad. Sci. USA.* **2013**, *110*, 8756.

[2] E. Longhin, J. A. Holme, K. B. Gutzkow, V. M. Arlt, J. E. Kucab, M. Camatini, M. Gualtieri, Cell cycle alterations induced by urban $PM_{2.5}$ in bronchial epithelial cells:

characterization of the process and possible mechanisms involved, *Part. Fibre Toxicol.* **2013**, *10*, 63.

[3] X. Deng, F. Zhang, W. Rui, F. Long, L. J. Wang, Z. H. Feng, D. L. Chen, W. J. Ding, $PM_{2.5}$-induced oxidative stress triggers autophagy in human lung epithelial A549 cells, *Toxicol. In Vitro* **2013**, *27*, 1762.

[4] J. Lin, D. Pan, S. J. Davis, Q. Zhang, K. He, C. Wang, D. G. Streets, D. J. Wuebbles, D. Guan, China's international trade and air pollution in the United States, *Proc. Natl. Acad. Sci. USA.* **2014**, *111*, 1736.

[5] T. Hu, J. Cao, Z. Shen, G. Wang, S. Lee, K. Ho, Size differentiation of individual atmospheric aerosol during winter in Xi'an, China, *Aerosol Air Qual. Res.* **2012**, *12*, 951.

[6] X. D. Feng, Z. Dang, W. L. Huang, L. Y. Shao, W. J. Li, Microscopic morphology and size distribution of particles in $PM_{2.5}$ of Guangzhou City, *J. Atmos. Chem.* **2010**, *64*, 37.

[7] H. J. Jung, B. W. Kim, M. A. Malek, Y. S. Koo, J. H. Jung, Y. S. Son, J. C. Kim, H. K. Kim, C. U. Ro, Chemical Speciation of Size-Segregated Floor Dusts and Airborne Magnetic Particles Collected at Underground Subway Stations in Seoul, Korea, *J. Hazard. Mater.* **2012**, *213-214*, 331.

[8] W. Yue, X. Li, J. Liu, Y. Li, X. Yu, B. Deng, T. Wan, G. Zhang, Y. Huang, W. He, W. Hua, L. Shao, W. Li, S. Yang, Characterization of $PM_{2.5}$ in the ambient air of Shanghai city by analyzing individual particles, *Sci. Total Environ.* **2006**, *368*, 916.

[9] G. Labrada-Delgado, A. Aragon-Pina, A. Campos-Ramos, T. Castro-Romero, O. Castro-Romero, R. Villalobos-Pietrini, Chemical and morphological characterization of $PM_{2.5}$ collected during MILAGRO campaign using scanning electron microscopy, *Atmos. Pollut. Res.* **2012**, *3*, 289.

[10] J. Qiu, Fight against smog ramps up, *Nature* **2014**, *506*, 273.

[11] P. G. Satsangi, S. Yadav, Characterization of $PM_{2.5}$ by X-ray diffraction and scanning electron microscopy–energy dispersive spectrometer: its relation with different pollution Sources, *Int. J. Environ. Sci. Technol.* **2014**, *11*, 217.

[12] K. Saitoh, K. Sera, T. Shirai, Characterization of atmospheric aerosol particles in a mountainous region in northern Japan, *Atmos. Res.* **2008**, *89*, 324.

[13] Y. Chen, N. Shah, F. E. Huggins, G. P. Huffman, W. P. Linak, C. A. Miller, Investigation of primary fine particulate matter from coal combustion by computer-controlled scanning electron microscopy, *Fuel Process. Technol.* **2004**, *85*, 743.

[14] S. Smith, M. Ward, R. Lin, R. Brydson, M. Dall'Osto, R. M. Harrison, Comparative study of single particle characterisation by Transmission Electron Microscopy and time-of-flight aerosol mass spectrometry in the London atmosphere, *Atmos. Environ.* **2012**, *62*, 400.

[15] U. Fernandes, M. Costa, Particle emissions from a domestic pellets-fired boiler, *Fuel Process. Technol.* **2012**, *103*, 51.

[16] T. Ancelet, P. K. Davy, W. J. Trompetter, A. Markwitz, D. C. Weatherburn, Carbonaceous aerosols in an urban tunnel, *Atmos. Environ.* **2011**, *45*, 4463.

[17] H. Fu, M. Zhang, W. Li, J. Chen, L. Wang, X. Quan, W. Wang, Morphology, composition and mixing state of individual carbonaceous aerosol in urban Shanghai, *Atmos. Chem. Phys.* **2012**, *12*, 693.

[18] D. M. Broday, R. Rosenzweig, Deposition of fractal-like soot aggregates in the human respiratory tract, *J. Aerosol Sci.* **2011**, *42*, 372.

[19] R. R. L. De Oliveira, D. A. C. Albuquerque, T. G. S. Cruz, F. M. Yamaji, F. L. Leite, in *Atomic Force Microscopy - Imaging, Measuring and Manipulating Surfaces at the Atomic Scale*, ed. V. Bellitto, InTech, Croatia, **2012**, 155-156.

[20] R. Szoszkiewicz, E. Riedo, in *Applied Scanning Probe Methods V*, EDX. B. Bhushan, S. Kawata, H. Fuchs, Springer, Germany, **2007**, 269-286.

[21] G. Köllensperger, G. Friedbacher, R. Kotzick, R. Niessner, M. Grasserbauer, In-situ atomic force microscopy investigation of aerosols exposed to different humidities, *Fresenius' J. Anal. Chem.* **1999**, *364*, 296.

[22] S. Kundu, R. Ganesan, N. Gaur, M. S. M. Saifullah, H. Hussain, H. Yang, C. S. Bhatia, Effect of angstrom-scale surface roughness on the self-assembly of polystyrene-polydimethylsiloxane block copolymer, *Sci. Rep.* **2012**, *2*, 617.

[23] User manual of the Dimension Icon AFM from Bruker, http://www.nanophys.kth.se/nanophys/facilities/nfl/afm/icon/bruker-help/DIcon_webhelp.htm (accessed: October 20, 2017).

[24] M. Lanza, Y. Wang, T. Gao, A. Bayerl, M. Porti, M. Nafria, Y. Zhou, G. Jing, Y. Zhang, Z. Liu, Electrical and mechanical performance of graphene sheets exposed to oxidative environments, *Nano Res.* **2013**, *6*, 485.

[25] Y. Shi, Y. Ji, H. Sun, F. Hui, J. Hu, Y. Wu, J. Fang, H. Lin, J. Wang, H. Duan, M. Lanza, Nanoscale characterization of $PM_{2.5}$ airborne pollutants reveals high adhesiveness and aggregation capability of soot particles, *Sci. Rep.* **2015**, *5*, 11232.

[26] $PM_{2.5}$ Regulations (Federal Register); www3.epa.gov/ttnamti1/pmcfr.html (accessed: September 15, 2016).

[27] S. Rubin, Liquid particles in atmospheric haze, *J. Atmos. Terr. Phys*. **1952**, *2*, 130.

[28] B. Cappella, G. Dietler, Force-distance curves by atomic force microscopy, *Surf. Sci. Rep.* **1999**, *34*, 1.

[29] L. Sirghi, O. Kylián, D. Gilliland, G. Ceccone, F. Ros, Cleaning and hydrophilization of atomic forcemicroscopy silicon probes, *J. Phys. Chem. B* **2006**, *110*, 25975.

[30] J. Evertsson, F. Bertram, F. Zhang, L. Rullik, L. R. Merte, M. Shipilin, M. Soldemo, S. Ahmadi, N. Vinogradov, F. Carlà, J. Weissenrieder, M. Göthelid, J. Pan, A. Mikkelsen, J.-O. Nilsson, E. Lundgren, The thickness of native oxides on aluminum alloys and single crystals, *Appl. Surf. Sci.* **2015**, *349*, 826.

[31] J. Marra, M. Voetz, H.-J. Kiesling, Monitor for detecting and assessing exposure to airborne nanoparticles, *J. Nanopart. Res.* **2010**, *12*, 21.

[32] Y. Guo, K. Wu, X. Huo, X. Xu, Sources, distribution, and toxicity of polycyclic aromatic hydrocarbons, *J. Environ. Health* **2011**, *73*, 22.

[33] M. Bartrons, J. Catalan, J. Penuelas, Spatial and temporal trends of organic pollutants in vegetation from remote and rural areas, *Sci. Rep.* **2016**, *6*, 25446.

[34] M. O. A. Mohammed, W.-W. Song, Y.-L. Ma, L.-Y. Liu, W.-L. Ma, W.-L. Li, Y.-F. Li, F.-Y. Wang, M.-Y. Qi, L. Na, D.-Z. Wang, A. U. Khan, Distribution patterns, infiltration and health risk assessment of PM2.5-bound PAHs in indoor and outdoor air in cold zone, *Chemosphere* **2016**, *155*, 70.

[35] F. Wang, T. Lin, J. Feng, H. Fu, Z. Guo, Source apportionment of polycyclic aromatic hydrocarbons in $PM_{2.5}$ using positive matrix factorization modeling in Shanghai, China, *Environ. Sci.: Processes Impacts* **2015**, *17*, 197.

[36] Y. Lin, Y. Ma, X. Qiu, R. Li, Y. Fang, J. Wang, Y. Zhu, D. Hu, Sources, transformation, and health implications of polycyclic aromatic hydrocarbons (PAHs) and their nitrated, hydroxylated, and oxygenated derivatives in fine particulate matter ($PM_{2.5}$) in Beijing, J. Geophys. *Res.: Atmospheres* **2015**, *120*, 7219.

[37] J. Ma, Z. Chen, M. Wu, J. Feng, Y. Horii, T. Ohura, K. Kannan, Airborne $PM_{2.5}$/PM_{10}-associated chlorinated polycyclic aromatic hydrocarbons and their parent compounds in a suburban area in Shanghai, China, *Environ. Sci. Technol.* **2013**, *47*, 7615.

[38] W. Wang, N. Jariyasopit, J. Schrlau, Y. Jia, S. Tao, T.-W. Yu, R. H. Dashwood, W. Zhang, X. Wang, S. L. M. Simonich, Concentration and Photochemistry of PAHs, NPAHs, and OPAHs and Toxicity of $PM_{2.5}$ during the Beijing Olympic Games, *Environ. Sci. Technol.* **2011**, *45*, 6887.

B 7 Supporting Information

Paper B: Interaction between $PM_{2.5}$ airborne pollutants and third bodies

Index

Figure S1. Example of the AFM panel for statistical analysis

Figures S2. Small particles in-situ collected on silicon substrate

Figures S3. Chemical composition between $PM_{2.5}$ particles with and without trace

Example of the AFM panel to statistically analyze $PM_{2.5}$ size transferred on Si

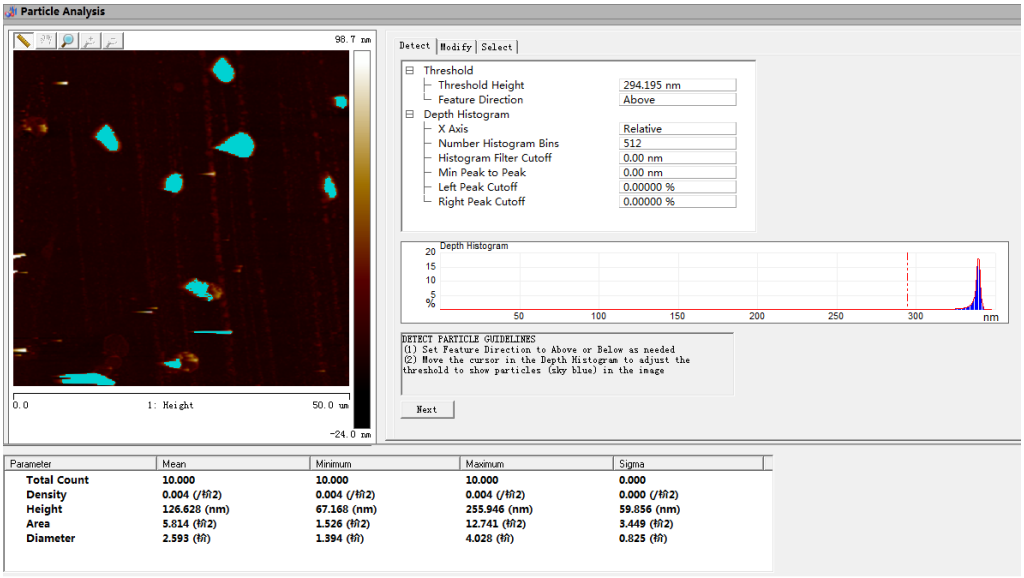

Figure S1. Example of an AFM analysis process shows the typical aspect of the processed images, with areas above a threshold height highlighted in blue. The threshold height was selected to be 10 nm above the most repeated value of the image histogram, which represents the average height of the silicon substrate. In total, 217 particles in different images were analyzed. The scan size of the image is 50 × 50 μm.

Small particles in-situ collected on silicon substrate

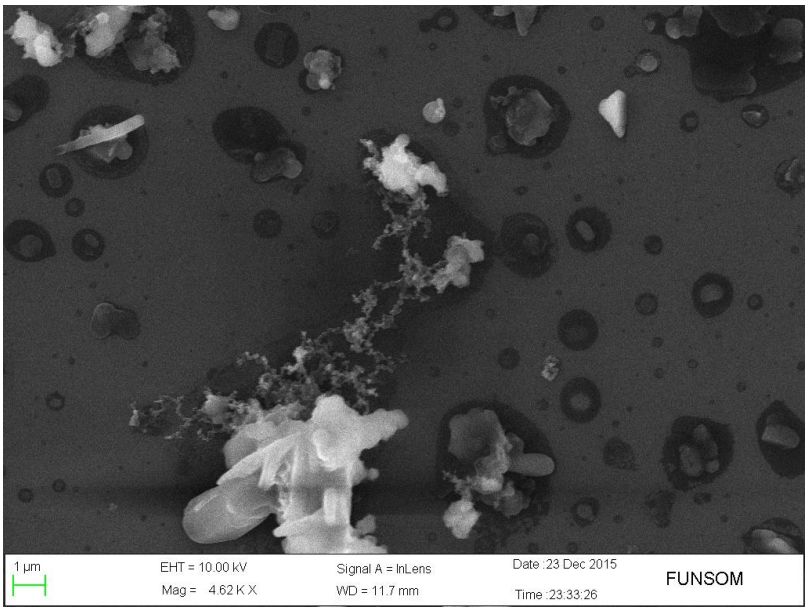

Figure S2. SEM image of the in-situ collected particles on the 300 nm SiO_2/Si wafers. Unlike after particle transfer, a large density of small particles has been observed to gather together on the SiO_2/Si wafers. The image here is an example of the small particles surrounded by the dark layers that may be related to liquid particles.

Chemical composition between $PM_{2.5}$ particles with and without trace

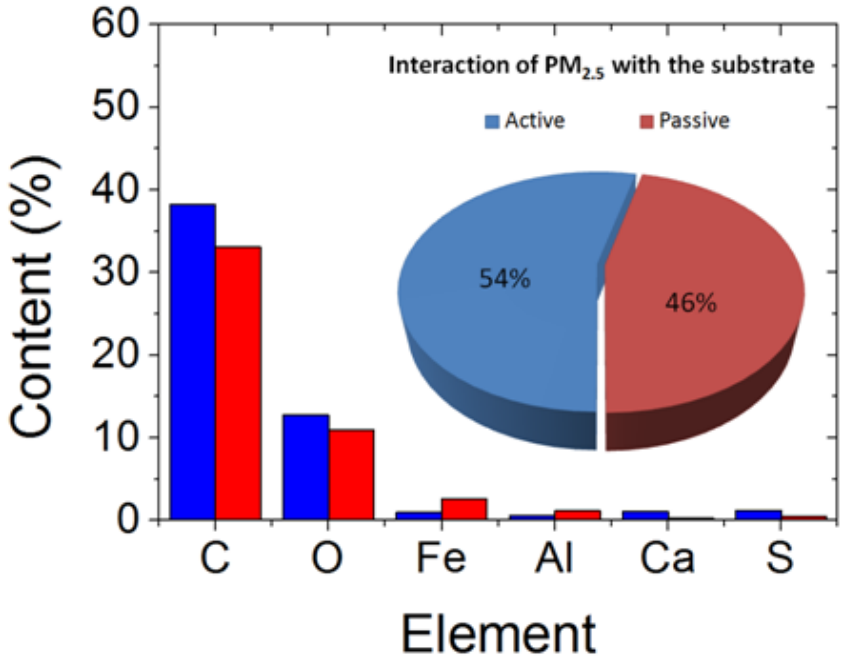

Figure S3. EDX Chemical composition histogram of the particles with trace (active) and without trace (passive); no clear chemical composition difference between the two groups has been observed.

References:

[1] J. Qiu, Fight against smog ramps up, *Nature* **2014**, *506*, 273.

[2] K. A. Miller, D. S. Siscovick, L. Sheppard, K. Shepherd, J. H. Sullivan, G. L. Anderson, J. D. Kaufman, Long-term exposure to air pollution and incidence of cardiovascular events in women, *N. Engl. J. Med.* **2009**, *356*, 447.

[3] P. G. Satsangi, S. Yadav, Characterization of $PM_{2.5}$ by X-ray diffraction and scanning electron microscopy–energy dispersive spectrometer: its relation with different pollution Sources, *Int. J. Environ. Sci. Technol.* **2014**, *11*, 217.

[4] T. Ancelet, P. K. Davy, W. J. Trompetter, A. Markwitz, D. C. Weatherburn, Carbonaceous aerosols in an urban tunnel, *Atmos. Environ.* **2011**, *45*, 4463.

[5] Y. Chen, N. Shah, F. E. Huggins, G. P. Huffman, W. P. Linak, C. A. Miller, Investigation of primary fine particulate matter from coal combustion by computer-controlled scanning electron microscopy, *Fuel Process. Technol.* **2004**, *85*, 743.

[6] D. Majumdar, S. P. M. P. William, Chalk dustfall during classroom teaching: particle size distribution and morphological characteristics, *Environ. Monit. Assess.* **2009**, *148*, 343.

[7] Z. Li, S. Zhao, R. Edwards, W. Wang, P. Zhou, Characteristics of individual aerosol particles over Ürümqi Glacier No. 1 in eastern Tianshan, central Asia, China, *Atmos. Res.* **2011**, *99*, 57.

[8] U. Fernandes, M. Costa, Particle emissions from a domestic pellets-fired boiler, *Fuel Process. Technol.* **2012**, *103*, 51.

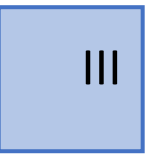

IV

Chapter 4:

Cheap metal oxides functionalized silicon photoanodes for photoelectrochemical water splitting

---

In this chapter, low cost metal (Cu and Ni) have been deposited on the earth abundant silicon photoanodes, which can form CuO and NiO_X and then serve as a protection layer for the silicon surface and also water oxidation catalyst. The stability and ageing mechanism of these photoanodes has been statistically analyzed. And after understanding the ageing mechanism, the interface between the metal oxides catalyst and silicon photoanodes has been engineered to reduce the overpotential for water oxidation reaction.

The chapter consist of the following independent papers:

Paper C Y. Shi, C. Gimbert-Suriñach, T. Han, S. Berardi, M. Lanza, A. Llobet, *ACS Appl. Mater. Interfaces* **2015**, *8*, 696.

Paper D T. Han[†], Y. Shi[†], X. Song, A. Mio, L. Valenti, F. Hui, S. Privitera, S. Lombardo, M. Lanza, *J. Mater. Chem. A*, **2016**, *4*, 8053. ([†] Equal Contribution)

Paper E Y. Shi, T. Han, C. Gimbert-Suriñach, X. Song, M. Lanza, A. Llobet, *J. Mater. Chem. A*, **2017**, *5*, 1996.

IV

Paper C: CuO functionalized silicon photoanodes for photoelectrochemical water splitting devices

Y. Shi, C. Gimbert-Suriñach, T. Han, S. Berardi, M. Lanza, A. Llobet, *ACS Appl. Mater. Interfaces* **2015**, 8, 696.

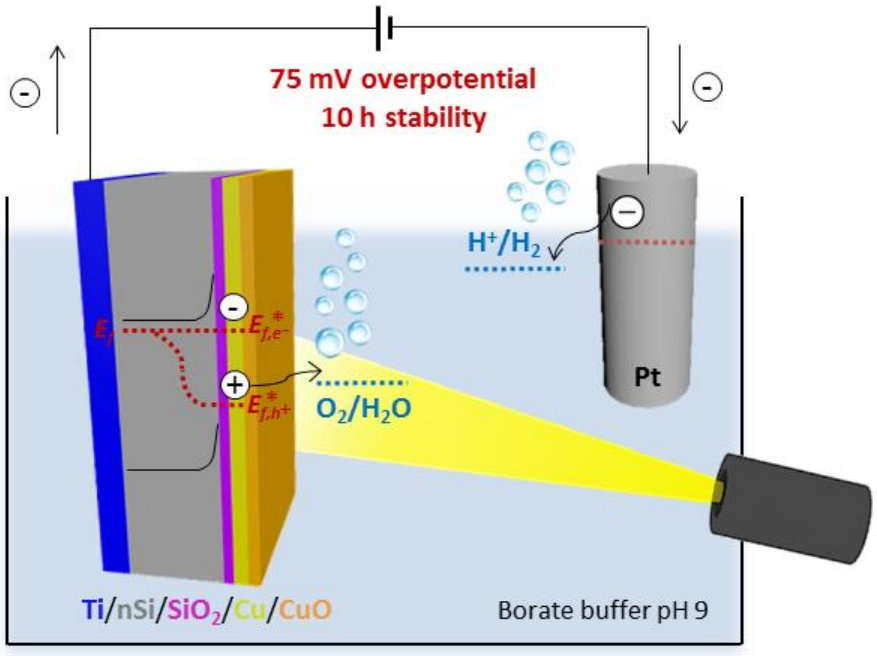

Abstract

One of the main difficulties for the technological development of photoelectrochemical (PEC) water splitting (WS) devices is the synthesis of active, stable and cost-effective photoelectrodes that ensure high performance. Here we report the development of a CuO/Silicon based photoanode, which shows an onset potential for the water oxidation of 0.53 V vs. SCE at pH 9, that is, an overpotential of 75 mV, and high stability above 10 hours. These values account for a photovoltage of 420 mV due to the absorbed photons by silicon, as proven by comparing with analogous CuO/FTO electrode that are not photoactive. The photoanodes have been fabricated by sputtering a thin film

of Cu^0 on commercially available n-type Si wafers, followed by a photoelectrochemical treatment in basic pH conditions. The resulting CuO/Cu layer acts as: (i) protective layer to avoid the corrosion of nSi, (ii) p-type hole conducting layer for efficient charge separation and transportation, and (iii) electrocatalyst to reduce the overpotential of the water oxidation reaction. The low cost, low toxicity and good performance of CuO-based coatings can be an attractive solution to functionalize unstable materials for solar energy conversion.

Contribution

Yuanyuan Shi deposited the metal films for fabricating the photoanodes, performed the photoelectrochemical and spectroscopic analysis and prepared the manuscript.

C 1 Introduction

Photoelectrochemical (PEC) cells exploit the built-in potential generated at semiconductor-liquid junctions under illumination to drive uphill chemical reactions, such as the splitting of water (Eq. 1), which can be used to produce hydrogen fuel in a clean manner.[1] The transformation of sunlight into chemical energy via the formation of new chemical bonds is attractive because it allows solar energy to be stored and transported.[2] The overall electrochemical water splitting can be divided in two half reactions, the reduction and oxidation, also named hydrogen evolution reaction (HER, Eq.2) and oxygen evolution reaction (OER, Eq. 3), respectively:

Overall water splitting: $2H_2O \rightarrow O_2 + 2H_2$ ($\Delta E = 1.23$ V) (Eq. 1)

HER: $2H^+ + 2\ e^- \rightarrow H_2 \uparrow$ ($E^0_{red} = 0.00$ V vs. NHE) (Eq. 2)

OER: $2H_2O + 4h^+ \rightarrow O_2 \uparrow + 4H^+$ ($E^0_{ox} = -1.23$ V vs. NHE) (Eq. 3)

where the redox potential values are reported versus the normal hydrogen electrode, NHE. The OER is considered the bottleneck of the overall process, being thermodynamically and kinetically demanding. Thus, enormous research efforts have been invested on developing efficient photoanodes for the OER, to be coupled, in a possible water spitting PEC device, to a dark Pt cathode, performing the HER (Figure 1). Several kinds of photoanodes have been used in this PEC set-up, including metal oxide semiconductors (Fe_2O_3, WO_3, $BiVO_4$, …), group III-V semiconductors (GaAs, GaP, InP, …) and amorphous silicon, all being excellent light absorbers and in most of the cases with good carrier mobility.[3-5] Among them, silicon is a particularly interesting candidate due to its low cost and good ability to absorb light. Unfortunately, silicon is only able to produce modest photocurrent densities of some $\mu A/cm^2$, which decay very fast (in the minutes time scale) due to premature corrosion.[6] The reason is that the thermodynamic oxidation potential of Si is less positive than that of water oxidation (1.23

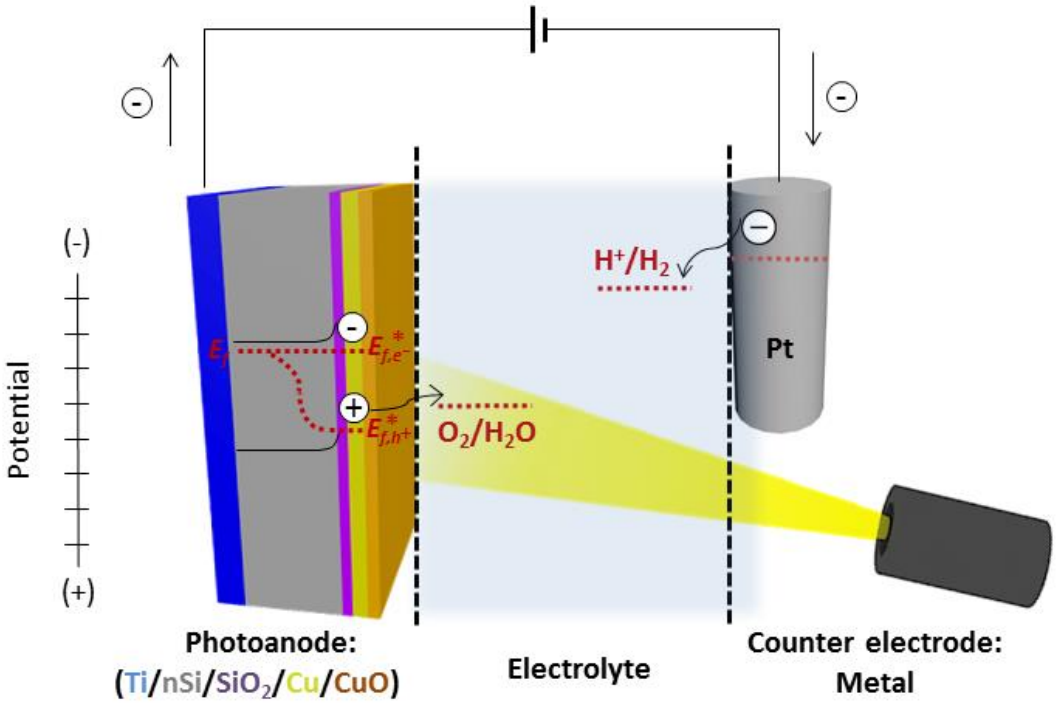

Figure 1. Scheme of the PEC cell developed in this work. The cell consists on a Cu-protected nSi photoanode connected to a Pt counter electrode through a potentiostat. When the sunlight illuminates the surface of the photoanode, it induces charge separation. The photogenerated holes migrate to the surface and are used to produce O2 from water. At the same time, the electrons promoted to the conduction band move to the counter electrode to reduce protons to hydrogen.

V vs. NHE at pH 0), thus making it susceptible to self-oxidation when interfaced with aqueous electrolytes.[7] Therefore passivating the surface of silicon with a cheap coating that can serve as corrosion-resistant and water oxidation catalyst (WOC) has become one of the main challenges in this field.[8-16] Among all candidate materials, TiO_2 has shown outstanding performance in protecting Si and other III-V materials from oxidation,[4] but in those cases an additional WOC layer (film) is needed to boost the PEC reaction. Superstructures made of Ir/TiO_2[17] have shown water oxidation activity and stability in acid and basic conditions, while NiO_X/TiO_2[4] achieved even larger current densities, but only at pH 14. In fact, Ni-based coatings can be used as both anti-corrosion and WOC simultaneously. For example, Kenney et al.[18] evaporated a 2 nm Ni layer on a silicon wafer (with its native oxide), leading to inexpensive Ni/SiO_2/nSi photoanodes with

extraordinary activity at pH 14 and enhanced stability at pH 9.5. Mei et al.[19] deposited Fe-modified NiO_x films on np+-Si junctions (which notably enhance charge separation) and achieved continuous OER during 300 hours. Recently Lewis' group overcame that performance using 35-160 nm thick NiO_x coatings on np+-Si and achieved continuous OER during more than 50 days at pH 14.[20] Even though these devices show higher activity, the cost of these photoanodes is still high, as the fabrication of the np+ junction requires both implementation and thermal processes.

Due to its low cost and toxicity, copper is an attractive material from an industrial perspective, but its use in photoanodes for PEC WS-devices has never been reported. Recent advances showed that copper oxides,[21-25] as well as molecular copper complexes,[26-29] can be used to catalyse the electrocatalytic water oxidation reaction. Sun and coworkers[21] reported a continuous OER over 10 hours at pH 9 using a copper oxide catalyst electrodeposited on fluorine doped tin oxide (FTO), and a similar performance was achieved by Meyer and coworkers[22] by forming a CuO film on the surface of a Cu foil, but in both cases the water oxidation reaction was induced by applying a high external voltage. In this work, we report copper-based photoanodes for water oxidation that have been fabricated from Cu films sputtered on nSi photoanodes. The resulting devices work at very low overpotential (η = 75 mV) and show good stability (10 hours) at pH 9. These findings point out the possibility of using copper-based composites as a promising photoanode for PEC-WS devices.

C 2 Experimental

Sample preparation

All reagents were purchased from Aldrich unless otherwise stated. The fluorine doped tin oxide (FTO) coated glass was purchased from XopFisica (thickness, 2.3-3.0

mm; visible transmittance, 80-81.5%; resistance, 6-9 Ω/cm^2). Before the deposition and characterization tests, the FTO-coated glass was ultrasonically cleaned in water containing a cleaning detergent (Hellma), deionized water and ethanol, for 10 minutes each. Standard single side polished, single crystal and phosphorous-doped [100] n-type silicon wafers (0.3-0.5 Ω•cm) were purchased from ProLog. Before all the deposition processes, the Si wafers were cleaned with acetone, ethanol and deionized water in an ultrasonic bath, for 10 minutes each. Cu^0 films with thicknesses of 5, 10, 15, 20 and 25 nm were deposited onto both FTO-coated glass and nSi photoanodes in the same vacuum chamber, by means of sputtering (ATC Orion 8-HV instrument, AJA International) at 100 W, with a deposition rate of 1.6 Å/s for 40, 80, 120, 160 and 200 s, respectively. An ohmic contact of 20 nm titanium was previously deposited onto the backside of the nSi wafers by e-beam evaporation (PVD75 Kurt J. Lesker). Copper tape was used to contact the working electrodes for electrochemical and PEC experiments.

Sample characterization

All the samples were tested at room temperature in a standard three-electrode configuration with saturated calomel electrode (SCE, saturated KCl) or Hg/Hg_2SO_4 (saturated K_2SO_4) reference electrodes and Pt wire as the counter electrode, using CHI 660D or CHI 660E potentiostats (CH Instruments, Inc.). The FTO samples were tested in a 20 mL one-compartment glass cell, and the nSi photoanodes in a 140 mL teflon cell, the areas exposed to OER were of ~1.0 and ~0.45 cm^2, respectively. In order to quantify the amount of O_2 produced, a two-compartment cell (in which anodic and cathodic sides are separated by a glass frit) was used. In this set-up, the Cu-coated nSi photoanodes were used as the working electrodes, Ag/AgCl (saturated KCl) as the reference and a Pt mesh as the counter electrode. All the cyclic voltammetry (CV) scans were collected with *i*R

compensation at a scan rate of 100 mV/s, while the current density versus time traces were obtained without *i*R compensation. For comprehensive comparison, all redox potentials reported herein will be referenced versus SCE. The experimental onset potential values reported in this paper have been taken at a current density of *ca.* 1 mA/cm^2. An oxygen sensitive OXNP15121 Clark electrode (Unisense) was used to measure the photoproduced O_2 under air, and in turn to calculate the Faradaic efficiency. The electrolyte consisted of 0.2 M borate buffer solution (pH 9), obtained by mixing a 0.05 M $Na_2B_4O_7$ solution and a 0.2 M H_3BO_3 solution in a ratio of 8:2 (v/v). All pH values were measured with a HI 4222 pH-meter (Hanna Instruments) using a calibrated Crison 5029 electrode (Crison Instruments). For the PEC characterization of the photoanodes, illumination was provided by 150 W Xe Arc Lamps (LS-150, ABET technology and 66906, Newport Corporation), equipped with a UV-light cut-off filter (λ < 400 nm) and calibrated to 1 sun (100 mW/cm^2) using a calibrated silicon photodiode at 25 °C. UV-Vis characterizations were performed using a Cary 50 (Varian) spectrophotometer. The morphological characterization of the samples was performed by means of Transmission Electron Microscopy (TEM, JEOL, model 1011) and Scanning Electron Microscopy (SEM, FEI Quanta 200FEG). The chemical composition of the samples was analyzed by X-ray Photoelectron Spectroscopy (XPS), using a KRATOS Axis ultra-DLD spectrometer equipped with a monochromatic Al Kα X-ray source ($h\nu$ = 1486.6 eV). The XPS analyzer uses hybrid magnification mode (both electrostatic and magnetic) and the take-off angle is 90°. Under slot mode, the analysis area is 700×300 µm. Analysis chamber pressure is less than 5×10^{-9} Torr. Pass energy of 80 eV and 20 eV are normally used for survey spectra and narrow scan spectra, respectively. The energy step size of 1 eV and 0.1 eVwere chosen for survey spectra and narrow scan spectra, respectively. In addition, binding energy range for a survey spectra is 0-1200 eV. The X-ray source power

is 75 W and 75-150 Wfor acquring survey spectrum and narrow scan spectra, respectivey.

C 3 Results and discussion

Copper films on FTO: electrocatalytic water oxidation

Metallic copper films of different thicknesses (from 5 to 25 nm) were sputtered on FTO substrates. The TEM images of the films show that the films are not homogeneous and that the surface morphology depends on their thickness; the thinner Cu films appear to be rougher than the thicker ones (Figure S1). The electrocatalytic water oxidation ability of the sputtered copper electrodes was tested in 0.2 M borate buffer solution at pH 9. Unless otherwise stated, all the reported electrochemical measurements were performed in this electrolytic solution. As shown in Figure 2a, regardless of their thickness, all the electrodes show similar onset potentials for the water oxidation reaction at 0.95 V vs. SCE (η = 495 mV), ~300 mV lower than that of the bare FTO. Current densities up to 7.5 mA/cm^2 were obtained at 1.1 V vs SCE. Similar results in terms of onset potential and Tafel plot slopes have been reported for other active CuO films, prepared using electrodeposition techniques, suggesting that the copper oxide active species may have similar performances (Figure S2 and Table S1).[21-22,24-25]

The stability of the generated CuO/Cu/FTO electrodes was assessed by means of successive CV scans, as well as by controlled potential electrolysis (CPE) at 1.1 V vs. SCE (Figures 2b and S4a). In particular, Figure 2b shows the remarkable stability of a 15 nm-thick CuO/Cu/FTO electrode. This sample maintains 80% of its activity after 12 hours of continuous OER. The small current decay observed is likely due to a loss of Cu^{2+} in solution, as shown by both electrochemical experiments on the electrolytic solution at the end of the CPE experiment (Figure S3) and UV-Vis spectroscopy before and after 1 hour of CPE at 1.1 V vs. SCE (Figure S4b). The ability of the films to oxidize water, together

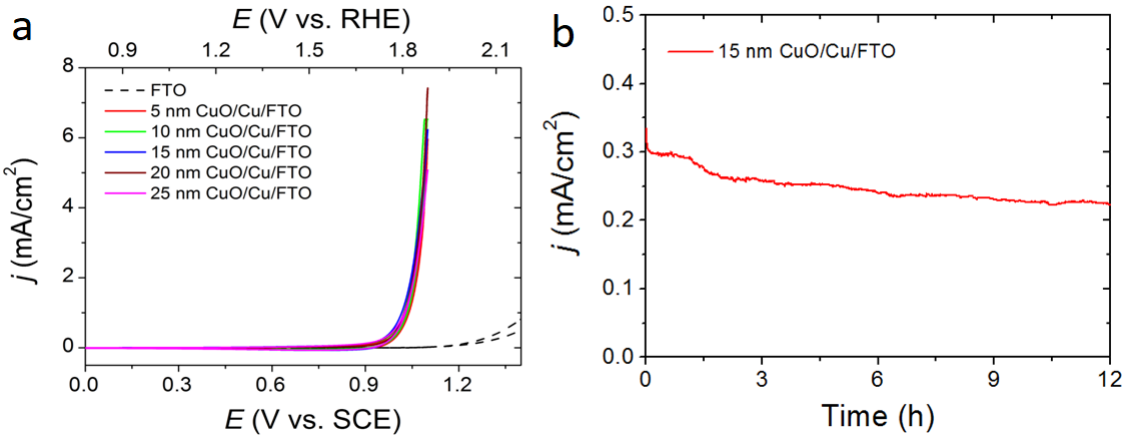

Figure 2. Electrochemical water oxidation performances of CuO/Cu/FTO electrodes. (a) CVs of bare FTO (dashed black curve) and 5, 10, 15, 20 and 25 nm-thick Cu/FTO in 0.2 M borate buffer solution (pH 9). All the CV scans were obtained with iR compensation by using a SCE reference electrode and Pt counter electrode at a scan rate of 100 mV/s. (b) Current density traces obtained by controlled-potential electrolysis (CPE) at 1.1 V vs. SCE (without iR compensation) for a 15 nm CuO/Cu/FTO electrode in 0.2 M borate buffer solution (pH 9).

with their good stability and transparency is further evidence that the thin sputtered Cu layer can act as an anti-corrosion and WOC film.

Copper films on nSi: photoelectrocatalytic water oxidation

Copper-coated nSi photoanodes were prepared by sputtering technique using the same methodology and parameters employed to prepare the Cu/FTO electrodes. The native SiO_2 on the nSi wafer was not etched, as it can serve as adhesive layer,[18] and a layer of 20 nm Ti was evaporated on the back side of the nSi wafer, leading to $Cu/SiO_2/nSi/Ti$ photoanodes. In total, nSi photoanodes with three different Cu^0 thicknesses (5, 10 and 15 nm) were prepared, avoiding thicker films, which can hinder the photon absorption by silicon. The current-density versus potential (*J*-*V*) plots in Figure 3a obtained from CV scans for the as-grown 5 nm $Cu/SiO_2/nSi/Ti$ photoelectrodes show very low activity and a large onset potential (~0.71 V vs. SCE). However, these Cu-coated nSi photoanodes can be activated by performing either (i) several CV scans in a larger

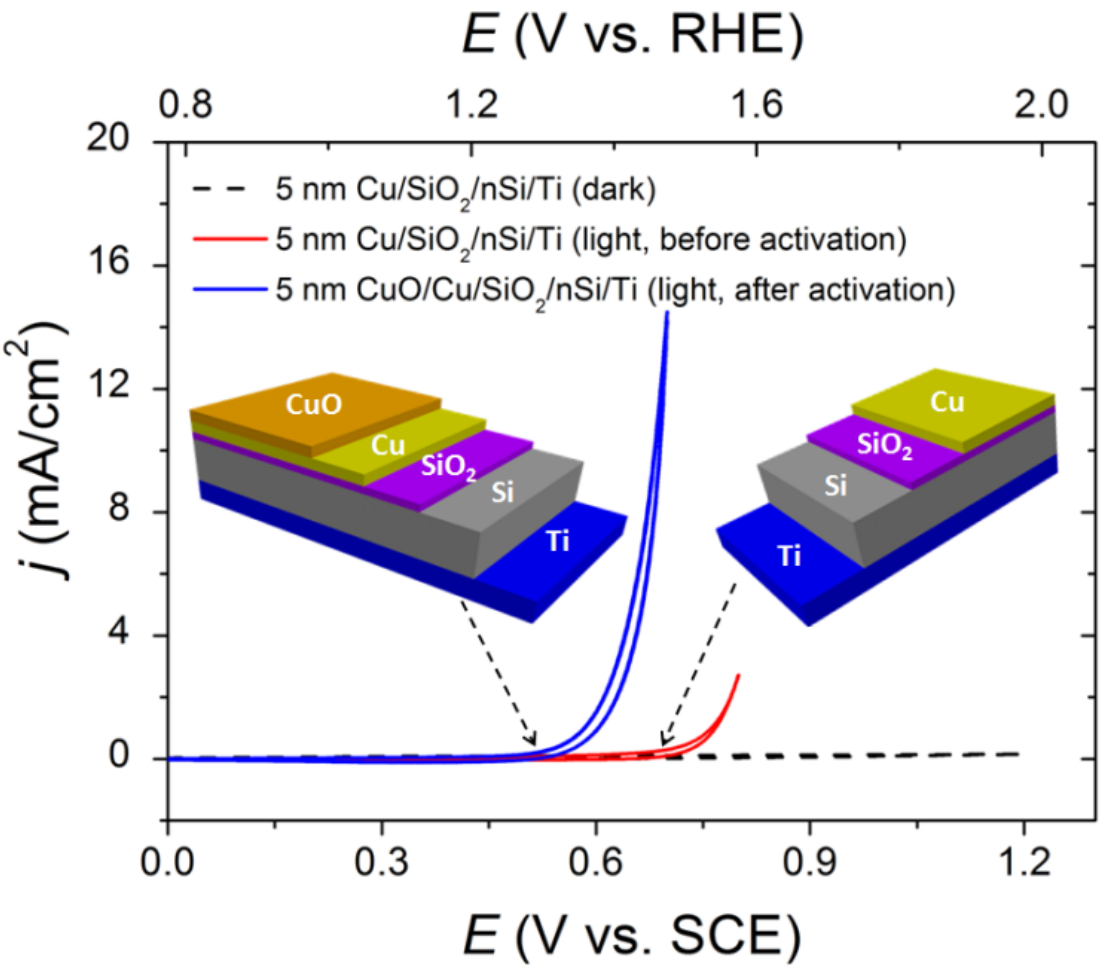

Figure 3. Activation of the $Cu/SiO_2/nSi/Ti$ photoanodes: CV scans of 5 nm $Cu/SiO_2/nSi/Ti$ before (red solid line) and after (blue solid line) activation under 1 sun illumination (see main text for activation details). The trace obtained in dark conditions is also reported (dashed black line). The CVs were obtained with iR compensation using a Pt counter electrode and Hg/Hg_2SO_4 reference electrode at a scan rate of 100 mV/s in 0.2 M borate buffer solution (pH 9). Insets: two 3D schematic representations, illustrating the activation process on the $Cu/SiO_2/nSi/Ti$ photoanodes. The activation of the photoanode may be related to the formation of CuO on Cu layer.

potential range (from -0.4 V to 0.8 V vs. SCE), (ii) chopped light linear sweep voltammetry (LSV) in the range from -0.4 to 0.9 V vs. SCE, or (iii) short or long time amperometric, current versus time (*I*-t) experiments (Figure S5). After the activation process, a significant shift of the onset potential for the OER (from ~0.71 V to ~0.53 V vs. SCE) and a remarkable increase of the current density (up to 14.5 mA/cm^2) can be obtained (compare red and blue lines in Figure 3). The mechanism of the activation process for the $Cu/SiO_2/nSi/Ti$ photoanodes is complex, possibly involving both soluble

and insoluble products and multiple formal oxidation states (Cu^{I}, Cu^{II}, Cu^{III}, and/or Cu^{IV} species) depending on the applied potential.[22,30,31] Two three-dimensional (3D) schematic representations of the electrode configuration are shown in the inset of Figure 3, indicating that the activation of the photoanodes may be related to the formation of CuO on the Cu layer, which may act as a p-type hole conducting layer to help the charge separation and transportation of holes to the electrode surface where the water oxidation catalysis take place.

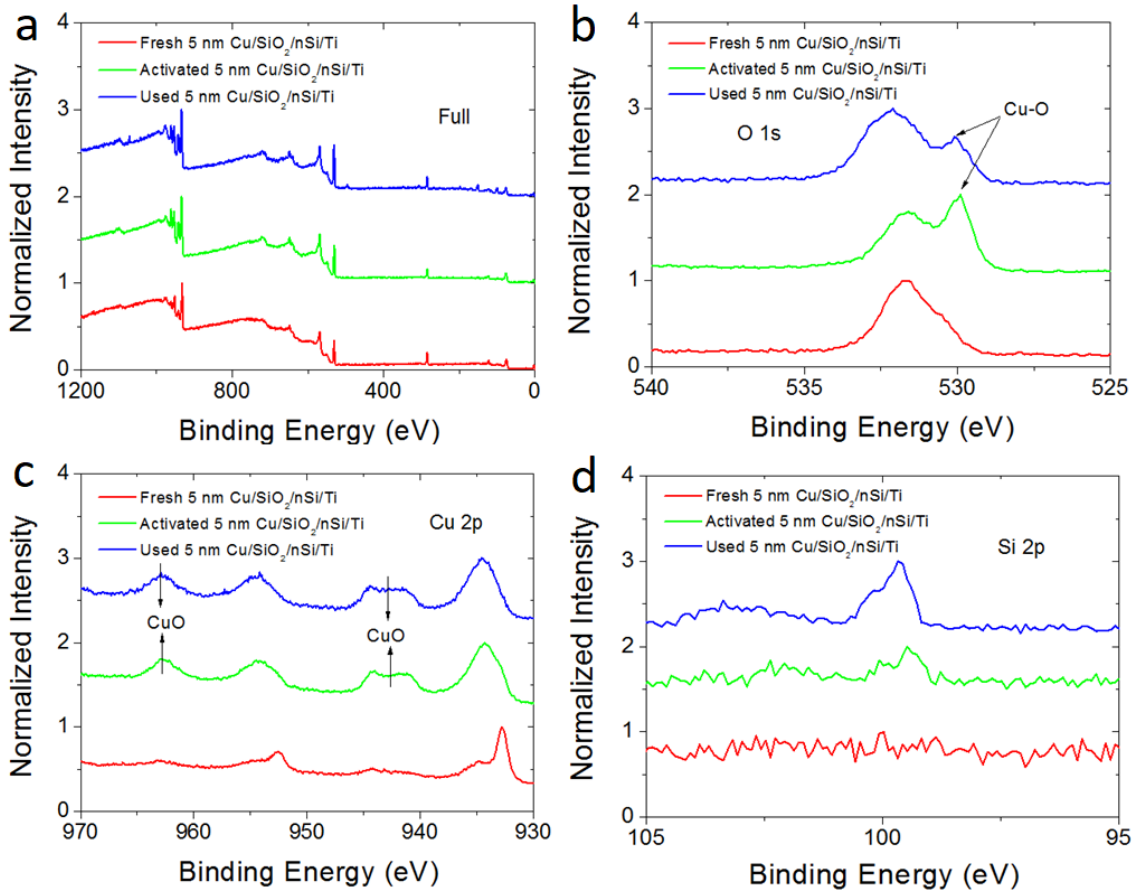

Figure 4. (a) Overall XPS spectra of 5 nm Cu/nSi/SiO_2/Ti. Fresh sample (red), activated sample (green), degraded sample (blue). (b)-(d) XPS binding energy regions of O 1s, Cu 2p and Si 2p, respectively

In order to identify the changes induced during the activation process, the chemical composition of the 5 nm Cu/SiO_2/nSi/Ti photoanodes was analyzed by means of XPS. Figure 4 shows the XPS peaks of O 1s, Cu 2p and Si 2p for the as-grown (red

lines), activated (green lines) and used (blue lines) samples. The term "used" refers to a fresh 5 nm Cu/SiO_2/nSi/Ti photoanode that was exposed to 20 hours CPE at 0.8 V vs. SCE under 1 sun illumination (Figure S10a). As reference, the wide binding energy regions of the samples are also exhibited in Figure 4a. The O 1s binding energy region of fresh samples (red trace in Figure 4b) shows just one component at 532 eV, corresponding to the oxygen on the surface.[32] This feature confirms the presence of a metallic copper component, since metallic Cu is reported to attract oxygen to the surface.[32] After the activation process a new peak at 529 eV was observed, which can be attributed to the CuO formation but also to a SiO_2 component that may be exposed to the XPS analysis after the activation treatment (green trace in Figure 4b).[32] On the other hand, in the Cu 2p binding energy region, the as-grown samples show two peaks at 932.7 eV and 952.6 eV (red trace in Figure 4c), respectively assigned to 2p3/2 and 2p1/2 binding energies of Cu^0 metal.[33,34] After the activation process, the 2p peaks shift to 934.4 eV and 954.2 eV (green trace in Figure 4c), indicating the oxidation of copper to higher oxidation states, consistent with the characteristic peaks[33,34] of CuO (green and blue traces in Figure 4c), as already pointed out by the analysis of the O 1s region, and also reported for copper foils electrochemically exposed to high positive potentials, previously reported in the literature.[22] Finally, the clear appearance of the Si peak[35] in the spectrum of the used sample further supports that the decrease in activity observed in these photoanodes may be related to partial loss of the CuO film (blue trace in Figure 4d). The reported XPS analyses are fully reproducible, and similar results have been obtained for the 10 and 15 nm thick counterparts (Figures S6 and S7). Interestingly, analogous XPS analysis of related CuO/Cu/FTO electrodes show that these electrodes don’t need the activation process but the CuO layer forms right after the metallic copper is deposited on the FTO plates (Figure S8).

IV

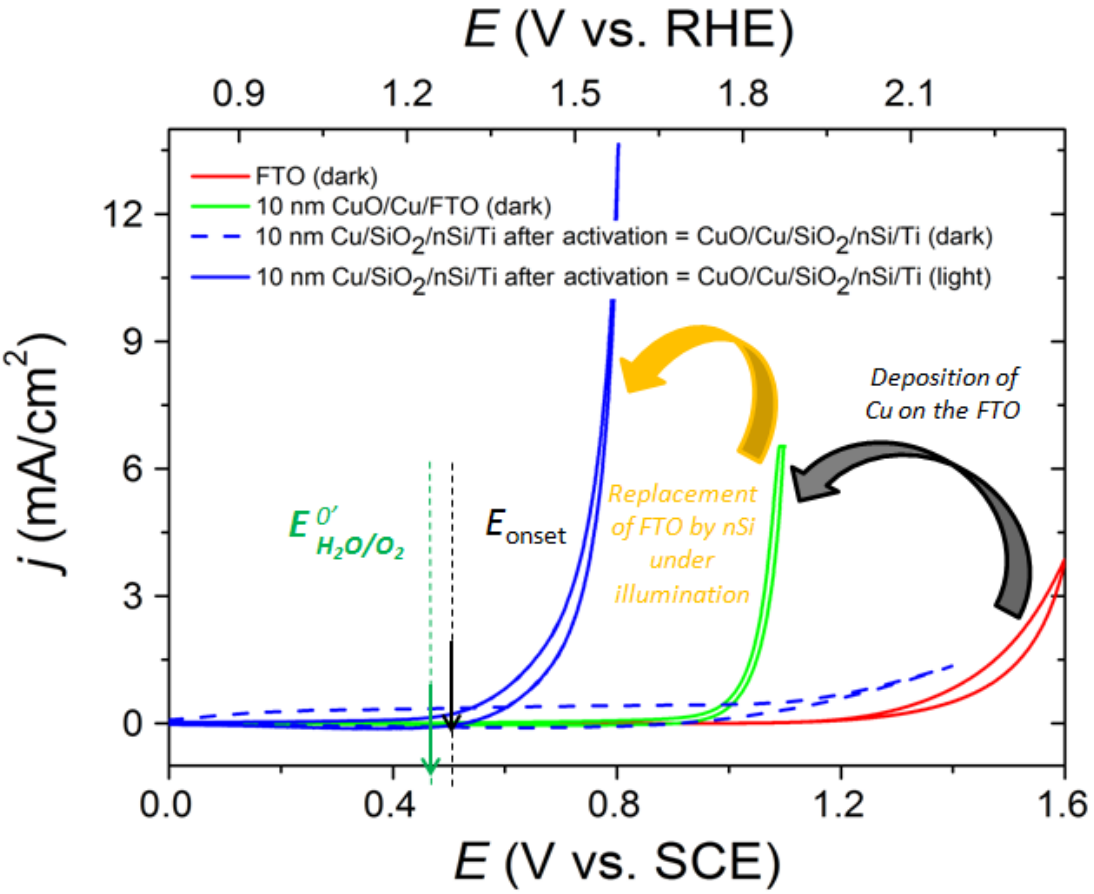

Figure 5. Comparison of the onset potential for the water oxidation reaction by the different (photo) electrodes prepared in this work. Bare FTO (red line); 10 nm-thick CuO/Cu/FTO (green line); activated 10 nmCuO/Cu/SiO_2/nSi/Ti in the dark (dashed blue line) and under 1 sun illumination (solid blue line). All the CVs were recorded using a Pt mesh as the counter electrode and a SCE or Hg/Hg_2SO_4 as the reference electrode, with iR compensation at a scan rate of 100 mV/s in a 0.2 M borate buffer solution (pH 9).

Figure 5 summarizes the *J-V* plots of electroactive CuO/Cu/FTO and photoelectroactive CuO/Cu/SiO_2/nSi/Ti electrodes obtained after activation of a 10 nm copper film in both cases. As it can be observed, the effect of the CuO/Cu film on the FTO produces a remarkable decrease of the onset potential for OER compared to the bare FTO electrode (~300 mV, from 1.25 V to 0.95 V vs. SCE, compare red and green traces). On the other hand, when the CuO film is deposited on the SiO_2/nSi/Ti substrate after the activation process, a remarkable further onset potential reduction of ~420 mV is achieved under illumination, leading to an absolute value of 0.53 V vs. SCE. This represents an impressive overpotential of 75 mV with regard to the thermodynamic value for the water

oxidation reaction. These values are in the range of the best reported results on n-type silicon based photoanodes made of iridium,[17] nickel[4,18-20] or iron[36] but are still 0.2-0.3 V above the onset potentials of np^+-type silicon modified with nickel oxide catalysts.[4,19,20] Additional advantages of the CuO/Cu/SiO_2/nSi/Ti electrodes reported here include the low price and low toxicity of copper and the use of n-type silicon, whose fabrication and implementation are well established. No difference in the performance of the CuO/Cu/FTO electrode was observed under light or dark illumination (Figure S9), indicative for negligible photoactivity induced by the CuO layer, that is, the observed photovoltage (solid and dashed blue lines) is induced uniquely by the silicon light absorption.

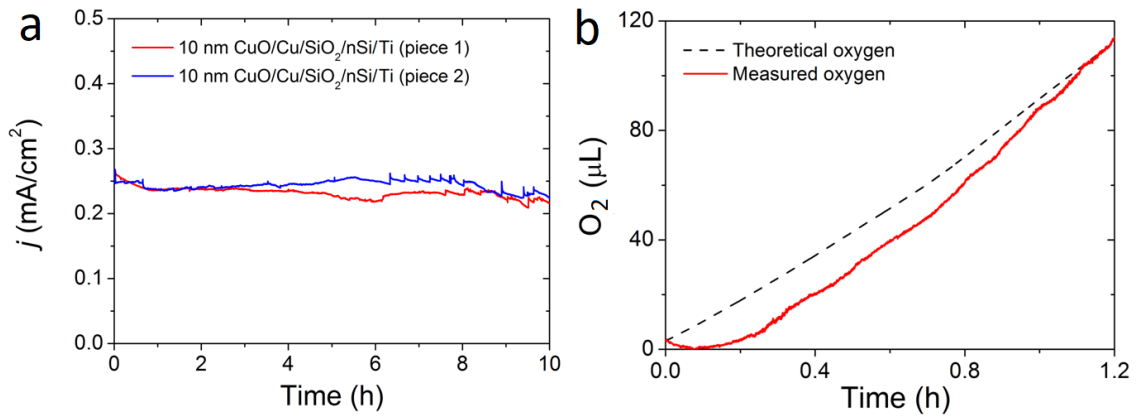

Figure 6. Stability and faradaic efficiency of the activated 10 nm CuO/Cu/SiO_2/nSi/Ti photoanodes. (a) Current density versus time traces obtained by controlled potential electrolysis at 0.8 V vs. SCE on two different10 nm Cu/SiO_2/nSi/Ti photoanodes in 0.2 M borate buffer (pH 9) under 1 sun illumination, showing good reducibility. (b) Oxygen evolution trace (red solid line) measured with an activated 10 nm Cu/SiO_2/nSi/Tiin 0.2 M borate buffer (pH 9) at 0.85 V vs. SCE, under 1 sun illumination. From the measured and the theoretical (black dashed line) oxygen amounts, a ~100 % faradaic efficiency can be calculated. Both (a) and (b) were obtained without iR compensation, illuminated by a simulated 1 sun and using a Pt mesh as counter electrode. A one-compartment cell made of Teflon and a SCE reference electrode were used for tracing the current density versus time (a) and a two-compartments glass cell and a Ag/AgCl reference electrode were used for the oxygen detection experiment (b).

The long-term stability of the produced photoanodes was tested by means of CPE experiments at 0.8 V vs. SCE. Figure 6a shows the current density traces obtained for two activated 10 nm CuO/Cu/SiO_2/nSi/Ti photoanodes, showing excellent reproducibility and

negligible variability. Once activated, both photoanodes are stable for 10 hours at a constant current density of 0.24 mA/cm^2 under PEC conditions. The overall (≥ 20 hours) CPE plots for 5, 10 and 15 nm-thick Cu/SiO_2/nSi/Ti photoanodes indicate that the activation process (i.e. the formation of the CuO film) is needed for all Cu thicknesses, and that thicker films need a longer activation process (Figure S10). The activation of the photoanodes takes place in a characteristic two-steps process: (i) a reduction of the initial current, probably related to a decreased conductivity associated to the formation of species at intermediate oxidation states, *e.g.* Cu^{I} or Cu^{II}, from metallic Cu that are not active for the water oxidation reaction; and (ii) a current increase related to the formation of the final active CuO film that boosts the OER and generates large current intensities. After that, the performance of the photoanodes becomes stable during long periods of time (up to 10 hours). As noted above, the activation process time depends on the thickness of the starting metallic copper layer. Those samples that have thicker layers require more time for the activation process due to the presence of more copper material that needs to be oxidized from the inner layer in contact with the silicon oxide all the way to the surface in contact with the electrolyte. Both the activation process as well as the photocatalytic mechanism are complex processes that require further studies in order to get a full understanding of the overall system.

The surface of the samples has been analysed by SEM before and after the catalytic process (Figure S11). While fresh 10 nm Cu/SiO_2/nSi/Ti photoanodes display relatively flat surfaces, the same samples after 37 hours CPE tests appear to be covered by nanoparticles. However, depending on the analyzed region of the photoanode surface, a partial depletion of the number of CuO nanoparticles can be observed (e.g. in Figure S11d), confirming that material loss is the major cause of current drop after long-term stability tests of this kind of photoanodes.

Finally, in order to prove that the photocurrent observed in the CPE experiments with the CuO/Cu/SiO2/nSi/Ti photoanodes is actually due to the water oxidation reaction, a quantitative O_2 measurement was performed, using an oxygen gas sensor (Clark electrode). Figure 6b shows the O_2 evolution profile obtained with an activated 10 nm CuO/Cu/SiO_2/nSi/Ti, held at a constant potential of 0.85 V vs. SCE, under simulated 1 sun illumination. A ~100% Faradaic efficiency can be calculated considering the theoretical and actual volume of O_2 produced (respectively, black dashed and red solid lines in Figure 6b). The small delay in the experimental measurement of the evolved O_2 by the Clark electrode with regard to the measured current is due to the slow diffusion of oxygen into the membrane of the electrode sensor.

C 4 Conclusions

In conclusion, we have fabricated nSi photoanodes for PEC water splitting devices using for the first time CuO as protective layer and water oxidation catalyst at the surface of a semiconductor. The devices show high activity at an impressively low overpotential of 75 mV. Furthermore they are stable for over 10 hours under 1 sun illumination in 0.2 M borate buffer at pH 9, with Faradic efficiencies close to 100%. Compared to the copper-based FTO electrode, the CuO-coated nSi photoanode shows an onset potential decrease for the OER of 420 mV under 1 sun illumination. Finally it is important to stress here that the photoelectrodes described in the present work are made of copper that is a cheap, earth-abundant and low toxicity metal. Furthermore all the operations carried out for the construction of the photoanode are industrially compatible and could be easily scaled up for commercial applications. This work thus offers a promising solution for the generation of clean and sustainable solar fuel.

IV

C 5 Acknowledgements

This work has been partially supported by the Young 973 National Program of the Chinese Ministry of Science and Technology (grant no. 2015CB932700), Young Scientists Fund of National Natural Science Foundation of China (NSFC) (grant no. 61502326), International (Regional) Cooperation and Exchange Program of NSFC (grant no. 41550110223) and Young Scientists Fund of Basic Research from Jiangsu Government (grant no. BK20150343). The Priority Academic Program Development of Jiangsu Higher Education Institutions is also acknowledged. The MINECO (CTQ-2013-49075-R, SEV-2013-0319; CTQ-2014-52974-REDC), "La Caixa" foundation and AGAUR (2014-SGR-915) are acknowledged for financial support. C.G.S is grateful to AGAUR for a "Beatriu de Pinós" postdoctoral grant. S.B. is grateful to the ICIQ-IPMP Marie Curie COFUND Project (291787ICIQ-IPMP). M. L. acknowledges generous start-up funding from Soochow University and from the "Young 1000 Talent Program" of China. European COST actions, CM1202 and CM1205 are also gratefully acknowledged.

C 6 References

[1] N. S. Lewis, D. G. Nocera, Powering the planet: chemical challenges in solar energy utilization, *Proc. Natl. Acad. Sci. USA* **2006**, *103*, 15729.

[2] J. A. Turner, A nickel finish protects silicon photoanodes for water splitting, *Science* **2013**, *342*, 811.

[3] S. Hu, C. Xiang, S. Haussener, A. D. Berger, N. S. Lewis, An analysis of the optimal band gaps of light absorbers in integrated tandem photoelectrochemical water-splitting systems, *Energy Environ. Sci.* **2013**, *6*, 2984.

[4] S. Hu, M. R. Shaner, J. A. Beardslee, M. Lichterman, B. S. Brunschwig, N. S. Lewis, Amorphous tio2 coatings stabilize si, gaas, and gap photoanodes for efficient water oxidation, *Science* **2014**, *344*, 1005.

[5] R. Liu, Z. Zheng, J. Spurgeon, X. Yang, Enhanced photoelectrochemical water-splitting performance of semiconductors by surface passivation layers, *Energy Environ. Sci.* **2014**, *7*, 2504.

[6] A. Q. Contractor, J. O. M. Bockris, Investigation of a protective conducting silica film on n-silicon, *Electrochim. Acta* **1984**, *29*, 1427.

[7] S. Chen, L. Wang, Thermodynamic Oxidation and Reduction Potentials of Photocatalytic Semiconductors in Aqueous Solution. *Chem. Mater.* **2012**, *24*, 3659.

[8] M. G. Walter, E. L. Warren, J. R. McKone, S. W. Boettcher, Q. Mi, E. A. Santori, N. S. Lewis, Solar water splitting cells, *Chem. Rev.* **2010**, *110*, 6446.

[9] M. Pourbaix, In *Atlas of Electrochemical Equilibria in Aqueous Solutions* (National Association of Corrosion Engineers, Houston, TX, ed. 2, **1974**).

[10] H. Gerischer, Photodecomposition of Semiconductors Thermodynamics, Kinetics and Application to Solar Cells. *Faraday Discuss. Chem. Soc.* **1980**, *70*, 137.

[11] K. Sivula, Metal Oxide Photoelectrodes for Solar Fuel Production, Surface Traps, and Catalysis. *J. Phys. Chem. Lett.* **2013**, *4*, 1624.

[12] B. Klahr, S. Gimenez, F. Fabregat-Santiago, J. Bisquert, T. W. Hamann, Photoelectrochemical and impedance spectroscopic investigation of water oxidation with "co-pi"-coated hematite electrodes, *J. Am. Chem. Soc.* **2012**, *134*, 16693.

[13] T. Hisatomi, F. Le Formal, M. Cornuz, J. Brillet, N. Tétreault, K. Sivula, M. Grätzel, Cathodic shift in onset potential of solar oxygen evolution on hematite by 13-group oxide overlayers, *Energy Environ. Sci.* **2011**, *4*, 2512.

[14] M. Liu, C. Y. Nam, C. T. Black, J. Kamcev, L. Zhang, Enhancing water splitting activity and chemical stability of zinc oxide nanowire photoanodes with ultrathin titania shells, *J. Phys. Chem. C* **2013**, *117*, 13396.

[15] Z. Li, W. Luo, M. Zhang, J. Feng, Z. Zou, Photoelectrochemical cells for solar hydrogen production: current state of promising photoelectrodes, methods to improve their properties, and outlook, *Energy Environ. Sci.* **2013**, *6*, 347-370.

[16] Z. Zhang, R. Dua, L. Zhang, H. Zhu, H. Zhang, P. Wang, Carbon-layer-protected cuprous oxide nanowire arrays for efficient water reduction, *ACS Nano* **2013**, *7*, 1709-1717.

[17] Y. W. Chen, J. D. Prange, S. Dühnen, Y. Park, M. Gunji, C. E. D. Chidsey, P. C. McIntyre, Atomic layer-deposited tunnel oxide stabilizes silicon photoanodes for water oxidation, *Nat. Mater.* **2011**, *10*, 539.

[18] M. J. Kenney, M. Gong, Y. Li, J. Z. Wu, J. Feng, M. Lanza, H. Dai, High-performance silicon photoanodes passivated with ultrathin nickel films for water oxidation, *Science* **2013**, *342*, 836.

[19] B. Mei, A. A. Permyakova, R. Frydendal, D. Bae, T. Pedersen, P. Malacrida, O. Hansen, I. E. L. Stephens, P. C. K. Vesborg, B. Seger, I. Chorkendorff, Iron-treated nio as a highly transparent p-type protection layer for efficient si-based photoanodes, *J. Phys. Chem. Lett.* **2014**, *5*, 3456.

[20] K. Sun, M. T. McDowell, A. C. Nielander, S. Hu, M. R. Shaner, F. Yang, B. S. Brunschwig, N. S. Lewis, Stable solar-driven water oxidation to o2(g) by ni-oxide-coated silicon photoanodes, *J. Phys. Chem. Lett.* **2015**, *6*, 592.

[21] F. Yu, F. Li, B. Zhang, H. Li, L. Sun, Efficient electrocatalytic water oxidation by a copper oxide thin film in borate buffer, *ACS Catal.* **2015**, *5*, 627.

[22] J. Du, Z. Chen, S. Ye, B. J. Wiley, T. J. Meyer, Copper as a robust and transparent electrocatalyst for water oxidation, *Angew. Chemie - Int. Ed.* **2015**, *54*, 2073.

[23] Z. Chen, T. J. Meyer, Copper(ii) catalysis of water oxidation, *Angew. Chemie - Int. Ed.* **2013**, *125*, 728.

[24] X. Liu, H. Jia, Z. Sun, H. Chen, P. Xu, P. Du, Nanostructured copper oxide electrodeposited from copper(ii) complexes as an active catalyst for electrocatalytic oxygen evolution reaction, *Electrochem. commun.* **2014**, *46*, 1.

[25] X. Liu, S. Cui, Z. Sun, P. Du, Copper oxide nanomaterials synthesized from simple copper salts as active catalysts for electrocatalytic water oxidation, *Electrochim. Acta* **2015**, *160*, 202.

[26] M. T. Zhang, Z. Chen, P. Kang, T. J. Meyer, Electrocatalytic water oxidation with a copper(ii) polypeptide complex, *J. Am. Chem. Soc.* **2013**, *135*, 2048.

[27] S. M. Barnett, K. I. Goldberg, J. M. Mayer, A soluble copper-bipyridine water-oxidation electrocatalyst, *Nat. Chem.* **2012**, *4*, 498.

[28] T. Zhang, C. Wang, S. Liu, J. L. Wang, W. Lin, A biomimetic copper water oxidation catalyst with low overpotential, *J. Am. Chem. Soc.* **2014**, *136*, 273.

[29] P. Garrido-Barros, I. Funes-Ardoiz, S. Drouet, J. Benet-Buchholz, F. Maseras, A. Llobet, Redox non-innocent ligand controls water oxidation overpotential in a new family of mononuclear cu-based efficient catalysts, *J. Am. Chem. Soc.* **2015**, *137*, 6758.

[30] G. Kear, B. D. Barker, F. C. Walsh, Electrochemical corrosion of unalloyed copper in chloride media--a critical review, *Corros. Sci.* **2004**, *46*, 109.

[31] L. D. Burke, M. J. G. Ahern, T. G. Ryan, An investigation of the anodic behavior of copper and its anodically produced oxides in aqueous solutions of high ph, *J. Electrochem. Soc.* **1990**, *137*, 553.

[32] Y.-K. Hsu, C.-H. Yu, Y.-C. Chen, Y.-G. Lin, Synthesis of novel Cu_2O micro/nanostructural photocathode for solar water splitting, *Electrochimica Acta* **2013**, *105*, 62.

[33] C. Wanger, C. W. Riggs, L. Davis, J. Moulder, G. Muilenberg, In *Handbook of x-ray photoelectron spectroscopy: a reference book of standard data for use in x-ray photoelectron spectroscopy*, PerkinElmer Corp., Physical Electronics Division, Eden Prairie, Minnesota, USA, **1979**, p. 82.

[34] J. Moulder, W. Stickle, P. Sobol, K. Bomben, In Handbook of x-ray photoelectron spectroscopy: a reference book of standard spectra for indentification and interpretation of XPS data, Perkin-Elmer Corp., Physical Electronics Division, Eden Prairie, Minnesota, USA, **1992**, p. 87.

[35] M. J. Choi, J. Y. Jung, M. J. Park, J. W. Song, J. H. Lee, J. H. Bang, Long-term durable silicon photocathode protected by a thin Al_2O_3/sioxlayer for photoelectrochemical hydrogen evolution, *J. Mater. Chem. A* **2014**, *2*, 2928.

[36] K. Jun, Y. S. Lee, T. Buonassisi, J. M. Jacobson, High photocurrent in silicon photoanodes catalyzed by iron oxide thin films for water oxidation, *Angew. Chemie - Int. Ed.* **2012**, *51*, 423.

C 7 Supporting information

Paper C: CuO functionalized silicon photoanodes for photoelectrochemical water splitting devices

Index

Figure S1. Morphology of the Cu films with different thicknesses

Figure S2. Tafel plot of a 10 nm CuO/Cu/FTO electrode

Table S1. Copper oxide based electrodes for electrocatalytic water oxidation reported in the literature

Figure S3. Cyclic voltammetry (CV) of 15 nm CuO/Cu/FTO electrode before and after 12 h electrolysis

Figure S4. Electrochemical stability and transparency of CuO/Cu/FTO electrodes

Figure S5. Flux diagram of the process used to activate the Cu/SiO_2/nSi/Tiphotoanodes

Figure S6. XPS analysis of 10 nm Cu/SiO_2/nSi/Ti photoanodes before and after the photoelectrochemical experiments

Figure S7. XPS analysis of 15 nm Cu/SiO_2/nSi/Ti photoanodes before and after photoelectrochemical experiments

Figure S8.XPS binding energy region of Cu 2p on the as-deposited 5, 10 and 15 nm Cu/FTO samples showing the typical profile for a CuO/Cu film.

Figure S9. Cyclic voltammetry (CV) of a 10 nm CuO/Cu/FTO electrodes in the dark and under light illumination

Figure S10. Long-term controlled potential electrolysis of CuO/Cu/SiO_2/nSi/Ti photoanodes with different thicknesses (5, 10 and 15 nm)

Figure S11. SEM images of 10 nm CuO/Cu/SiO_2/nSi/Tiphotoanodes before and after photoelectrochemical experiments

IV

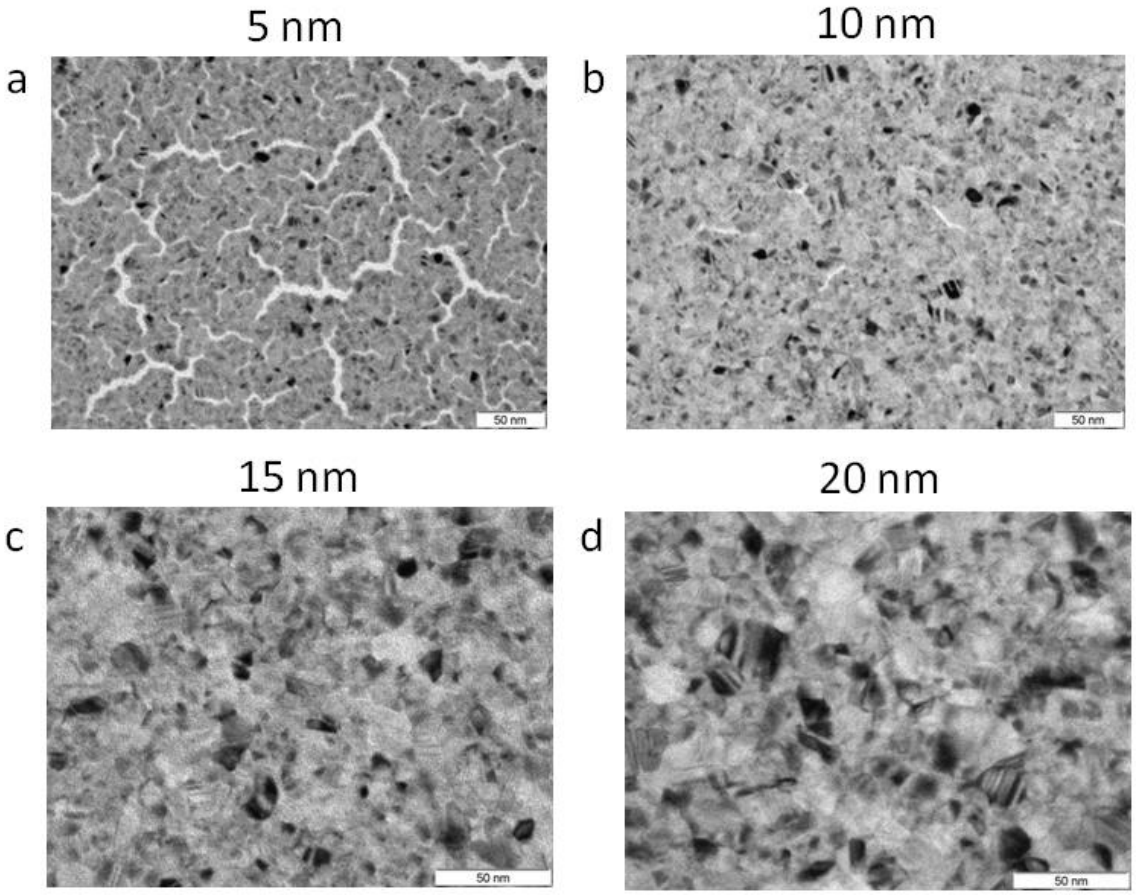

Figure S1. Morphology of the Cu films prepared by sputteringon copper grids suitable for TEM analysis.TEM images of 5, 10, 15, 20 nm Cu films at nanoscale. The scale bars are 50 nm for (a-d). For the thicker Cu films (25 nm), the TEM images were harder to obtain.

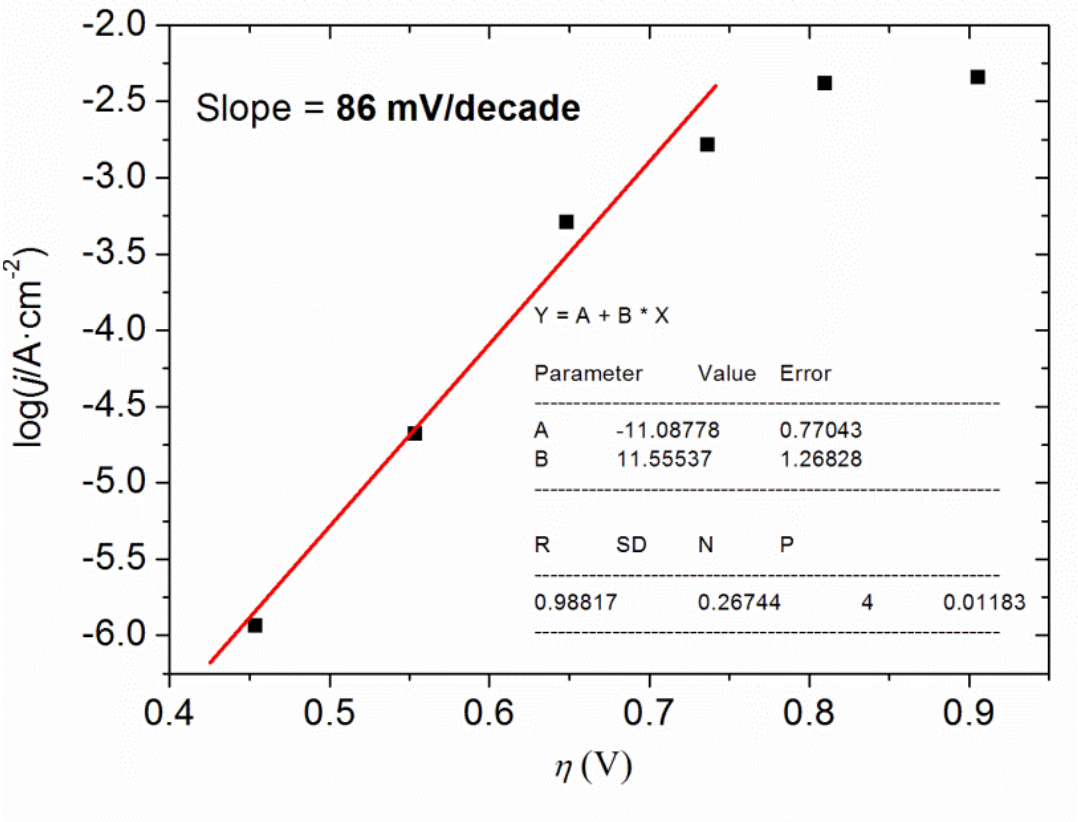

Figure S2. Tafel plot of a 10 nmCuO/Cu/FTO electrode in 0.2 M borate buffer pH 9, showing a calculated Tafel slope (B^{-1}) of 86 mV·dec^{-1} (similar values have been obtained for electrodes with different thicknesses). The steady-state current densities (*j*) were measured by means of chronoamperometric experiments collected at different applied potentials(the latter corrected for the *i*R drop in the solution, V_{appl}-iR), and plotted *versus* the overpotential $\eta = (V_{appl} - iR) - E_{O2/H2O}$(pH 9).

Table S1. Copper oxide based electrodes for electrocatalytic water oxidation reported in the literature.

Year	Fabrication Method	Precursor	Sample	Stability/Condition	Tafel plot Slope mV/decade	Ref
2014	Oxidative electro-deposition	copper(II) molecular complexes	CuO/ FTO	120 min/ 0.1 M borate buffer (pH 9.2)	56	1
2015	Chemical reactionand calcination	Copper salts	CuO/ FTO	10 h/0.1 M KBi (pH 9.2)	54.5	2
2015	Oxidative electro-deposition	$Cu(NO_3)_2$	CuO/ FTO	10 h/ 0.2 M borate buffer (pH 9)	89	3
2015	Oxidation of copper foil	Cu foil	CuO/Cu	10 h/ 1 M Na_2CO_3 (pH 10.8)	90	4

IV

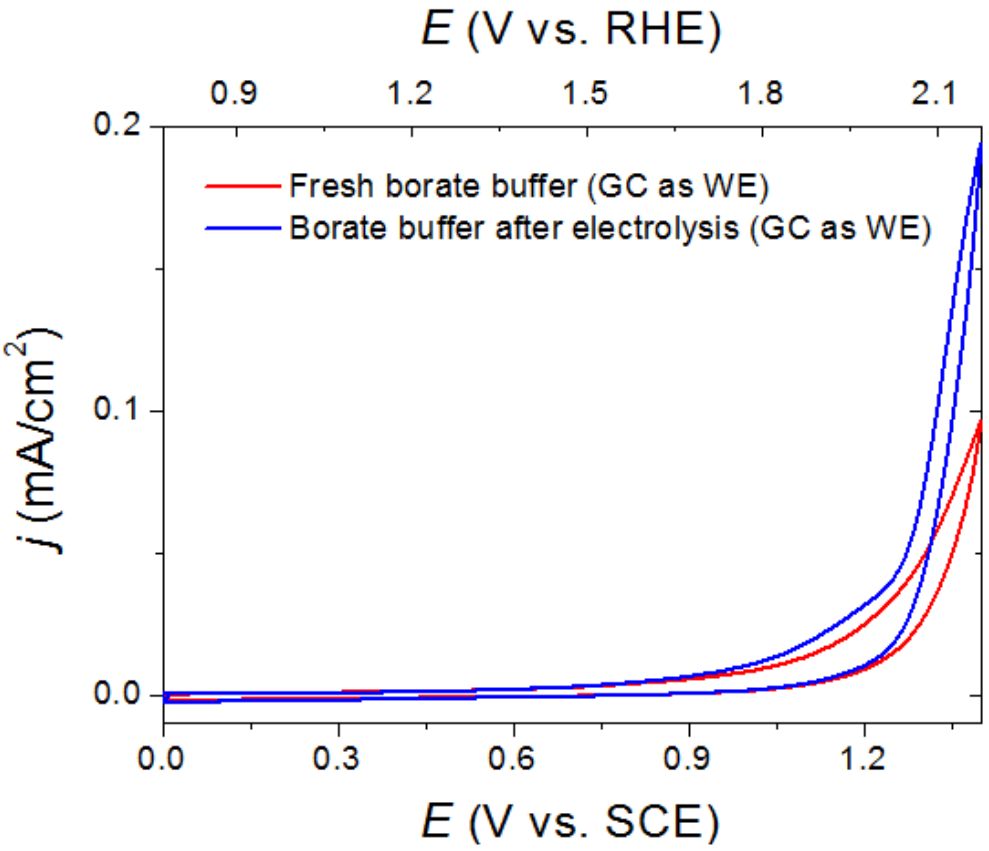

Figure S3. Comparison of the CV scansobtained for the electrolytic solution (0.2 M borate buffer, pH 9) before (red trace) and after (blue trace) performing a CPE (at 1.1 V vs. SCE for 12 hours) using a 15 nm CuO/Cu/FTO electrode to check if there is free Cu^{2+} in solution after CPE. The CV scans were collected with iR compensation, using a glassy carbon, a SCE and a Pt respectively as the working, the reference and the counter electrode,at a scan rate of 100 mV/s.

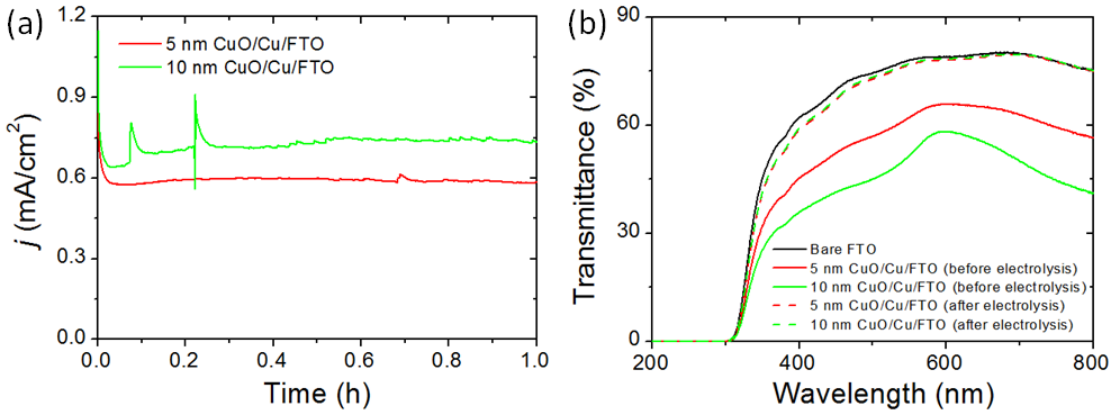

Figure S4. (a) Current density traces obtainedin the controlled potential electrolysis at 1.1 V vs. SCE (without iR compensation) of 5 and 10 nm CuO/Cu/FTO electrodes (respectively, red and green traces) in 0.2 M borate buffer solution (pH 9). (b) UV-Vis transmittance spectra of 5 nm (red) and 10 nm (green) CuO/Cu/FTO before (solid lines) and after (dashed lines) 1 hour controlled potential electrolysis (see b). The transmittance of the bare FTO is also shown as reference (black line).

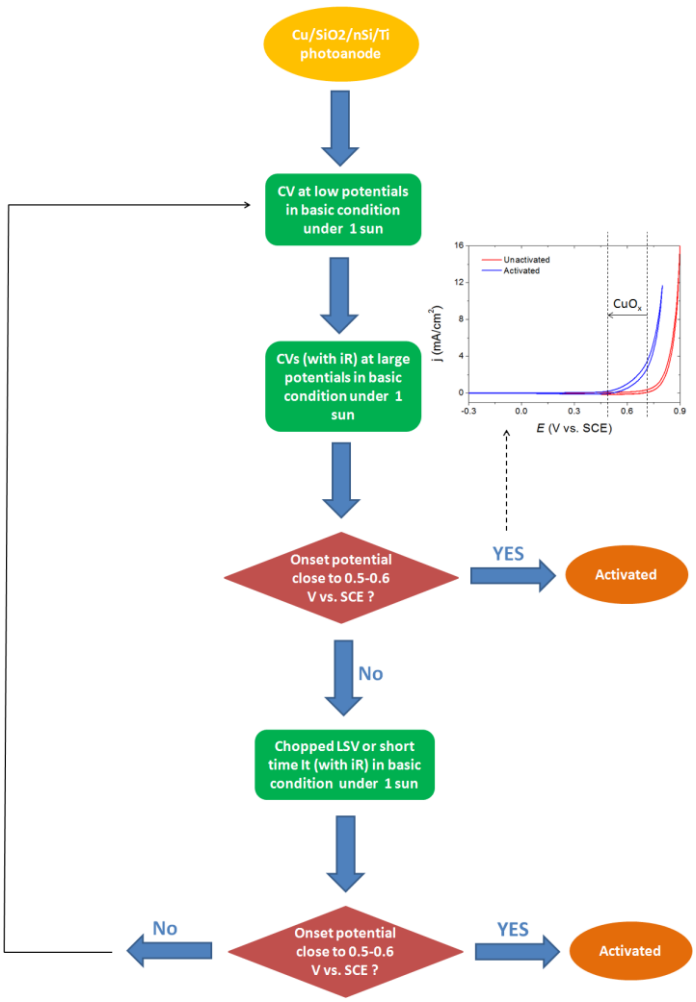

Figure S5. Flux diagram of the process used to activate the $Cu/SiO_2/nSi/Ti$ photoanodes.

IV

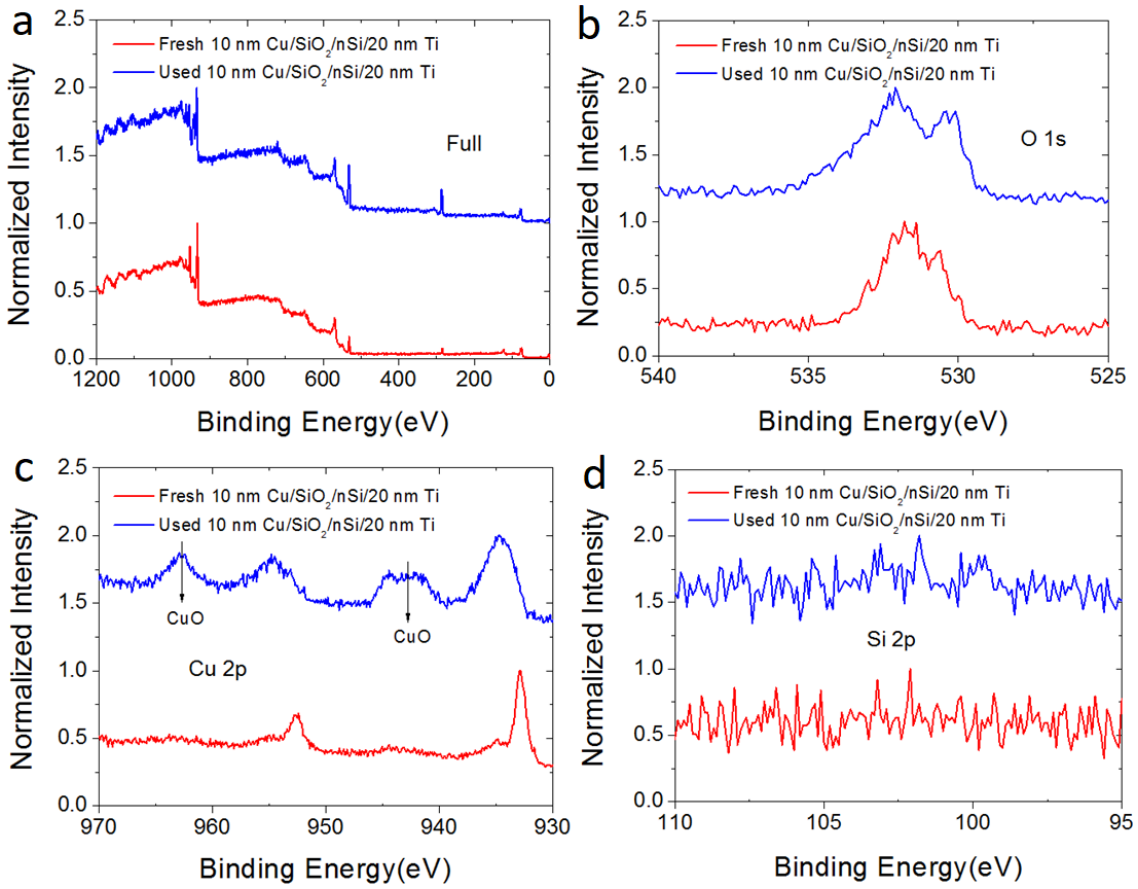

Figure S6. (a) Overall XPS spectrum of fresh (red) and used (blue) 10 nm Cu/nSi/SiO_2/Tiphotoanodes. (b)-(d) XPS binding energy regions of 1s O, 2p Cu and 2p Si, respectively.

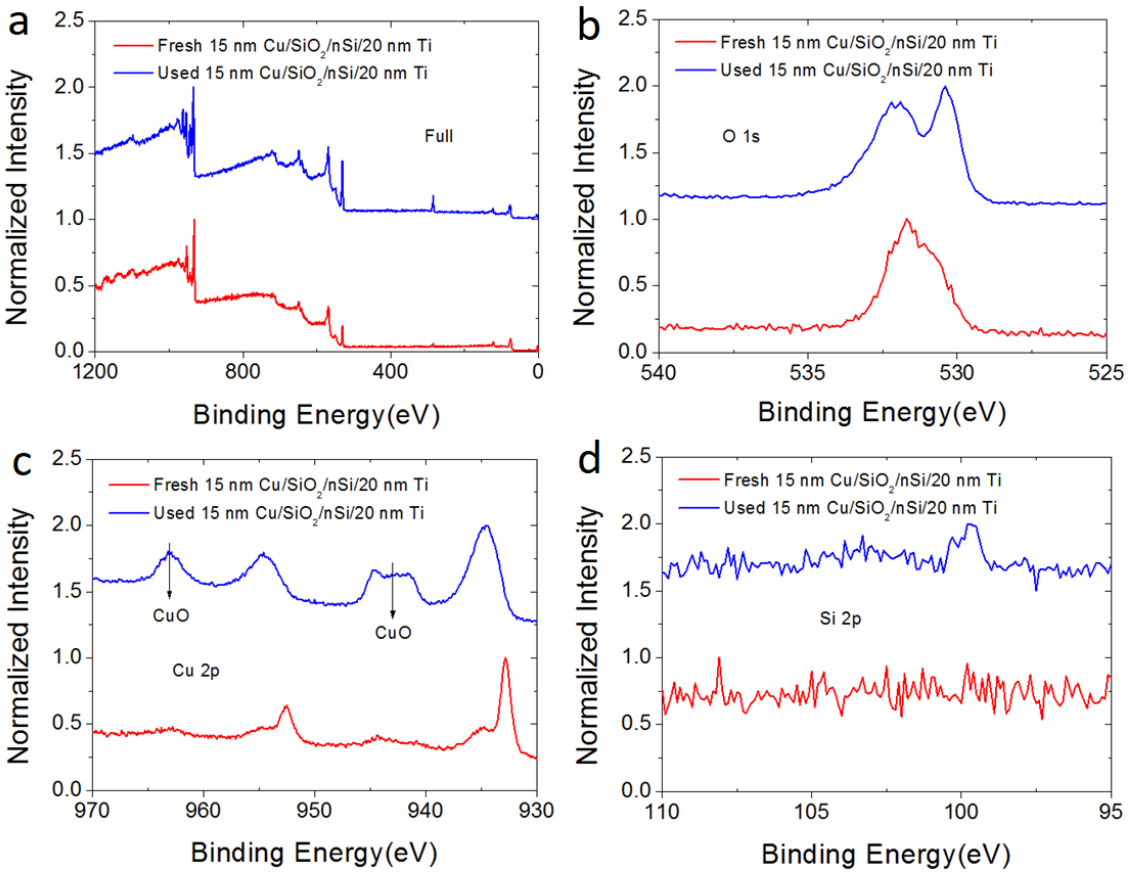

Figure S7. (a) Overall XPS spectrum of fresh (red) and used (blue) 15 nm Cu/nSi/SiO_2/Ti photoanodes. (b)-(d) XPS binding energy regions of 1s O, 2p Cu and 2p Si, respectively.

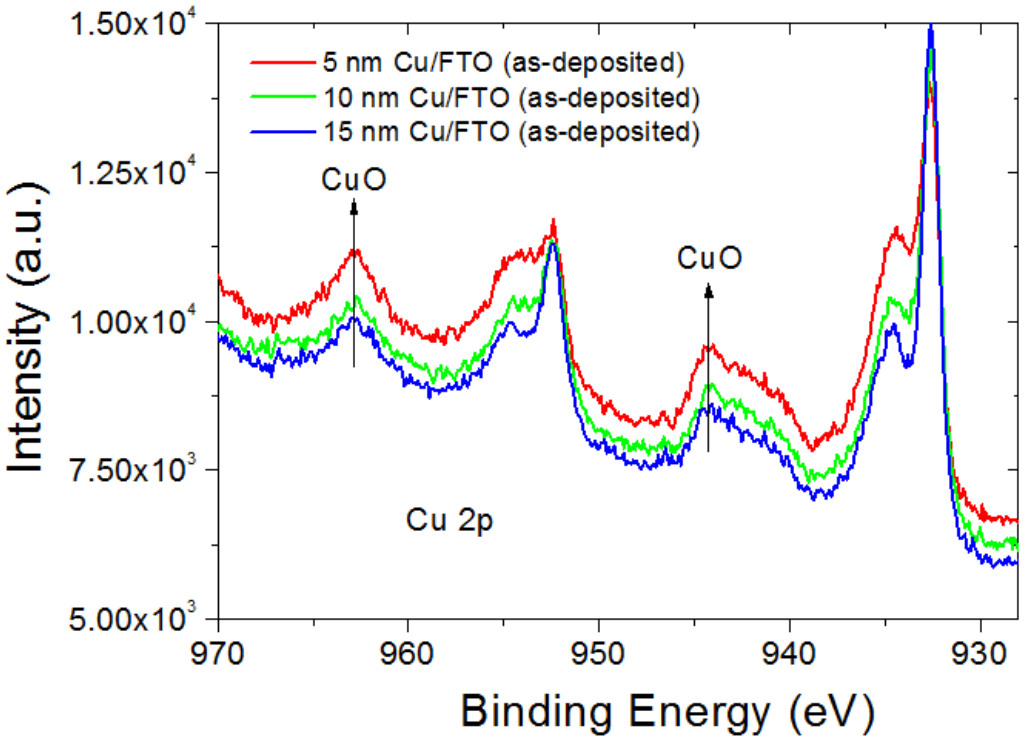

Figure S8. XPS binding energy region of Cu 2p on the as-deposited 5, 10 and 15 nm Cu/FTO samples showing the typical profile for a CuO/Cu film.

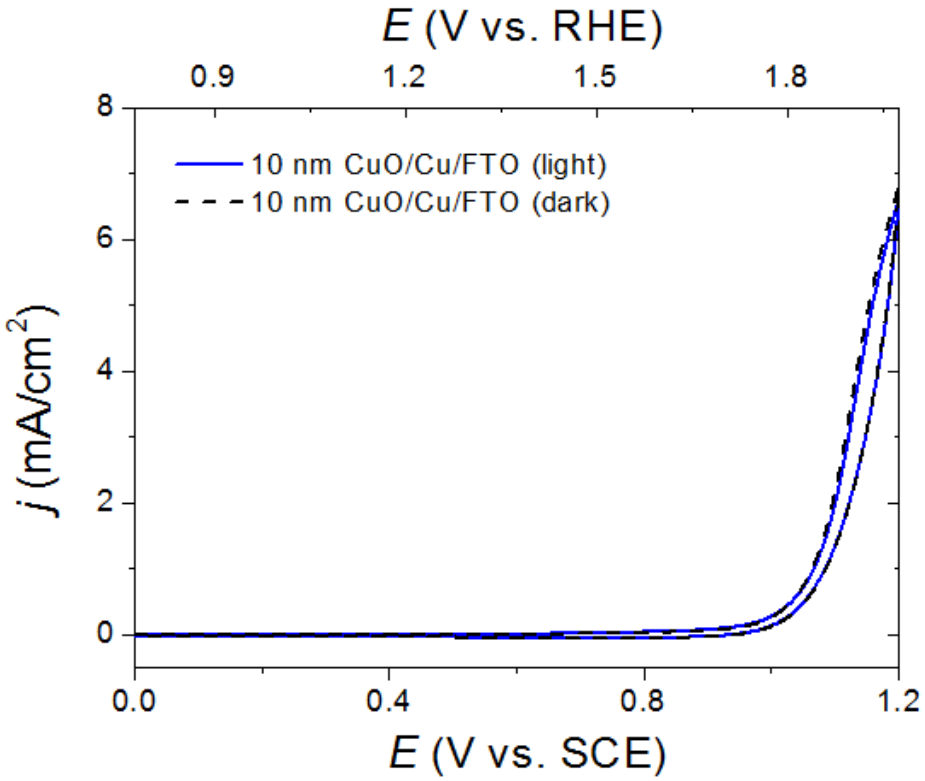

Figure S9. CV scans obtained for a 10 nm CuO/Cu/FTO electrodes under dark (black dashed curve) and simulated 1-sun illumination (blue solid curve) in 0.2 M borate buffer solution (pH 9). The CV scans were collected with iR compensation, using a SCE and a Pt respectively as the reference and the counter electrode, at a scan rate of 100 mV/s.

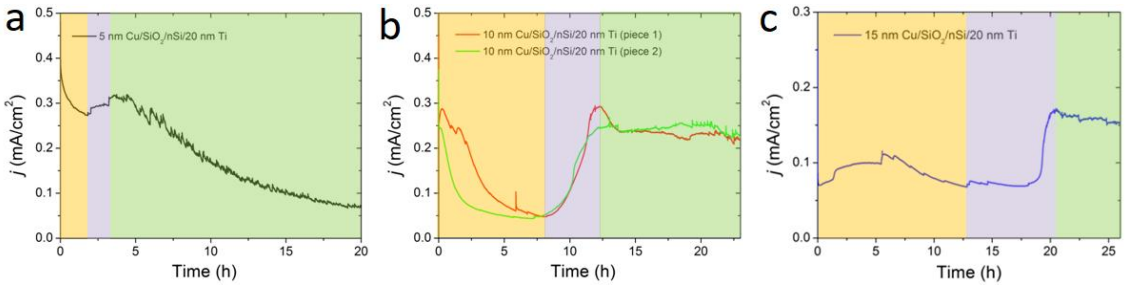

Figure S10.(a-c) Current density traces of 5 (black), 10 (red and blue) and 15 nm (green) Cu/SiO_2/nSi/Ti photoanodes.The regions dealing with the *(i)* decrease in conductivity due to intermediate products formed during the transition from Cu to CuO; *(ii)* activation process; and *(iii)* actual performances of the activated photoanodes, are respectively evidenced in yellow, violet and green. All the traces are collected without iR compensation and at controlled potential of 0.8 V vs. SCE under 1 sun illumination in 0.2 M borate buffer solution (pH 9).

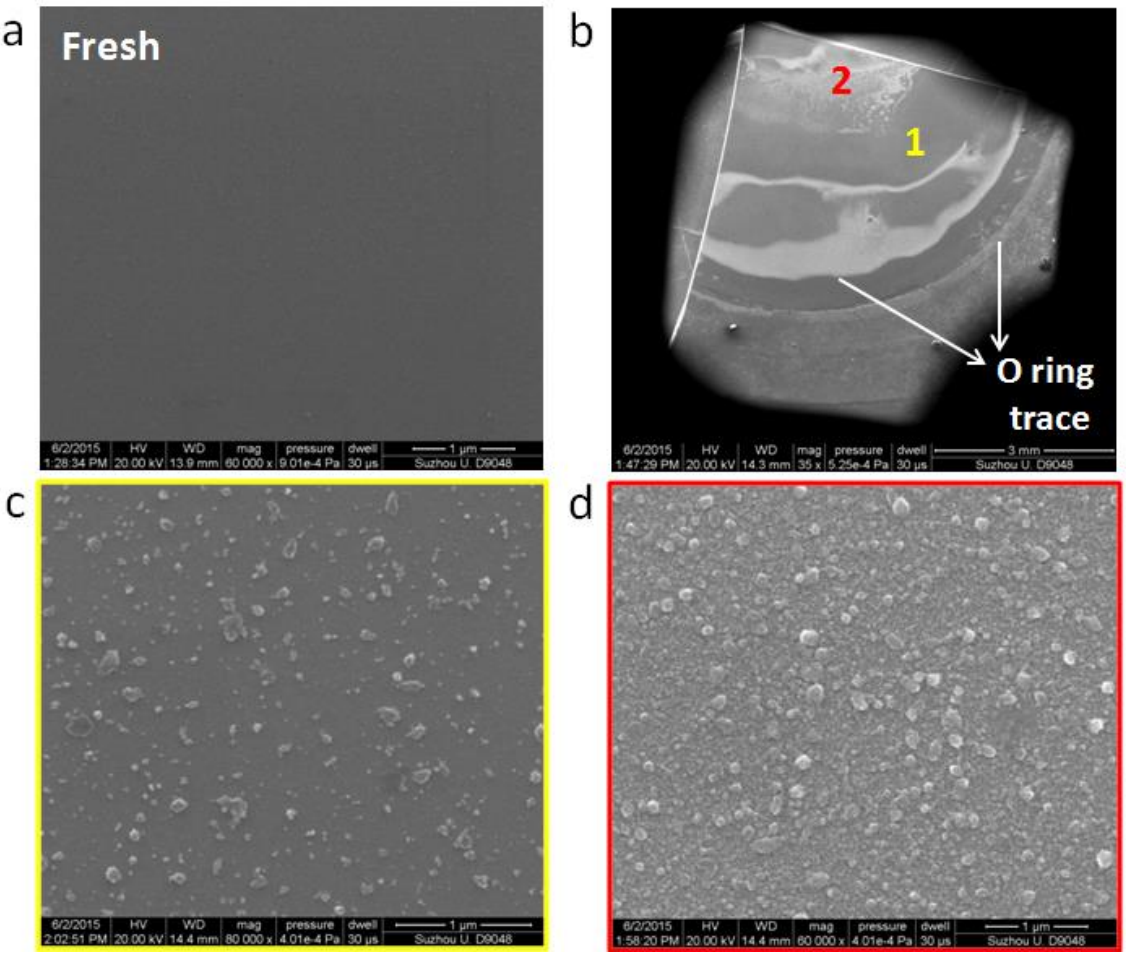

Figure S11. SEM images of 10 nm Cu/SiO_2/nSi/Ti photoanodes before (a) and after (b-d) 37 hours controlled potential electrolysis at 0.8 V vs. SCE (without iR compensation), under 1 sun illumination in 0.2 M borate buffer. (c) and (d) are the zoom-in images at position 1 and 2 in (b). The formed CuO film consists ofcompact nanoparticles, partially depleted with the testing time.

References:

IV

[1] X. Liu, H. Jia, Z. Sun, H. Chen, P. Xu, P. Du, Nanostructured copper oxide electrodeposited from copper(ii) complexes as an active catalyst for electrocatalytic oxygen evolution reaction, *Electrochem. commun.* **2014**, *46*, 1.

[2] X. Liu, S. Cui, Z. Sun, P. Du, Copper oxide nanomaterials synthesized from simple copper salts as active catalysts for electrocatalytic water oxidation, *Electrochim. Acta* **2015**, *160*, 202.

[3] F. Yu, F. Li, B. Zhang, H. Li, L. Sun, Efficient electrocatalytic water oxidation by a copper oxide thin film in borate buffer, *ACS Catal.* **2015**, *5*, 627.

[4] J. Du, Z. Chen, S. Ye, B. J. Wiley, T. J. Meyer, Copper as a robust and transparent electrocatalyst for water oxidation, *Angew. Chemie - Int. Ed.* **2015**, *54*, 2073.

Paper D: Ageing mechanisms of highly active and stable nickel-coated silicon photoanodes for water splitting

IV

T. Han†, Y. Shi†, X. Song, A. Mio, L. Valenti, F. Hui, S. Privitera, S. Lombardo, M. Lanza, *J. Mater. Chem. A*, **2016**,*4*, 8053. (†Equal Contribution)

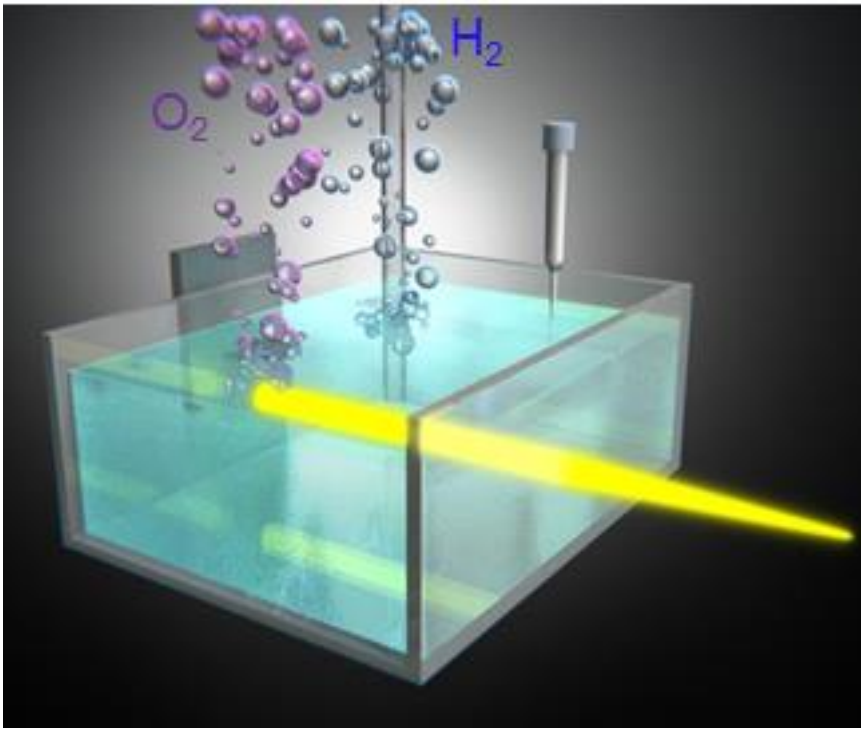

Abstract

The photoelectrochemical (PEC) water splitting cell, a device that uses sunlight to produce hydrogen, has raised massive interest due to its simple structure, low fabrication cost and good performance. In these cells, a semiconductor photoelectrode is immersed in a liquid and, when illuminated, hydrogen and/or oxygen can be generated on its surface by electrolysis. Metal catalysts are often used to enhance the activity of the semiconductor, but the lifetime is still the main bottleneck of this technology. In this manuscript we report the ageing mechanisms of silicon photoanodes coated with nickel films of different thicknesses (under light-driven oxygen evolution reaction, OER). The

IV

2 nm, 5 nm and 10 nm nickel-coated n-Si photoanodes show lifetimes of ~18 h, ~150 h and >260 h, respectively. While the 2 nm sample degrades due to the formation of a highly resistive NiO_X with abundant potassium contamination (from the electrolyte), the performance of the thicker samples decreased due to the formation of holes. The 5 nm and 10 nm thick nickel films turned into an homogeneous potassium-free NiO_X film suitable for water-splitting, which remarkably enhanced the performance of the cells. The density/size of holes in the surface decreased/increased with the metal thickness. The potassium contamination in the 2 nm Ni sample takes place in the form of nanofilaments, and we demonstrate that the widely used X-ray photoelectron spectroscopy tests are blind to these features, which may have been ignored in all previous reports. These results could be useful to understand the degradation and enhance the yield of water-splitting solar cells.

Contribution

Yuanyuan Shi designed the experiments, perfomed the photoelectrochemical measurements and help with the preparation of the manuscript.

D 1 Introduction

The use of solar energy to produce storable and transportable clean fuels has attracted worldwide attention as renewable energy source,[1,2] as it solves the problems of sunlight intermittence and location dependency, while avoiding the use of contaminant and every time more scarce fossil fuels. In a PEC water splitting solar cell, electricity generated in a photovoltaic system is used to break down water (H_2O) into hydrogen and oxygen by electrolysis.[3,4] Due to its low cost and good ability to absorb light, silicon is one of the most preferred semiconductor photoelectrodes but, unfortunately, using semiconductor materials the amounts of hydrogen and oxygen produced are very modest, and the chemical reactions decay after some minutes due to surface corrosion. To overcome these problems, the most advanced water splitting cells use a catalyst and protective coating deposited directly on the semiconductor surface. Several metal-based catalysts including Ru,[5] Ni,[6] NiO_X,[7,8] Ir[9], Cu,[10] CuO_X,[11] MnO_X[12] and Co[13] have been demonstrated to enhance the activity of semiconductor photoelectrodes for water splitting, achieving current densities up to tens of mA/cm^2.[7] While cell activity amply exceeds the requirements of this technology, stability is still a major concern. Among all catalysts used, there is consensus that nickel based oxides and compounds are the best cost-effective and durable solution.[6-8,14-17] In our previous work, we observed that silicon photoanodes coated with ultrathin (2 nm) layers of nickel can generate current densities of 10 mA/cm^2 during more than 80 hours.[6] Recently, Mei et al.[17] achieved stable water splitting during 300 h using p^+n silicon photoanodes coated with 50 nm thick Fe-treated NiO films, and Sun et al.[7] reported lifetimes above 1200 h using even thicker 35~160 nm NiO_X films on np^+ silicon. It is worth noting that the use of thick coatings reduces the light transmittance to the silicon, leading to larger onset potentials and smaller saturation currents.[6] Moreover, the fabrication of buried np^+-Si junctions involves additional fabri-

-cation steps that increase the cost of the photoelectrodes.

Despite the long lifetimes reported, the ageing mechanisms that produce activity decay and device failure in water splitting solar cells are still not understood, and one of the main reasons is the important lack of in-depth reliability studies at the nano and atomic scales. The widely used scanning electron microscopy (SEM) is unable to provide clear-cut information about the samples, and it has been mainly used to display the thickness of the coatings[6,7,17] and to have a loose idea about surface roughness[16]. Surface roughness has been quantitatively analyzed by Atomic Force Microscope (AFM)[7,14,15], but no work provides a thorough characterization depending on the testing time, precluding the detection of degradation trends and ageing mechanisms. X-ray photoelectron spectroscopy (XPS)[18-20], energy-dispersive X-ray spectroscopy (EDX)[16,17] and Auger electron spectroscopy (AES)[6] have been widely used for chemical characterization, but the lateral resolution of these techniques is ~10 µm, ~1 µm and ~20 nm (respectively), and they can mask local phenomena and defects produced during PEC. Few groups reported the use of cross sectional Transmission Electron Microscope (XTEM) to obtain information at the atomic leve[l9,14,16,18,21], but only images of fresh samples are provided (to prove the thickness of the layers).

In this work we fabricate nickel-coated silicon photoanodes with long lifetimes above 260 hours, and we exhaustively analyze their ageing mechanisms at nano and atomic scales. Characterization tools traditionally used in the field of water splitting solar cells, such as SEM, XPS and AFM are combined with XTEM, and we introduce for the first time the use of Electron Energy Loss Spectroscopy (EELS) in the study of water splitting solar cells. Our results demonstrate that the ageing of the photoanodes is strongly linked to the thickness of the catalyst coating, and we report remarkable differences on surface roughness, stack homogeneity, conduction mechanisms and formation of defect-

-ive holes.

IV

D 2 Experimental Section

D 2.1 Fabrication of electrodes

As-received phosphorous-doped (100) n-type silicon wafers (from Prolog Semicor) with a resistivity of 0.3-0.5 Ohm·cm were cleaned using a three-steps process. First, the wafers were immersed in acetone for 10 minutes, then in ethyl alcohol for 10 minutes more, and finally in deionized water for another 10 minutes. For all cleaning steps, the ultrasonic bath was used. After that, the samples were dried with an N_2 gun. As reference, one n-Si sample was immersed in water-diluted hydrofluoric acid ($HF:H_2O$ volume ratio 1:5) for 10 seconds to remove the native oxide. Once the n-Si wafers were cleaned a thin layer of nickel (with a thicknesses of 2 nm, 5 nm or 10 nm) was evaporated on their top surface. On the back side of the wafer, 20 nm titanium was evaporated to form an Ohmic contact. The electron beam evaporator used was the PVD75 from Kurt J. Lesker at a deposition rates of ~0.15 Å/s and ~0.45 Å/s for the Ni and Ti layers, respectively. Copper tape was used to contact the Ti on the backside for electrochemical experiments.

D 2.2 Electrochemical characterization

The electrodes were tested in a square container with two circular apertures located at opposite faces, and with sizes of 0.5 $cm^2$and 2 cm^2. The small aperture was sealed by the electrode using a rubber ring and a back tap fixed by four screws. Similarly, the bigger aperture was sealed using a glass, through with a light flux was driven to the surface of the electrode. The light flux was generated using a 150 W Xenon lamp from Newport Corporation, and the electrodes were irradiated using a light power density of ~50 mW/cm^2, which was corroborated with an optical power meter from Newport

Corporation (model 1918-R). A saturated calomel electrode (SCE, saturated KCl) was used as reference electrode, and a stainless steel electrode as counter electrode. Electrochemical experiments were performed in a three-electrode system controlled by a CHI 660E potentiostat. Before the experiments, the container was filled with an electrolyte consisting of 1 M potassium hydroxide (KOH, pH=14), prepared by dissolving 5.6 g KOH (from Sinopharm Chemical Reagent) in 100 mL deionized water. Before every measurement, bubbles were removed from the aperture using a plastic pipette. When testing the long-time I-t curves, the production of bubbles decreased the amount of electrolyte in the container, and more KOH was poured. Before and after the electrochemical tests, the electrical resistance of the system was registered. During the experiments, cyclic voltammetry (CV), linear sweep voltammetry (LSV) and amperometric I-t curves were measured. All CVs and LSVs were collected at 100 mV/s, and 10 mV/s, respectively.

D 2.3 Materials Characterization

After electrochemical characterization, the photoanodes were rinsed with water for 10 seconds, washed again in deionized water for 3 minutes and dried with the N_2 gun. The morphological changes induced by the electrochemical tests were analyzed with two different the Scanning Electron Microscopes (SEM), the FEI Quanta 200FEG and the Zeiss SUPRA55, and also by means of Atomic Force Microscopy (AFM), using the MultiMode V from Veeco working in tapping mode and using NanoWorld Pointprobe tips (model NCH, item no. 78131F6L965). The chemical composition of the samples was analyzed with the X-ray Photoelectron Spectroscopy (XPS), model Shimadzu KRATOS AXIS Ultra DLD Scanning XPS Microprobe. Additionally, atomic scale morphologic and chemical information was gained combining cross-sectional Transmission Electron

Microscopy (XTEM) coupled with the Electron Energy Loss Spectroscopy (EELS) acquired in scanning mode (STEM), using a JEOL JEM 2010F electron microscope with a 200 kV accelerating voltage. Between photoelectrochemical experiments and XTEM analyses, the photoanodes were protected with 50 nm Au to avoid the effect of the environment. The Leica Microsystems (DM4000M) Fluorescence optical microscope was used to analyze the surface of the samples. The conductivity of fresh and tested photoanodes was analyzed at both the nanoscale and the device level. The electrical conductivity of the photoanodes has been measured using the Bruker Multimode VIII conductive AFM (CAFM), using Pt-varnished silicon tips from Nano World (model PPP-CONTPt, item no. 80064F11L1115). In order to characterize the photocurrents through the photoanodes, the current maps were collected under illumination (provided by the built-in laser of the CAFM) and without applying any external bias. For device level characterization, metallic electrodes made of 50 nm Au were evaporated directly on the surface of the Ni photoanodes using a laser-patterned shadow mask from Tecan (UK). The devices were characterized by collecting current-voltage (I-V) curves using a probe station (Cascade, model: M150) and a semiconductor parameter analyzer (Keithley, model: 4200-SCS). It is worth noting that the morphological characterization of the samples by AFM, SEM, TEM and EELS was performed ex-situ. Despite the surface of the samples in operation (in contact with the electrolyte) and during ex-situ characterization (in air or vacuum) may be different, the permanent damage induced by the PEC tests can be effectively demonstrated, as many other authors did.[6, 9, 12]

D 3 Results and discussion

N-type silicon wafers (with their native oxide) were coated, by electron beam evaporation, with nickel layers of different thicknesses (2 nm, 5 nm and 10 nm). The

resulting photoanodes were tested under potassium hydroxide (KOH, pH = 14) in a three-electrode system, using a saturated calomel electrode (SCE) and a stainless steel counter electrode. Sequences of cyclic voltammograms (CV) and amperometric current-time (I-t) curves have been measured under an illumination of 50 mW/cm^2 and in the dark. Figure 1a shows the schematic of the setup used to characterize the samples, and Figure 1b is the XTEM image of a 5 nm nickel-coated silicon photoanode. More details about fabrication and characterization processes can be found in the methods section and supplementary information.

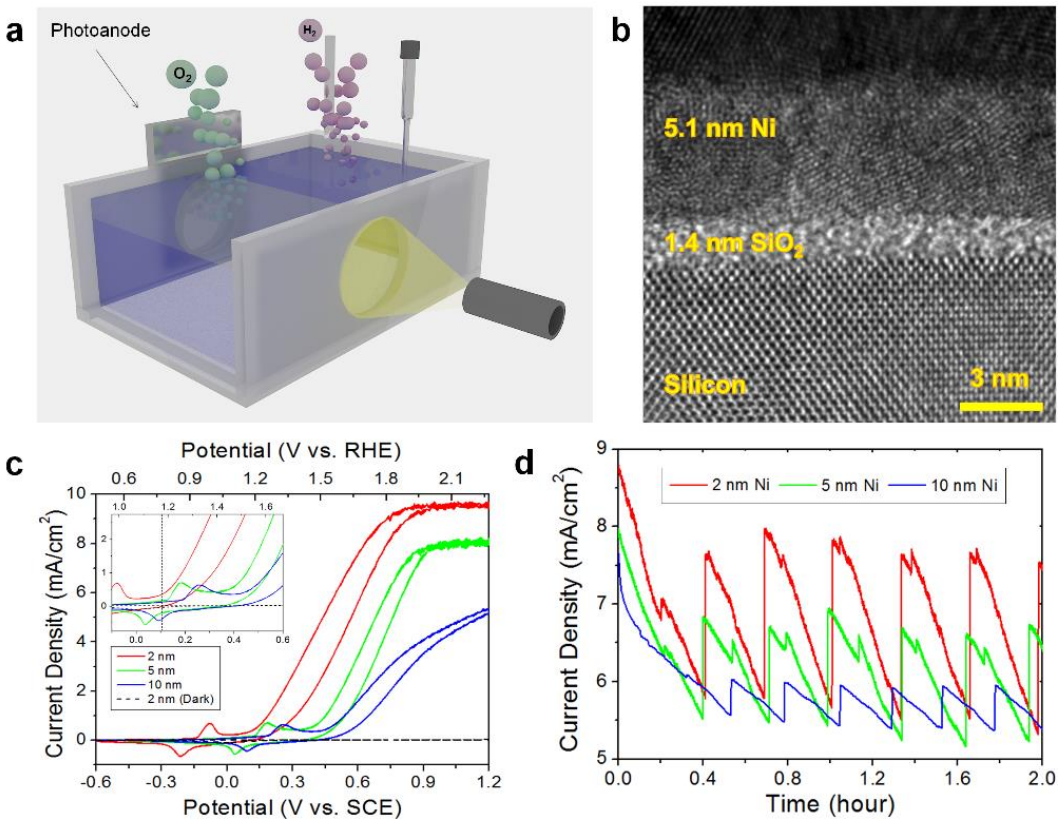

Figure 1. Fabrication and characterization of Ni/SiO_X/n-Si photoanodes. (a) 3D schematic of the setup used to characterize the photoanodes. (b) Cross sectional TEM image of a fresh 5 nm Ni/SiO_X/n-Si photoanode. (c) Typical cyclic voltammograms measured for the Ni/SiO_X/n-Si photoanodes with Nickel thicknesses of 2 nm, 5 nm and 10 nm, tested in 1 M KOH under illumination of 50 mW/cm^2. (d) Short time amperometric I-t curves measured at the constant potential of 1.8 V vs. SCE for the three Ni/SiO_X/n-Si photoanodes with different Ni thicknesses.

Figure 1c shows the typical CVs recorded for the three types of Ni/SiO_X/n-Si photoanodes. The 2 nm Ni sample shows the lowest onset potential (~80 mV vs. SCE)

and the largest saturation currents (~10 mA/cm^2 under 50 mW/cm^2 and ~27 mA/cm^2 under 100 mW/cm^2, see Figure S1), due to the higher light transmittance into the silicon.[6,21] As reference, the 2 nm Ni layer was also deposited on a native-oxide-free n-Si photoanode (after etching the native SiO_2 by HF solution). As we can observe in Figure S2†, the current of this photoanode decreases after each CV scan, which indicates that the native SiO_2 is necessary for ensuring good cell stability. It has been suggested that the SiO_2 layer may work as adhesive to retain the Ni.[6] The short time I-t curves (Figure 1d) reveal stable currents during the first two hours for all samples, showing the characteristic saw tooth shape related to oxygen bubble formation during OER (see Figure S3).

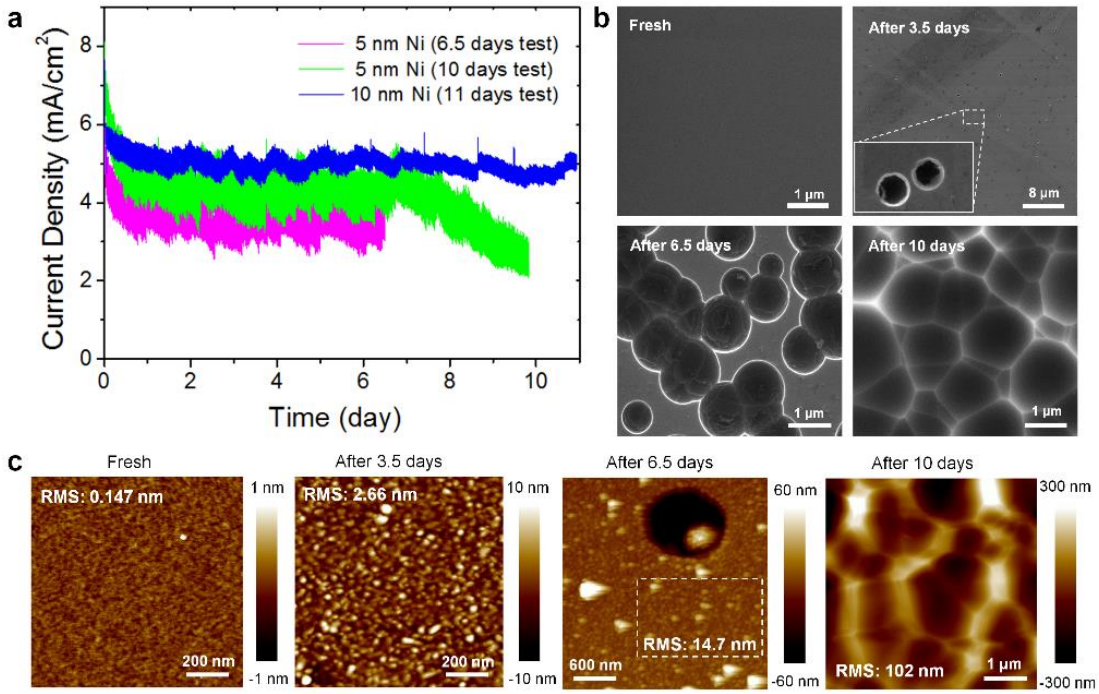

Figure 2. Degradation process of 5 nm and 10 nm Ni coated silicon photoanodes. (a) Representative amperometric I-t curves measured at the controlled potential of 1.8 V vs. SCE for the 5 nm and 10 nm Ni/SiO_X/n-Si/Ti photoanodes in 1 M KOH under illumination of 50 mW/cm^2. (b) and (c) show the SEM and AFM images collected after different testing times for the 5 nm Ni coated silicon photoanodes. The images of the fresh samples are also shown as reference. The 5 nm sample shows the formation of a rough layer that, unlike for the 2 nm Ni sample, is able to split water, and the sample only degrades when the density of holes is critical (after 6.5 days).

The lifetime and ageing mechanisms of the photoanodes are analyzed by means of long time PEC tests. Figure 2a shows representative I-t curves for 5 nm and 10 nm

nickel-coated silicon electrodes tested during different times. In total four 5 nm and three 10 nm nickel photoanodes (fabricated in three different batches) were measured. As it can be observed, the 5 nm sample shows stable currents during 6.5 days, and after that the current signal linearly decreases. Figures 2b and 2c correspond to the SEM and AFM images collected on 5 nm Ni samples after different testing times. The initial root mean square (RMS) roughness of the fresh 5 nm nickel layer is 0.147 nm (which is very similar to that of bare silicon[22]) and it increases with the testing time, reaching 2.66 nm after 3.5 days. Interestingly, this morphological change didn't degrade the performance of the sample, indicating the formation of a rough layer able to split water. For longer times, both the SEM and AFM images reveal the progressive formation of defective holes, and after 6.5 days, the density of holes is prohibitive and the performance of the cell starts to decay linearly. After 10 days, the SEM images show the typical picture of a silicon substrate etched by KOH,[6] (see also Figure S4) indicating that the nickel coating was completely etched. This is further supported by a dramatic increase of the sample roughness in the AFM maps. The chemical composition of this sample is analyzed by means of XPS (Figure S5). The spectra collected after different testing times reveal a change on the nickel (Ni^0 to Ni^{3+}) and oxygen peaks, indicating the formation of an effective NiO_X layer after 24 h PEC test. The XPS data also reveal the presence of potassium from the electrolyte after the test. The absence of a strong silicon signal indicates the presence of the coating after 24 h PEC test (in agreement with the SEM pictures, which show corrosion only after 6.5 days).

These observations are corroborated by means of XTEM and EELS, which provide morphological and chemical information with sub-nanometer lateral resolution. Figures 3a and 3b show the XTEM pictures for the 5 nm sample before and after 24 h PEC test, respectively. The nickel layer in the fresh sample shows polycrystalline

structure, and its thickness is very close to the theoretical one indicated to the evaporator. After the test, the thickness of the coating increases up to 6 nm, and the resulting layer is very homogeneous. The chemical maps obtained with EELS (Figure 3c) indicate the formation of an effective NiO_X layer on the SiO_X. This volume expansion in going from 5 nm Ni to 6 nm NiOx film was expected, since it is known that oxygen evolution is preceded by three-dimensional oxide film formation,[23] on which discharge of OH and/or O takes place. The surface of the sample tested for 24 h (Figure 3b) also reveals the formation of a very thin bright layer on top of the NiO_X, which is probably related to the potassium from the electrolyte, as suggested by the XPS data (Figure S5c).

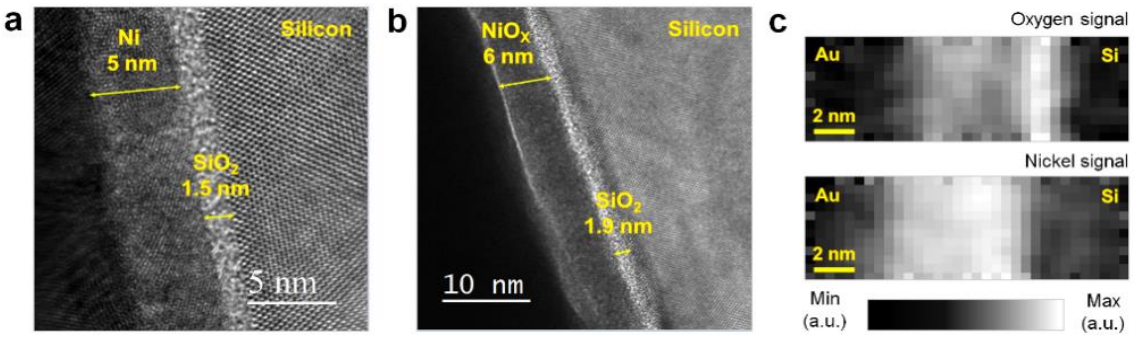

Figure 3. Atomic scale information of fresh and tested 5 nm Ni coated silicon photoanodes. Cross sectional TEM images for the 5 nm $Ni/SiO_X/n$-Si sample (a) before and (b) after 24 hours PEC tests. (c) Oxygen and nickel maps collected with EELS on the sample tested after 24h. The relative thickness increase is smaller and the formation of an effective NiO_X layer is proved.

The 10 nm nickel-coated sample shows stable photocurrents during the whole 11 days tests (Figure 2a). As for the 5 nm nickel electrode, a clear roughness increase can be easily observed after some hours test (Figure S6a), again corroborating the formation of a rough layer that is able to split water. In this case, the sample shows a much longer lifetime (above 11 days) when exposed to continuous OER, and most of the sample surface shows holes-free morphology (Figure S6b). The thicker nature of the layer probably reduced the initial density of pinholes,[24] leading to a less ion-permeable layer that is less susceptible to corrosion.

IV

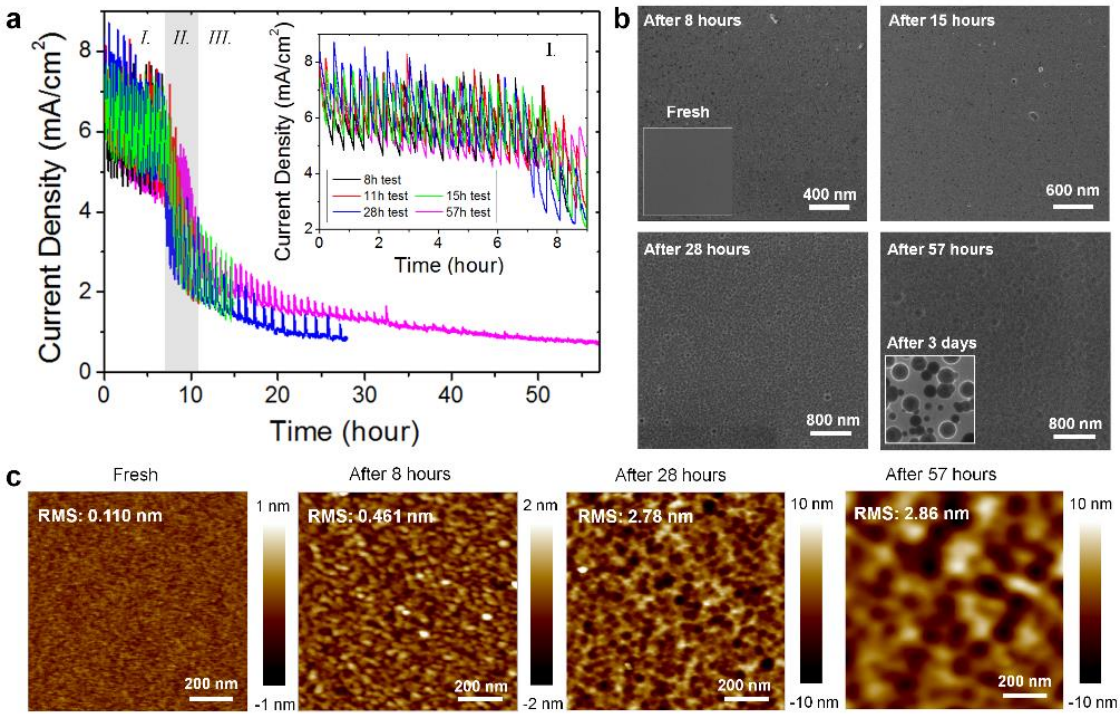

Figure 4. Degradation process of 2 nm Ni coated silicon photoanodes. (a) Amperometric I-t curves measured at the constant potential of 1.8 V vs. SCE on five different 2 nm Ni/SiO_X/n-Si/Ti photoanode sduring different times in 1 M KOH under an illumination of 50 mW/cm^2. The degradation of the sample takes place in three steps clearly distinguished (I, II and III). The inset shows the magnification of the first step, and excellent reproducibility can be observed. (b) and (c) show the SEM and AFM images collected on the Ni coated silicon photoanodes after different testing times. The images of the fresh samples are also shown as reference. The sample shows dramatic degradation after 57 hours test, which is accompanied by a roughness increase, but almost no holes were detected (they appeared only after three days test).

Similar experiments were performed for the 2 nm nickel-coated samples. Figure 4a shows the I-t curves collected after 8 h, 11 h, 15 h, 28 h and 57 h OER tests for five 2 nm nickel photoanodes fabricated in three different batches, showing excellent repeatability and small variability. Interestingly, the degradation process of all 2 nm nickel photoanodes show important differences compared to the 5-10 nm ones, and three characteristic degradation steps can be distinguished: *I*) slow current decay during the first 7 hours; *II*) severe current degradation between the hours 7^{th} and 11^{th}; and *III*) slow decay with a slope similar to that observed in the first step. Again, both SEM and AFM images (Figures 4b and 4c respectively) reveal an increase of the surface roughness with

the testing time: the initial roughness (0.11 nm) progressively increased up to 2.86 nm after 57 hours. During this degradation process, there are two factors that should be highlighted: i) the final roughness of the sample (2.86 nm) is much smaller than the one measured for the 5 nm Ni sample(102 nm), and also smaller than that of a piece of silicon corroded by KOH (24.07 nm in Figure S4); and ii) the SEM images don't reveal the formation of large defective holes in the catalyst (see Figure 4b).[6,8] The absence of holes during the first 57 hours test is further corroborated by exposing the samples to even longer water splitting tests, which revealed that defective holes started to appear on the electrode only after 3 days (see inset in Figure 4b and Figure S7a). Sun et al.[7] associated the formation of holes to silicon corrosion through small pores and/or grain boundaries in the NiO_X film. Our sequences of SEM images provide new insights on the formation of defective holes: the average diameter of the holes increases with the thickness of the nickel coating (Figure S7), and the sizes for each nickel thickness show relatively low variability (i.e. the largest holes for the 2 nm sample are always smaller than the smallest holes in the 5 nm one).

The absence of holes in the 2 nm samples before 3 days indicates that the degradation of the cells is not related to the apparition of defective holes during OER, but it is linked to the formation of a rough layer unable to split water. It is worth noting that the 5-10 nm samples maintained the initial saw tooth shape during the whole degradation process (see Figure S8b), while in the 2 nm samples the initial saw tooth shape for bubble formation changed into sharp peaks (see Figure S8a), indicating a change in the conduction mechanisms through the photoanode. This behavior was in-depth analyzed at the nanoscale and device level using the CAFM and the probestation (respectively). Figures 5a and 5d show the CAFM current maps of the fresh and tested 2 nm Ni/SiOX/n-Si photoanode (under illumination and without bias). The abundant photocurrents

observed in fresh samples completely vanished in the sample exposed to OER during 16 hours. For the device level characterization, squared Au electrodes of different sizes were patterned on the fresh and tested samples using a shadow mask and an evaporator (Figures 5b and 5e). The measured IV curves collected on the fresh samples (Figure 5c) show typical photocurrent at 0V, as well as an overpotential of ~ 60 mV. On the contrary, the sample exposed to 16 hours OER shows almost negligible photocurrent and overpotential, as well as much smaller currents at high potentials (Figure 5f), indicating that the conductivity of the photoanode has been dramatically reduced.

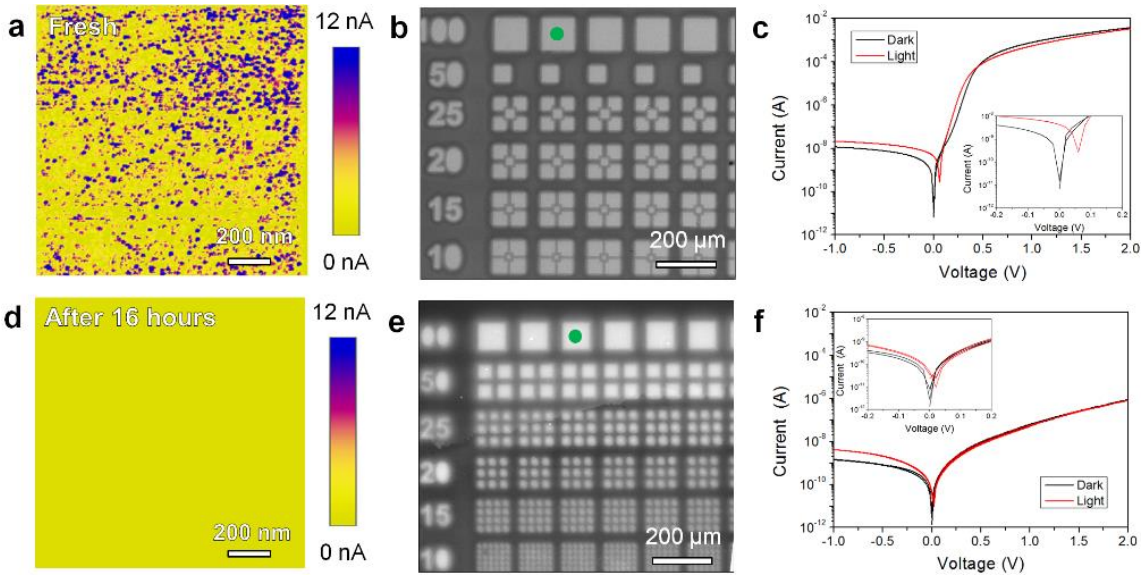

Figure 5. Electrical characterization of the 2 nm Ni coated silicon photoanodes. CAFM current maps of the 2 nm Ni/SiO_X/n-Si photoanode before (a) and after (d) continuous OER during 16 hours. The maps were obtained without bias and under illumination. (b) and(e) show the SEM images of the patterned squared electrodes on the fresh and tested samples (respectively). (c) and(f) show the I-V curves collected with the probestation for the fresh and tested samples (respectively). The black/red lines correspond to the I-V curves collected in the dark/illumination. The I-V curves shown in (c) and (f) were collected at the capacitors highlighted with green spots in (b) and (e).

The XPS analysis (Figure S9) of the 2 nm Ni samples didn't reveal any significant change compared to the 5 nm ones: the nickel, oxygen and potassium profiles are very similar, and the only remarkable change is the larger silicon signal, due to the smaller thickness of the nickel coating. Interestingly, there is a correlation between the

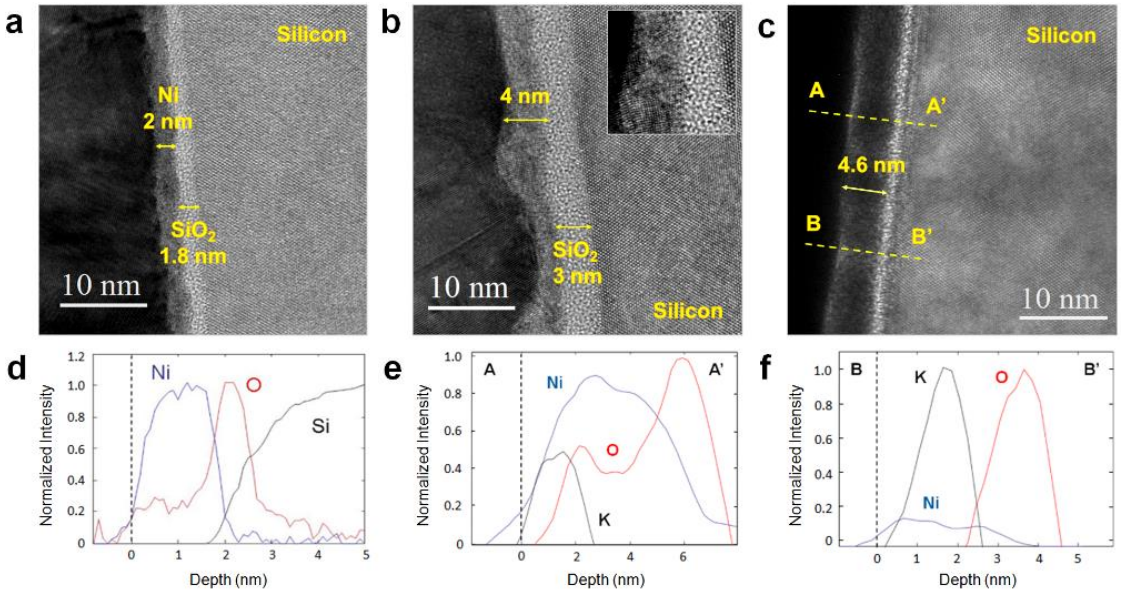

Figure 6. Atomic scale information of fresh and tested 2 nm Ni coated silicon photoanodes. Cross sectional TEM images for the 2 nm Ni/SiO_X/n-Si sample (a) before the PEC tests, (b) after 1 hour test and (c) after 24 hours test. Panel (b) has been intentionally collected in a location that shows high surface roughness and film modification. (d) shows the EELS chemical composition of the fresh sample. (e) and (f) show the EELS chemical composition of the sample tested after 24 hours test, along the sections A-A' and B-B' highlighted in (c), respectively.

potassium signal and the degradation of the sample. Further observations were made when the sample was analyzed with XTEM and EELS. Again, the fresh sample showed correct thickness, chemical composition and polycrystalline structure (Figures 6a and 6c). After 1 h, the XTEM images clearly display the roughness increase. Figure 6b intentionally shows a part of the sample that is specially corroded, and the local changes on the morphology of the material are clearly identified (see inset). After 24 hours test (Figure 6c), the thickness of the Ni layer increased up to 4.6 nm, the film became darker and, interestingly, some light nanofilaments connecting both sides of the coating can be distinguished. The EELS chemical profiles (sections A-A' and B-B', displayed in Figures 6e and 6f, respectively) reveal the formation of a NiO_X layer rich in potassium on its surface (Figure 6e), in clear agreement to the XPS data. The large lateral resolution of this technique allowed to assess the chemical composition of the light nanofilaments, revealing that they are rich in potassium, which can penetrate in the nickel layer and reach

the underlying SiO_X layer (Figure 6f). This unprecedented observation demonstrates that XPS may mask essential information related to the degradation process of the samples.

D 4 Conclusions

In summary, the degradation process of Ni/SiO_X/n-Si photoanodes under light-driven OER has been analyzed using sub-nanometer characterization tools. The main conclusions of our work are: i) the activity/lifetime of the cells is lower/longer using thick Ni coatings; ii) 2 nm nickel coated samples fail within ~18 hours due to the formation of a potassium-rich NiO_X layer, which is highly resistive and unable to split water; iii) 5 nm and 10 nm nickel coated samples showed stable currents during more than ~150 and ~ 260 hours, respectively. In this case the Ni films also turned into NiO_X, but the resulting layer was very homogeneous and free of impurities. The degradation of these samples was related to the formation of holes in the active NiO_X layer, and the size/density of holes depends on its thickness; and iv) we demonstrate that essential information is masked in the XPS profiles, as the potassium contamination in the NiO_X film can only be detected by combining TEM and EELS, indicating that previous reports in the field of water-splitting (which normally use traditional characterization tools with low spatial resolution) may be ignoring essential degradation phenomena. These findings may be of interest for the water-splitting community, as they reveal essential information that could be useful to enhance the lifetime of the cells.

D 5 Acknowledgement

This work has been partially supported by the Young 973 National Program of the Chinese Ministry of Science and Technology (grant no. 2015CB932700), the Major State Basic Research Development Program of China (grant no. 2011CB013101), the National Natural Science Foundation of China (grants no. 11225208, 11521202, 11172001,

10872003, 10932001, 11072230 and 11375127), and the Natural Science Foundation of Jiangsu Provence (grant BK20130280). The Project Funded by the Priority Academic Program Development of Jiangsu Higher Education Institutions (PAPD) is also acknowledged. Professor Mario Lanza acknowledges generous start-up funding from Soochow University and from the "Young 1000 Talent Program" of China. M.J. Kenney from Stanford University is also acknowledged for results discussion.

D 6 References

[1] T. R. Cook, D. K. Dogutan, S. Y. Reece, Y. Surendranath, T. S. Teets, D. G. Nocera, Solar energy supply and storage for the legacy and nonlegacy worlds, *Chem. Rev.* **2010**, *110*, 6474.

[2] M.G. Walter, E.L. Warren, J.R. McKone, S.W. Boettcher, Q. Mi, E.A. Santori, N.S. Lewis, Solar water splitting cells, *Chem. Rev.* **2010**, *110*, 6446.

[3] A.W. Bott, Electrochemistry of Semiconductors, *Current Separations* 1998, *17*, 87.

[4] Z.B. Chen, H.N. Dinh, E. Miller, SpringerBriefs in Energy, first ed., Springer, New York, 2013.

[5] L. Li, L. Duan, Y. Xu, M. Gorlov, A. Hagfeldt, L. Sun, A photoelectrochemical device for visible light driven water splitting by a molecular ruthenium catalyst assembled on dye-sensitized nanostructured TiO2, *Chem. Commun.* **2010**, *46*, 7307.

[6] M. J. Kenney, M. Gong, Y. Li, J. Z. Wu, J. Feng, M. Lanza, H. Dai, High-performance silicon photoanodes passivated with ultrathin nickel films for water oxidation, *Science* **2013**, *342*, 836.

[7] K. Sun, M. T. McDowell, A. C. Nielander, S. Hu, M. R. Shaner, F. Yang, B. S. Brunschwig, N. S. Lewis, Stable Solar-Driven Water Oxidation to O2(g) by Ni-Oxide-Coated Silicon Photoanodes, *J. Phys. Chem. Lett.* **2015**, *6*, 592.

[8] K. Sun, F. H. Saadi, M. F. Lichterman, W. G. Hale, H.-P. Wang, X. Zhou, N. T. Plymale, S. T. Omelchenko, J.-H. He, K. M. Papadantonakis, B. S. Brunschwig, N. S. Lewis, Stable solar-driven oxidation of water by semiconducting photoanodes protected by transparent catalytic nickel oxide films, *Proc. Natl. Acad. Sci. USA* **2015**, *112*, 3612.

[9] Y. W. Chen, J. D. Prange, S. Dühnen, Y. Park, M. Gunji, C. E. D. Chidsey, P. C. McIntyre, Atomic layer-deposited tunnel oxide stabilizes silicon photoanodes for water oxidation, *Nat. Mater.* **2011**, *10*, 539.

[10] J. Du, Z. Chen, S. Ye, B. J. Wiley, T. J. Meyer, Copper as a robust and transparent electrocatalyst for water oxidation, *Angew. Chemie - Int. Ed.* **2015**, *54*, 2073.

[11] F. Yu, F. Li, B. Zhang, H. Li, L. Sun, Efficient Electrocatalytic Water Oxidation by a Copper Oxide Thin Film in Borate Buffer, *ACS Catal.* **2015**, *5*, 627.

IV

[12] N. C. Strandwitz, D. J. Comstock, R. L. Grimm, A. C. Nichols-Nielander, J. Elam, N. S. Lewis, Photoelectrochemical Behavior of n-type Si(100) Electrodes Coated with Thin Films of Manganese Oxide Grown by Atomic Layer Deposition, *J. Phys. Chem. C* **2013**, *117*, 4931.

[13] V. Artero, M. Chavarot-Kerlidou, M. Fontecave, Splitting water with cobalt, *Angew. Chemie - Int. Ed.* **2011**, *50*, 7238.

[14] K. Sun, N. Park, Z. Sun, J. Zhou, J. Wang, X. Pang, S. Shen, S. Y. Noh, Y. Jing, S. Jin, P. K. L. Yu, D. Wang, Nickel oxide functionalized silicon for efficient photo-oxidation of water, *Energy Environ. Sci.* **2012**, *5*, 7872.

[15] K. Sun, S. Shen, J. S. Cheung, X. Pang, N. Park, J. Zhou, Y. Hu, Z. Sun, S. Y. Noh, C. T. Riley, P. K. L. Yu, S. Jin, D. Wang, Si photoanode protected by a metal modified ITO layer with ultrathin NiO(x) for solar water oxidation, *Phys. Chem. Chem. Phys.* **2014**, *16*, 4612.

[16] S. Hu, M. R. Shaner, J. A. Beardslee, M. Lichterman, B. S. Brunschwig, N. S. Lewis, Amorphous TiO_2 coatings stabilize Si, GaAs, and GaP photoanodes for efficient water oxidation, *Science* **2014**, *344*, 1005.

[17] B. Mei, A. A. Permyakova, R. Frydendal, D. Bae, T. Pedersen, P. Malacrida, O. Hansen, I. E. L. Stephens, P. C. K. Vesborg, B. Seger, I. Chorkendorff, Iron-Treated NiO as a Highly Transparent p-Type Protection Layer for Efficient Si-Based Photoanodes, *J. Phys. Chem. Lett.* **2014**, *5*, 3456.

[18] K. Jun, Y. S. Lee, T. Buonassisi, J. M. Jacobson, High photocurrent in silicon photoanodes catalyzed by iron oxide thin films for water oxidation, *Angew. Chemie - Int. Ed.* **2012**, *51*, 423.

[19] J. Yang, K. Walczak, E. Anzenberg, F. M. Toma, G. Yuan, J. Beeman, A. Schwartzberg, Y. Lin, M. Hettick, A. Javey, J. W. Ager, J. Yano, H. Frei, I. D. Sharp, Efficient and sustained photoelectrochemical water oxidation by cobalt oxide/silicon photoanodes with nanotextured interfaces, *J. Am. Chem. Soc.* **2014**, *136*, 6191.

[20] B. Mei, B. Seger, T. Pedersen, M. Malizia, O. Hansen, I. Chorkendorff, P. C. K. Vesborg, Protection of p(+)-n-Si Photoanodes by Sputter-Deposited Ir/IrOx Thin Films, *J. Phys. Chem. Lett.* **2014**, *5*, 1948.

[21] A. G. Scheuermann, J. D. Prange, M. Gunji, C. E. D. Chidsey, P. C. McIntyre, Effects of catalyst material and atomic layer deposited TiO2 oxide thickness on the water oxidation performance of metal–insulator–silicon anodes, *Energy Environ. Sci.* **2013**, *6*, 2487.

[22] C. Gui, M. Elwenspoek, N. Tas, J. G. E. Gardeniers, The effect of surface roughness on direct wafer bonding, *J. Appl. Phys.* **1999**, *85*, 7448.

[23] B. Conway, T. Liu, Experimental evaluation of adsorption behaviour of intermediates in anodic oxygen evolution at oxidized nickel surfaces, *J. Chem. Soc., Faraday Trans.1* **1987**, *83*, 1063.

[24] M. Miyazaki, H. Hirayama, Thickness- and deposition temperature-dependent morphological change in electronic growth of ultra-thin Ag films on Si(111) substrates, *Surf. Sci.* **2008**, *602*, 276.

IV

D 7 Supporting Information

Paper D: Ageing mechanisms of highly active and stable nickel-coated silicon photoanodes for water splitting

Index

Figure S1. Cyclic voltammetry of nickel photoanodes of different thicknesses

Figure S2. Cyclic voltammetry of 2 nm nickel coated silicon photoanode without native SiO_2

Figure S3. Formation process of oxygen bubbles in I-t curves

Figure S4. Roughness of a piece of silicon corroded in potassium hydroxide

Figure S5. XPS spectra for the 5 nm nickel coated silicon photoanode after different testing times

Figure S6. AFM and SEM roughness analysis of a 10 nm nickel coated silicon photoanode

Figure S7. Relationship between the nickel thickness and the size of the corrosion-related holes

Figure S8. Analysis of the shape of I-t curves after short and long testing times

Figure S9. XPS spectra for the 2 nm nickel coated silicon photoanode after different testing times

IV

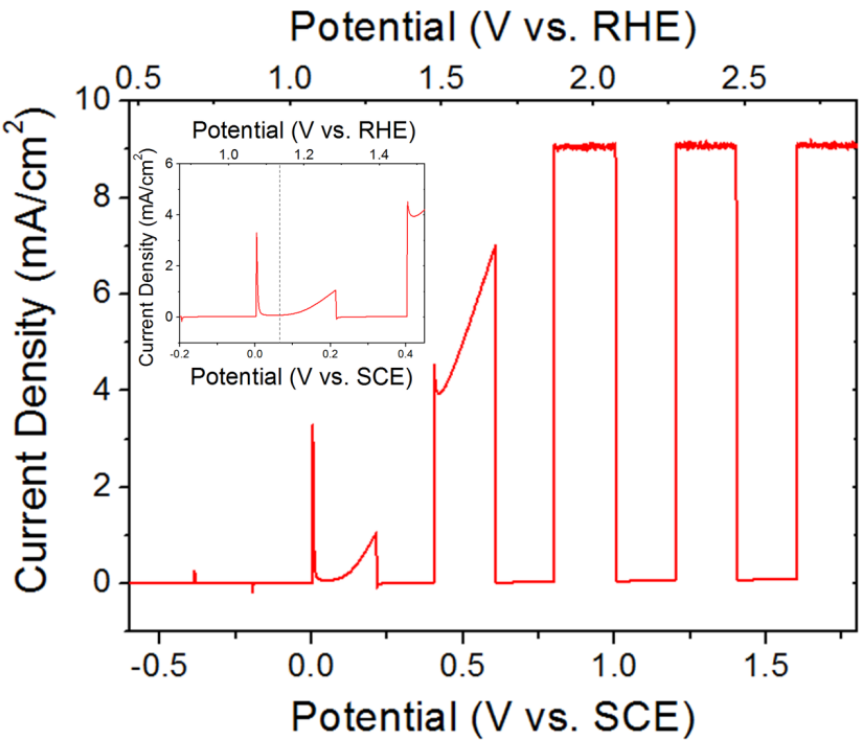

Figure S1. Linear sweep voltammetry (LSV) recorded for a 2 nm Ni coated silicon photoanode under an illumination of 50 mW/cm^2. In the LSV, the light is being chopped.

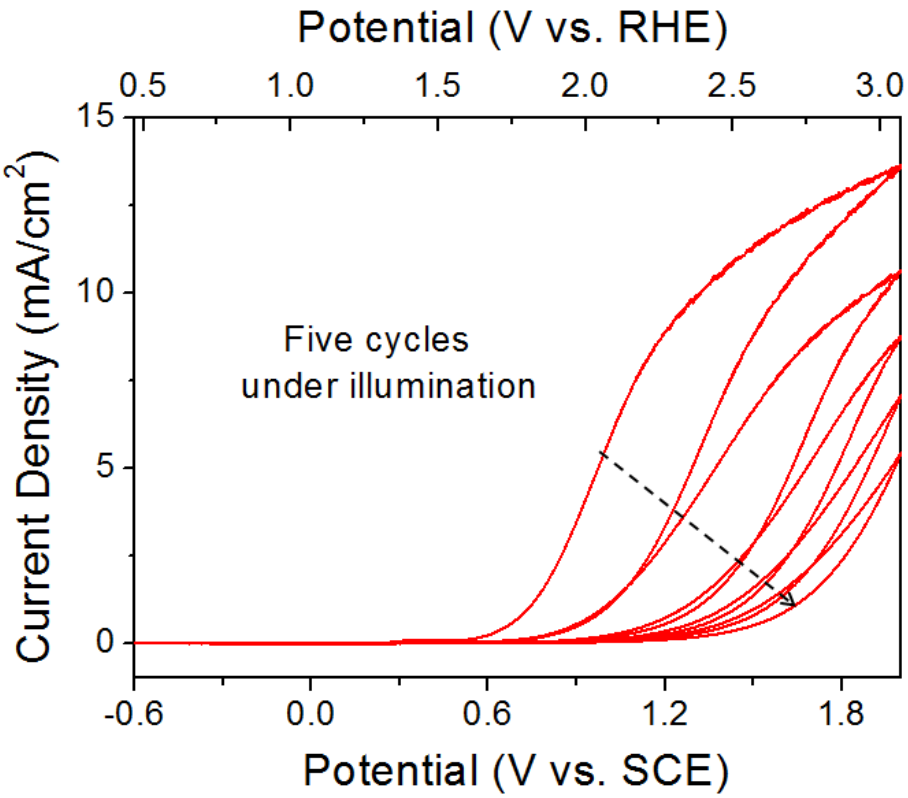

Figure S2. Consecutive five cycles cyclic voltammograms recorded for a 2 nm Ni coated silicon photoanode (without native SiO_2) under an illumination of 50 mW/cm^2. The native SiO_2 was etched by HF solution before nickel deposition. The fast decay indicates that SiO_2 is beneficial to the stability of the photoanode.

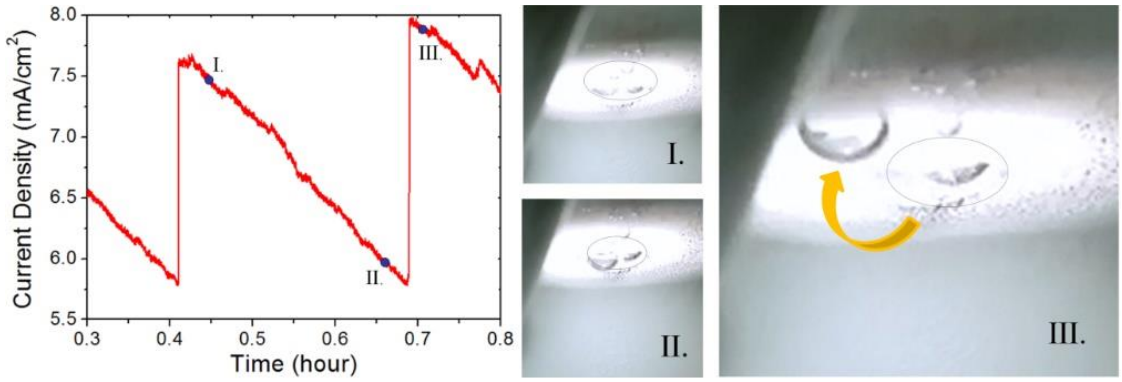

Figure S3. Amperometric I-t curve measured at 1.8 V vs. SCE for the 2 nm Ni photoanode under an illumination of 50 mW/cm^2. The I-t curve clearly displays the typical saw tooth shape related to the formation process of a bubble. On the right, the digital camera pictures of the detachment of a bubble in the points I, II and III highlighted in the I-t curve.

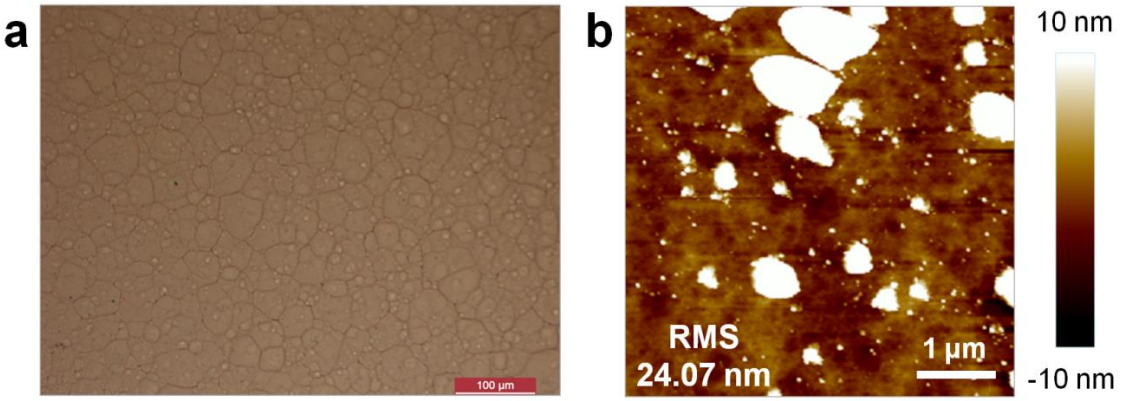

Figure S4. (a) Optical microscope and (b) AFM images of a piece of silicon corroded in potassium hydroxide during 5 days, showing a high surface roughness.

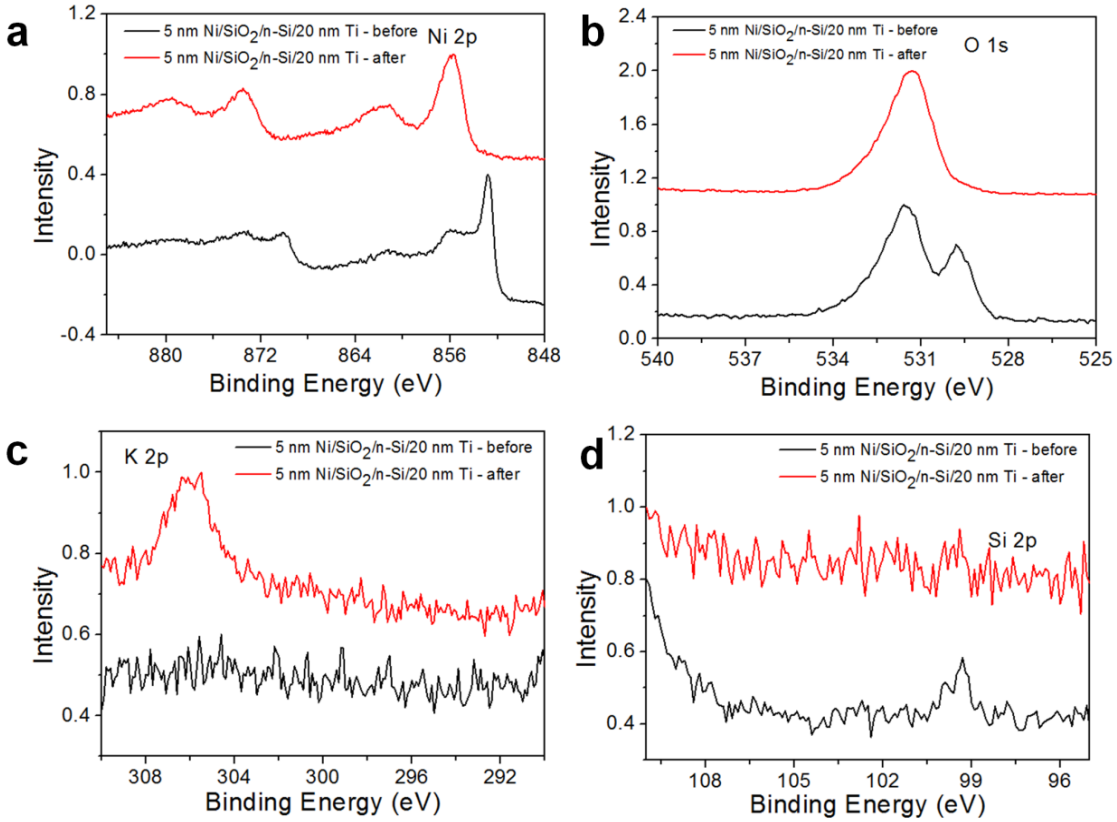

Figure S5. XPS spectra for the 5 nm Ni photoanode after 24 h PEC tests (red line). The spectra of the fresh sample are also showed as reference (black).

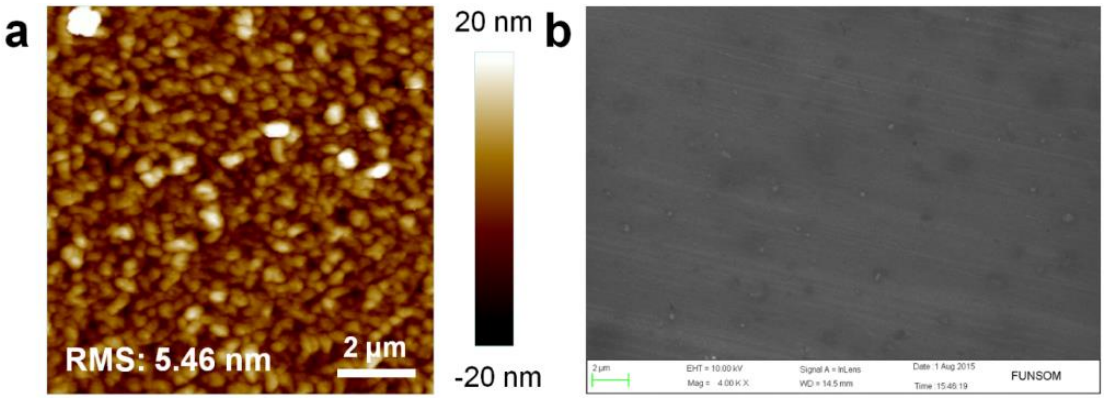

Figure S6. (a) AFM and (b) SEM images for the 10 nm sample after 11 days OER test under 50 mW/cm^2 illumination. The AFM image corroborates the increase of the surface roughness.

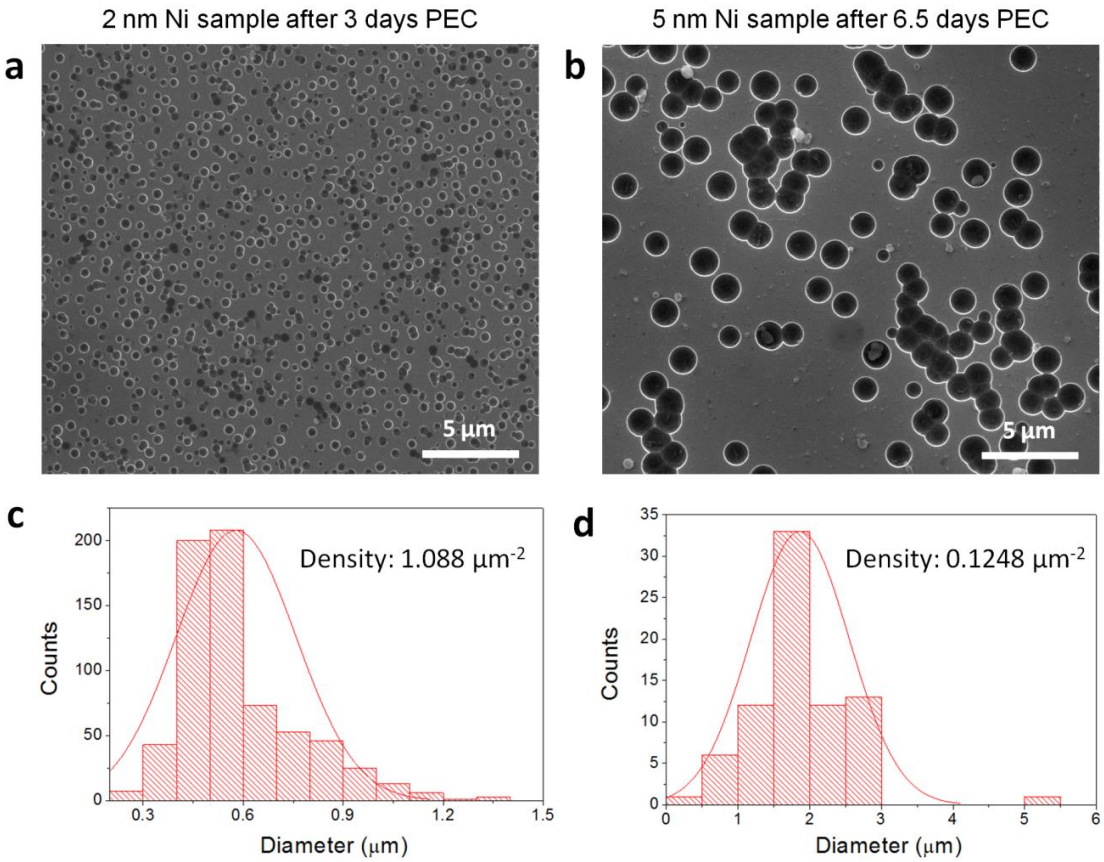

Figure S7. SEM images of the two photoanodes fabricated in this work after different testing times under 50mW/cm^2 light illumination. The corrosion-related holes start to appear at different times and they have different sizes. Also the amount of holes per µm^2 is different.

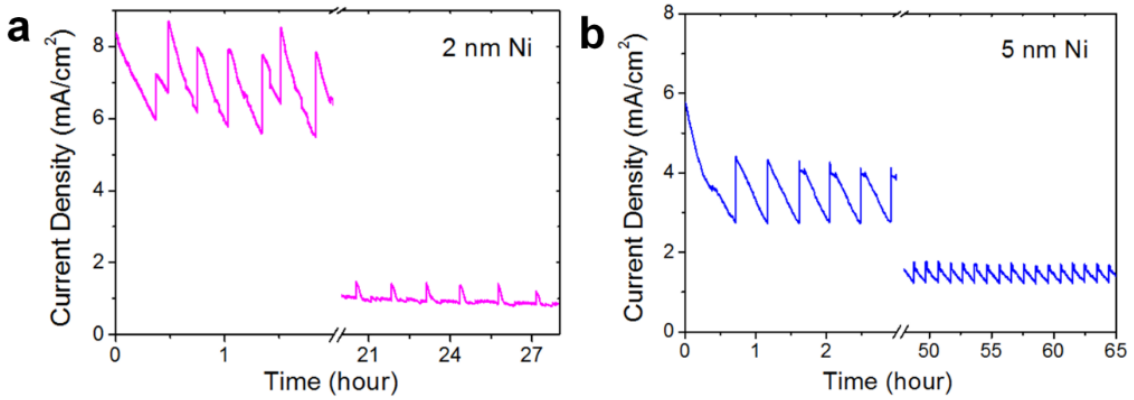

Figure S8. I-t curves measured for the 2 nm and 5 nm nickel-coated silicon photoanodes under collected under 50 mW/cm^2 light intensity in KOH by applying 1.8 V vs. SCE. The plots display the different shapes (conduction mechanisms) of the I-t curve for initial and final times.

IV

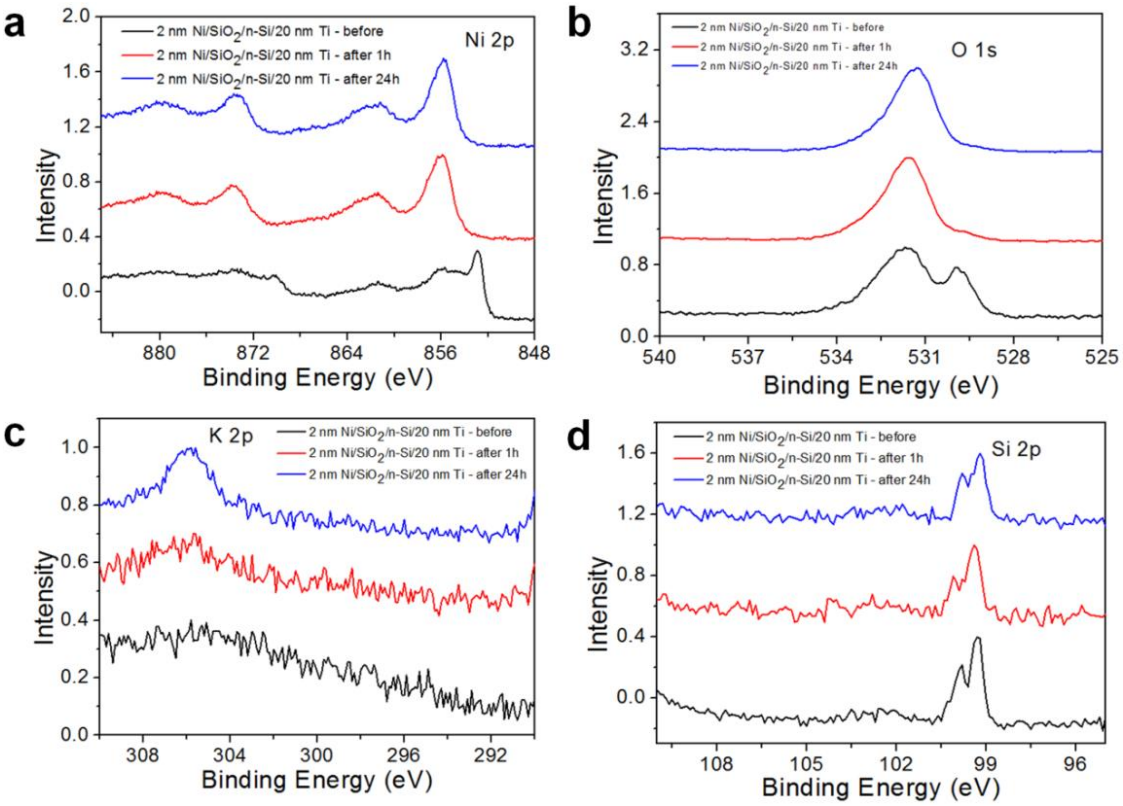

Figure S9. XPS spectra for the 2 nm Ni photoanodes after 1 h (red) and 24 h (blue) PEC tests. The spectra of the fresh sample are also showed as reference (black).

Paper E: Substitution of native silicon oxide by titanium in Ni-coated silicon photoanodes for water splitting solar cells

IV

Y. Shi, T. Han, C. Gimbert-Suriñach, X. Song, M. Lanza, A. Llobet

J. Mater. Chem. A, **2017**, *5*, 1996.

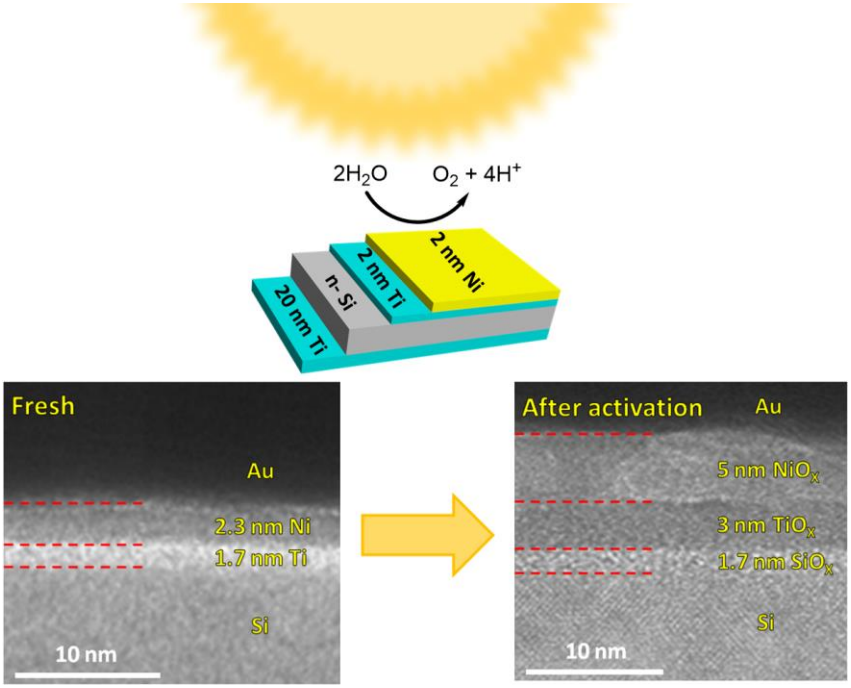

Abstract

Using an ultrathin (2 nm) evaporated Ti film to replace the native SiO_X of the nSi photoanode and then coating it by thin (2 and 5 nm) Ni layers, the resulting 2 nm Ni/2 nm Ti coated nSi photoanodes (without the native SiO_X) reach a photocurrent onset potential of -42 mV relative to SCE reference electrode in 1 M KOH under 1 simulated sun illumination (-202 mV relative to the potential for oxygen evolution reaction). With increasing the thickness of the Ni layer to 5 nm, the 5 nm Ni/2 nm Ti/nSi photoanodes show 50 mV lower onset potential than 5 nm Ni directly coated on native SiO_X/nSi

IV

photoanodes and exhibit a very stable photoelectrochemical performance, which keep 100 % activity (10 mA/cm^2 at 0.8 V vs. SCE) for ~6.5 days. These results can be comparable to those of the typical NiO_X coated nSi photoanodes with n-p^+ buried homojunctions. Using Ti layer to replace the native SiO_X of the nSi photoanodes increases the conductivity of the sample and helps the charge transfer process. In addition, the interlayer Ti film absorbs the oxygen from nearby layers or from the atmosphere, making the Ti layer partially oxidized. The in situ TiO_X layer formed from evaporated Ti has more electron defects than the ALD deposited TiO_2, and could be responsible for the improved hole conduction process.

Contribution

Yuanyuan Shi designed the interface engineering for the photoanodes fabrication, performed the photoelectrochemical measurements, morphological and chemical characterizations, and wrote the manuscript.

E 1 Introduction

Environmental and energy issues are producing global concern, not only due to the massive pollution generated by traditional fossil fuels, but also because our reserves are expected to be depleted within ~ 100 years.[1] Since human demand for energy is continuously growing, the use of clean and inexhaustible sources of energy is of utmost importance. Sunlight is an abundant and renewable energy source, but its intermittency and location dependency, as well as its difficulty for being stored and transported strongly make its definitive establishment difficult. One possible solution is the development of photoelectrochemical (PEC) devices that use the power of sunlight to produce clean chemical fuels (like hydrogen), and among them solar-driven water splitting device is one of the most promising PEC devices due to its inexpensive costs, simple device design, efficient and renewable energy production.[2,3] The first demonstration in this direction dates from 1972,[4] when Fujishima and Honda observed for the first time the splitting of water (into hydrogen and oxygen) using a n-type TiO_2 semiconductor photoelectrode. The chemical reactions involved in this fuel generation process are:

* Overall water splitting: $2H_2O \rightarrow O_2 \uparrow + 2H_2 \uparrow$ (*Eq. 1*)

* Oxygen evolution reaction (OER): $2H_2O + 4h^+ \rightarrow O_2 \uparrow + 4H^+$ (*Eq. 2*)

* Hydrogen evolution reaction (HER): $4H+ + 4\ e^- \rightarrow 2H_2 \uparrow$ (*Eq. 3*)

Modern water splitting devices use a tandem cell containing a photoanode and a photocathode (with electrocatalysts) immersed in an aqueous solution and isolated to each other by a proton exchange membrane, and this feature also allows studying them individually. Both photoelectrodes are usually made of semiconducting materials, so that when illuminated, free electron-hole pairs can be generated and driven in opposite

directions, leading to a net current able to split water by electrolysis. When electrons/holes are transferred from the photoanode/photocathode to the electrolyte, OER/HER is produced on their surface. The clue for the development of efficient, robust and scalable PEC water splitting systems is to find cost-effective, active and durable semiconducting photoelectrodes that ensure the generation of abundant OER/HER reaction during long periods of time. In this direction, the main trade-off is to use a material with a band gap small enough for adsorbing high percentage of light, and at the same time providing effective charge separation.

Silicon is cheap and a good light absorber, which makes it a good candidate material for the photoelectrodes. However, its activity is too small and the continuous generation of OER/HER on its surface could corrode it, leading to dramatic performance decay.[5,6] To solve these problems, cutting-edge PEC water splitting solar cells coat the surface of silicon using one or few protective layers. For example, metal/TiO_2 bilayer stacks have become very popular coatings to protect the surface of n-type Si photoanodes for water splitting, as the TiO_2 film can serve as anti-corrosion coating,[7-11] while the metallic layers can provide electrocatalysts to boost the OER reaction. Another solution is to use a metal based coating that carries out both protective and catalytic functions.[12-22] Among them, Ni and its derivates (like Ni-Fe and Ni-Cr) have shown the best performances when protecting the surface of Si.[12-18] Later works combined both methods and the resulting Ni/TiO_2/nSi photoanodes showed to be both active and stable.[11] Interestingly, in all these reports the native oxide of the Si wafers (from now on SiO_X) was not removed; Han *et al.*[18] reported that the SiO_X layer is necessary for ensuring a correct adhesion between the Si and the protective coatings. Esposito *et al.*[23] replaced the native SiO_X layer by a 2 nm thick rapid thermal oxidation (RTO) grown SiO_2, which provides high quality SiO_2/Si interface with low interfacial defects.[24] Nevertheless, the

function of the native SiO_X is still intriguing, and in this investigation we asked ourselves if other materials could play the role of adhesion layer even better than native SiO_X.

Titanium metallic layers are widely used in microelectronics for enhancing the adhesion between different materials, including Si substrates and metallic electrodes like Pt and Au.[25,26] Moreover, Ti is a non-precious metal compatible with the semiconductors industry, and it can be easily deposited on the surface of Si using different standard techniques, including electron beam evaporator, sputtering and atomic layer deposition (ALD).[26-28] In this work we use for the first time an ultra-thin film of Ti to replace the native SiO_X layer in nSi photoanodes for water splitting. The resulting Ni/Ti/nSi photoanodes show one of the lowest onset potentials ever achieved in metal-coated nSi photoanodes,[17, 22] even comparable to that of more complex and expensive cells using n-p^+ junctions. Furthermore, the currents are stable during long periods of time above 6.5 days. The results here presented can help to remarkably enhance the performance and reduce the cost of photoanodes for water splitting devices.

E 2 Materials and Methods

E 2.1 Sample fabrication

Phosphorus-doped [100] and single side polished n-type silicon wafers with a resistivity of 0.2 – 0.6 Ω·cm (525 ± 10 μm thick) were purchased from ProLog. The Ti, Ni and Au films were deposited using an e-beam evaporator (PVD 75, Kurt J. Lesker) using targets from Zhongnuo Xincai Technology with a purity of 99.999%. All the organic solvents were analytically pure with the volume of 500 mL from Sinopharm Chemical Reagent Co., Ltd. Before the metallic coatings deposition, the silicon wafers were cleaned with acetone and ethanol in an ultrasonic bath for 10 min each, and then dried with N_2 gas flow (40 L, ≤ 4N, 13.5 ± 0.5 MPa, MESSER). For some of the silicon

wafers, the native SiO_X layer was etched with HF (Sigma-Aldrich, 25 mL, no. 695068) in water (Volume ratio: HF/H_2O=1/4) for 10 s. After etching the native SiO_X in HF, the silicon wafers were rinsed with deionized water and dried with N_2 gas flow. Immediately after the cleaning and the etching process, 2 nm Ti films were deposited at a rate of 0.4 Å/s on the silicon wafers, then 2, 5, or 10 nm Ni films were deposited at a rate of 0.2 Å/s on the 2 nm Ti film. For each sample, a small piece of the sample was taken to deposit 50 nm Au at a rate of 0.5 Å/s right after the Ni deposition, which makes it ready for the cross-sectional transmission electron microscope (TEM) characterization. For all the samples, 20 nm Ti films were evaporated on the backside of the silicon to increase the conductivity of the sample.

E 2.2 PEC characterization

After the sample fabrication, the samples were pasted on a copper tape for the PEC characterization in a standard three-electrodes configuration in a 140 mL Teflon box at room temperature connecting the sample (as working electrode) with a saturated calomel (SCE, saturated KCl) reference electrode and a Pt wire counter electrode through 660E potentiostat (CH Instruments, Inc.). The exposed area of the samples for the oxygen evolution reaction (OER) in the Teflon box is around 0.5 cm^2. The redox potentials reported in this work are all referenced vs. SCE, an auxiliary axis with conversion to the RHE electrode is given at the top of the electrochemistry graphs. The onset potential values reported in this work are taken at a current density of ca. 1 mA/cm^2. The electrolyte used for the PEC characterization is 1 M KOH, which was prepared by dissolving 22.4 g KOH into 400 mL of deionized water. The KOH solid is analytical pure and purchased from Sinopharm Chemical Reagent Co., Ltd (<0.001 % Fe). The samples were illuminated by 1 simulated sun, which was provide by 150 W Xe Arc Lamps (LS-150,

ABET technology and 66906, Newport Corporation), and a light intensity meter (Newport, 1918R) was used to calibrate the light to 1 sun (100 mW/cm^2) at room temperature.

E 2.3 Micro and nanoscale characterization

The morphology of the samples before and after the PEC tests was characterized by means of scanning electron microscopy (SEM, FEI Quanta 200FEG), cross-sectional TEM (at a high tension of 200 KV, FEI Titan), and AFM (in tapping mode, Brucker Multimode V). The samples for the cross-sectional TEM are all protected by 50 nm Au and cut by focused ion beam (FIB, FEI 450S). A silicon tip without any coating (NanoWorld, NCH-50) was used for the AFM tapping mode, and all the AFM images were analyzed by the NanoScope Analysis software (version 1.4). The chemical composition of the samples was characterized by the energy dispersive spectrometry (EDX, combined with TEM), and X-ray photoelectron spectroscopy (XPS). The X-ray source for the XPS is a mono-chromatic Al Kα ($h\nu$ = 1486.6 eV) equipped with a KRATOS Axis ultra-DLD spectrometer. High resolution spectra were acquired with a pass energy of 20 eV at a base pressure of < 5×10^{-9} Torr. All the element peaks have been corrected by the position of C 1s peak in the XPS spectrum, which is prescribed to be at 285.0 eV.

E 3 Results and discussion

Figure 1a shows the XTEM image of an as fabricated 2 nm Ni/native SiO_X/nSi photoanode for water splitting. The top 50 nm Au film is a protective and image contrast layer for XTEM characterization, and has not been used in PEC experiments. As it can be observed, the native silicon oxide is 1.8 nm thick, and the real thickness of the Ni layer

matches the theoretical one (2 nm). The green line in Figure 1d shows the typical cyclic voltammogram (CV) measured for this sample in 1 M KOH electrolyte under 1 sun illumination. As it can be observed, the onset potential is ~ 0.15 V vs. SCE, in agreement with previous works.[18] Kenney *et al.*[13] achieved a lower onset potential of 0 V vs. SCE in similar samples (probably due to differences on the type of nSi and/or the SiO_X interlayer used in their work).

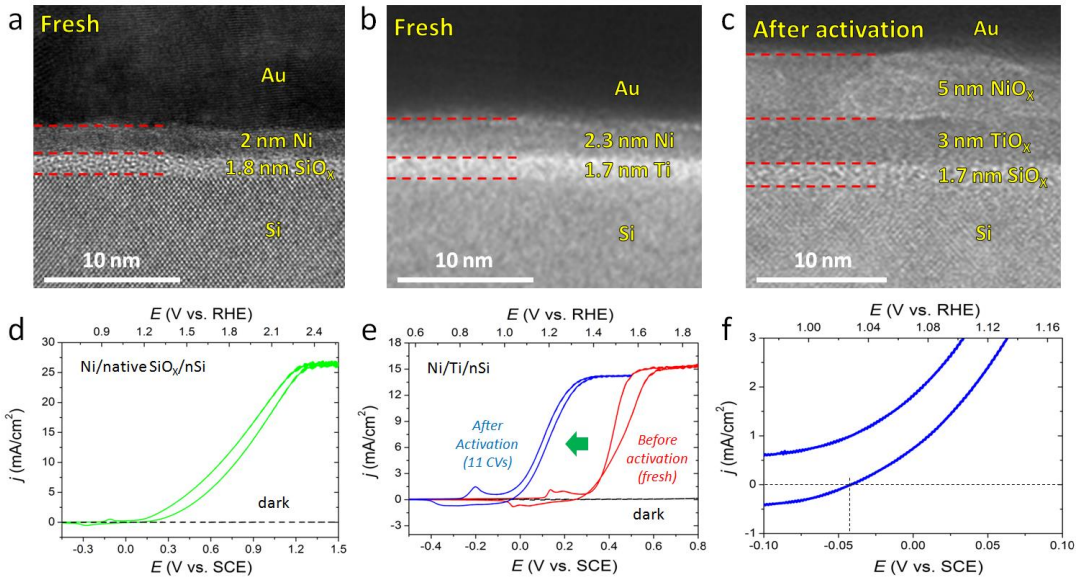

Figure 1. Sample structure and PEC performance of 2 nm Ni coated nSi photoanodes, with and without using Ti interlayer to replace the native SiO_X layer. (a) is the cross-sectional TEM image of the fresh 2 nm Ni/native SiO_X/nSi sample. (b) and (c) are cross-sectional TEM images of 2 nm Ni/2 nm Ti/nSi photoandes before and after the PEC activation tests, respectively. This kind of photoanodes were etched with HF solution to remove the native SiO_X before the metal depositions. 50 nm Au layers were deposited rightly (a-b) after the deposition of the Ni layer and (c) after the PEC tests to avoid the contamination from the atmosphere. Cyclic voltammetry (CV) scans collected on fresh 2 nm Ni coated nSi photoanode (d) without and (e) with using metallic Ti to replace the native SiO_X layer. The photoanode shows an activation process after a period of PEC tests in the solution (from the red lines to blue lines). (f) is one zoom-in image of (e), which indicates the 2 nm Ni/2 nm Ti/nSi photoanode shows a low onset potential, about -42 mV vs. SCE. All the CV scans were obtained at a scan rate of 100 mV/s with iR compensation in 1 M KOH electrolyte under 1 simulated sun illumination. The dashed black lines are the CV scans obtained in the dark condition.

In the next step, the native SiO_X was replaced by a 2 nm thick Ti layer. To do so, the SiO_X layer was etched by immersing the nSi wafers in HF solution (volume ratio: HF: H_2O = 1 : 4) for 10 seconds, and then the 2 nm Ti and 2 nm Ni films were evaporated on

Table 1. Comparative study of the Ni or NiO_X based Si photoanodes

Year	Photoelectrode	Onset potential (vs. SCE)	Conditions	Ref.
2012	Sol-gel 37 nm NiO_X/SiO_X/nSi	0.45 V	pH 7.2 1 sun	12
2013	2 nm Ni/SiO_X/nSi	0 V	1 M KOH 2 suns	13
2014	100 nm Ni islands/4-143 nm TiO_2/np^+ Si or nSi	0.05 V	1 M KOH 1.25 suns	8
2014	Fe-treated 50 nm NiO/5 nm Ni/np+ Si	-0.02 V (300 h)	1 M KOH 1 sun	14
2015	50-112 nm NiO_X/np^+ Si	-0.08 ~ 0 V (1200 h)	1 M KOH 1 sun	15, 16
2015	5-8 nm Ni/TiO_2/nSi	0.13 V	1 M KOH 1 sun	11
2015	NiO_x/2 nm CoO_X/SiO_X/nSi	-0.08 V (1500h)	1 M KOH 1 sun	17
2016	2 nm Ni/2 nm Ti/nSi	-0.05 ~ -0.03 V	1 M KOH 1 sun	This work

top. The XTEM images (Figure 1b) show reasonably good agreement between the real and theoretical thickness of each layer. The first CV collected for this sample under illumination (red line in Figure 1e) reveals an increase of the onset potential up to 300 mV vs. SCE (100 mV higher than in the Ni/SiO_X/nSi counterpart). Interestingly, after 11 successive CV scans the onset potential remarkably decreased down to -42 mV (see blue lines in Figure 1e and Figure 1f), one of the lowest overpotentials reported in the literature for nSi based photoanodes (see Table 1). As depicted in Table 1, comparable onset potential values have been achieved using n-p^+ Si junctions (instead of nSi), but that makes the overall fabrication process much more complex and expensive, as implementation, high temperature and/or epitaxy processes are required.[7,15] Activation processes of nickel oxide anodes and photoanodes have been observed before,[16,29-31] and

in most of the times they were related to the incorporation of iron into the nickel layer forming a better Ni-Fe catalyst for the oxygen evolution reaction. However, in the previously reported activation processes, the maximum decrease in overpotential was in the order of 150 mV while in the present work we observed a 342 mV shift, suggesting that other factors might contribute to the activation phenomenon. In order to get further insights in the intrinsic mechanisms of the activation process shown in Figure 1e, the tested 2 nm Ni /2 nm Ti/nSi photoanodes have been analyzed with XTEM. As shown in Figure 1c, the number of layers on the nSi and their thicknesses change after the activation process: *i)* the thickness of the Ni layer increased from 2.3 nm to 5 nm, *ii)* the Ti layer increased from 1.7 nm to 3 nm, and *iii)* a new layer with a thickness of ~ 1.7 nm was formed below the Ti layer, most probably SiO_X layer. At few positions of the sample the Ni/Ti interface is not so clear (Figure S1), leading to a NiTi mixed layer with a thickness of ~ 7.2 nm.

EDX analysis of the Ni/Ti/nSi samples allowed us to explore the atomic rearrangements during the activation process. Figures 2a and 2b show the Ni, Ti, O and Si maps of the nanostructured photoanodes before and after 11 CVs. For the fresh sample, the Ni/Ti/nSi sandwiched structure can be very clearly observed and the signals don't overlap, confirming the correct fabrication of the sample. Interestingly, an unexpected large amount of O overlaps the Ti layer. Parts of the oxygen signal in Figure 2a is a bit below the titanium signal, which may be due to the ultrathin (0.1-0.2 nm) re-formed SiO_X during 5-10 min exposure in air atmosphere at room temperature after the native SiO_X etching process.[32] Additional characterization by XPS (Figure 2c) revealed that: *i)* the main binding energy of Ni $2p_{3/2}$ peak in the fresh Ni/Ti/nSi sample is at 852.6 eV, which belongs to pure metallic Ni^0;[33] *ii)* the Ti $2p_{3/2}$ peak in the fresh Ni/Ti/nSi sample is at 458.8 eV, which is the typical binding energy of the Ti element in TiO_2;[33] *iii)* the binding energy

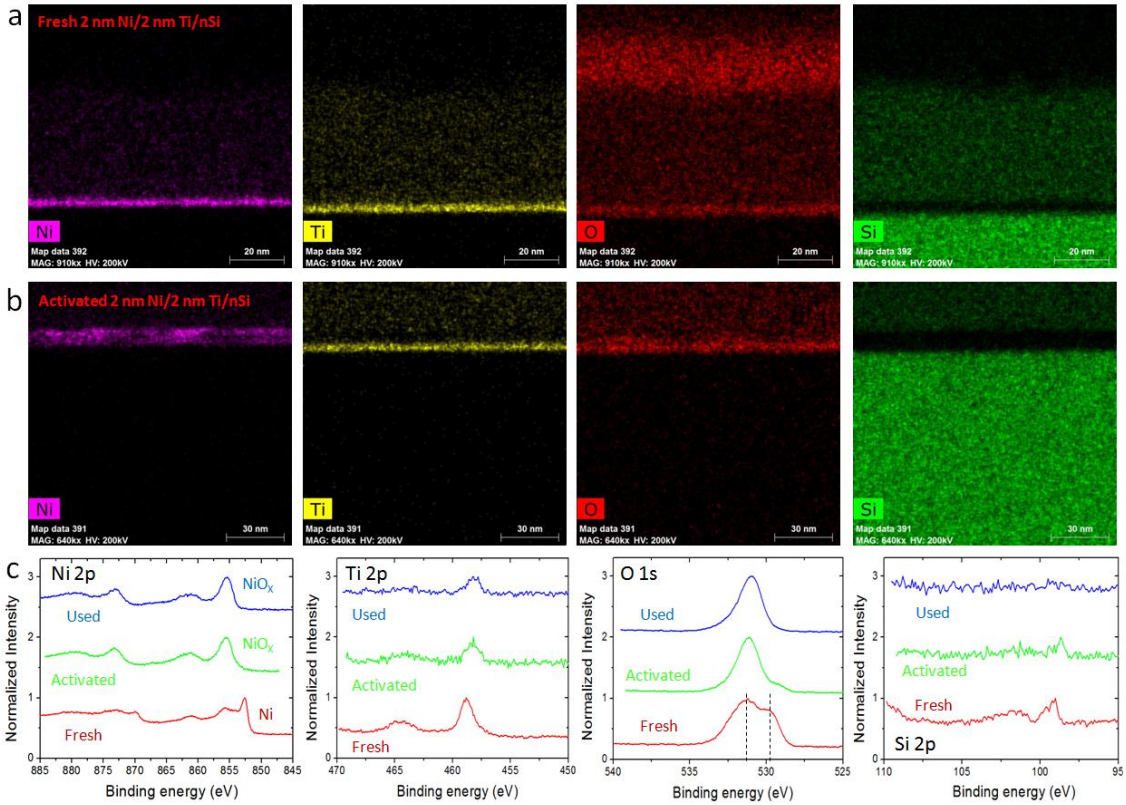

Figure 2. Chemical composition analysis of the 2 nm Ni/2 nm Ti/nSi photoanodes before and after the PEC activation process. Cross-sectional EDX maps of (a) fresh and (b) activated 2 nm Ni/2 nm Ti/nSi photoanodes. The Ni, Ti, O and Si element composition maps are exhibited in both (a) and (b) to observe the difference between these two samples. (c) XPS spectra of fresh (red), activated (green) and used (blue) 2 nm Ni/2 nm Ti/nSi photoanodes. Used sample means the photoanode has lost the activity. The binding energy regions of Ni 2p, Ti 2p, O 1s and Si 2p are all shown to track the change of each sample after the each period of the PEC tests.

of O 1s in the fresh Ni/Ti/nSi sample shows two peaks at 529.7 eV and 531.2 eV; the first one (529.7 eV) is related to the presence of metal oxides in the sample. As the Ni peak shows to be metallic, this observation suggests that the Ti film oxidized, becoming TiO_X; the second one (531.2 eV) could be related to the presence of hydroxides and/or carbonates in the sample.[33,34] These observations could be explained as follows: most probably Ti reacted with the atmosphere and got partially/totally oxidized during the fabrication process, as we needed to break the vacuum (10^{-5} torr) in the e-beam evaporator for changing the metal source (this process took ~10 minutes). Moreover, despite the time between the fabrication and XPS characterization was only 1 day, the top Ni coating is so

thin (2 nm) that O and H atoms may filtrate until reaching the Ti film. In any case, it is expected that when exposed to the atmosphere some Ti atoms bond with oxygen and form TiO_X, but some still remain in their metallic Ti state.

After activation the Ni signal in the EDX maps spreads (see Figure 2b), which is consistent with the thickness increase observed in the XTEM images (Figure 1c). Moreover, the O signal becomes much stronger and it partially overlaps with the Ni layer, indicating its oxidation. This observation is further corroborated by the XPS spectra (Figure 2c, green lines), which show: *i)* a $2p_{3/2}$ peak at 855.5 eV in the Ni 2p region; this relates to NiO_X ($x > 0$) and confirms that during the activation process the Ni layer has been oxidized; *ii)* the Ti peak at the Ti $2p_{3/2}$ binding energy region slightly shifted (now it is located at 458.2 eV), indicating again the presence of TiO_X; *iii)* the O signal shows that the metal oxide peak at 531.2 eV almost disappeared (not completely, as the curve is not totally symmetric), and now all the oxygen signal points to hydroxides (531.2 eV).[33,34] The almost complete fading of the O peak related to metal oxides and the remarkable reduction of the Ti peak may be related to the thickness increase experienced by the Ni layer (the XPS technique is not so sensitive at higher depths), indicating that the O peak at 531.2 eV may be related to the formation of hydroxides in the Ni film. Feng *et al.*[35] proposed that Ni coatings in nSi photoanodes for water splitting can be overcharged to form Ni(O)(OH) under OER. This is further supported by the fact that the Si 2p signal almost disappeared, indicating that the XPS cannot image so well the species below the thicker Ni layer. In any case, the presence of TiO_X in the sample is very clear from the EDX maps and XPS spectra (Ti 2p region). It should be highlighted that the formation of a SiO_X interfacial layer after activation is not specially well supported from the EDX and XPS data, but it is clear in the XTEM.

Therefore, after activation the 2 nm Ni film became 5 nm thick hydroxide-rich

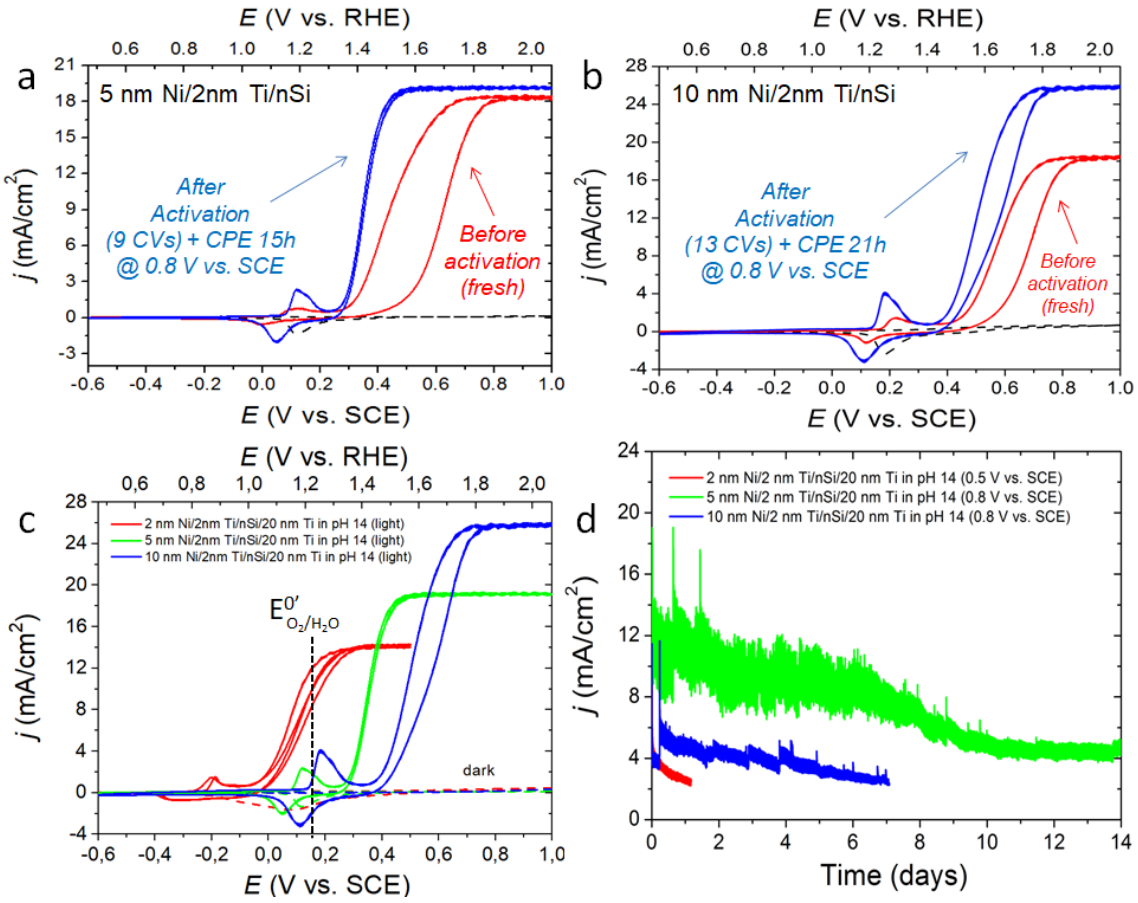

Figure 3. PEC performance of 2 nm Ti/nSi photoanodes coated with Ni layers of different thicknesses. (a) and (b) are CV scans of 5 nm Ni and 10 nm Ni coated 2 nm Ti/nSi photoanodes in 1 M KOH, respectively. All of these photoanodes show an activation process after a period of PEC tests in the solution (from the red lines to blue lines), but the activation degree is much smaller than the 2 nm Ni/2 nm Ti/nSi photonaodes as shown in Figure. 1. The comparison of the PEC activity and stability tests on activated 2 nm Ni (red), 5 nm Ni (green), 10 nm Ni (blue) based 2 nm Ti/nSi photoanodes is shown in (c) and (d). All the CV scans and current-time traces are obtained in 1 M KOH solution (pH 14), and the photoanodes are illuminated by 1 simulated sun. And all the CVs are with iR compensation at a scan rate of 100 mV/s and the current-time traces are without iR compensation at a constant potential.

NiO_X, the initially partially oxidized Ti film got severely oxidized, and an additional SiO_X layer was formed in the structure. The impressive activity improvement shown in Figures 1e and 1f should be related to the presence of a naturally grown TiO_X film. First, the onset potential shift cannot be related to the Ni to hydroxide-rich NiO_X transition, as $Ni/SiO_X/nSi$ photoanodes show no activation process.[13,18] Second, it has been observed that the deposition of a TiO_2 film on a SiO_X/nSi substrate forms a highly conductive rectifying junction.[7,8,11] This is indeed indicating that during the activation process the Ti

film acquired significant amounts of O, as initially the onset potential was not so competitive (see red curve in Figure 1e); this is also consistent with the more intense O signal in EDX maps (Figure 2b), which also overlaps with the Ti one. Interestingly, compared to previous reports using atomic layer deposited (ALD) TiO_2[8,11] our naturally grown TiO_X shows the advantage of a ~ 172 mV lower onset potential (see also Table 1). The onset potential shown by this Ni/TiO_X/SiO_X/nSi photoanode (-42 mV vs. SCE) is one of the lowest in the literature for this kind of samples. Only using n-p^+ Silicon samples similar activity performances have been observed (Table 1),[8,14-16] but as mentioned their fabrication process is much more complex and expensive. And third, it is striking that despite the activated sample includes an extra insulating SiO_X layer (Figure 1c), the overall currents measured are still larger. Again, this points to a higher built-in potential in the activated sample, thanks to the formation of an effective TiO_X/SiO_X/nSi interface.[11,36]

In the next step we studied the performances of 5 and 10 nm Ni/2 nm Ti/nSi photoanodes, without native SiO_X (see Figures 3a and 3b, respectively). In both cases, a very similar activation process was observed, and further conclusions can be extracted: *i)* the thicker the Ni coating the longer the activation time, i.e. bulk electrolysis of 15 and 21 hours was needed; and *ii)* the thicker the Ni coating the lower the onset potential shift. The activity and stability of the 2, 5 and 10 nm Ni/2 nm Ti/nSi (without native SiO_X) under 1 M KOH electrolyte are compared in Figures 3c and 3d, respectively. The 2 nm Ni/2 nm Ti/nSi photoanode shows the lowest onset potential (-42 mV), but shows poor stability for long experiments. The onset potential of the 5 nm Ni/2 nm Ti/nSi sample is also very competitive (just 0.25 V vs SCE), which is 50 mV lower than the one previously reported by Kenney *et al.*[13] in 5 nm Ni/native SiO_X/nSi photoanodes. Moreover, the stability of the 5 nm Ni coated photoanode is very good, as it retains almost 100 % activity

during the first ~ 6.5 days (10 mA/cm^2 at 0.8 V vs. SCE) and becomes stable at 50 % activity for times above 2 weeks (5 mA/cm^2 at 0.8 V vs. SCE). Compared to the performances previously reported for Ni/SiOX/nSi samples, the Ni/Ti/nSi photoanodes (without native SiO_X) here presented show better activity and stability. Therefore, the replacement of native SiO_X by Ti seems to be beneficial for this technology. The phenomena here reported are reproducible and have been observed in batches fabricated on different dates.

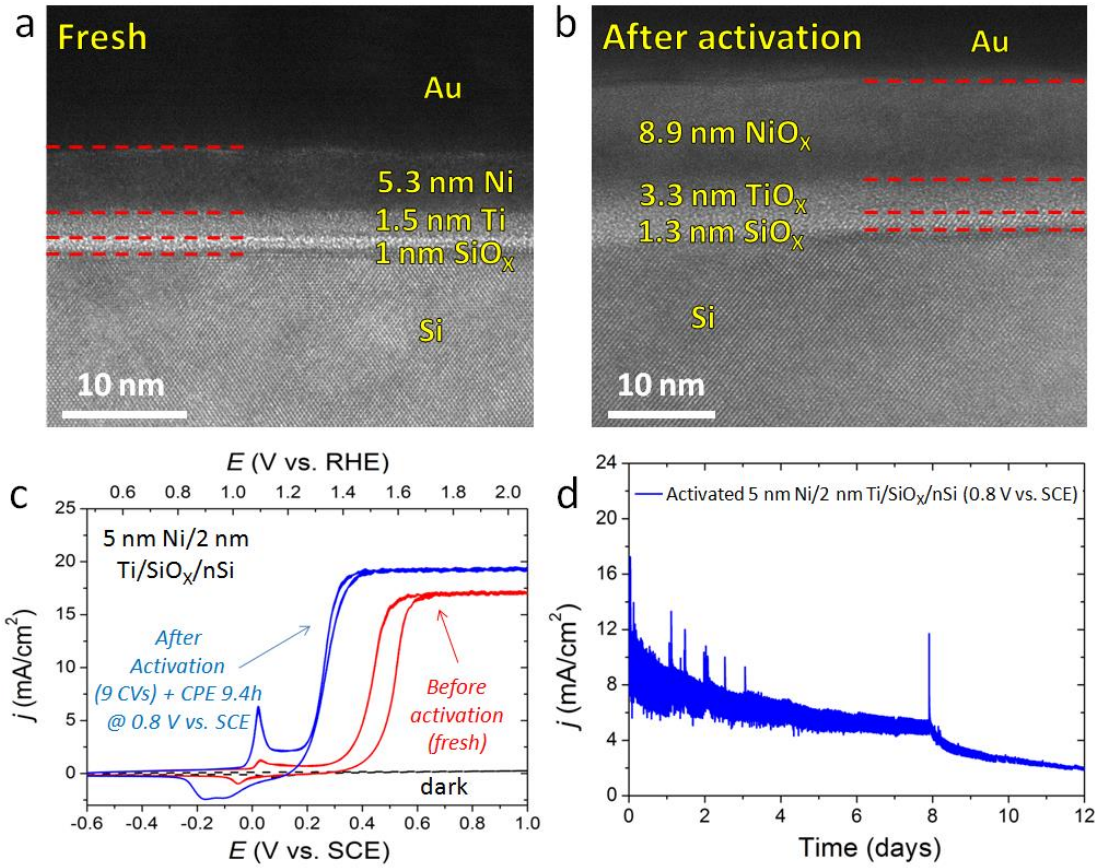

Figure 4. Sample structure and PEC performance of 5 nm Ni/2 nm Ti/SiO_X/nSi photoanode. (a) and (b) are cross-sectional TEM images of 5 nm Ni/2nm Ti/SiO_X/nSi photoandes before and after the PEC activation tests, respectively. 50 nm Au layers were deposited rightly (a) after the deposition of the Ni layer and (b) after the PEC tests. (c) and (d) are the PEC activity (CVs) and stability (current-time traces) of 5 nm Ni/2 nm Ti coated nSi photoanodes with the native SiO_X. Like the counterpart without the native SiO_X layer, the sample with the native SiO_X also shows an activation process. The PEC tests were all performed in 1 M KOH electrolyte under 1 simulated sun illumination. The dashed CVs in (c) were obtained in the dark condition. All the CVs were collected at a scan rate of 100 mV/s with iR compensation, and the current-time traces were collected under a constant potential without iR compensation.

The role of the native SiO_X layer has been in-depth analyzed by fabricating similar Ni/Ti junctions but without removing the native SiO_X layer. The first CV collected for the 2 nm Ni/2 nm Ti/native SiO_X/nSi photoanode (blue solid curves in Figure S2) shows an onset potential ~ 0.25 V vs. SCE, slightly better than the fresh SiO_X-free counterpart (see green solid curves in Figure S2), but after subsequent CVs, the 2 nm Ni/2 nm Ti counterpart with the native SiO_X starts to decay (black curves in Figure S2). In the next step we increase the thickness of the Ni coating. The XTEM image of a fresh 5 nm Ni/2 nm Ti/native SiO_X /nSi photoanode is presented in Figure 4a (again, the Au layer only used in XTEM experiments). Compared to Figure 1b, the additional native SiO_X layer can be clearly observed, and its thickness is ~ 1 nm, in agreement with previous reports.[11,17,18] The real and theoretical thicknesses of each layer agree reasonably well. The first CV measured in this sample (Figure 4c, red line) shows an onset potential of ~ 0.32 V vs. SCE, similar to its SiO_X-free counterpart (compare to Figure 3a, red line). Unlike the 2 nm Ni coated Ti/SiO_X/nSi sample, the 5 nm Ni coated one shows an activation process (Figure 4c, blue line), after which its onset potential (0.14 V vs. SCE) is better than that of its SiO_X-free counterpart (0.26 V vs. SCE, see Figure 3a, blue line). This activation phenomenon is also observed for the 10 nm Ni electrode with native SiO_X that shows a slight negative shift, but inferior than that of the 5 nm Ni electrode. Figure S3 shows the comparison of the activated 5 nm and 10 nm Ni/2nm Ti/nSi sample with and without native oxide. Considering both the PEC activity (Figure S3) and stability (Figure 4d and green curve in Figure 3d) of the 5 Ni/Ti coated samples with and without SiO_X, their PEC performance is quite similar. XTEM images (Figure 4b) reveal that the thicknesses of the Ni and Ti layers increased after activation process. The Ni layer changes from 5.3 to 8.9 nm, and the Ti layer changes from 1.5 to 3.3 nm. However, the thickness of the native SiO_X layer increased from 1 to 1.3 nm. CPE tests (Figure 4d) reveal

good stability comparable to that of the SiO_X-free counterpart (see Figure 3d, geen line for comparison). The EDX maps and XPS spectra for the Ni, Ti, O, and Si elements for the fresh and activated 5 nm Ni/2 nm Ti/native SiO_X/nSi sample are shown in Figure S4. Again, after activation the Ni layer became oxidized and rich in hydroxides similarly to what was observed for the most active electrode 2 nm Ni/2 nm Ti/nSi (Figure 2). These results suggest that the activation process is strongly influenced by the NiOx/TiOx/SiOx/nSi interlayer interconversion and that small variations dramatically change the performance of this kind of photoanodes.

E 4 Conclusion

In conclusion, 2 nm thick Ti layers have been successfully used to replace the native SiO_X layer in nSi photoanodes for water splitting with improved performance. 2 nm Ni/2 nm Ti/nSi photoandoes (without native SiO_X) show an activation process, and the resulting 5 nm NiO_X/3 nm TiO_X/1.6 nm SiO_X/nSi electrodes exhibit an impressive negative onset potential of -42 mV vs. SCE (in 1 M KOH under 1 sun illumination). Electron Microscopy analysis revealed that after the activation, a naturally grown NiO_X/TiO_X/SiO_X/nSi sample is formed, that shows an onset potential ~ 172 mV lower than those previously reported in similar NiO_X/TiO_2/SiO_X/nSi photoanodes intentionally grown using ALD/sputtering techniques. By using a 5 nm thick Ni coating we achieve currents of 10 mA/cm^2 (at 0.8 V vs. SCE in pH 14 under 1 sun illumination) for ~ 6.5 days, and it still keeps 50 % activity (5 mA/cm^2 at 0.8 V vs. SCE) after ~ 14 days. For the 5 nm Ni sample, we also observed that combining the Ti with native SiO_X layers further reduces the onset potential of the samples (0.14 V vs. SCE in pH 14). These values are comparable to those of samples using n-p$^+$ junctions, but with the advantage of a much easier and cheaper fabrication process.

E 5 Acknowledgements

This work has been supported by the Young 1000 Global Talent Recruitment Program of the Ministry of Education of China, the National Natural Science Foundation of China (grants no. 61502326, 41550110223, 11661131002), the Jiangsu Government (grant no. BK20150343), the Ministry of Finance of China (grant no. SX21400213) and the Young 973 National Program of the Chinese Ministry of Science and Technology (grant no. 2015CB932700). The Collaborative Innovation Center of Suzhou Nano Science & Technology, the Jiangsu Key Laboratory for Carbon-Based Functional Materials & Devices and the Priority Academic Program Development of Jiangsu Higher Education Institutions are also acknowledged. Professor Paul C. McIntyre is acknowledged here for the discussion about the Ti interface layer's function.

E 6 References

[1] E. McLamb, Fossil Fuels vs. Renewable Energy Resources, http://www.ecology.com/2011/09/06/fossil-fuels-renewable-energy-resources/ (access on July 21, 2016)

[2] F. E. Osterloh and B. A. Parkinson, Recent developments in solar water-splitting photocatalysis, *MRS Bull* **2011**, *36*, 17.

[3] J. R. McKone, N. S. Lewis and H. B. Gray, Will solar-driven water-splitting devices see the light of day? *Chem. Mater.* 2014, 26, 407-414.

[4] A. Fujishima, K. Honda, Electrochemical photolysis of water at a semiconductor electrode, *Nature* **1972**, *238*, 37.

[5] A. Q. Contractor and J. O. M. Bockris, Investigation of a protective conducting silica film on n-silicon, *Electrochim. Acta*, **1984**, *29*, 1427.

[6] S. Chen and L.-W. Wang, Thermodynamic oxidation and reduction potentials of photocatalytic semiconductors in aqueous solution, *Chem. Mater.* **2012**, *24*, 3659.

[7] A. G. Scheuermann, J. P. Lawrence, K. W. Kemp, T. Ito, A. Walsh, C. E. D. Chidsey, P. K. Hurley and P. C. McIntyre, Design principles for maximizing photovoltage in metal-oxide-protected water-splitting photoanodes, *Nat. Mater.* **2016**, *15*, 99.

[8] S. Hu, M. R. Shaner, J. A. Beardslee, M. Lichterman, B. S. Brunschwig and N. S. Lewis, Amorphous TiO_2 coatings stabilize Si, GaAs, and GaP photoanodes for efficient water oxidation, *Science* **2014**, *344*, 1005.

[9] A. G. Scheuermann, J. D. Prange, M. Gunji, C. E. D. Chidsey and P. C. McIntyre,

Effects of catalyst material and atomic layer deposited TiO_2 oxide thickness on the water oxidation performance of metal–insulator–silicon anodes, *Energy Environ. Sci.* **2013**, *6*, 2487.

[10 Y. Chen, J. D. Prange, S. Dühnen, Y. Park, M. Gunji, C. E. D. Chidsey and P. C. McIntyre, Atomic layer-deposited tunnel oxide stabilizes silicon photoanodes for water oxidation, *Nat. Mater.* **2011**, *10*, 539.

[11] M. T. McDowell, M. F. Lichterman, A. I. Carim, R. Liu, S. Hu, B. S. Brunschwig and N. S. Lewis, The Influence of Structure and Processing on the Behavior of TiO_2 protective layers for stabilization of n-Si/ TiO_2/Ni photoanodes for water oxidation, *ACS Appl. Mater. Interfaces* **2015**, *7*, 15189.

[12] K. Sun, N. Park, Z. Sun, J. Zhou, J. Wang, X. Pang, S. Shen, S. Y. Noh, Y. Jing, S. Jin, P. K. L. Yu and D. Wang, Nickel oxide functionalized silicon for efficient photo-oxidation of water, *Energy Environ. Sci.* **2012**, *5*, 7872.

[13] M. J. Kenney, M. Gong, Y. Li, J. Z. Wu, J. Feng, M. Lanza and H. Dai, High-performance silicon photoanodes passivated with ultrathin nickel films for water oxidation, *Science* **2013**, *342*, 836.

[14] B. Mei, A. A. Permyakova, R. Frydendal, D. Bae, T. Pedersen, P. Malacrida, O. Hansen, I. E. L. Stephens, P. C. K. Vesborg, B. Seger and I. Chorkendorff, Iron-treated NiO as a highly transparent p-type protection layer for efficient Si-based photoanodes, *J. Phys. Chem. Lett.* **2014**, *5*, 3456.

[15] K. Sun, M. T. McDowell, A. C. Nielander, S. Hu, M. R. Shaner, F. Yang, B. S. Brunschwig and N. S. Lewis, Stable solar-driven water oxidation to O_2(g) by Ni-oxide-coated silicon photoanodes, *J. Phys. Chem. Lett.* **2015**, *6*, 592.

[16] K. Sun, F. H. Saadi, M. F. Lichterman, W. G. Hale, H.-P. Wang, X. Zhou, N. T. Plymale, S. T. Omelchenko, J.-H. He, K. M. Papadantonakis, B. S. Brunschwig and N. S. Lewis, Stable solar-driven oxidation of water by semiconducting photoanodes protected by transparent catalytic nickel oxide films, *Proc. Natl. Acad. Sci. USA* **2015**, *12*, 3612.

[17] X. Zhou, R. Liu, K. Sun, D. Friedrich, M. T. McDowell, F. Yang, S. T. Omelchenko, F. H. Saadi, A. C. Nielander, S. Yalamanchili, K. M. Papadantonakis, B. S. Brunschwig and N. S. Lewis, Interface engineering of the photoelectrochemical performance of Ni-oxide-coated n-Si photoanodes by atomic-layer deposition of ultrathin films of cobalt oxide, *Energy Environ. Sci.* **2015**, *8*, 2644.

[18] T. Han, Y. Shi, X. Song, A. Mio, L. Valenti, F. Hui, S. Privitera, S. Lombardo and M. Lanza, Ageing mechanisms of highly active and stable nickel-coated silicon photoanodes for water splitting, *J. Mater. Chem. A* **2016**, *4*, 8053.

[19] K. Jun, Y. S. Lee, T. Buonassisi and J. M. Jacobson, High Photocurrent in Silicon Photoanodes Catalyzed by Iron Oxide Thin Films for Water Oxidation, *Angew. Chem.- Int. Ed.*, **2012**, *51*, 423.

[20] Y. Shi, C. Gimbert-Suriñach, T. Han, S. Berardi, M. Lanza and A. Llobet, CuO-functionalized silicon photoanodes for photoelectrochemical water splitting devices, *ACS Appl. Mater. Interfaces* **2016**, *8*, 696.

[21] J. C. Hill, A. T. Landers and J. A. Switzer, An electrodeposited inhomogeneous metal–insulator–semiconductor junction for efficient photoelectrochemical water oxidation, *Nat. Mater.* **2015**, *14*, 1150.

IV

[22] X. Zhou, R. Liu, K. Sun, K. M. Papadantonakis, B. S. Brunschwig and N. S. Lewis, 570 mV photovoltage, stabilized n-Si/CoOx heterojunction photoanodes fabricated using atomic layer deposition, *Energy Environ. Sci.* **2016**, *9*, 892.

[23] D. V. Esposito, I. Levin, T. P. Moffat and A. A. Talin, H_2 evolution at Si-based metal–insulator–semiconductor photoelectrodes enhanced by inversion channel charge collection and H spillover, *Nat. Mater.* **2013**, *12*, 562.

[24] P. Mur, M. N. Semeria, M. Olivier, A. M. Papon, C. Leroux, G. Reimbold, P. Gentile, N. Magnea, T. Baron, R. Clerc and G. Ghibaudo, Ultra-thin oxides grown on silicon (1 0 0) by rapid thermal oxidation for CMOS and advanced devices, *Appl. Surf. Sci.* **2001**, *175*, 726.

[25] Z.-L. Tseng, L.-C. Chen, W.-Y. Li and S.-Y. Chu, Resistive switching characteristics of sputtered AlN thin films, *Ceram. Int.* **2016**, *42*, 9496.

[26] Y. Ji, C. Pan, M. Zhang, S. Long, X. Lian, F. Miao, F. Hui, Y. Shi, L. Larcher, Larcher, E. Wu and M. Lanza, Boron nitride as two dimensional dielectric: Reliability and dielectric breakdown, *Appl. Phys. Lett.* **2016**, *108*, 012905.

[27] C. Li, W. Dai, M. Li, H. Li, S. Xu, X. Wu and B. Yang, Effect of sputtered titanium interlayers on the properties of nanocrystalline diamond films, *J. Appl. Phys.* **2016**, *119*, 135306.

[28] R. W. Johnson, A. Hultqvist and S. F. Bent, A brief review of atomic layer deposition: from fundamentals to applications, *Mater. Today* **2014**, *17*, 236.

[29] D. A. Corrigan, The catalysis of the oxygen evolution reaction by iron impurities in thin film nickel oxide electrodes, *J. Electrochem. Soc.* **1987**, *134*, 377.

[30] M. W. Louie and A. T. Bell, An investigation of thin-film Ni–Fe oxide catalysts for the electrochemical evolution of oxygen, *J. Am. Chem. Soc.* **2013**, *135*, 12329.

[31] L. Trotochaud, S. L. Young, J. K. Ranney and S. W. Boettcher, Nickel–iron oxyhydroxide oxygen-evolution electrocatalysts: the role of intentional and incidental iron incorporation, *J. Am. Chem. Soc.* **2014**, *136*, 6744.

[32] G. Mende, Oxidation of etched silicon in air at room temperature; Measurements with ultrasoft X-ray photoelectron spectroscopy (ESCA) and neutron activation analysis, *Surf. Sci.* **1983**, *128*, 169.

[33] J. F. Moulder, W. F. Stickle, P. E. Sobol and K. D. Bomben, In Handbook of X-ray Photoelectron Spectroscopy: A Reference Book of Standard Spectra for Indentification and Interpretation of XPS Data; Chastain J. Ed.; Perkin-Elmer Corp., Physical Electronics Division: Eden Prairie, Minnesota **1992**; pp 44-85.

[34] B. Mei, B. Seger, T. Pedersen, M. Malizia, O. Hansen, I. Chorkendorff and P. C. K. Vesborg, Protection of p+-n-Si Photoanodes by Sputter-Deposited Ir/IrOx Thin Films, *J. Phys. Chem. Lett.* **2014**, *5*, 1948.

[35] J. Feng, M. Gong, M. J. Kenney, J. Z. Wu, B. Zhang, Y. Li and H. Dai, Nickel-coated silicon photocathode for water splitting in alkaline electrolytes, *Nano Res.* **2015**, *8*, 1577.

[36] P. F. Satterthwaite, A. G. Scheuermann, P. K. Hurley, C. E. D. Chidsey and P. C. McIntyre, Engineering interfacial silicon dioxide for improved metal–insulator–semiconductor silicon photoanode water splitting performance, *ACS Appl. Mater. Interfaces* **2016**, *8*, 13140.

E 7 Supporting information

Paper E: Substitution of native silicon oxide by titanium in Ni-coated silicon photoanodes for water splitting solar cells

Index

Figure S1. Another typical cross-sectional TEM images of the activated 2 nm Ni/2 nm Ti/nSi photoanodes.

Figure S2. Cyclic voltammetry (CV) scans of 2 nm Ni/2 nm Ti coated nSi photoanodes without and with the native SiO_X layer.

Figure S3. Activity comparison of activated 5 and 10 nm Ni/2 nm Ti based nSi photoanodes without and with the native SiO_X layer.

Figure S4. Chemical composition analysis of the 5 nm Ni/2 nm Ti/SiO_X/nSi photoanodes before and after the PEC activation process.

IV

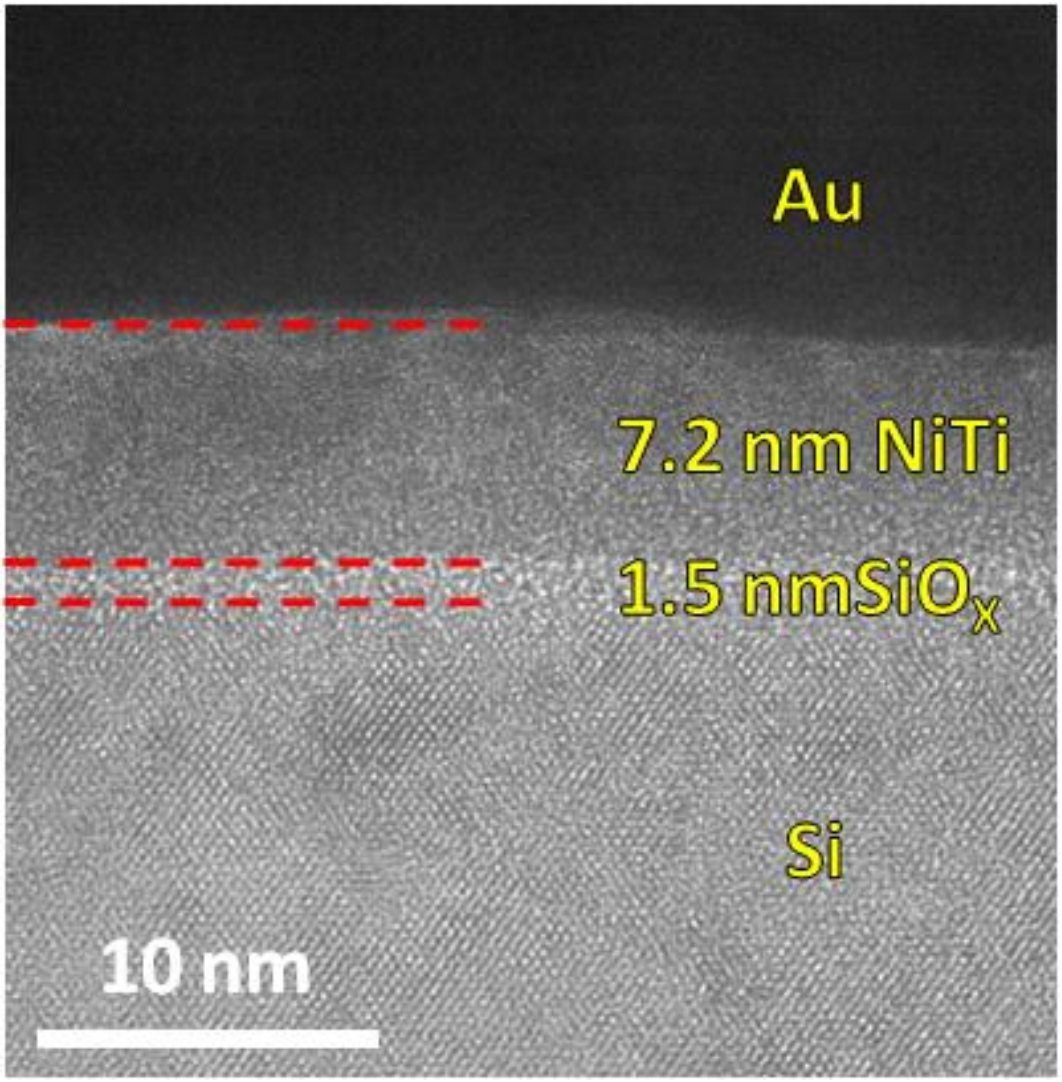

Figure S1. Another typical cross-sectional TEM images of the activated 2 nm Ni/2 nm Ti/nSi photoanodes (without the native SiO_X), which has been protected by depositing 50 nm Au right after the PEC tests. The Ni and Ti interface disappeared at these positions, and the thickness of the mixed layer is around 7.2 nm. There is also one layer formed below the mixed layer, that we attribute to SiO_X.

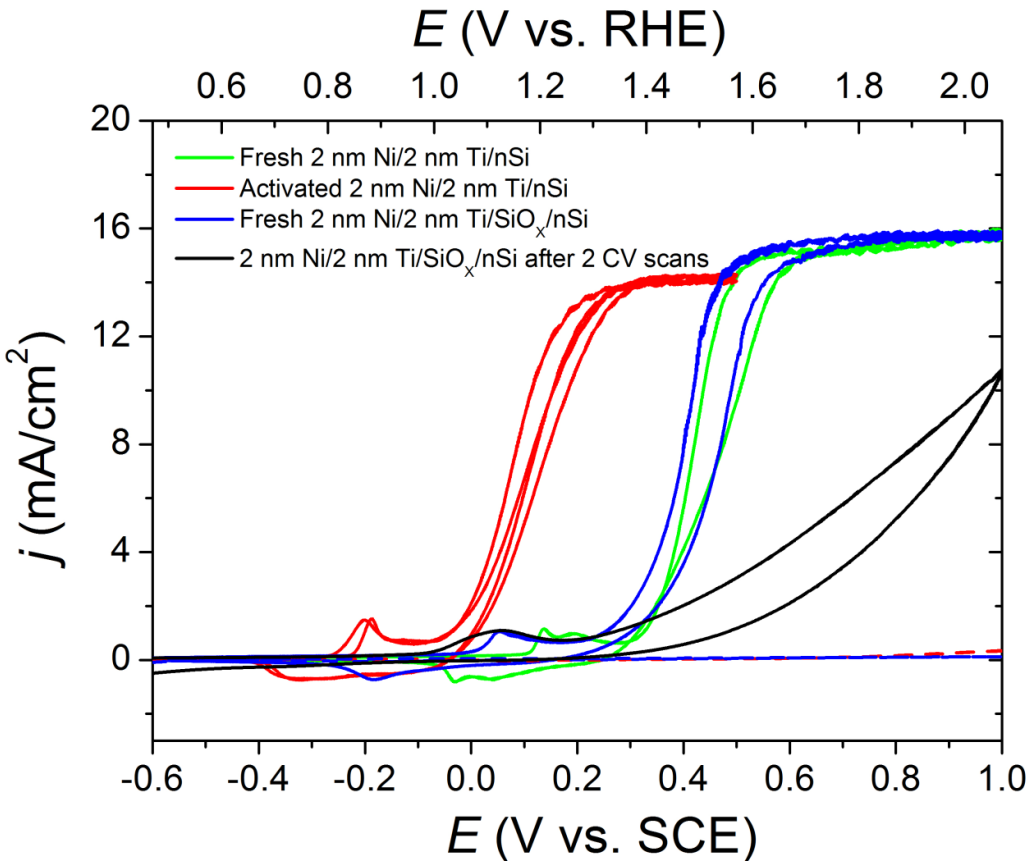

Figure S2. CV scans of 2 nm Ni/2 nm Ti coated nSi photoanodes without (green and red lines) and with (blue lines) the native SiO_X layer. The 2 nm Ni/2 nm Ti coated nSi photoanodes without SiO_X shows an activation process (red lines), however the one without SiO_X doesn't show any activation, it decays after each CV scan (black lines). All the CVs are in 1M KOH electrolyte under 1 sun illumination. The CVs were obtained at a scan rate of 100 mV/s with iR compensation.

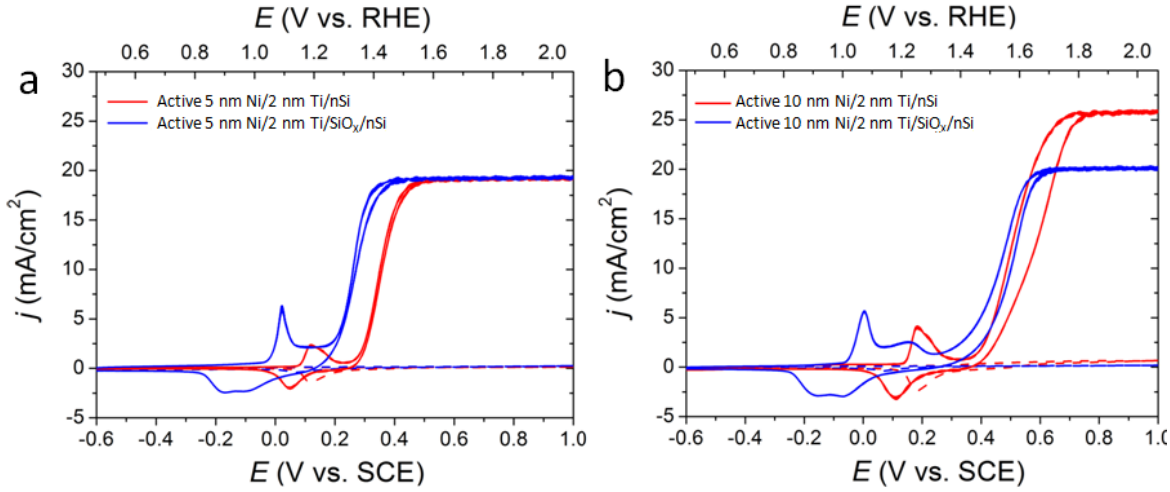

Figure S3. Activity comparison of activated 5 nm (a) and 10 nm (b) Ni/2 nm Ti based nSi photoanodes without (red lines) and with (blue lines) the native SiO_X layer in 1 M KOH electrolyte. After activation, the 5 and 10 nm Ni/2 nm Ti coated sample with native SiO_X shows a slightly better activity than the counterpart without the native SiO_X. The CV scans were obtained at a scan rate of 100 mV/s with iR compensation.

IV

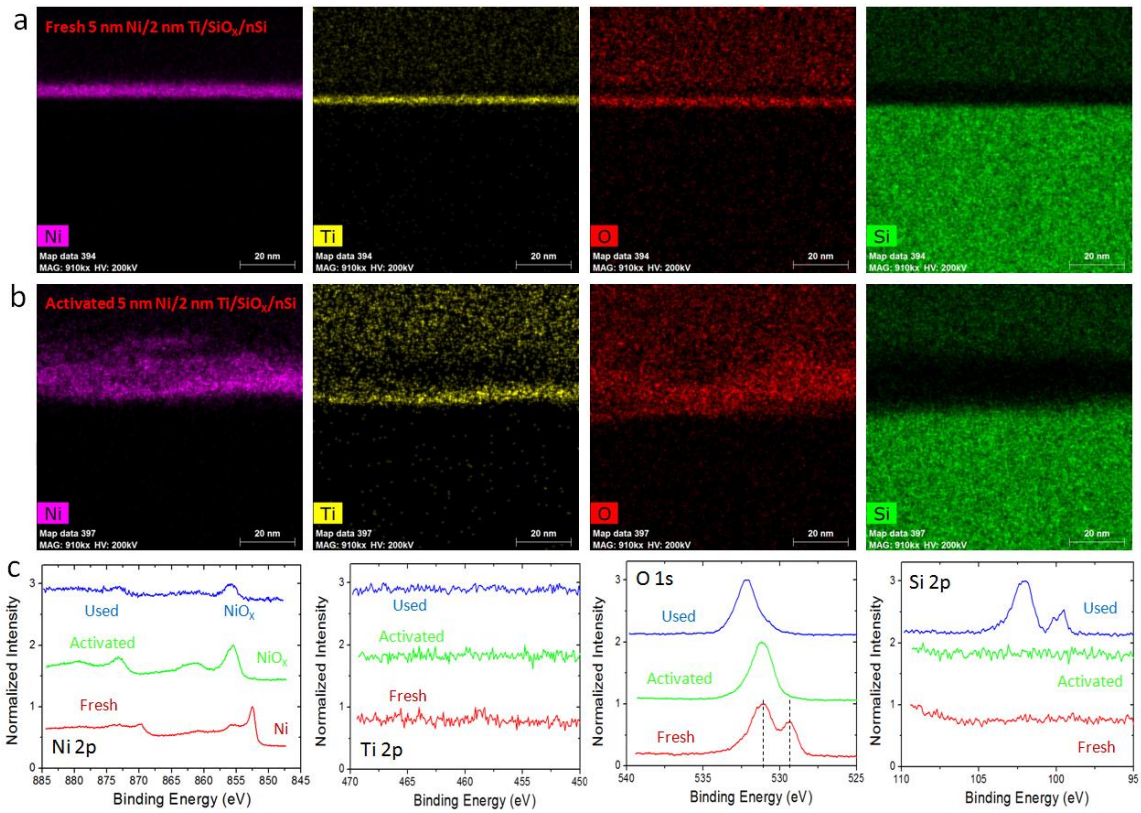

Figure S4. Chemical composition analysis of the 5 nm Ni/2 nm Ti/SiO_X/nSi photoanodes before and after the PEC activation process. Cross-sectional EDX maps of (a) fresh and (b) activated 5 nm Ni/2 nm Ti/SiO_X/nSi photoanodes. The Ni, Ti, O and Si element composition maps are exhibited in both (a) and (b) to observe the difference between these two samples. (c) XPS spectra of fresh (red), activated (green) and used (blue) 5 nm Ni/2 nm Ti/SiO_X/nSi photoanodes. The binding energy regions of Ni 2p, Ti 2p, O 1s and Si 2p are all shown to track the change of each sample after the each period of the PEC tests.

Chapter 5:

Molecular catalysts for photovoltaic-electrolysis water splitting devices

V

In this chapter, an integrated photovoltaic-elecrolysis (PV-EC) water splitting system is developed. It is based on a very efficient anode made of conductive carbon nanotubes covered by a highly active water oxidation catalytic material. The latter is characterized by an oligomeric structure of repetitive ruthenium metal centers {Ru^{II}(tda)(bipy)} (where tda = [2,2':6',2"-terpyridine]-6,6"-dicarboxylato and bipy = 4,4'-bipyridine)) that are analogous to that of the fastest molecular water oxidation catalyst reported to date. Two types of photovoltaic cells have been used in this work. In the first example, state of the art perovskite sollar cell with efficiencies up to 18 % have been used, achieving STH of 13.2 %. In the second example, a commercially available solar cell made of Group III/IV elements has been used. In this latter example, a record efficiency of STH = 21.2 % at neutral pH (room temperature) has been obtained with no loss of activity after 4 hours of continuous working. This result provides new oppurtinities for the practical application of large scale hydrogen generation.

The chapter consist of the following paper:

Paper F An anode based on a ruthenium molecular water oxidation catalyst for a photovoltaic-electrolysis water splitting with solar to hydrogen efficiency of 21.2 %, **2018**, *in preparation*

V

Paper F: An anode based on a ruthenium molecular water oxidation catalyst for a photovoltaic-electrolysis water splitting with solar to hydrogen efficiency of 21.2 %

Y. Shi, T.-Y. Hsieh, C. Gimbert-Suriñach, M. A. Hoque, S. Chen, T.-C. Wei, E. Palomares, M. Lanza, A. Llobet (2018, *in preparation*)

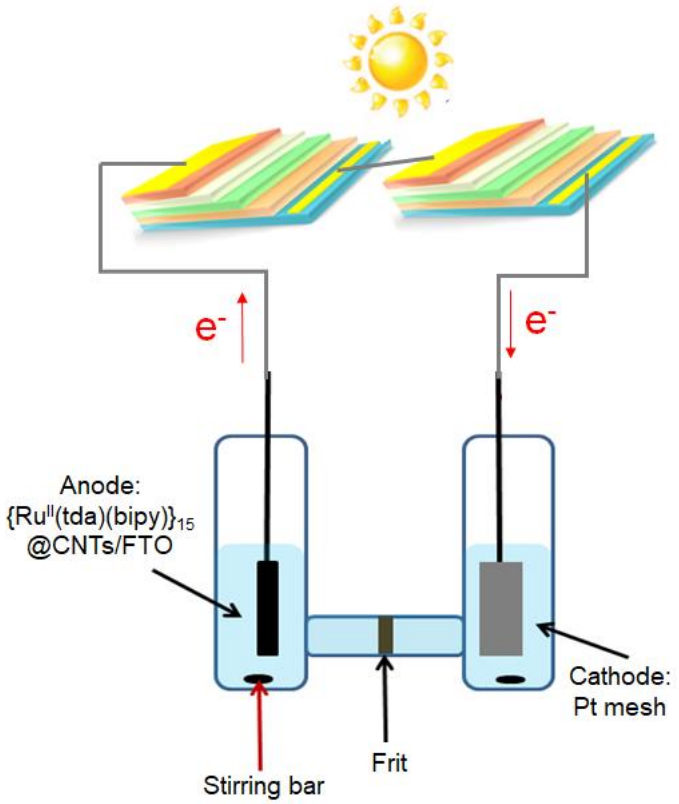

Abstract

Pollution-free hydrogen production from the solar-driven water splitting reaction is a very promising strategy to make the inexhaustible solar energy storable and transportable. However, there is still no solar-driven water splitting devices available in the commercial market even after decades of studies. In this study, we use a highly active molecular water oxidation catalyst on the surface of the anode integrated into a photovoltaic-electrolysis

(PV-EC) water splitting configuration in combination with a perovskite based solar cell or a commercially available InGaP/GaAs/Ge triple junction solar cell. To the best of our knowledge, the latter integrated PV-EC water splitting device showed the highest solar-to-hydrogen efficiency of 21.2 % at netural pH (room temperature) reported to date. This study paves the way of molecular catalysts application in the PV-EC solar-driven water splitting devices, which may help the practical realization of large scale hydrogen harvesting converted from solar energy and solve the energy problems for the whole society.

Contributions

Yuanyuan Shi has designed the configuration, fabricated the ruthenium molecular complex based anodes, performed the electrochemical, morphological and chemical charatcerizations as well as the light induced water splitting experiments. She also wrote the manuscript.

V

F 1 Introduction

To maintain the global energy consumption of modern lifestyle, 87 % of this energy is from the burning of traditional fossil fuels such as oil, coal, natural gas, etc., which not only causes the current energy problems,[1] but also leads to serious environmental issues, especially air pollution and emission of greenhouse gas.[2] It has been estimated that the average energy consumption rate will increase from 16 TW in early 2000s to 30 TW by 2050.[3,4] Therefore, the exploration of clean and sustainable energy is necessary and urgent for the development of our society. Generating hydrogen (fuel) through solar-driven water splitting provides an opportunity for the exploration of clean energy, since hydrogen is storable, transportable and can be consumed without generating any greenhouse gas and harmful byproducts.[5-10] Overall water splitting (Equation 1) is a reaction that happens with a thermodynamic voltage of 1.23 V at 298 K,[11,12] while the practically required operating voltage is in the range from 1.5 V to 1.9 V for the most active electrocatalytic systems.[11,13] The overall water splitting can be divided in two half reactions indicated in Equation 2 and Equation 3, i.e., the oxygen evolution reaction (OER) and the hydrogen evolution reaction (HER), respectively.

Overall water splitting: $2H_2O \rightarrow O_2 \uparrow + 2H_2 \uparrow$, $\Delta E = 1.23$ V (*Equation 1*)

OER: $2H_2O + 4h^+ \rightarrow O_2 \uparrow + 4H^+$ (*Equation 2*)

HER: $4H^+ + 4\,e^- \rightarrow 2H_2 \uparrow$ (*Equation 3*)

There are three kinds of solar-driven water splitting spontaneous systems widely proposed, which are photovoltaic-electrolysis (PV-EC) cells, integrated photoelectrochemical (PEC) cells and mixed colloid system.[14] Among them, the PV-EC solar-driven water splitting configuration is the most mature technology thanks to the development of photovoltaic cells. However, the relatively high cost of this technology blocks its application in the commercial market.[14] In order to develop commercially

competitive solar-driven water splitting devices, the solar-to-hydrogen (STH) efficiency of the devices needs to be as high as possible while keeping a low cost for the overall cell materials and manufacture. It has been predicted through theoretical studies that the maximum STH efficiency that can be achieved by the PEC water spitting system is between 23% and 32 %,[15-18] while the PV-EC water splitting system have been demonstrated to reach higher STH efficiencies.[19-25] For instance, the best multi-junction PV cell has been reported to perform with a solar-to-electricity efficiency of 46 % under concentrated illumination,[26] which accounts for an ideal STH up to 33-37 % assuming a working voltage of 1.5-1.9 V and 100% Faradaic efficiency.[27]

In a PV-EC water splitting system, one of the most important parameters is the good matching between current-voltage characteristics of the water splitting electrolyser with those of the PV cells. As stated above, the practical operating voltage of the overall water splitting reaction is in the range from 1.5 V to 1.9 V, so normally two or more junctions based PV cells are needed. The reason is that the available single junction PV cells have open circuit voltages (V_{OC}) of 0.7-1.4 V.[28-31] Many kinds of PV cells have been used in the PV-EC solar-driven water splitting configuration, including inter-connected $CuIn_xGa_{1-x}Se_2$ (CIGS) cells,[32] triple junction silicon solar cells or commercial silicon solar cell modules,[33,34] triple junction polymer solar cells,[35] triple junction III-V semiconductors based solar cell or connected single junction III-V solar cells,[23,36-38] as well as series connected perovskite solar cells.[39] Among them, the highest reported STH efficiency achieved is 30 % under concentrated illumination (42 suns) by combining a triple junction InGaP/GaAs/GaInAs solar cell with Millipore water (heated at ~80 °C), which uses iridium oxide and metallic platinum as the water oxidation and water reduction catalysts, respectively.[36] Moreover, the concentrated illumination, and the use of high amounts of nobel metal oxides as catalysts will also increase the cost of this PV-

EC water splitting device when used in large scale applications. Metal oxides based catalysts have been widely studied for the water oxidation reaction required in the anodic compartment of the water splitting cell.[40-47] Despite the study on molecular water oxidation catalysts started around 80 years later than that of the metal oxides,[48] the former have been demonstrated to show excellent catalytic activity and provided unique mechanistic information of the OER reaction.[49-52] However, none of these molecular catalysts has been integrated into a PV-EC system. In this work, we introduce for the first time a highly active water oxidation material based on a molecular catalyst in the anode of PV-EC solar-driven water splitting devices under neutral pH (pH 7 electrolyte). Two different types of solar cells are used to drive the reaction and test the performance of this novel anode. The first system is based on a state of the art perovskite solar cells with a solar to electricity efficiency of ~18 %, while the second example uses a commercially available InGaP/GaAs/Ge triple junction solar cells with solar to electricity efficiency of ~34.1 %. The performance of the overall water splitting cells is assessed in terms of STH and long-term durability.

F 2 Experimental Section

Fabrication of Perovskite solar cells: Fluoride-doped tin oxide (FTO) substrates were patterned in a chemical way using zinc powder and 5 M hydrochloride acid solution. The patterned substrates were then ultrasonically cleaned in i) 2% Hellmanex detergent and ii) deionised water for 30 min. The substrates were exposed to UV-ozone environment for 10 min before use. A thin titanium dioxide (TiO_2) film was deposited on a cleaned FTO substrate by spin coating a solution that was composed of 0.3 M titanium diisopropoxide bis(acetylacetonate) (Sigma-Aldrich, 75wt% in isopropanol) diluted in isopropanol (IPA) at 4000 rpm for 30 s. The substrate was heated on a hotplate at 120°C

for 5 min followed by sinteringd at 450°C for 30 min. After slowly cooling down to room temperature, the substrate was immersed into a 40 mM titanium tetrachloride solution (Sigma-Aldrich, 90mM, diluted in deionised water) at 70°C for 30 min. After mildly rinsing with i) deionised water and ii) ethanol, the substrate was dry by airflow. A mesoporous TiO_2 layer was deposited using a diluted TiO_2 paste (30 nm in particle size, dyesol) in a ratio of paste/ethanol, 1/7 (w/w) at 6000 rpm for 30 s. Then, the substrate was heated on a hotplate at 120°C for 5 min and followed by a calcination at 500°C for 30 min. 1.2 M lead iodide (PbI_2) solution was prepared by dissolving PbI_2 powder (Alfa Aeser, 99.9985%) in a blend of dimethylformamide (DMF, Sigma-Aldrich, anhydrous) and dimethyl sulfoxide (DMSO, Sigma-Aldrich, ACS reagent grade) at a volume ratio of 9/1. The perovskite layer was prepared by means of two-step spin-coating process. Firstly, the PbI_2 solution (kept at 70°C during whole process) was spin coated on the previously prepared mesoporous layer at 3000 rpm for 30 s in dynamic way. Secondly, 100 μL of an organic solutioncomposed of 195 mM methylammonium iodide (MAI), 55 mM formamidinium iodide (FAI), 28 mM methylammonium bromine (MABr) and 70 mM methylammonium chloride (MACl) in IPA, was dropped on the PbI_2 coated substrate by spin coating at 2000 rpm for 30 s. The as prepared perovskite film was heated on a hotplate at 120°C for 20 min. After cooling down to room temperature, a layer of hole transporting material was spin coated on the top using a solution, composed of 60 mM 2,2',7,7'- Tetrakis-(N,N-di-4-methoxyphenylamino)-9,9'-spirobifluorene (spiro-OMeTAD, 1-Material), 32 mM lithium bis(trifluoromethylsulphonyl)imide (Li-TFSI, Sigma-Aldrich), and 195 mM tert-butylpyridine (tBP, Sigma-Aldrich, 96%) in chlorobenzene (Sigma-Aldrich, anhydrous, 99.8%) at 4000 rpm for 30 s. Finally, a gold layer of 80-nm thickness was thermal evaporated on the top as a terminal electrode. The entire fabrication process was conducted in a glove box with both moisture and oxygen

controlled.

Measurements of Perovskite solar cells: The current-voltage response of new devices was measured under a Sun 2000 solar simulator (150 W, ABET Technologies) equipped with a Keithley 2400 digital source meter. The illumination intensity was calibrated using a commercial silicon photodiode at 1 sun (100 mW/cm^2). No bias or illumination was pretreated on devices in every measurement. During the scan, the scan step, integration time and delay time were set at 10 mV, 3 ms and 50 ms, respectively, which corresponded to a scan rate of 42.9 mV/s. ND filters were applied as measurements under different light intensities.

Synthesis of oligomericruthenium molecular complex {Ru^{II}(tda)(bipy)}$_{15}$ (where tda = [2,2':6',2''-terpyridine]-6,6''-dicarboxylato and bipy = 4,4'-bipyridine): The synthesis of the ruthenium molecular complex oligomer follows a modified reported procedure as described in Ref. [53] for complex [Ru^{II}(tda)(py)$_2$] (where py = pyridine) by substituting pyridine by 4,4'-bipyridine bridging ligand. The final compound has been been found to contain 15 units of the {Ru^{II}(tda)(bipy)} metallic centers. The chemical structure of this novel ruthenium molecular catalyst is shown in Figure S1, and it is indicated in this work as {Ru^{II}(tda)(bipy)}$_{15}$.

Preparation of the anodes containing the {Ru^{II}(tda)(bipy)}$_{15}$ material: Two kinds of {Ru^{II}(tda)(bipy)}$_{15}$ molecular complex based anodes are prepared, depending on the conductive substrate where the catalystis is deposited. The first kind consists of conductive FTO coated glass from XopFisica (thickness, 2.3-3.0 mm; resistance, 6-9 Ω/cm^2) and the second kind consists of glassy carbon plate from HTW® (20 mm x 10 mm x 180 mm) substrates. Before loading the water oxidation catalyst on the surface of the substrates, the FTO coated glass is cleaned by an alkaline solution ($V_{HELLANEX}$: $V_{Milli\text{-}Q\ water}$ =100:1, Hellmanex is one kind of powerful alkaline and purchased from Hellma

GmbH & CO. KG), Milli-Q water and ethanol. Each cleaning step are under 10 min sonication and then rinsed by the corresponding solvents. After all these steps, the FTO coated glass is dried in the oven at 100 ℃ overnight, and then annealed at 300 ℃ for 30 min in the furnace to remove the organic contaminations on the surface and ensure a good conductivity. The carbon plates are just rinsed with Milli-Q water and dried with fiber-free wipers. After cleaning these substrates, 10 mg of multi wall carbon nanotubes (MWCNTs, CAS# 99685-96-8, Nanostructured & Amorphous Materials, Inc.) powders are suspended in 10 mL of Tetrahydrofuran (THF, dried, purity ≥ 99%, CAS number# 109-99-9, Sigma-Aldrich) under 40 min sonication. Then this CNTs suspension solution are used to cover the surface of ~1.87 cm^2 cleaned FTO glass and ~1.5 cm^2 carbon plates by drop casting with 15 drops (20 µL per drop), and each drop is placed after the last drop is totally dried. Then 4.3 mg of $\{Ru^{II}(tda)(bipy)\}_{15}$ powder is dissolved in 5 mL of 2,2,2-Trifluoroethanol (TFE, CAS number# 75-89-8, Sigma-Aldrich), which is with a concentration of 0.86 mg/mL. Finally, the $\{Ru^{II}(tda)(bipy)\}_{15}$ solution is drop casted on the CNTs covered FTO glass and carbon plates (3 drops, 20 µL per drop), new drops are added only after the last drop is totally dried on the substrate. The resulting anodes are indicated as $\{Ru^{II}(tda)(bipy)\}_{15}$@CNTs/FTO and $\{Ru^{II}(tda)(bipy)\}_{15}$@CNTs/C-plate, respectively. A schematic describing the whole preparation process on FTO coated glass substrate can be observed in Figure S2.

Morphology characterization of the $\{Ru^{II}(tda)(bipy)\}_{15}$@CNTs/FTO: The surface of the $\{Ru^{II}(tda)(bipy)\}_{15}$@CNTs/FTO electrodes have been characterized by scanning electron microscopy (SEM, JEOL JSM-6400 model) from both cross-sectional and top views (Figure S3). For the cross-sectional view characterization, the prepared electrodes are cut carefully, and the fresh edges are used for the analysis. The resulting cross sectional SEM image in Figure S3b shows that the thickness of the

$\{Ru^{II}(tda)(bipy)\}_{15}$@CNTs is around 50 μm. The chemical composition of the electrode surface has also been analyzed by the energy-dispersive X-ray spectroscopy (EDX), which still shows the ruthenium element signal after 1.5 hours electrochemical test at pH 7 (Figure S3d).

Electrochemical test: All electrochemical experiments are performed by using a CHI 660D and CHI 620E potentiostat (CH Instruments, Inc.). Two kinds of phosphate based electrolytes are used for the electrochemical test, which are pH 7 buffer made of 9.785 g NaH_2PO_4 and 19.945 g Na_2HPO_4 (ionic strength: 1M) and pH 12 buffer made of 0.5187 g $NaHPO_4$ and 1.033 g Na_3PO_4 (ionic strength: 0.1M). The pH values of the buffer electrolytes are measured by a pH meter (Mettler toledo, Inc.). In three electrode configuration system, all the electrochemical experiments are done in a one compartment cell (25 mL volume) with the $\{Ru^{II}(tda)(bipy)\}_{15}$@CNTs/FTO or $\{Ru^{II}(tda)(bipy)\}_{15}$@CNTs/C-plate as working electrode, Pt mesh as counter electrode and Hg/Hg_2SO_4 (saturated K_2SO_4) as reference electrode. However, in the two electrode configuration, all the measurements are performed in a two-compartments cell (10 mL per compartment) with a separation frit, and without using any reference electrode (the working lead connects with the $\{Ru^{II}(tda)(bipy)\}_{15}$@CNTs/FTO or $\{Ru^{II}(tda)(bipy)\}_{15}$@CNTs/C-plate, and the auxiliary lead is connected together with the reference lead to the Pt mesh). All the cyclic voltammetries (CVs), chronopotentiometry and constant potential electrolysis are collected in three-electrode configuration. The CVs are with iR compensation and at a scan rate of 100 mV/s, while chronopotentiometry and constant potential electrolysis are obtained without iR compensation. All the linear sweep voltammetries (LSVs) are collected in two-electrode configuration without iR compensation and at a scan rate of 10 mV/s. When the electrodes are placed inside the sealed two-compartment cell, the electrolyte are degassed with N_2 for 15-20 min prior to

the LSV measurements. The loading of the ruthenium molecular catalyst Γ (mol/cm^2) on the substrate can be calculated by the averaged charge (Q_{Ru}) under the Ru^{III}/Ru^{II} and Ru^{IV}/Ru^{III} oxidation waves in the second CV scan (the first CV is always unstable) of the anodes, with the formula $\Gamma(mol/cm^2)= Q_{Ru}/(A\times F)$. A is the geometrical area of the $\{Ru^{II}(tda)(bipy)\}_{15}$@CNTs/FTO or $\{Ru^{II}(tda)(bipy)\}_{15}$@CNTs/C-plate electrode and F is the Faradaic constant. According to this calculation, the loadings of the ruthenium molecular catalyst in $\{Ru^{II}(tda)(bipy)\}_{15}$@CNTs/FTO (1.87 cm^2) and $\{Ru^{II}(tda)(bipy)\}_{15}$@CNTs/C-plate (1.5 cm^2) are 16 nmol/cm^2 and 6.2 nmol/cm^2, respectively.

PV-EC solar-driven water splitting: All the experiments are performed in a two-compartment, and two-electrode configuration. The two-compartments cell is filled with 6 mL phosphate buffer (pH 7, 1 M) at each compartment, and the electrolyte is also degassed with N_2 flow for 10-20 min after placing the anodes and cathodes. The photocurrent generated during the light driven PV-EC water splitting experiment is monitored with a CHI 620E potentiostat by performing a bulk electrolysis at 0V bias, which works as an ammeter in this case. A schematic and digital photograph of the setup is shown in Figure S4. As it is shown in Figure S4, the PV cells are illuminated by a 150 W Xenon lamp (LS-150, ABET technology) equipped with a filter to block UV light (λ < 400 nm). The light intensity can be measured by using a calibrated silicon photodiode at 25 °C, and the illumination reaching the PV cells is tuned by using different optical filters depending on the desired current. In the case of the perovskite cell (0.18 cm^2), the light intensity was set to 0.28 sun while a 0.36 sun light intensity was used for the InGaP/GaAs/Ge triple junction solar cell (0.18 cm^2, purchased from Fullsuns Energy Technology Co., Ltd). Two metallic meshes are also used to obtain a large and uniform illumination. The cathode side of the PV cells is connected with the working lead of the

potentiostat, while the reference and auxiliary leads are connected together to the cathode of the electrolyser. Finally, an additional electrical wire is needed to connect the anode side of the PV cells to the anode of the electrolyser. The resistance of this configuration is measured before starting the illumination, which is in the range of 210-240 Ω. Once we turn on the light, the spontaneous water splitting is triggered. During the process the generated photocurrent is monitored through the potentiostat while the generated oxygen (O_2) and hydrogen (H_2) gases are monitored through an O_2 sensitive OX-NP15127 Clark electrode (Unisense) and a H_2 sensitive H2-NP706731Clark electrode (Unisense), respectively.

F 3 Results and Discussion

F 3.1 Fabrication and characterization of the perovskite solar cells

Figure 1a shows a schematic representation of the structure of a perovskite solar cell, which has been fabricated by following the methods discussed in the Experimental section. The water splitting reaction happens at a theoretically thermodynamically potential of 1.23 V but additional potentials are needed due to the reaction kinetics with currently available electrolysers.[11-13] Therefore, at least two perovskite solar cells (like the one shown in Figure 1a) need to be connected in sereies to reach a V_{OC} that is large enough for triggering the water splitting reaction.[39] In our study, we connected two pieces of our fabricated perovskite solar cells in series, generating an effective illumination area of 0.18 cm^2. The typical current density versus voltage (*J*-*V*) characteristics of the series-connected cells under illumination of various light intensities and in the dark are shown in Figures 1b and 1c. As it can be observed, the V_{OC} and solar-to-electric power conversion efficiency (PCE) of the connected cells reach around 2 V and 18 %, respectively (see also the table in Figure 1c for variabilities depending on light intensities).

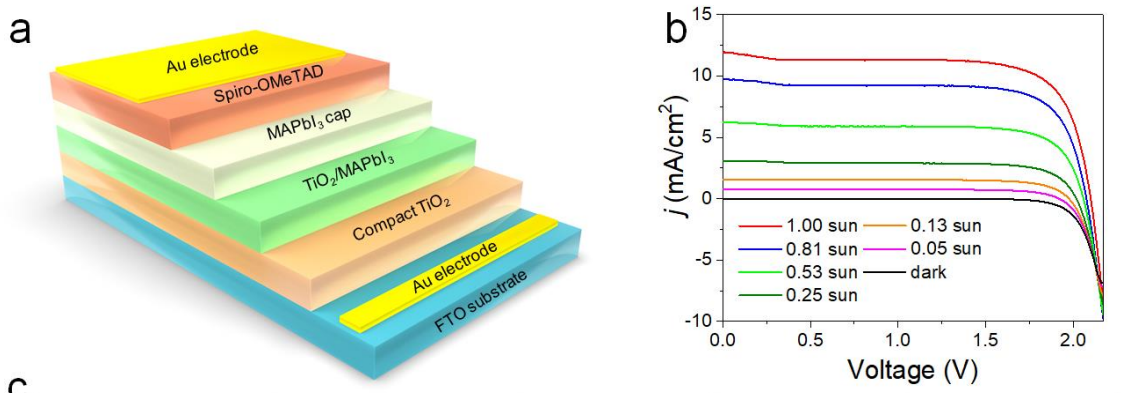

c

Light intensity	J_{SC} (mA/cm²)	V_{OC} (V)	FF	PCE (%)
1.00 sun	11.9	2.10	0.72	18.1
0.81 sun	9.7	2.08	0.73	18.1
0.53 sun	6.2	2.06	0.73	18.2
0.25 sun	3.1	2.02	0.72	17.9
0.13 sun	1.6	1.98	0.75	18.2
0.05 sun	0.8	1.92	0.74	20.5

Figure 1. (a) Schematic representation of a single perovskite solar cell. (b) The *J-V* characteristics of two series-connected perovskite solar cells under the illumination at different light intensities and in the dark. (c) Main parameters for the two series-connected solar cells, which are taken from the measurements of the *J-V* characteristics in (b). J_{SC}, short circuit current; V_{OC}, open circuit potential; FF, Fill factor; PCE, power conversion efficiency.

The energy conversion efficiency of the perovskite solar cells built in our lab is comparable to other reported perovskite solar cells, in which the PCE improves from 2.2 %[54] in the first reports to the latest 22.1 %[55] during the last decade. The short circuit current density (J_{sc}) of the solar cells decreases by lowering the light intensity. In this study, we have decided to use low light intensity for the illumination since the sunlight on the earth depends on the geographical location and the seasons, and the intensity of the sunlight can just maintain 100 mW/cm^2 (standard 1 sun intensity) for several hours during a day. It is also interesting to explore low light working conditions to explore the feasibility to perform indoor experiments, in which case the intensity of sunlight will also be lower than 100 mW/cm^2.

V

F 3.2. $\{Ru^{II}(tda)(bipy)\}_{15}$ complex based anode and electrolyser set-up

With the highly efficient perovskite solar cells in hand, the following step of our study is to implement them in a water splitting cell for hydrogen fuel production by connecting them to an electrolyser system that works at suitable potential, i.e, close to the maximum power point of the PV cell. The water oxidation reaction in the anodic side of the cell is usually the limiting reaction, which requires higher overpotential.[56] In this work we explore a novel water oxidation catalytic material based on a molecular $\{Ru^{II}(tda)(bipy)\}_{15}$ catalytic site (where tda = [2,2':6',2"-terpyridine]-6,6"-dicarboxylato and bipy = 4,4'-bipyridine). This type of complex has shown excellent performance in homogeneous[57] and in heterogeneous[53, 58-59] systems. Thus, catalyst precursor $\{Ru^{II}(tda)(bipy)\}_{15}$ has been loaded both on FTO coated glass and carbon plates with the assistance of multi wall carbon nanotubes CNTs (see details in the experimental section). It is worth to note that the as-prepared $\{Ru^{II}(tda)(bipy)\}_{15}$@CNTs/FTO electrodes show great catalytic activity after an activation process that generates the real catalytic Ru-aqua species $\{Ru^{III}(tda)(OH)(bipy)\}_{15}$@CNTs/FTO.[57] As observed in Figure 2a, the catalyst precursor $\{Ru^{II}(tda)(bipy)\}_{15}$@CNTs/FTO and active catalyst can be distinguished by

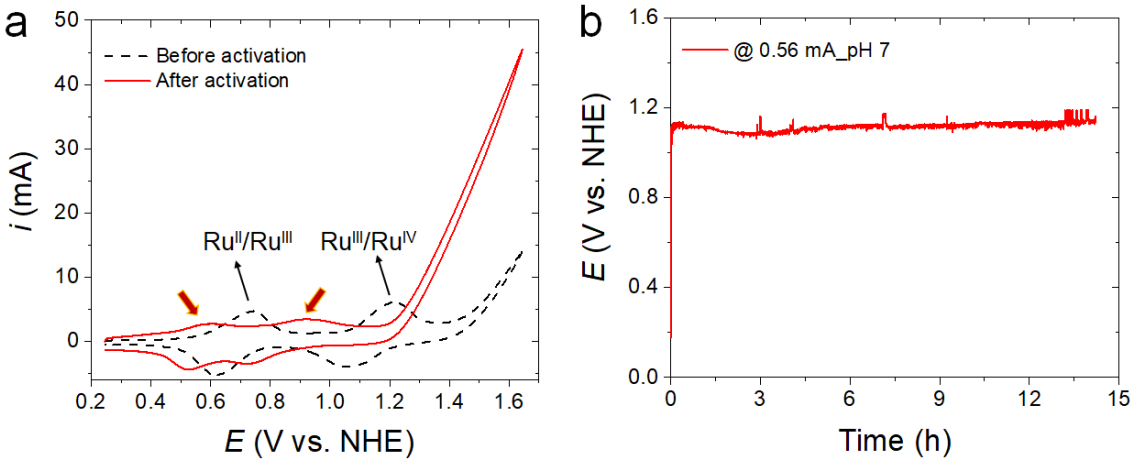

Figure 2. (a) Typical CVs of the $\{Ru^{II}(tda)(bipy)\}_{15}$@CNTs/FTO electrode before (dashed curve) and after activation (solid curve). (b) Chronopotentiometry experiment at a constant current of 0.56 mA for $\{Ru^{II}(tda)(bipy)\}_{15}$@CNTs/FTO as working electrode. All the experiments in (a) and (b) are performed at pH 7 phosphate buffer with an ionic strength of 1 M. The counter and reference electrodes are Pt mesh and Hg/Hg_2SO_4 (saturated K_2SO_4), respectively.

their corresponding redox couples attributed to the Ru^{III}/Ru^{II} and Ru^{IV}/Ru^{III} oxidation peaks (compare black dashed curve with red solid curve respectively). These waves are also very useful to rule out the featureless RuO_2, that is also an active catalyst for the water oxidation reaction.[35] After half an hour constant potential (1.25 V vs. NHE) electrolysis at pH 12 (Figure S5), the Ru^{III}/Ru^{II} and Ru^{IV}/Ru^{III} redox peaks of the precursor disappear and two new peaks of the Ru-aqua active species are formed.[53] The activated anode, was coupled to a platinum mesh cathode in a two-compartment electrolytic cell and its performance was assessed by chronopotentiometry experiments. With a very little amount of molecular $\{Ru^{II}(tda)(bipy)\}_{15}$ catalyst (the loading is around 16 nmol/cm^2), the prepared $\{Ru^{II}(tda)(bipy)\}_{15}$@CNTs/FTO electrodes show efficient catalytic behaviors with long stability at a current of 0.56 mA which corresponds to the photocurrent generated by the series connected perovskite solar cells under 0.25 sun illumination (> 14 hours, Figure 2b).

F 3.3 PV-EC water splitting

After demonstrating that the series connected perovskite solar cells hold a high PCE and large V_{OC}, and also that the electrolytic system composed of $\{Ru^{II}(tda)(bipy)\}_{15}$@CNTs/FTO anode and platinum mesh cathode for the OER and HER respectively is efficient and robust, the PV-EC water splitting device has been assembled (Figure 3a). The details related to the combination of the solar cells and electrolyser are shown in the experimental section and Figure S4. Figure 3b shows the J-V characteristics of the connected perovskite solar cells under 0.28 sun illumination and the electrolyser under two-electrode configuration at pH 7, which overlaps at 1.63 V with a current density of 3.1 mA/cm^2. This overlapping point indicates the working conditions the whole system should perform upon illumination. Indeed, Figure 3c shows that the co-

V

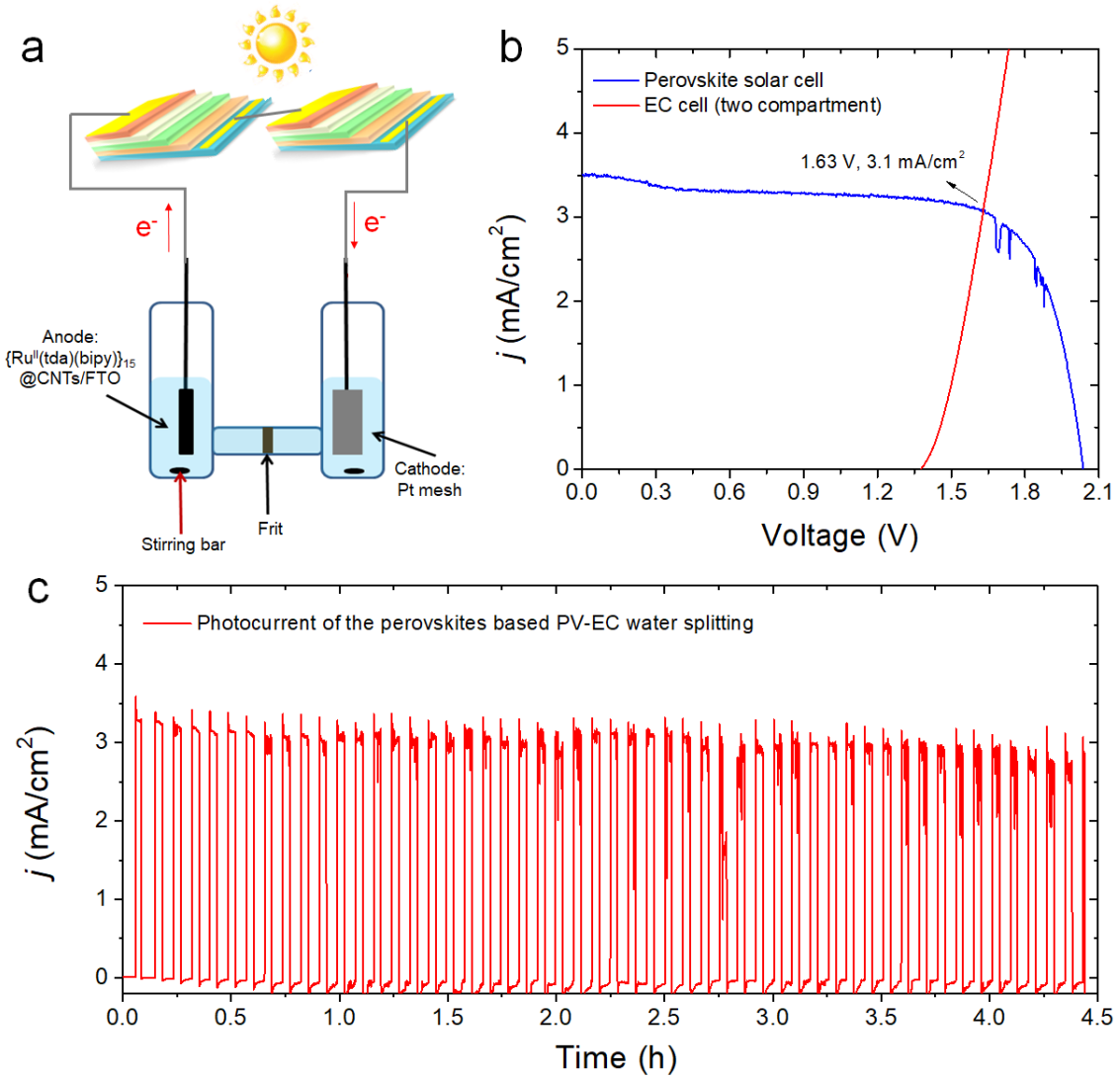

Figure 3. (a) Schematic diagram of the combined PV-EC water splitting device with the $\{Ru^{II}(tda)(bipy)\}_{15}$@CNTs/FTO as anode. (b) *J-V* curves of the two connected perovskite solar cells under simulated 0.28 sun illumination, and the $\{Ru^{II}(tda)(bipy)\}_{15}$@CNTs/FTO anode involved eletrolyser in a two-electrode configuration. The overlapping point indicates operation voltage and current of the spontaneous PV-EC water splitting. The effective illuminated surface area of the perovskite cells is 0.18 cm^2, and the geometric size of the anode is 1.87 cm^2. (c) The photocurrent density vs. time plot of the spontaneous PV-EC water splitting device under chopped light and without applying any external bias at pH 7.

-llected photocurrent is stable around 3 mA/cm^2 at pH 7 under chopped 0.28 sun illumination without any external bias for more than 4 hours. Moreover, when this spontaneous PV-EC water splitting happens, the working voltage has been monitored by using a multimeter to measure the potential between the anode and the cathode. The collected working voltages (Table S1) are in a range from 1.6 V to 1.64 V, which also

match well with the overlapping point in Figure 3b. The oxygen and hydrogen generated during the spontaneous water splitting experiment in Figure 3c has also been measured with Clark electrode sensors, and they are compared to the theoretically generated gas (calculated from the passed charge during the reaction). In Figures 4a and 4b, a Faradic efficiency close to 100 % can been observed for both oxygen and hydrogen gas evolution, indicating that the solar converted carriers are fully used for water splitting reaction and no side reactions happen. The solar-to-hydrogen efficiency of the PV-EC water splitting devices can be calculated through *Equation 4*, where η_F is the Fadadic efficiency calculated from the gas evolution, J_{OP} is the operation current density of the solar-driven PV-EC water splitting reaction, and P_{solar} is the solar intensity of the illumination, which is 28 mA/cm^2 for the solar-driven water splitting reaction in Figure 3c.

$$STH = \frac{(1.23\ V)\times\eta_F\times J_{op}}{P_{solar}} \qquad (Equation\ 4)$$

From this formula, a STH efficiency of ~13.2 % can be calculated for the PV-EC water splitting in Figure 3c. The *J-V* characteristics of the {Ru^{II}(tda)(bipy)}$_{15}$@CNTs/FTO electrode and perovskite solar cells have also been measured after the reaction in Figure 3c, and compared with those before the reaction (Figures 4c and 4d, respectively). We observe that the {Ru^{II}(tda)(bipy)}$_{15}$@CNTs/FTO electrode is very stable, which shows no change after > 4 hours PV-EC water splitting. It is worth to note that the CV (inset of Figure 4c) of the {Ru^{II}(tda)(bipy)}$_{15}$@CNTs/FTO electrode after the PV-EC water splitting still shows the related redox peaks of the Ru-aqua groups, which means the {Ru^{II}(tda)(bipy)}$_{15}$ molecular catalyst performs the catalytic behavior rather than RuO_2 during the whole reaction. However, the perovskite solar cells suffers a slight decay of their performance (Figure 4d) after the PV-EC water splitting, which can block the practical application of PV-EC water splitting devices.

In order to solve the stability problem of the solar cells, we have also combined

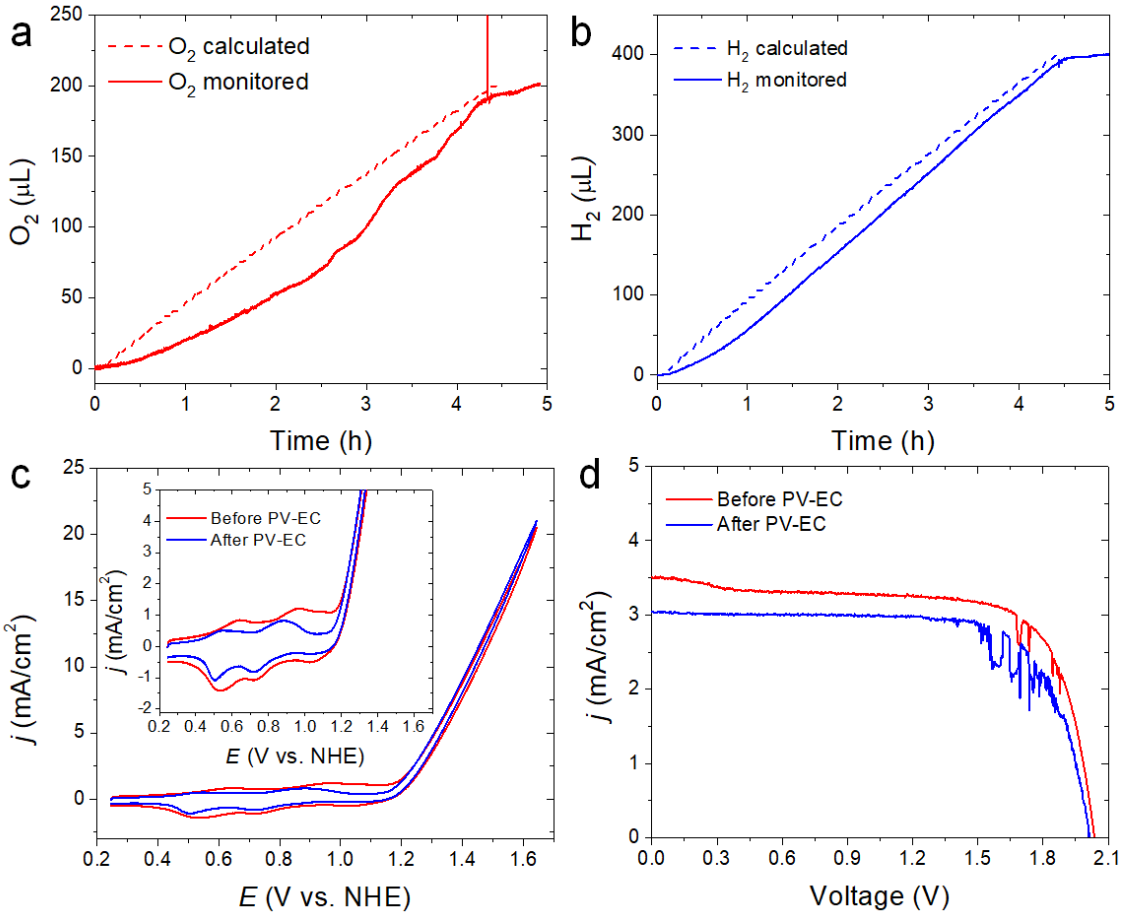

Figure 4. (a) Oxygen and (b) hydrogen evolution during the solar-driven PV-EC water splitting at pH 7 in Figure 3c. The dashed lines represent the theoretically generated oxygen and hydrogen during the spontaneous water splitting, calculated from the charges passed through the circuit, while the solid lines represents the oxygen and hydrogen measured by the Clark electrode sensors during the reaction. *J-V* characteristics of the $\{Ru^{II}(tda)(bipy)\}_{15}$@CNTs/FTO electrode at pH 7 (c) and perovskite solar cells (d) before and after the solar-driven PV-EC water splitting in Figure 3c. The inset image is a zoom-in image of (c).

our electrolyser with a commercially available InGaP/GaAs/Ge triple junction solar cell. Figure 5a shows the *J-V* characteristics of a single InGaP/GaAs/Ge triple junction solar cell under the illumination of 0.36 sun, and an electrolyser made of $\{Ru^{II}(tda)(bipy)\}_{15}$@CNTs/C-plate as anode and Pt mesh as cathode at pH 7 in two-electrode configuration. This commercially available triple junction solar cell shows a V_{OC} of 2.37 V, J_{SC} of 6.2 mA/cm^2, fill factor of 84.9 % and PCE of 34.1% under 0.36 sun illumination, which surpass the properties of the perovskite solar cells studied before. As

shown in Figure 5a, the *J-V* curves overlap at 1.9 V with a current density of 6.2 mA/cm^2. This voltage and current density match with the values when the triple junction solar cell is connected to the eletrolyser as discussed below. In this integrated configuration, the {Ru^{II}(tda)bi(py)}$_{15}$@CNTs/C-plate electrode is used instead of {Ru^{II}(tda)(bipy)}$_{15}$@CNTs/FTO as anode, because the glassy carbon plate substrate was found to be more conductive than that of the FTO, helping with a faster reaction kinetics. Figure 5b shows that the integrated PV-EC water splitting device performs with a stable photocurrent of 6.2 mA/cm^2 under 0.36 sun illumination without any external bias at pH 7. The corresponded working photovoltages have also been recorded, which range from 1.9-1.95 V. Longer time experiments have been performed and the corresponding photocurrent-time plot and photovoltages have been collected in Figure S6 and Table S2. The gas generated during the PV-EC water splitting reaction in Figure 5b has been also monitored in Figures 5c and 5d, which show a 100 % Faradic efficiency for both oxygen and hydrogen. Furthermore, we have calculated the STH efficiency of this commercially available triple junction solar cell based PV-EC water splitting device, and it achieves 21.2 % under 0.36 sun illumination at pH 7 (room temperature), which is the highest value ever reported without using a concentered light illumination (see Table S3, which summarizes and compares the STH efficiency of all the reported PV-EC water splitting devices to date). The *J-V* properties of the {Ru^{II}(tda)(bipy)}$_{15}$@CNTs/C-plate electrode and the triple junction solar cell before and after the PV-EC water splitting have been measured and are shown in Figures 5e and 5f. As it can be observed, both the electrode and solar cell don't show any decay. Moreover, the Ru-aqua peaks can be observed very clearly in the CVs (inset of Figure 5e) before and after PV-EC water splitting, indicating the great catalytic behavior and stability of the {Ru^{II}(tda)(bipy)}$_{15}$ molecular catalyst.

V

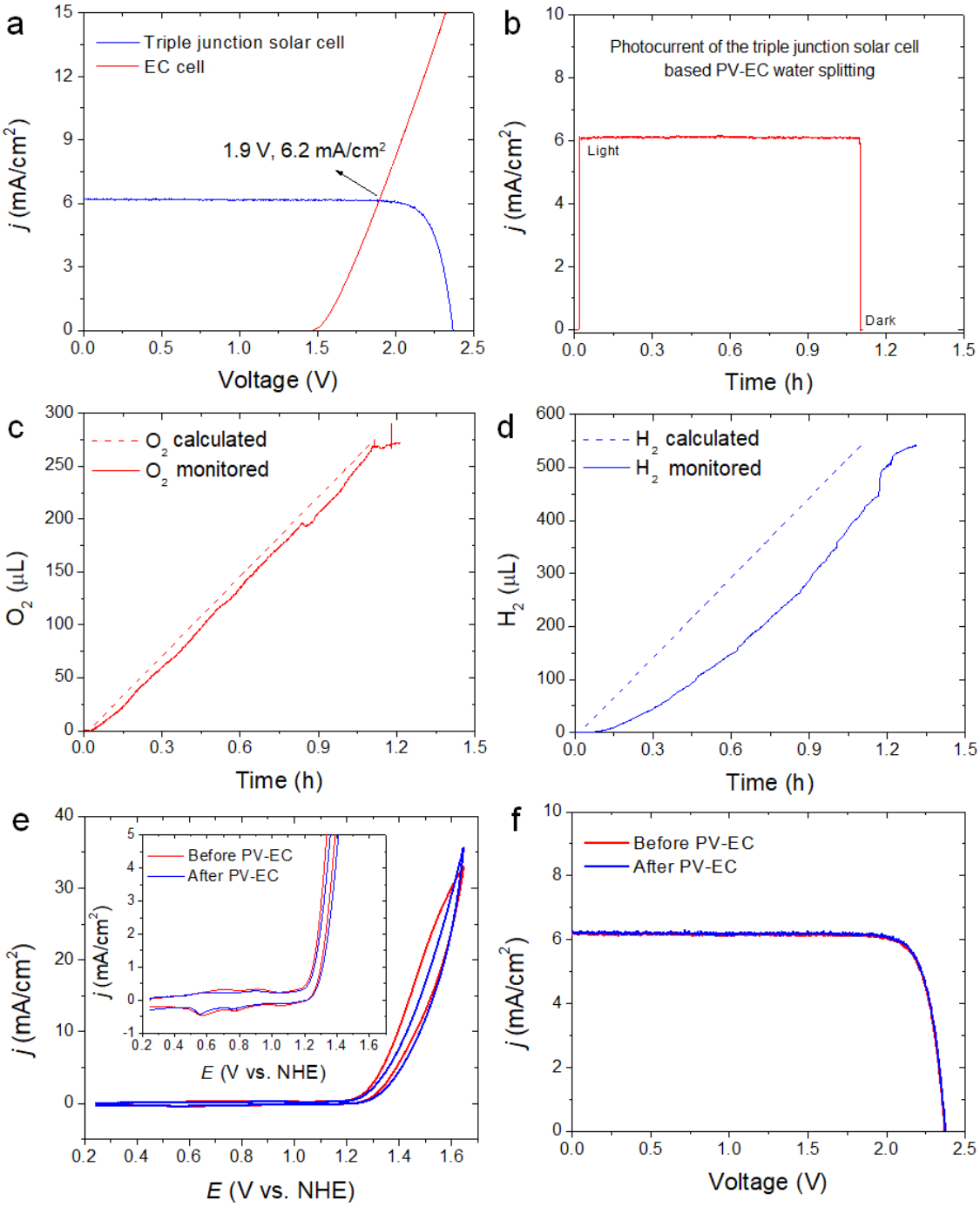

Figure 5. (a) *J-V* curves of the triple junction InGaP/GaAs/Ge solar cell under simulated 0.36 sun illumination, and electrolyser using $\{Ru^{II}(tda)(bipy)\}_{15}$@CNTs/C-plate as anode and Pt mesh as cathode in a two-electrode configuration. The effective illuminated surface area of this solar cell is 0.18 cm^2, and the geometric size of the anode is 1.5 cm^2. (b) The photocurrent density vs. time plot of the triple junction solar cell based PV-EC water splitting device under 0.36 sun and without applying any external bias at pH 7. (c) Oxygen and (d) hydrogen evolution during the reaction in (b). The dashed lines indicate the gas generated in theory calculated from the charge passed through the circuit, while the solid lines represent the measured gas. *J-V* cahracteristics of the (e) $\{Ru^{II}(tda)(bipy)\}_{15}$@CNTs/C-plate electrode and (f) triple junction solar cell before and after 4 hours solar-driven PV-EC water splitting in Figure S6.

V

F 4 Conclusions

In conclusion, we have implemented for the first time a molecular water oxidation catalytic material into PV-EC solar-driven water splitting devices. The integrated PV-EC water splitting devices have been built by using either state of art perovskite solar cells or commercially available triple junction Group III/IV solar cells. By using the novel ruthenium molecular based anodes and Pt cathodes for the electrolyser, the combined PV-EC devices reache STH efficiencies from 13.2% for the former to a top of 21.2% for the latter with no decay in activity for >4 hours at neutral pH (room temperature). The use of ruthenium molecular catalyst in this PV-EC configuration gives new opportunities to enhance the performance of the integrated PV-EC water splitting devices, which may promote the practical application of the PV-EC water splitting for large scale hydrogen production.

F 5 Acknowledgements

This work has been supported by the Young 1000 Global Talent Recruitment Program of the Ministry of Education of China, the National Natural Science Foundation of China (grants no. 61502326, 41550110223, 11661131002), the Jiangsu Government (grant no. BK20150343), the Ministry of Finance of China (grant no. SX21400213). The Collaborative Innovation Center of Suzhou Nano Science & Technology, the Jiangsu Key Laboratory for Carbon-Based Functional Materials & Devices and the Priority Academic Program Development of Jiangsu Higher Education Institutions are also acknowledged. MINECO and FEDER (CTQ2016-80058-R, CTQ2015-73028-EXP, SEV 2013-0319, ENE2016-82025-REDT, CTQ2016-81923-REDC), and AGAUR (2017-SGR-1631), are also gratefully acknowledged for providing financial support. Dr. Werther Cambarau is gratefully acknowledged for helping with experimental setup at the begining of the study.

V

F 6 References

[1] P. C. K. Vesborg, T. F. Jaramillo, Addressing the terawatt challenge: scalability in the supply of chemical elements for renewable energy, *RSC Adv.* **2012**, *2*, 7933.

[2] F. Perera, Pollution from fossil-fuel combustion is the leading environmental threat to global pediatric health and equity: solutions exist, *Int. J. Environ. Res. Public. Health* **2017**, *15*, 16.

[3] N. S. Lewis and D. G. Nocera, Powering the planet: Chemical challenges in solar energy utilization, *Proc. Natl. Acad. Sci. USA* **2006**, *103*, 15729.

[4] N. Armaroli and V. Balzani, Angew. Chem.- Int. Ed., **2007**, *46*, 52.

[5] T. Abbasi, S. A. Abbasi, 'Renewable' hydrogen: Prospects and challenges, *Renew. Sustainable Energy Rev.* **2011**, *15*, 3034.

[6] M. Balat, Potential importance of hydrogen as a future solution to environmental and transportation problems, *Int. J. Hydrogen Energy* **2008**, *33*, 4013.

[7] J. Nowotny, C. Sorrell, L. Sheppard, T. Bak, Solar-hydrogen: Environmentally safe fuel for the future, *Int. J. Hydrogen Energy* **2005**, *30*, 521.

[8] J. Turner, G. Sverdrup, M. K. Mann, P.-C. Maness, B. Kroposki, M. Ghirardi, R. J. Evans, D. Blake, Renewable hydrogen production, *Int. J. Energy Res.* **2008**, *32*, 379.

[9] M. G. Walter, E. L. Warren, J. R. McKone, S. W. Boettcher, Q. Mi, E. A. Santori, N. S. Lewis, Solar water splitting cells, *Chem. Rev.* **2010**, *110*, 6446.

[10] E. Bozoglan, A. Midilli, A. Hepbasli, Sustainable assessment of solar hydrogen production techniques, *Energy* **2012**, *46*, 85.

[11] M. G. Walter, E. L. Warren, J. R. McKone, S. W. Boettcher, Q. Mi, E. A. Santori, N. S. Lewis, Solar water splitting cells, *Chem. Rev.* **2010**, *110*, 6446.

[12] J. Li, N. Wu, Semiconductor-based photocatalysts and photoelectrochemical cells for solar fuel generation: a review, *Catal. Sci. Technol*. **2015**, *5*, 1360.

[13] T. Bak, J. Nowotny, M. Rekas, C. C. Sorrell, Photo-electrochemical hydrogen generation from water using solar energy. Materials-related aspects. *Int. J. Hydrogen Energy* **2002**, *27*, 991.

[14] J. R. McKone, N. S. Lewis, H. B. Gray, Will solar-driven water-splitting devices see the light of day? *Chem. Mater.* **2014**, *26*, 407.

[15] L. R. Bolton, S. J. Strickler, J. S. Connolly, Limiting and realizable efficiencies of solar photolysis of water. Nature **2015**, *316*, 495.

[16] S. Hu, C. Xiang, S. Haussener, A. D. Berger, N. S. Lewis, An analysis of the optimal band gaps of light absorbers in integrated tandem photoelectrochemical water-splitting systems, *Energy Environ. Sci*. **2013**, *6*, 2984.

[17] R. E. Rocheleau, E. L. Miller, Photoelectrochemical production of hydrogen: engineering loss analysis, *Int. J. Hydrogen Energy* **1997**, *22*, 771.

[18] L. C. Seitz, Z. Chen, A. J. Forman, B. A. Pinaud, J. D. Benck, T. F. Jaramillo, Modeling practical performance limits of photoelectrochemical water splitting based on the current state of materials research, *ChemSusChem.* **2014**, *7*, 1372.

[19] J. D. Holladay, J. Hu, D. L. King, Y. Wang, An overview of hydrogen production technologies, *Catal. Today* **2009**, *139*, 244.

[20] K. E. Ayers, E. B. Anderson, C. Capuano, B. Carter, L. Dalton, G. Hanlon, J. Manco, M. Niedzwiecki, Research advances towards low cost, high efficiency PEM electrolysis, *ECS Transact.* **2010**, *33*, 3.

[21] M. Carmo, D. L. Fritz, J. Mergel, D. Stolten, A comprehensive review on PEM water electrolysis, *Int. J. Hydrogen Energy* **2013**, *38*, 4901.

[22] K. Fujii, S. Nakamura, M. Sugiyama, K. Watanabe, B. Bagheri, Y. Nakano, Characteristics of hydrogen generation from water splitting by polymer electrolyte electrochemical cell directly connected with concentrated photovoltaic cell, *Int. J. Hydrogen Energy* **2013**, *38*, 14424.

[23] A. Nakamura, Y. Ota, K. Koike, Y. Hidaka, K. Nishioka, M. Sugiyama, K. Fujii, A 24.4% solar to hydrogen energy conversion efficiency by combining concentrator photovoltaic modules and electrochemical cells, *Appl. Phys. Express* **2015**, *8*, 107101.

[24] G. Peharz, F. Dimroth, U. Wittstadt, Solar hydrogen production by water splitting with a conversion efficiency of 18%, *Int. J. Hydrogen Energy* **2007**, *32*, 3248.

[25] S. Licht, B. Wang, S. Mukerji, T. Soga, M. Umeno, H. Tributsch, Efficient solar water splitting, exemplified by RuO_2 -catalyzed AlGaAs/Si photoelectrolysis, *J. Phys. Chem. B* **2000**, *104*, 8920.

[26] M. A. Green, K. Emery, Y. Hishikawa, W. Warta, Solar cell efficiency tables (version 37), *Prog. Photovolt: Res. Appl.* **2011**, *19*, 84.

[27] A. De Vos, Detailed balance limit of the efficiency of tandem solar cells, *J. Phys. D Appl. Phys.* **1980**, *13*, 839.

[28] S. Guha, J. Yang, P. Nath, M. Hack, Enhancement of open circuit voltage in high efficiency amorphous silicon alloy solar cells, *Appl. Phys. Lett.* **1986**, *49*, 218.

[29] E. Edri, S. Kirmayer, M. Kulbak, G. Hodes, D. Cahen, Chloride Inclusion and Hole Transport Material Doping to Improve Methyl Ammonium Lead Bromide Perovskite-Based High Open-Circuit Voltage Solar Cells, *J. Phys. Chem. Lett.* **2014**, *5*, 429.

[30] E. Edri, S. Kirmayer, D. Cahen, G. Hodes, High Open-Circuit Voltage Solar Cells Based on Organic-Inorganic Lead Bromide Perovskite, *J. Phys. Chem. Lett.* **2013**, *4*, 897.

[31] S. Ryu, J. H. Noh, N. J. Jeon, Y. Chan Kim, W. S. Yang, J. Seo, S. I. Seok, Voltage output of efficient perovskite solar cells with high open-circuit voltage and fill factor, *Energy Environ. Sci.* **2014**, *7*, 2614.

[32] T. J. Jacobsson, V. Fjällström, M. Sahlberg, M. Edoff, T. Edvinsson, A monolithic device for solar water splitting based on series interconnected thin film absorbers reaching over 10% solar-to-hydrogen efficiency, *Energy Environ. Sci.* **2013**, *6*, 3676.

V

[33] O. Khaselev, High-efficiency integrated multijunction photovoltaic/electrolysis systems for hydrogen production, *Int. J. Hydrog. Energy* **2001**, *26*, 127.

[34] J. Li, Y. Wang, T. Zhou, H. Zhang, X. Sun, J. Tang, L. Zhang, A. M. Al-Enizi, Z. Yang, G. Zheng, nanoparticle superlattices as efficient bifunctional electrocatalysts for water splitting, *J. Am. Chem. Soc.* **2015**, *137*, 14305.

[35] X. Elias, Q. Liu, C. Gimbert-Suriñach, R. Matheu, P. Mantilla-Perez, A. Martinez-Otero, X. Sala, J. Martorell, A. Llobet, Neutral water splitting catalysis with a high FF triple junction polymer cell, *ACS Catal.* **2016**, *6*, 3310.

[36] J. Jia, L. C. Seitz, J. D. Benck, Y. Huo, Y. Chen, J. W. D. Ng, T. Bilir, J. S. Harris, T. F. Jaramillo, Solar water splitting by photovoltaic-electrolysis with a solar-to-hydrogen efficiency over 30%, *Nat. Commun.* **2016**, *7*, 13237.

[37] M. Gong, W. Zhou, M. J. Kenney, R. Kapusta, S. Cowley, Y. Wu, B. Lu, M.-C. Lin, D.-Y. Wang, J. Yang, B.-J. Hwang, H. Dai, Blending Cr_2O_3 into a NiO–Ni electrocatalyst for sustained water splitting, *Angew. Chem.- Int. Ed.* **2015**, *54*, 11989.

[38] S.-H. Hsu, J. Miao, L. Zhang, J. Gao, H. Wang, H. Tao, S.-F. Hung, A. Vasileff, S. Z. Qiao, B. Liu, An earth-abundant catalyst-based seawater photoelectrolysis system with 17.9% solar-to-hydrogen efficiency, *Adv. Mater.* **2018**, *30*, 1707261.

[39] J. Luo, J.-H. Im, M. T. Mayer, M. Schreier, M. K. Nazeeruddin, N.-G. Park, S. D. Tilley, H. J. Fan, M. Gratzel, Water photolysis at 12.3% efficiency via perovskite photovoltaics and Earth-abundant catalysts, *Science* **2014**, *345*, 1593.

[40] Y. Gorlin, T. F. Jaramillo, A bifunctional nonprecious metal catalyst for oxygen reduction and water oxidation, *J. Am. Chem. Soc.* **2010**, *132*, 13612.

[41] R. D. L. Smith, M. S. Prévot, R. D. Fagan, Z. Zhang, P. A. Sedach, M. K. J. Siu, S. Trudel, C. P. Berlinguette, photochemical route for accessing amorphous metal oxide materials for water oxidation catalysis, *Science* **2013**, 1233638.

[42] S. Y. Reece, J. A. Hamel, K. Sung, T. D. Jarvi, A. J. Esswein, J. J. H. Pijpers, D. G. Nocera, wireless solar water splitting using silicon-based semiconductors and earth-abundant catalysts, *Science* **2011**, *334*, 645.

[43] M. J. Kenney, M. Gong, Y. Li, J. Z. Wu, J. Feng, M. Lanza, H. Dai, High-performance silicon photoanodes passivated with ultrathin nickel films for water oxidation, *Science* **2013**, *342*, 836.

[44] T. Han, Y. Shi, X. Song, A. Mio, L. Valenti, F. Hui, S. Privitera, S. Lombardo, M. Lanza, Ageing mechanisms of highly active and stable nickel-coated silicon photoanodes for water splitting, *J. Mater. Chem. A* **2016**, *4*, 8053.

[45] Y. Shi, T. Han, C. Gimbert-Suriñach, X. Song, M. Lanza, A. Llobet, Substitution of native silicon oxide by titanium in Ni-coated silicon photoanodes for water splitting solar cells, *J. Mater. Chem. A* **2017**, *5*, 1996.

[46] C. C. L. McCrory, S. Jung, I. M. Ferrer, S. M. Chatman, J. C. Peters, T. F. Jaramillo, Benchmarking hydrogen evolving reaction and oxygen evolving reaction electrocatalysts for solar water splitting devices, *J. Am. Chem. Soc.* **2015**, *137*, 4347.

[47] Y. Shi, C. Gimbert-Suriñach, T. Han, S. Berardi, M. Lanza, A. Llobet, CuO-functionalized silicon photoanodes for photoelectrochemical water splitting devices, *ACS Appl. Mater. Interfaces* **2016**, *8*, 696.

[48] C. W. Cady, R. H. Crabtree, G. W. Brudvig, Functional models for the oxygen-evolving complex of photosystem II, *Coord. Chem. Rev.* **2008**, *252*, 444.

[49] S. Berardi, S. Drouet, L. Francas, C. Gimbert-Surinach, M. Guttentag, C. Richmond, T. Stolla, A. Llobet, Molecular artificial photosynthesis, *Chem. Soc. Rev.* **2014**, *43*, 7501.

[50] P. Garrido-Barros, C. Gimbert-Surinach, R. Matheu, X. Sala, A. Llobet, How to make an efficient and robust molecular catalyst for water oxidation, *Chem. Soc. Rev.* **2017**, *46*, 6088.

[51] Y. Hou, B. L. Abrams, P. C. K. Vesborg, M. E. Björketun, K. Herbst, L. Bech, A. M. Setti, C. D. Damsgaard, T. Pedersen, O. Hansen, J. Rossmeisl, S. Dahl, J. K. Nørskov, I. Chorkendorff, Bioinspired molecular co-catalysts bonded to a silicon photocathode for solar hydrogen evolution, *Nat. Mater.* **2011**, *10*, 434.

[52] Fukuzumi, Y. Yamada, T. Suenobu, K. Ohkubo, H. Kotani, Catalytic mechanisms of hydrogen evolution with homogeneous and heterogeneous catalysts, *Energy Environ. Sci.* **2011**, *4*, 2754.

[53] J. Creus, R. Matheu, I. Peñafiel, D. Moonshiram, P. Blondeau, J. Benet-Buchholz, J. García-Antón, X. Sala, C. Godard, A. Llobet, A million turnover molecular anode for catalytic water oxidation, *Angew. Chem.- Int. Ed.* **2016**, *55*, 15382.

[54] A. Kojima, K. Teshima, R. Yaegashi, T. Miyasaka, Y. Shirai, Novel photoelectrochemical cell (I) using a halogenated lead compound as a visible light sensitizer, 73rd Congress of the Electrochemical Society of Japan, Tokyo Metropolitan University, April 1, 2006; Paper 1118.

[55] W. S. Yang, B.-W. Park, E. H. Jung, N. J. Jeon, Y. C. Kim, D. U. Lee, S. S. Shin, J. Seo, E. K. Kim, J. H. Noh, S. I. Seok, Iodide management in formamidinium-lead-halide-based perovskite layers for efficient solar cells, *Science* **2017**, *356*, 1376.

[56] H. Inoue, T. Shimada, Y. Kou, Y. Nabetani, D. Masui, S. Takagi, H. Tachibana, The water oxidation bottleneck in artificial photosynthesis: how can we get through it? An alternative route involving a two-electron process, *ChemSusChem* **2011**, *4*, 173.

[57] R. Matheu, M. Z. Ertem, J. Benet-Buchholz, E. Coronado, V. S. Batista, X. Sala, A. Llobet, Intramolecular proton transfer boosts water oxidation catalyzed by a Ru complex, *J. Am. Chem. Soc.* **2015**, *137*, 10786.

[58] R. Matheu, I. A. Moreno-Hernandez, X. Sala, H. B. Gray, B. S. Brunschwig, A. Llobet, N. S. Lewis, photoelectrochemical behavior of a molecular ru-based water-oxidation catalyst bound to TiO_2-protected Si photoanodes, *J. Am. Chem. Soc.* **2017**, *139*, 11345.

[59] S. Grau, S. Berardi, A. Moya, R. Matheu, V. Cristino, J. Vilatela, C. A. Bignozzi, S. Caramori, C. Gimbert Suriñach, A. Llobet, A hybrid molecular photoanode for efficient light induced water oxidation, *Sustainable Energy Fuels* **2018**, *2*, 1979.

F 7 Supporting Information

V

Paper F: An anode based on a ruthenium molecular water oxidation catalyst for a photovoltaic-electrolysis water splitting with solar to hydrogen efficiency

Index

Figure S1. Chemical structure of the $\{Ru^{II}(tda)(bipy)\}_{15}$ molecular catalyst

Figure S2. Fabrication process of the $\{Ru^{II}(tda)(bipy)\}_{15}$@CNTs/FTO electrode

Figure S3. Integrated PV-EC water splitting setup

Figure S4. Morphology and chemical composition of the fabricated $\{Ru^{II}(tda)(bipy)\}_{15}$ @CNTs/FTO electrodes

Figure S5. Activation process of a $\{Ru^{II}(tda)(bipy)\}_{15}$@CNTs/FTO electrode

Table S1. The recorded photocurrents and working voltages during the PV-EC water splitting in Figure 3c

Figure S6. The whole I-t plot of the solar-driven PV-EC water splitting in Figure 5b

Table S2. The recorded photocurrents and working voltages during the PV-EC water splitting in Figure S6

Table S3. A summary of all the integrated PV-EC water splitting devices that have been reported before.

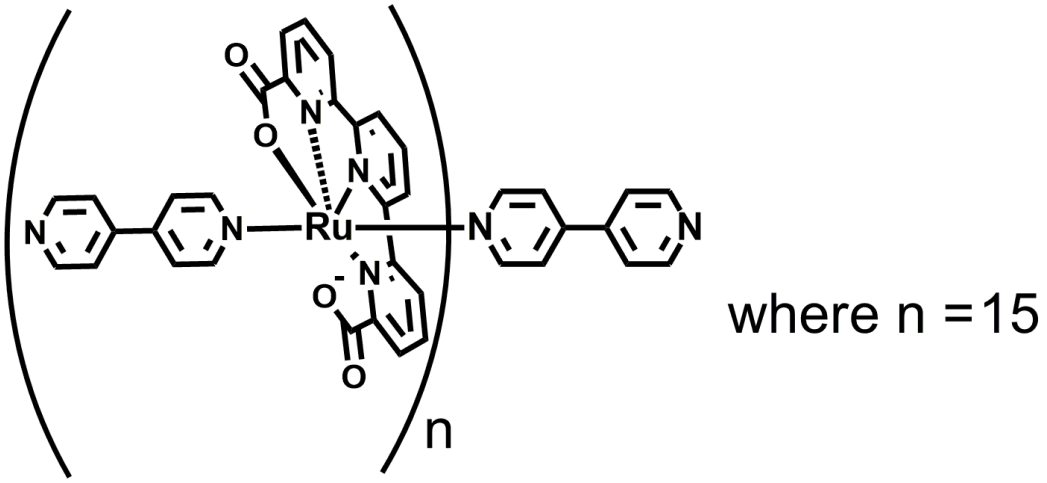

Figure S1. Chemical structure of the novel ruthenium molecular catalyst used in our study, which is indicated as $\{Ru^{II}(tda)(bipy)\}_{15}$.

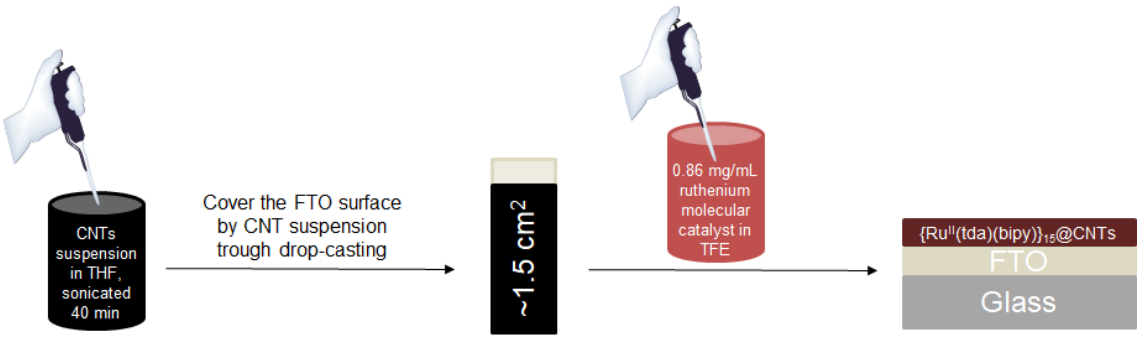

Figure S2. Schematic of the whole preparation process of the $\{Ru^{II}(tda)(bipy)\}_{15}$@CNTs/FTO electrodes.

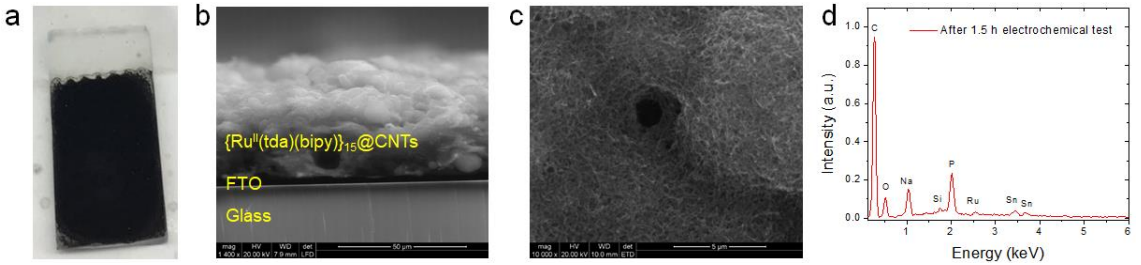

Figure S3. Digital photo (a), cross-sectional and top view scanning electron microscopy (SEM) images (b, c) of a fresh $\{Ru^{II}(tda)(bipy)\}_{15}$@CNTs/FTO electrode. (d) Energy-dispersive X-ray spectroscopy (EDS) of a tested $\{Ru^{II}(tda)(bipy)\}_{15}$@CNTs/FTO electrode. The width of the electrode in (a) is 1 cm.

V

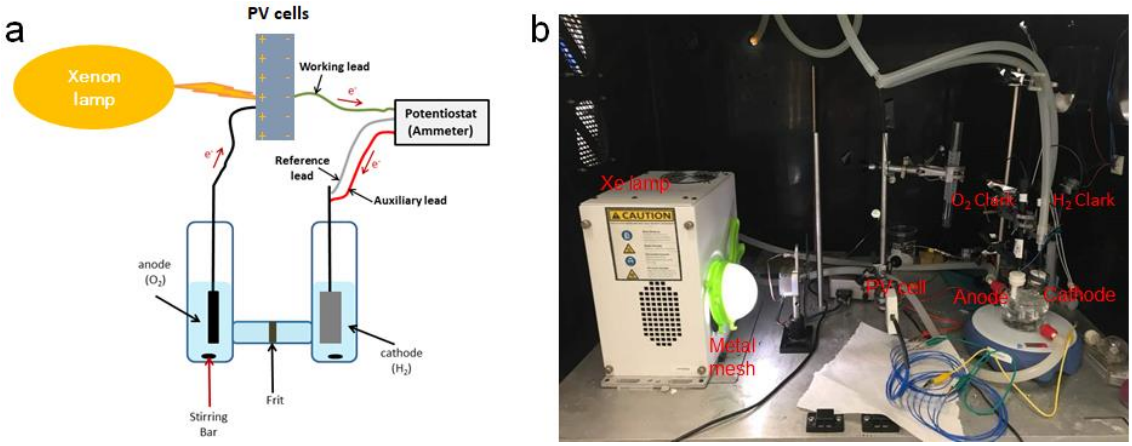

Figure S4. Schematic (a) and digital photo (b) of the setup to monitor the photocurrent and generated gas for solar-driven PV-EC water splitting.

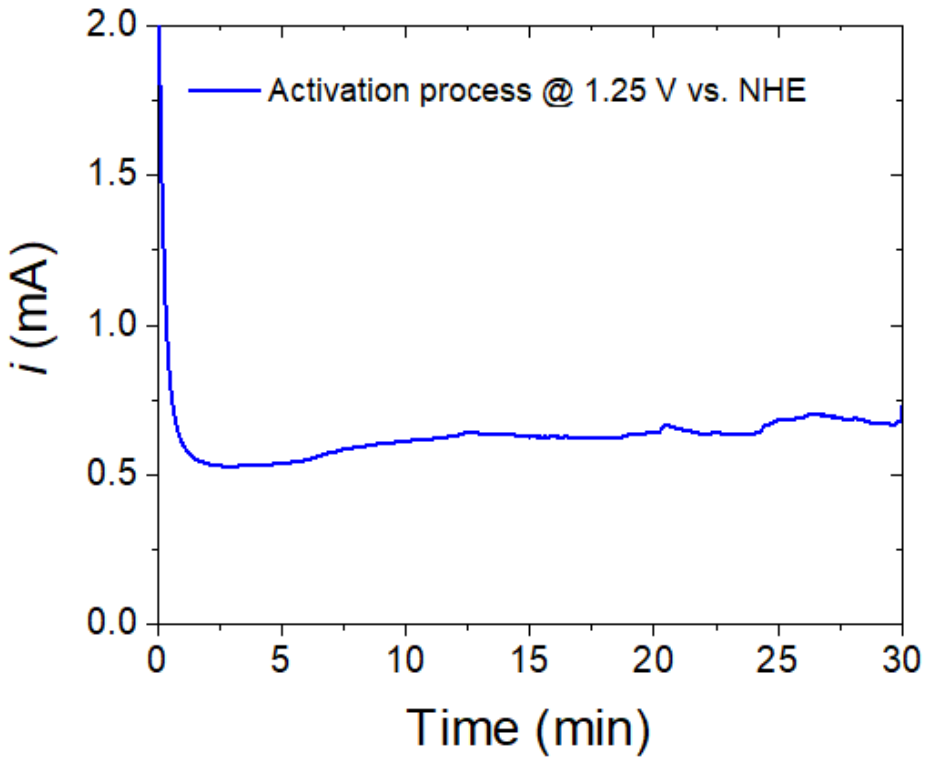

Figure S5. Activation process of a $\{Ru^{II}(tda)(bipy)\}_{15}$@CNTs/FTO electrode, which is achieved by half an hour constant potential electrolysis. The applied potential is 1.25 V vs. NHE and the electrolyte is pH 12 phosphate buffer with an ionic strength of 0.1 M.

Table S1. The monitored photocurrents and working voltages during the solar-driven PV-EC water splitting at pH 7 in Figure 3c.

Time (h)	ΔE (V)	*j* (mA/cm^2)
0.12	1.60 ~ 1.625	3.28
0.25	1.63	3.22
0.84	1.625 ~ 1.638	3.06
1.85	1.63 ~ 1.64	3
2.62	1.63 ~ 1.64	3.06
4.04	1.64	2.95

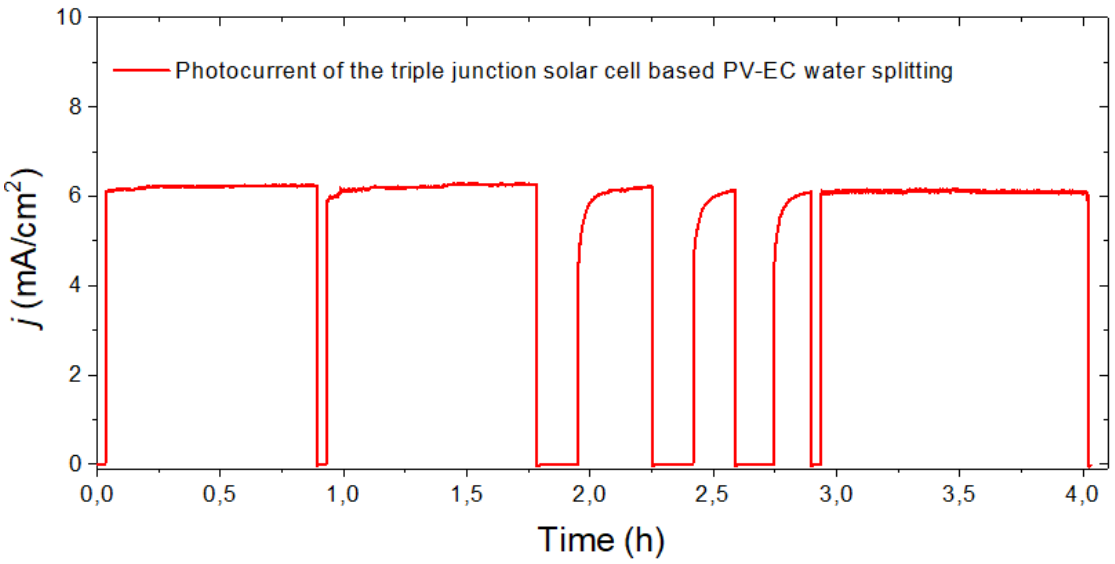

Figure S6. The whole photocurrent-time plot of the solar-driven PV-EC water splitting in Figure 5b, which has been collected under 0.36 sun illumination and at pH 7 electrolyte.

V

Table S2. The monitored photocurrents and corresponding photovoltages during the solar-driven PV-EC water splitting at pH 7 in Figure S6.

Time (h)	ΔE (V)	*j* (mA/cm^2)
0.1917	1.9	6.15
0.8394	1.935~1.936	6.25
1.4833	1.930~1.934	6.23
2.8861	1.95	6.2
2.9589	1.936~1.941	6.2

Table S3. A summary of all the integrated PV-EC water splitting devices that have been reported before. The PV-PEC configurations are not considered here.

PV cell	Electrolyser	Electrolyte	STH Efficiency	Stability	References
Two perovskite solar cells connected in series (0.318 cm^2)	NiFe LDH/Ni foam (5 cm^2, both sides)	1 M NaOH	12.3 %	2 h (~ 78 %)	Science 345,1593 (2014)
A commercial Si solar cell module (5 cm^2)	CoMnO@CN (both sides)	1 M KOH	8 %	120 h (~ 100 %)	J. Am. Chem. Soc. 137, 14305 (2015)
Two GaAs solar cells connected in series (5.36 cm^2)	Anode: NiFe LDH Cathode: Ni@Cr2O3-NiO (1 cm^2, both sides)	1 M KOH	15 %	24 h (~ 100 %)	Angew. Chem. Int. Ed. 54, 11989 (2015)
Triple junction polymer solar cell (0.09 cm^2)	Anode: GC-RuO_2 (4.1 cm^2) Cathode: SST-NiMoZn (1 cm^2)	0.1 M phosphate buffer (pH 7)	6 %	50 h (~77.8 %)	ACS Catal. 6, 3310 (2016)
Single InGaP/GaAs/GaInNAs(Sb) triple juction solar cell (0.316 cm^2)	Anode: Ir/Nafion/Ti mesh Cathode: Pt/Nafion/carbon paper (6.25 cm^2, both sides)	Millipore water (80 °C)	30 % under 42 suns	48 h (90 %) under 42 suns	Nat. Commun. 7, 13237 (2016)
Single InGaP/GaAs/Ge triple junction solar cell (0.3025 cm^2)	Anode: metal Hexacyanometallates@basic cobalt carbonate/ carbon fiber cloth Cathode: NiMoS/carbon fiber cloth (1 cm^2, both sides)	Buffered seawater electrolyte (pH 7)	17.9 %	100 h (90 %)	Adv. Mater. 30, 1707261 (2018)
Two perovskite solar cells connected in series (0.18 cm^2)	Anode{Ru^{II}(tda)(bipy)}$_{15}$@ CNTs/FTO (1.87 cm^2) Cathode: Pt mesh	1 M phosphate buffer (pH 7)	13.2 % under 0.28 sun	4.4 h (~90 %) under 0.28 sun	This work
Single InGaP/GaAs/Ge triple junction solar cell (0.18 cm^2)	Anode: {Ru^{II}(tda)(bipy)}$_{15}$@CNTs/C-plate (1.5 cm^2) Cathode: Pt mesh	1 M phosphate buffer (pH 7)	21.2 % under 0.36 sun	4 h (100 %) under 0.36 sun	This work

Chapter 6:

General conclusions and perspectives

VI

The detailed conclusions of all the research performed in this thesis have been deeply described at the end of each corresponding Chapters 3-5. Here in this chapter, I will make a general conclusions about this thesis and explain the perspective applications of our research studies.

VI

With the motivation to make our contribution to improving the globally environmental and energy problems, in this PhD thesis I carried out an investigation about of airbone pollutants, and then peformed the exploration of novel materials and molecules for pollution free clean energy, which maily focused on solar energy converted hydrogen through water splitting in this thesis. During the past years investigation, I have learned how to grow high quality metal/metal oxide thin films through physical vapor depositions, such as sputtering, e-beam evaporation and ALD. I have learned how to built/assemble the configurations for various solar-driven water splitting devices, including PEC and PV-EC water splitting devices. The (photo)electrochemical analysis is one of the most important characterization methods in my research, and I have gained lots of experiences form this basic analysis to understand my metal oxides or molecular catalysts better. I have also learned how to perform a series of morphological/topographical, electrical, mechanical and chemical characterizations at nanoscale/microscale through AFM, SEM, EDX, TEM, and XPS.

In this first part of my thesis, I have statistically analyzed more than 500 small airbone pollutant particles (mainly $PM_{2.5}$ particles), which were *in situ* collected from the polluted air. Different from other literatures, in our study, we for the first time combined the mechanical characterization with the morphorlogic and chemical charaterizations on the PM2.5 particles, which helps to understand how airbone pollutant particles look like regarding to its shape, size, chemical composition and adhension property. From my stduy we can draw the following conclusions:

- The $PM_{2.5}$ particles mainly show three main shapes, which are fluffy soot particles, elongated minerals, and spherical fly ash. The soot particles are rich in carbon, whcih are mainly from incomplete combustion of hydrocarbons. The elongated

minerals are with high content of metals from coal-fired power plants. And the spherical fly ash is mainly made of metal silicates from road dust, construction, coal combustion and secondary atmospheric reactions.

- The carbon-rich fluffy soot particles are always more unstable and much stickier than enlongated minerals and spherical fly ash, and they how very high adhesiveness and aggregation, which make them compile other chemical composition easily. These results indicate the soot aggregates can be more toxic/dangerous than enlongated minerals and spherical fly ash for the human bodies.
- More than 50% $PM_{2.5}$ particles strongly interact with the substrate through a ultra-thin (< 10 nm) dark trace layer. The statistical analysis shows that this dark trace layer is very stable even under mechanical stress and it is consisted of alkali metals, hydrogen and CH groups. This result may provide new ideas to remove the $PM_{2.5}$ particles in our body from biomedical views.

After the statistically characterizations on the airborne pollutant particles, I realized that the only way we can reduce the pollutant air emmission is to reduce/replace the traditional fossil fules by sustainable and clean energies. In my research, I focus on transferring sunlight to storable and transportable hydrogen through water spliiting. There are three kinds of soalr water splitting devices mostly proposed. In this thesis, I performed my research related to two of them. The first one is PEC water splitting devices, in whcih I have mainly focused on the exploration of cheap metal oxides catalysts functionalized silicon photonodes. My main acheivenments related to the PEC water splitting deevices are:

VI

- The CuO thin films has been for the first time used as protecting and catalytic layer in the silicon photoanodes, which is formed through the oxidation of the sputtering deposited copper thin films. And this resulting CuO based silicon photoanode shows an onset potentail (@ 1 mA/cm^2) of 0.53 V vs. SCE at pH 9 for water oxidation (75 mV overpotential) and a good stability of more than 10 hours under 1 sun illumination. Compared to the analogous CuO based FTO electrodes, the light sensitive CuO based Si photoanodes can generate a photovoltage of 420 mV. This study provides new materilas for fabricating low cost, active and stable photoelectrodes for PEC water splitting devices.
- Differnt thicknesses (2 nm, 5 nm and 10 nm) based nickel thin films coated silicon photoanodes have been fabricated and their stability has been statistically analyzed. The stability of the photoanodes increased with the thickness of the nickel films, which are ~18 h for 2 nm, ~150 h for 5 nm and >260 h for 10 nm nickel coated silicon photoanodes under light illumination at pH 14. For 2 nm nickel coated silicon photoanodes, they decayed due to the electrolyte contaminations and dramatic thickness increase of the native SiO_2 layer, while for 5 and 10 nm nickel coated photoanodes, they degraded due to the formation of many pin-holes on the surface. This study can help understand the ageing mechanism of the photoelectrodes and may provide new insights to enhace the stability for PEC water splitting devices.
- After understanding the ageing mechanism of the nickel coated silicon photoanodes, the nickel and silicon interface has been enigeered. This interface engineering has been achieved by replacing the native SiO_2 layer of the silicon by evaporated thin titanium layer, which results in Ni/Ti/Si photoanodes. Compared to the thin nikel film directly coated silicon photoanodes (published in Science in

2013), this Ni/Ti coated photoanode lowers the onset potential (more cathodic) of ~42 mV for water oxidation under 1 sun illumination at pH 14. In principle, the onset potential of the photoanode should be as cathodic as possible. Moreover, this Ni/Ti/Si photoanode shows a very long stblity for ~6.5 days at 10 mA/cm^2 under 1 sun illumination at pH 14. This study provides new ideas about interface engineering for the photoelectrodes and is very promising for long stability PEC water splitting devices.

Finally, we moved to another kind of solar-driven water splitting configuration, which is PV-EC water splitting. In this configuration, I have generated oxygen and hydrogen without applying any external bias, which is achieved by just absorbing soalr illumiantion. The mian conclusions of this work are:

- A molecular catalyst for water oxidation has been used for the first time in PV-EC water splitting devices, which shows active and stable catalytic behavior. This result provides more opportunities for enhancing the performance of PV-EC water splitting devices since molecular catalysts are easier to tune and analyze compared to the commonly used electrolysers based on metal oxides.
- The PV-EC water splitting device is integrated through combining the PV cells to absorb solar energy with an electrolyser consisting of a ruthenium molecular complex based anode and Pt cathode. Two kinds of PV cells are used in the PV-EC water splitting configuration in this thesis, including series connected perovskite solar cells and a commercially available triple junction III-V semiconductors based solar cell. The III-V semiconductors based solar cell integrated PV-EC water splitting device shows the highest STH efficiency of 21.2 %

VI

at neutral pH (room temperature) just under solar illumination without applying any external bias. The stability of the device is also good (> 4 hours at 6.2 mA/cm^2) under light illumination at pH 7. This result provides possibilities to make large scale solar-driven water splitting devices pratically available.

Appendix A: Scientific curriculum vitae

Personal Information

Name: Yuanyuan Shi
Date of Birth: August 10th, 1990
Place of Birth: Anhui Province, China
Languages: Chinese (native), English
Phone/Email: +34 698-561-550/syy0909078@126.com
Google Scholar: https://scholar.google.com/citations?user=YnfCqQkAAAAJ&hl=en

Education Background

October 2018	PhD in Nanoscience, Materials and Chemical Engineering Institute of Chemical Research of Catalonia (ICIQ, Spain) **Supervisor: Prof. Antoni Llobet & Prof. Mario Lanza**
July 2018	PhD in Nanoscience (Information Enigineering) Department of Engineering University of Barcelona (Spain) **Supervisor: Prof. Mario Lanza**
01/09/2016 - 31/08/2017	Visiting PhD student in Electrical Engineering Stanford University (US) **Supervisor: Prof. H.-S. Philip Wong**
September 2015	Master in Nanoscience, Materials and Processes Institute of Chemical Research of Catalonia (ICIQ, Spain) **Supervisor: Prof. Antoni Llobet & Prof. Mario Lanza**
July 2013	Bachelor in Chemistry (Education) Anhui Normal University (China) **Thesis Director: Prof. Zhenghua Wang**

Research Experience

Research skills:

1) Materials synthesis: High quality 2D materials using chemical vapor deposition (CVD), High-k materials using atomic layer deposition (ALD) and sputtering, Metallic films using E-beam evaporation, Carbon quantum dots by hydrothermal method.

2) Device fabrication: Photolithography, Electron Beam lithography, Laser-patterned shadow mask.

3) Materials and device characterization: Deep conductive atomic force microscopy (CAFM) and scanning thermal microscopy (SThM) analyses (statistics, high resolution maps, topography-current correlation, fittings to models, in situ degradation studies), probe station, optical microscopy, scanning electron microscopy (SEM), transmission electron microscopy (TEM), electron energy loss spectroscopy (EELS), energy Dispersive X-ray Spectroscopy (EDX), Raman spectroscopy, ultraviolet-visible spectroscopy (UV-Vis), X-ray photoelectron spectrometer (XPS), fluorescence spectroscopy, electrochemical analyzer workstation, gas chromatography (GC).

Technical Software:

1) Familiar with the software of Origin for preparing all kinds of curves and histograms, NanoScope Analysis for processing AFM data, XPS Peak for analyzing XPS peaks, Labspec for processing Raman spectroscopy data, and Nano Measure for analyzing particles in microscopy images.

2) Familiar with layout to design the shadow mask for photolithography, and learned how to do basic density functional theory (DFT) simulation by VNL-ATK.

Research projects:

- **For PhD in Nanoscience (Information Enigineering):**

1) **Origin of resistive switching (RS) in polycrystalline HfO_2 thin films (09/2013-03/2015):** In this project, we have performed the first nanoscale electromechanical study of RS by using CAFM, since the tip of CAFM allows applying both electrical and mechanical stresses. And our study reveals that RS always takes place at those locations of the sample that are mechanically weaker.

2) **Synthesis and characterization of 2D materials (09/2013-08/2017)**: In this project, I have learned how to grow high quality 2D materials (mainly graphene and hexagonal boron nitride, *h*-BN) by CVD, and deeply analyzed the fundamental properties and performances of graphene and *h*-BN.

3) **Use of 2D materials in resistive switching devices (01/2016-now):** In this project, we have designed, fabricated and analyzed 2D materials based the metal-insulator-metal (MIM) structure-like RS devices. The observation of the coexistence of volatile and non-volatile RS in h-BN based devices, allows us to use the h-BN based RS devices to emulate the electronic synapses for neuromorphic computing.

- **For PhD in Nanoscience, Materials and Chemical Engineering:**

4) **Nanoscale characterization on airborne pollutant particles (12/2013-05/2015)**: In this project, we for the first time have analyzed the mechanical properties of air pollutant particles ($PM_{2.5}$) and revealed that the most toxic $PM_{2.5}$ particles are the stickiest ones (rich in carbon).

5) **Cheap metal oxides based silicon photoanodes for photoelectrochemical (PEC) water splitting (07/2014-09/2016)**: In this project, CuO_X and NiO_X functionalized silicon photoanodes have been designed and fabricated, respectively. This project paves the way of using cheap and abundant materials to transfer sunlight into storable H_2 energy.

6) **Molecular catalyst for photovoltaic-electrolysis (PV-EC) water splitting (10/2017-now)**: This project uses a photovoltaic solar cell to absorb light, and the excited electrons and holes can split water without any external bias. This work contributes to making the spontaneous solar-driven water splitting devices commercial available.

Research Papers (41 papers, citations: 275)

- **For PhD in Nanoscience (Information Enigineering):**

1) **Y. Shi**, X. Liang, B. Yuan, V. Chen, H. Li, F. Hui, Z. Yu, F. Yuan, E. Pop, H.-S. P. Wong, M. Lanza, Electronic synapses made of layered two-dimensional materials, ***Nature Electronics***, 1, 458-465 (2018). **Highlighted by Nature Electronics News & Views.**

2) **Y. Shi**, C. Pan, V. Chen, N. Raghavan, K. L. Pey, F. Puglisi, E. Pop, H.-S. P. Wong, M. Lanza, Coexistence of volatile and non-volatile resistive switching in 2D *h*-BN based electronic synapses, ***IEDM Technical Digest***, DOI: 10.1109/IEDM.2017.8268333 (2017).

3) **Y. Shi**, Y. Ji, F. Hui, M. Nafria, M. Porti, G. Bersuker, M. Lanza, *In situ* demonstration of the link between mechanical strength and resistive switching in conductive filament based non-volatile memories, ***Advanced Electronic Materials,*** 1, 1400058 (2015).

4) **Y. Shi**, Y. Ji, F. Hui, M. Nafria, M. Porti, G. Bersuker, M. Lanza, New insights on the origin of resistive switching in HfO_2 thin films: the role of local mechanical strength, ***22nd International Symposium on the physical and Failure Analysis of Integrated Circuits (IPFA)***, DOI: 10.1109/IPFA.2015.7224435 (2015).

5) **Y. Shi**, Y. Ji, F. Hui, M. Lanza, On the ageing mechanisms of graphene-on-metal electrodes, ***10th Spanish Conference on Electron Devices (CDE)***, DOI: 10.1109/CDE.2015.7087446 (2015).

6) **Y. Shi**, Y. Ji, F. Hui, V. Iglesias, M. Porti, M. Nafria, E. Miranda, G. Bersuker, M. Lanza, Elucidating the origin of resistive switching in ultrathin hafnium oxides through high spatial resolution tools, ***ECS Transactions***, 64, 19-28 (2014).

7) **Y. Shi**, Y. Ji, F. Hui, H.-H. Wu, M. Lanza, Ageing mechanisms and reliability of graphene-based electrodes, ***Nano Research***, 7, 1820-1831 (2014). **Front cover.**

8) G. Parekh†, **Y. Shi**†, J. Zheng†, X. Zhang, S. Leporatti, Nano-carriers for targeted delivery and biomedical imaging enhancement, ***Therapeutic delivery***, 9, 451-468 (2018). - (†Equal contribution).

9) L. Jiang†, **Y. Shi**†, F. Hui†, K. Tang, Q. Wu, C. Pan, X. Jing, H. J Uppal, F. Roberto M. Palumbo, G. Lu, T. Wu, H. Wang, M. A Villena, X. Xie, P. C McIntyre, M. Lanza, Dielectric breakdown in chemical vapor deposited hexagonal boron nitride, ***ACS Applied Materials & Interfaces***, 9, 39758-39770 (2017). - (†Equal contribution).

10) M. Lanza, **Y. Shi** et al., Recommended methods to study resistive switching devices, ***Advanced Electronic Materials***, 1800143 (2018).

11) F. Hui, M. A Villena, W. Fang, A.-Y. Lu, J. Kong, **Y. Shi**, X. Jing, K. Zhu, M. Lanza, Synthesis of large-area multilayer hexagonal boron nitride sheets on iron substrates and its use in resistive switching devices, ***2D Materials***, 5, 031011(2018).

12) B. Wang, N. Xiao, C. Pan, **Y. Shi**, F. Hui, X. Jing, K. Zhu, B. Guo, M. A Villena, E. Miranda, M. Lanza, Experimental observation and mitigation of dielectric screening in hexagonal boron nitride based resistive switching devices, ***Crystal Research and Technology***, 53, 1800006 (2018).

13) F. Palumbo, X. Liang, B. Yuan, **Y. Shi**, F. Hui, M. A Villena, M. Lanza, Bimodal dielectric breakdown in electronic devices using chemical vapor deposited hexagonal boron nitride as dielectric, ***Advanced Electronic Materials***, 4, 1700506 (2018).

14) X. Liang, B. Yuan, **Y. Shi**, F. Hui, X. Jing, M. Lanza, F. Palumbo, Enhanced reliability of hexagonal boron nitride dielectric stacks due to high thermal conductivity, ***IEEE Reliability Physics Symposium (IRPS)***, DOI: 10.1109/IRPS.2018.8353666 (2018).

15) S. Fujii, J. A. Incorvia, F. Yuan, S. Qin, F. Hui, **Y. Shi**, Y. Chai, M. Lanza, H.-S. P. Wong, Scaling the CBRAM Switching Layer Diameter to 30 nm Improves Cycling Endurance, ***IEEE Electron Device Letters***, 99, 1-4 (2018).

16) K. Tang, A. C Meng, F. Hui, **Y. Shi**, T. Petach, C. Hitzman, A. L. Koh, D. Goldhaber-Gordon, M. Lanza, P. C McIntyre, Distinguishing oxygen vacancy electromigration and conductive filament formation in TiO_2 resistance switching using liquid electrolyte contacts, ***Nano Letters***, 17, 4390-4399 (2017).

17) C. Pan, Y. Ji, N. Xiao, F. Hui, K. Tang, Y. Guo, X. Xie, F. M. Puglisi, L. Larcher, E. Miranda, L. Jiang, **Y. Shi**, I. Valov, P. C McIntyre, R. Waser, M. Lanza, Coexistence of grain-boundaries-assisted bipolar and threshold resistive switching in multilayer hexagonal boron nitride, ***Advanced Functional Materials***, 27, 1604811 (2017). **Selected as frontispiece.**

18) N. Xiao, M. A Villena, B. Yuan, S. Chen, B. Wang, M. Eliáš, **Y. Shi**, F. Hui, X. Jing, A. Scheuerman, K. Tang, P. C McIntyre, Mario Lanza, Resistive random access memory cells with a bilayer TiO_2/SiO_X insulating stack for simultaneous filamentary and distributed resistive switching, ***Advanced Functional Materials***, 1700384 (2017).

19) C. Pan, E. Miranda, M. A Villena, N. Xiao, X. Jing, X. Xie, T. Wu, F. Hui, **Y. Shi**, M. Lanza, Model for multi-filamentary conduction in graphene/hexagonal boron-nitride/graphene based resistive switching devices, ***2D Materials***, 4, 025099 (2017).

20) X. Song, F. Hui, K. Gilmore, B. Wang, G. Jing, Z. Fan, E. Grustan-Gutierrez, **Y. Shi**, L. Lombardi, S. Hodge, A. Ferrari, M. Lanza, Enhanced piezoelectric effect at the edges of stepped molybdenum disulfide nanosheets, ***Nanoscale***, 9, 6237 (2017).

21) F. Hui, S. Chen, X. Liang, B. Yuan, X. Jing, **Y. Shi**, M. Lanza, Graphene coated nanoprobes: A review, ***Crystals***, 7, 269 (2017).

22) X. Song, F. Hui, T. Knobloch, B. Wang, Z. Fan, T. Grasser, X. Jing, **Y. Shi**, Mario Lanza, Piezoelectricity in two dimensions: Graphene vs. molybdenum disulfide, ***Applied Physics Letters***, 111, 083107 (2017).

23) F. Hui, P. Vajha, Y. Ji, C. Pan, E. Grustan-Gutierrez, H. Duan, P. He, G. Ding, **Y. Shi**, M. Lanza, Variability of graphene devices fabricated using graphene inks: atomic force microscope tips, ***Surface & Coatings Technology***, 320, 391-395 (2017).

24) L. Jiang, N. Xiao, B. Wang, E. Grustan-Gutierrez, Xu Jing, P. Babor, M. Kolíbal, G. Lu, T. Wu, H. Wang, F. Hui, **Y. Shi**, B. Song, X. Xie, M. Lanza, High resolution characterization of hexagonal boron nitride coatings exposed to aqueous and air oxidative environments, ***Nano Research***, 10, 2046-2055 (2017).

25) F. Puglisi, L. Larcher, C. Pan, N. Xiao, **Y. Shi**, F. Hui, M. Lanza, 2D *h*-BN based RRAM devices, ***IEDM Technical Digest***, DOI: 10.1109/IEDM.2016.7838544 (2016).

26) X. Jing, E. Panholzer, X. Song, E. Grustan-Gutierrez, F. Hui, **Y. Shi**, G. Benstetter, Y. Illarionov, T. Grasser, M. Lanza, Fabrication of scalable and ultra low power photodetectors with high light/dark current ratios using polycrystalline monolayer MoS_2 sheets, ***Nano Energy***, 30, 494-502 (2016).

27) Y. Ji, C. Pan, F. Hui, **Y. Shi**, L. Jiang, N. Xiao, L. Larcher, M. Lanza, Nanoscale homogeneity and degradation process of two dimensional atomically thin hexagonal boron nitride dielectric stacks, ***23rd IEEE International Symposium on the Physical and Failure Analysis of Integrated Circuits (IPFA)***, DOI: 10.1109/IPFA.2016.7564323 (2016).

28) F. Hui, C. Pan, Y. Ji, **Y. Shi**, M. Lanza, On the use of two dimensional hexagonal boron nitride as dielectric, ***Microelectronic Engineering***, 163, 119-133 (2016).

29) Y. Ji, F. Hui, **Y. Shi**, V. Iglesias, D. Lewis, J. Niu, S. Long, M. Liu, A. Hofer, W. Frammelsberger, G. Benstetter, A. Scheuermann, P. C. McIntyre, M. Lanza, Characterization of the photocurrents generated by the laser of atomic force microscopes, ***Review of Scientific Instruments***, 87, 083703 (2016).

30) F. Hui, **Y. Shi**, Y. Ji, M. Lanza, H. Duan, Mechanical properties of locally oxidized graphene electrodes, ***Archive of Applied Mechanics,*** 85, 339-345 (2015).

31) Y. Ji, C. Pan, M. Zhang, S. Long, X. Lian, F. Miao, F. Hui, **Y. Shi**, L. Larcher, E. Wu, M. Lanza, Boron nitride as two dimensional dielectric: reliability and dielectric breakdown, ***Applied Physics Letters,*** 108, 012905 (2015).

32) F. Hui, P. Vajha, **Y. Shi**, Y. Ji, H. Duan, A. Padovani, L. Larcher, X.-R. Li, J.-J. Xu, M. Lanza, Moving graphene devices from lab to market: advanced graphene- coated nanoprobes, ***Nanoscale***, 8, 8466-8473 (2015). **Front cover.**

33) Y. Ji, F. Hui, **Y. Shi**, T. Han, X. Song, C. Pan, M. Lanza, Note: Fabrication of a fast-response and user-friendly environmental chamber for atomic force microscopes, ***Review of Scientific Instruments***, 86, 106105 (2015).

34) J. Hu, Y. Ji, **Y. Shi**, F. Hui, H. Duan, M. Lanza, A Review on the use of graphene as a protective coating against corrosion, ***Annals of Materials Science and Engineering***, 1, 16 (2014).

- **For PhD in Nanoscience, Materials and Chemical Engineering:**

1) **Y. Shi**, T. Han, C. Gimbert-Suriñach, X. Song, M. Lanza, A. Llobet, Substitution of native silicon oxide by titanium in Ni-coated silicon photoanodes for water splitting solar cells, ***Journal of Materials Chemistry A***, 5, 1996-2003 (2017). **Front cover.**

2) **Y. Shi**, C. Gimbert-Suriñach, T. Han, S. Berardi, M. Lanza, A. Llobet, CuO-functionalized silicon photoanodes for photoelectrochemical water splitting devices, ***ACS Applied Materials & Interfaces,*** 8, 686-702. (2016).

3) **Y. Shi**, Y. Ji, H. Sun, F. Hui, J. Hu, Y. Wu, J. Fang, H. Lin, J. Wang, H. Duan, M. Lanza, Nanoscale characterization of $PM_{2.5}$ airborne pollutants reveals high adhesiveness and aggregation capability of soot particles, ***Scientific Reports***, 5, 11232 (2015). **Reported by 90 News Medias, including Xinhua News agency, China Science & Technology Daily.**

4) T. Han[†], **Y. Shi**[†], X. Song, A. Mio, L. Valenti, F. Hui, S. Privitera, S. Lombardo, M. Lanza, Ageing mechanisms of highly active and stable nickel-coated silicon photoanodes for water splitting, ***Journal of Materials Chemistry A***, 4, 8053-8060 (2016). **Back cover.** - ([†]Equal contribution).

5) T. Han, S. Privitera, R. G. Milazzo, C. Bongiorno, S. D. Franco, F. L.Via, X. Song, **Y. Shi**, M. Lanza, S. Lombardo, Photo-electrochemical water splitting in silicon based photocathodes enhanced by plasmonic/catalytic nanostructures, ***Materials Science and Engineering: B***, 225, 128-133 (2017).

6) **Y. Shi**, B. Wang, M. Bartrons, M. Kolíbal, P. Bábor, X. Zhang, E. Grustan-Gutierrez, M. Lanza, Interaction between $PM_{2.5}$ airborne pollutants and third bodies, *Submitted* (2018).

7) **Y. Shi**, T.-Y. Hsieh, C. Gimbert-Suriñach, M. A. Hoque, S. Chen, T.-C. Wei, E. Palomares, M. Lanza, A. Llobet, An anode based on a ruthenium molecular water oxidation catalyst for a photovoltaic-electrolysis water splitting with solar to hydrogen efficiency of 21.2 %, *in preparation* (2018).

Book Chapters

- C. Pan, **Y. Shi**, F. Hui, E. Grustan-Gutierrez, M. Lanza, "Conductive Atomic Force Microscopy: Applications in Nanomaterials-Chapter 1: Introduction, history and status of the CAFM", Publisher*: Wiley-VCH,* ISBN: 978-3-527-34091-0, August 2017.

Patents

- **Y. Shi**, F. Hui, M. Lanza, Cost-effective fabrication of ultra-durable atomic force microscope tips using graphene powder coatings, *International Patent*, Ref. no. WO2016/074305, July 16th of 2016. In September 2016 **this patent received 1 M$ investment** from the Beijing Institute of Collaborative Innovation for creating a start-up and introducing this product in the market. (This can be considered as an example of **participation in industrial innovation**)

- **Y. Shi**, Y. Ji, C. Pan, F. Hui, N. Xiao, M. Lanza, Hexagonal boron nitride as dielectric medium for resistive random access memories, International Patent, 201510968511.7 (Provisional patent, December 22nd 2015).

Conferences

- **Y. Shi,** H.-S. P. Wong, M. Lanza, Electronic synapses made of layered two-dimensional materials, ***BIT's 5th Annual World Congress of Smart Materials***, March 6th-8th 2019, Rome, Italy. **(Invited talk)**

- **Y. Shi**, T. Han, C. Gimbert-Suriñach, M. Lanza, A. Llobet, Metal-oxide-semiconductor (MOS) structures based silicon photoanodes for photoelectrochemical water splitting, ***15th Doctoral Day in Nanoscience, Materials and chemical Engineering***, May 23rd 2018, Rovira i Virgili Unviersity, Tarragona, Spain.

- K. Tang, A. Meng, F. Hui, **Y. Shi**, T. A. Petach, D. Goldhaber-Gordon, M. Lanza, P. C McIntyre, Distinguishing oxygen vacancy electromigration and conductive filament formation in TiO_2 resistance switching using liquid electrolyte contacts, ***48th IEEE Semiconductor Interface Specialists Conference***, December 6th-9th 2017, San Diego, CA, USA.

- **Y. Shi**, K. Tang, V. Chen, P. C McIntyre, E. Pop, H.-S. P. Wong, M. Lanza, 2D hexagonal boron nitride (*h*-BN) based RRAM devices, ***International Symposium on Memory Devices for Abundant Data Computing***, September 22nd-24th 2017, Hong Kong Polytechnic University, Hong Kong.

- Mario Lanza, M. A. Villena, **Yuanyuan Shi**, Shaochuan Chen, Fei Hui, Xu Jing, Status and prospects of 2D materials based memristors, ***XXVI International Materials Research Congress***, August 20th-25th 2017, Cancun, Mexico.

- **Y. Shi**, M. Lanza, H.-S. P. Wong, Multilayer Hexagonal Boron Nitride based RRAM Devices, ***China RRAM International Workshop***, June 12th-13th 2017, Suzhou, China. **(Invited talk)**

- **Y. Shi**, K. Tang, V. Chen, F. Hui, P. C McIntyre, E. Pop, H.-S. P. Wong, M. Lanza, 2D hexagonal boron nitride (*h*-BN) based RRAM devices, ***Non-Volatile Memory Technology Research Initiative (NMTRI) Review Meeting***, May 11th 2017, Stanford University, CA, USA.

- **Y. Shi**, T. Han, X. Song, C. Gimbert-Suriñach, M. Lanza, A. Llobet, CuO and NiOx fictionalized silicon photoanodes for photoelectrochemical water splitting, ***2017 Stanford University Photonics Retreat (SUPR 9)***, April 28th-30th 2017, Pacific Grove, CA, USA.

- **Y. Shi**, C. Pan, F. Hui, M. Lanza, Grain boundaries driven bipolar resistive switching in multilayer hexagonal boron nitride, ***2nd International Symposium on Science and Technology of 2D Materials***, February 3rd-4th 2017, Orlando, FL, USA.

- F. Hui, W. S. Leong, **Y. Shi**, J. Kong, M. Lanza, Scalable resistive random access memories made of multilayer h-BN grown by CVD on Iron and Platinum electrode, ***2nd International Symposium on Science and Technology of 2D materials***, February 3rd-4th 2017, Orlando, FL, USA.

- N. Xiao, C. Pan, X. Jing, F. Hui, **Y. Shi**, P. Babor, M. Kolíbal, M. Lanza, A resistive random access memory cell with both filamentary and distributed resistive switching, ***2016 International Workshop on Resistive Memories***, October 10th-11th 2016, Stanford, CA, USA.

- **Y. Shi**, T. Han, X. Song, M. Lanza, Reliability and ageing mechanisms of ultrathin nickel coated silicon photoanodes for water splitting, ***Thin Solid Films conference***, July 12th-15th 2016, Singapore.

- **Y. Shi**, T. Han, X. Song, M. Lanza, Silicon photoanodes for photoelectrochemical water splitting devices, 19th Workshop on Dielectrics for Microelectronics, June 27th-30th, 2016, Catania, Italy.

- **Y. Shi**, T. Han, C. Gimbert-Suriñach, X. Song, S. Berardi, A. Llobet, M. Lanza, Metal oxides coated silicon photoanodes for photoelectrochemical water splitting devices, 2nd Molecules and Materials for Artificial Photosynthesis Conference, Feb. 25th-28th, 2016, Cancun, Mexico.

Scientific Seminars

- **Y. Shi**, C. Pan, V. Chen, N. Raghavan, K. Pey, F Puglisi, E. Pop, H.-S. P. Wong, M. Lanza, Coexistence of volatile and non-volatile resistive switching in 2D *h*-BN based electronic synapses, ***Invited talk***, April 14th, 2018, University of Science and Technology of China (USTC), Hefei, China.

Membership, Reviewer and Awards

- **IEEE Electron Devices Society (EDS) excellent PhD student fellowship**
- **Student Member of IEEE and Electron Devices Society** (since September 2016)
- **Student Member of the Royal Society of Chemistry** (since October 2015)
- **Reviewer of Thin Solid Films** (Since June 2018): Review 1 paper
- **Reviewer of ChemElectroChem** (Since December 2017): Review 2 papers
- **Reviewer of Scientific Reports** (since October 2016): Review 3 papers
- **Reviewer of Surface Coatings and Technology** (since June 2016): Review 1 paper
- **Review of ICMTCF**: Review 1 paper

- **National Scholarship** (2014): Award to top students by the Ministry of Education of the People's Republic of China. The awarded students must be authors of high-level academic achievement.
- **Outstanding graduation thesis of Anhui University** (2013): Award to the best graduated students for his/her bachelor thesis
- **National Encouragement Scholarship** (2010): Award to top students by the Ministry of Education of the People's Republic of China
- **Second-class Scholarship of Anhui University** (2010): Award to students who got high scores in all of the examinations during 2009-2010 (top 10%)
- **Merit Student of Anhui University** (2010): Award to students who had a comprehensive development in moral, intelligence and sports

Supervising and Mentoring

- 03/2018-present: Supervising the experiments of Shaochuan Chen (PhD student) on electrical characterization of layered two-dimensional materials based electronic synapses
- 09/2015-09/2016: Supervising the experiments of Bingru Wang (Master student) on nanoscale characterization of $PM_{0.1}$ air pollutant particles
- 09/2014-09/2016: Supervising the experiments of Tingting Han (Master student) on silicon photoanodes based PEC water splitting
- 10/2012-11/2012: Internship as a chemistry teacher at High School of Xuancheng (China)

Participation in Funded Projects

- Funding 1: MIM structure based RS devices for neuromorphic computing and information storage. (Received Funding: ¥ 600,000 for 3 years)
- Funding 2: Synthesis and Characterization of MIM structure based devices. (Received Funding: ¥ 400,000 for 2 years)
- Funding 3: Integration of new generation memory devices made of 2D layered structure. (Received Funding: ¥ 3000,000 for 3 years)
- Funding 4: Young 1000 Global Talent Recruitment Program (SX21400213). (Received Funding: ¥ 3000,000 for 3 years)
- Funding 5: Reliability of transition metal dichalcogenide field effect transistors (Joint project with Prof. Tibor Grasser). (Received Funding: ¥ 2200,000 for 3 years)
- Funding 6: Companies of the Non-Volatile Memory Technology Research Initiative (NMTRI) at Stanford University
- Funding 7: National Science Foundation EFRI 2-DARE EFRI: Energy-Efficient Electronics with Atomic Layers (E3AL). (award # 1542883)
- Funding 8: European School on Artificial Leaf: Electrodes Devices. (Ref # 765376 for 5 years)

Appendix B: Acronyms

2,2,2-Trifluoroethanol	TFE
2,2',7,7'-Tetrakis-(N,N-di-4-methoxyphenylamino)-9,9'-spirobifluorene	spiro-OMeTAD
Aerodynamic diameter	d_a
Atomic force microscope	AFM
Atomic layer deposition	ALD
Auger electron spectroscopy	AES
Band gap energy	E_g
Conduction band	CB
Conductive atomic force microscopy	CAFM
Controlled potential electrolysis	CPE
Cross sectional Transmission Electron Microscope	XTEM
$CuIn_xGa_{1-x}Se_2$	CIGS
Current-density versus potential	J-V
Current-time	I-t
Current-voltage	I-V
Cyclic voltammetry	CV
Dimethyl sulfoxide	DMSO
Dimethylformamide	DMF
Electron Energy Loss Spectroscopy	EELS
Energy Information Administration	EIA
Fill factor	FF
Fluorine doped tin oxide	FTO
Focused ion beam	FIB

Force-Distance	F-Z
Formamidinium iodide	FAI
High-resolution Transmission Electron Microscope	HRTEM
Hydrogen evolution reaction	HER
Inter/Intramolecular coupling	I2M
Isopropanol	IPA
Linear sweep voltammetry	LSV
Lithium bis(trifluoromethylsulphonyl)imide	Li-TFSI
Methylammonium bromine	MABr
Methylammonium chloride	MACl
Methylammonium iodide	MAI
Multi wall carbon nanotubes	MWCNTs
National Oceanic and Atmospheric Administration	NOAA
Normal hydrogen electrode	NHE
Open circuit potentials	V_{OC}
Oxygen evolution reaction	OER
Particulate matter	PM
Photoelectrochemical	PEC
Photovoltaic-electrolysis	PV-EC
Polycyclic aromatic hydrocarbons	PAH
Power conversion efficiency	PCE
Quantitative Nanomechanical Mapping	QNM
Rapid thermal oxidation	RTO
Reversible hydrogen electrode	RHE
Saturated calomel electrode	SCE

Scanning electron microscope images	SEM
Short circuit current density	J_{sc}
solar-to-hydrogen	STH
tert-butylpyridine	Tbp
Tetrahydrofuran	THF
Time-of-Flight Secondary Ion Mass Spectrometry	ToF-SIMS
Total primary energy supply	TPES
Transmission Electron Microscope	TEM
Turnover Frequency	TOF
valence band	VB
Water nucleophilic attack	WNA
Water oxidation catalyst	WOC
Water splitting	WS
World Health Organization	WHO
X-ray Photoelectron Spectroscopy	XPS

UNIVERSITAT ROVIRA I VIRGILI
MATERIALS AND MOLECULES FOR POLLUTION FREE CLEAN ENERGY
Yuanyuan Shi

UNIVERSITAT ROVIRA I VIRGILI
MATERIALS AND MOLECULES FOR POLLUTION FREE CLEAN ENERGY
Yuanyuan Shi

UNIVERSITAT
ROVIRA i VIRGILI